

NEW PHYSICAL INSIGHTS ABOUT TIDAL DISRUPTION EVENTS
FROM A COMPREHENSIVE OBSERVATIONAL INVENTORY AT X-RAY WAVELENGTHSKATIE AUCHETTL^{1,2}, JAMES GUILLOCHON^{3,4}, AND ENRICO RAMIREZ-RUIZ⁵*Submitted to ApJ*

ABSTRACT

We perform a comprehensive study of the X-ray emission from 70 transient sources which have been classified as a tidal disruption event (TDE) in the literature. We explore the properties of these candidates using nearly three decades of X-ray observations to quantify the properties and characteristics of X-ray TDEs observationally. We find that the emission from X-ray TDEs increase by two to four orders of magnitude compared to pre-flare constraints, which evolves significantly with time and decays with powerlaw indices that are typically shallower than the canonical $t^{-5/3}$ decay law, implying that X-ray TDEs are viscously delayed. These events exhibit enhanced column densities relative to Galactic and are quite soft in nature, with no strong correlation between the amount of detected soft and hard emission. At peak, jetted events have an X-ray to optical ratio $\gg 1$, while non-jetted events have a ratio ~ 1 , which suggests that these events undergo reprocessing at different rates. X-ray TDEs have long T_{90} values consistent with that expected from a viscously-driven accretion disk formed by the disruption of a main-sequence star by a black hole with a mass $< 10^7 M_\odot$. The isotropic luminosities of X-ray TDEs is bimodal such that jetted and non-jetted events are separated by a “reprocessing valley” which we suggest is naturally populated by optical/UV TDEs that most likely produce X-rays, but due to reprocessing this emission is “veiled” from observations. Our results suggest that non-jetted X-ray TDEs likely originate from partial disruptions and/or disruptions of low mass stars.

Keywords: black hole physics – accretion, accretion disks – galaxies:active – general: X-rays

1. INTRODUCTION

Black holes (BHs) with masses greater than approximately $10^{5-6} M_\odot$ are thought to reside in the central nuclei of all active Galaxies (see e.g., Kormendy & Richstone 1995; Magorian et al. 1998; Rees 1998; Gültekin et al. 2009, and a recent reviews by Ho 2008; Kormendy & Ho 2013; Graham 2016). Currently the most direct evidence for the existence of these massive objects comes from the detection of an Active Galactic Nuclei (AGN). AGN activity is characterised generally by recurring luminous X-ray flare emission, and Fe K line variability. The properties of these objects can only be explained by the continual accretion of material onto an object that must have a mass $> 10^6 M_\odot$ (e.g., Lynden-Bell 1969; Hoyle & Fowler 1963). However, based on accretion models of black hole evolution (e.g., Marconi et al. 2004) it is expected that there exists a large number of quiescent, weakly or non-accreting black holes BHs in which gas accretion occurs at a significantly slower rate (e.g., Kormendy & Gebhardt 2001). Evidence for the presence of these dormant BHs in non-active Galaxies such as the one found in our Milky Way arises from mostly indirect methods (e.g., Genzel et al. 2003; Ghez et al. 2003), making it difficult to probe the properties of these interesting objects. However, a more direct detection of a dormant massive BH at the center of a non-active Galaxy arises in the form of a tidal disruption event (TDE) (Hills 1975; Frank & Rees 1976; Kato & Hōshi 1978; Lid-

skii & Ozernoi 1979; Gurzadian & Ozernoi 1979; Carter & Luminet 1982; Luminet & Marck 1985; Rees 1988).

A TDE occurs when a star with a mass M_\star that is orbiting around a massive BH of mass M_{BH} approaches the BH at a radius less than the tidal disruption radius $R_t = (M_{BH}/M_\star)^{1/3}$ (Hills 1975; Rees 1988). At this point the star is subjected to the strong tidal forces of the BH which can exceed the self-gravity of the star, ripping the star apart (Hills 1975; Lacy et al. 1982; Rees 1988)⁶. A fraction of the stellar debris of this now destroyed star will be expelled on unbound orbits and escape from the BH, while $\sim 0.5 M_\star$ will be confined to highly eccentric, bound orbits (Rees 1988; Evans & Kochanek 1989; Ayal et al. 2000). This material will eventually be accreted onto the BH producing a luminous, short-lived accretion-powered flare (Lacy et al. 1982; Rees 1988; Evans & Kochanek 1989; Phinney 1989), which can emit above the Eddington Luminosity for a BH with $M_{BH} < 10^7 M_\odot$ (Strubbe & Quataert 2009; Lodato & Rossi 2011; De Colle et al. 2012). This accretion powered flare peaks in the UV and/or soft X-ray bands (Ulmer 1999)⁷. The luminosity of these events is thought to loosely follow a power law decline characterised by $t^{-5/3}$, which is set by the timescale in which the stellar debris eventually returns to pericenter (e.g., Evans & Kochanek 1989; Phinney 1989; Cannizzo et al. 1990; Rees 1990). However, exactly how depends heavily on the evolution and physics within the accretion stream (e.g., Kochanek 1994; Ramirez-Ruiz & Ross-wog 2009; Lodato & Rossi 2011; Guillochon & Ramirez-Ruiz 2013; Cheng & Bogdanović 2014; Guillochon & Ramirez-Ruiz 2015; Shiokawa et al. 2015). In addition to this highly

¹ Center for Cosmology and Astro-Particle Physics, The Ohio State University, 191 West Woodruff Avenue, Columbus, OH 43210, USA

² Department of Physics, The Ohio State University, 191 W. Woodruff Avenue, Columbus, OH 43210, USA

³ Harvard-Smithsonian Center for Astrophysics, 60 Garden St., Cambridge, MA 02138 USA

⁴ Einstein Fellow

⁵ Department of Astronomy and Astrophysics, University of California, Santa Cruz, CA 95064, USA

⁶ One should note that for $M_{BH} > 10^{8-9} M_\odot$ and a main sequence star, R_t resides within the Schwarzschild radius of the black hole. As a consequence no TDE can occur (see Kesden 2012)

⁷ For BHs with $M_{BH} > 10^7 M_\odot$ the peak luminosity will be sub-Eddington (Strubbe & Quataert 2009; Lodato & Rossi 2011)

luminous UV/X-ray flare, there are several other sources of radiation that can be produced during this accretion event. This includes the formation of a non-thermal jet (e.g., [Cheng et al. 2006](#); [Burrows et al. 2011](#); [Bloom et al. 2011b](#); [van Velzen et al. 2016](#)), emission from the collision of tidal streams in bound orbits (e.g., [Kim et al. 1999](#); [Jiang et al. 2016](#)) or IR/optical/UV emission lines from photoionised ambient medium (e.g., [Komossa et al. 2009](#)).

The detection and analysis of the observational properties of TDEs covering a wide range of redshifts can provide a wealth of knowledge about a number of important astrophysical processes (see reviews by [Komossa & Zensus 2015](#); [Komossa 2015](#)). This includes probing the physics associated with accretion and accretion disc formation under extreme conditions, as well as the formation and evolution of jets. TDEs also provide a way to determine the properties of the dormant BHs (such as mass and spin) in distant Galaxies, as well as aiding in the search for intermediate mass BHs and recoiling BHs. Similarly they can also highlight the properties of the gaseous environment surrounding a BH, allow one to characterise stellar kinematics in different Galaxies and learn about the populations of stars in their centres ([MacLeod et al. 2012](#); [Kochanek 2016](#)).

Theoretically, the rate at which TDEs are thought to occur is low. Assuming $M_{\text{BH}} \lesssim 10^{7.5} M_{\odot}$, the theoretical rate is $\sim 10^{-4}$ events per year ([Magorrian & Tremaine 1999](#); [Wang & Merritt 2004](#); [Stone & Metzger 2016](#)). As a consequence, time domain surveys covering a wide field of view, such as the All-Sky Automated Survey for SuperNovae (ASAS-SN) ([Shappee et al. 2014](#)), Palomar Transient Factory (PTF) ([Law et al. 2009](#)), Panoramic Survey Telescope and Rapid Response System (PanSTARRS) ([Kaiser et al. 2002](#)) and the Sloan Digital Sky Survey (SDSS) ([van Velzen et al. 2011](#)), have been particularly important in detecting, and characterising the optical/UV light curves of these events. However, a significant fraction of the luminosity arising from a TDE accretion powered flare falls within the soft X-ray band, with a maximum luminosity of $10^{45} \text{ erg s}^{-1}$ for a BH with $M_{\text{BH}} < 10^7 M_{\odot}$. As a consequence, the X-ray emission from a TDE will dominate the fainter, extended and more permanent X-ray emission of its host Galaxy (if this emission is present). As such searching for TDEs in the X-ray energy band has proven to be most fruitful in this endeavour, with the number of TDE candidates detected in X-rays now outnumbering those detected in UV/optical alone.

The first soft X-ray TDE candidates were discovered with the X-ray observatory *ROSAT*. Due to its high sensitivity to soft X-rays (0.1–2.4 keV), low detector background, all-sky coverage and its eight year mission operation, these properties made it an ideal instrument to detect these transient events. Using the results from the *ROSAT* All-Sky Survey (RASS) that was completed by *ROSAT* during its first year of operation, strong, luminous flares from inactive galaxies⁸ were detected. The first soft X-ray TDEs were identified from NGC5905 ([Bade et al. 1996](#); [Komossa & Bade 1999](#)), IC3599 ([Grupe et al. 1995](#); [Brandt et al. 1995](#)), RX J1242-1119 ([Komossa & Greiner 1999](#)), RX J1624+7554 ([Grupe et al. 1999](#)) and RX J1420+5334 ([Greiner et al. 2000](#)). These “*ROSAT*” events are characterised by a very soft X-ray flare that peaks with a luminosity of $\sim 10^{44} \text{ erg s}^{-1}$; the X-ray luminosity

hardens and declines over a timescale of months to years and appeared to follow the $t^{-5/3}$ law as determined using follow up observations of these sources using current X-ray satellites such as *Chandra* (e.g., [Halpern et al. 2004](#); [Vaughan et al. 2004](#); [Komossa et al. 2004](#)) and *XMM-Newton* (e.g., [Komossa et al. 2004](#)); are coincident with the center of the host Galaxy (within the error circle of *ROSAT*); and the host galaxies showed no evidence of permanent AGN activity.

Since *ROSAT*, the *Chandra* X-ray Observatory, *XMM-Newton* Space Observatory and particularly the *Swift* Gamma-ray Burst Mission has dramatically changed our ability to be able to detect, and follow-up potential TDEs in the X-ray energy band. The increased sensitivity, as well as spatial and spectral resolution of these instruments, has allowed us to determine the location, and luminosity and spectral evolution of these events in detail. Using both dedicated observations of TDEs (e.g., ASASSN-14li: [Miller et al. 2015](#); [Holoien et al. 2016b](#); *Swift* J1644+57: [Bloom et al. 2011a,b](#); [Burrows et al. 2011](#)) and serendipitous discoveries (e.g., *XMM-Newton* slew survey: [Esquej et al. 2007](#)), this has significantly increased the number of TDE candidates detected in X-rays. In addition, leading to the discovery of rapid variability in the X-ray emission during the first few weeks of detection (e.g., [Saxton et al. 2012](#)), the possible discovery of jet formation from these events (e.g., [Bloom et al. 2011b](#); [Burrows et al. 2011](#)), and the discovery of TDEs occurring in dwarf Galaxies and clusters of Galaxies (e.g., [Cappelluti et al. 2009](#); [Maksym et al. 2010, 2013, 2014a](#); [Donato et al. 2014](#)).

Currently, there are ~ 70 TDE candidates listed in the literature⁹. Apart from the TDE candidates in which an X-ray observation was triggered through long term monitoring programs such as those run by *Swift*, or via a detailed follow up program such as that completed for the *ROSAT* TDEs, only a handful of these sources have detailed long term X-ray light curves. The vast majority of these TDE candidates have only short time period X-ray data (e.g., only one X-ray data point or an X-ray upperlimit) or no X-ray analysis has been published (this is particularly the case for those TDEs which were originally detected in optical). This makes it difficult to be able to characterise the long term X-ray emission from these events, or from the host Galaxy. One of the main issues associated with current studies of TDEs is that AGN activity can mimic the expected X-ray emission of TDEs. This can make it difficult to be able disentangle the emission from these two different components ([van Velzen et al. 2011](#)). Long term X-ray light curves can help alleviate this issue quickly, as periodic X-ray flares characteristic of AGNs should become obvious in these light curves, thus ruling out particular flaring events as TDEs.

In addition, due to the differences in focuses, and analysis techniques of current studies of the X-ray emission of TDEs listed in the literature, it is difficult to be able to complete a comparative study of the X-ray emission arising from these events. For the sources in which either short term (e.g., single data point or upper limit) or long term X-ray emission has been published in the literature, the X-ray fluxes and count rates are usually extracted over different energy bands, using different source and background regions, spectral models (i.e., powerlaw or blackbody or something more complicated), and analysis methods. In addition, with the exception for the well-studied X-ray TDEs such as *NGC 5905*, *Swift* J1644+57 or

⁸ These Galaxies were classified as inactive based on lack of radio, optical and X-ray emission prior to and after the flare was detected.

⁹ see <https://tde.space> for a listing of all TDEs so far mentioned in published papers, or Astronomer’s Telegram

ASASSN-14li, only a fraction of the available X-ray data for each source has been analysed.

Thus, to be able to fully characterise the long term X-ray emission from each TDE candidate, such that individual and comparative class studies can be completed, it is imperative to perform a comprehensive and systematic analysis of the X-ray emission from each TDE using *ROSAT*, *Chandra*, *XMM-Newton*, and *Swift*. Here we have undertaken this task in an attempt to characterise the long term X-ray emission from all events which have been classified as a TDE in the literature, allowing us to characterise the properties of X-ray TDEs as a whole. Our analysis method is systematic and takes into account intricacies associated with the X-ray analysis of point sources. This includes taking into account pileup, the encircled energy fraction, binning of spectral data and whether the number of source photons detected is significantly above background (i.e., Poisson fluctuation). Using these data products we study the global and individual properties of these candidates, and classify each candidate based on their derived and literature properties. We also make available all data products (count rates, fluxes, luminosities, light curves) derived in this study publicly available on the *open TDE catalog* which can be found at the following URL: <https://tde.space>.

In this paper, we present the details of our systematic analysis of all available X-ray data from either *ROSAT*, *Chandra*, *XMM-Newton*, and/or *Swift* for 70 TDE candidates listed in the literature. In Section 2 we describe our data analysis for each of the four X-ray instruments used in this study. In Section 3 we classify each TDE candidate based on their properties into one of six categories, producing a list of X-ray TDE candidates that best constitute the properties of an X-ray TDE. In Section 4 we analyse the properties of these candidates allowing us to quantify the properties of what defines an X-ray TDE, while in Section 5 we discuss what this tells us about these type of events. In Section 6 we summarise our results, while in the Appendix we summarise the properties of each individual TDE candidate as derived from this analysis and from the literature, as well as list the products of our analysis.

2. DATA ANALYSIS

To perform our analysis, we selected all possible candidates that have been claimed in the literature or inferred by us to potentially be a TDE, regardless of whether the currently favoured interpretation of this source is a TDE or another astrophysical phenomenon. In Table 1, we list the name of the TDE candidates, the host galaxy, the right ascension and declination of the host and the TDE, and redshift of all 70 candidates that we selected for our study. As this list is continually growing as new events are discovered and new observations becoming available all the time, not all potential/confirmed TDEs or their observations, found in Table 1, are included and analysed. In addition, due to the proprietary nature of some observations, not all data has been analysed for all events since at the time of writing, these data were not publicly available (e.g., follow-up *Chandra* observations of ASASSN-15lh are not available until the end of 2017: Margutti et al. 2016).

2.1. Data reduction

For each TDE candidate listed in Table 1, we searched for and analysed available *ROSAT*, *Chandra*, *XMM-Newton*, and *Swift* observations of these sources. As we are focusing on the 0.2-10.0 keV X-ray emission from these events, we did not

use data from *MAXI* or *INTEGRAL* which detect X-ray emission in the 0.7-7.0 keV and 3-35 keV energy bands respectively. Using the positions listed in Table 1, we obtained all available data of each source from these four X-ray missions using the High Energy Astrophysics Science Archive Research Center (*HEASARC*) data archive¹⁰, the *ROSAT* X-ray All-Sky Survey (RASS) catalogue¹¹, and the *XMM-Newton* science archive¹². We analysed *ROSAT* PSPB/PSPC pointed, *ROSAT* RASS, *Chandra* ACIS pointed, *XMM* EPIC pointed, *XMM* slew and *Swift* XRT observations for each source, when data was available.

Due to the low resolution (or large half equivalent width) of the PSF of the Advanced Satellite for Cosmology and Astrophysics (*ASCA*) and *Suzaku* satellites compared to that of *ROSAT*, *XMM*, *Chandra* and *Swift*¹³, we did not use observations from these satellites for our analysis. As one of the main aims of this study is to determine the long term X-ray emission from each TDE candidate, we analysed data from sources that have two or more observations of the source taken at different times. As such out of the 70 candidates that we selected, eight candidates had only one observation overlapping the position of the candidate. This includes NGC 6021, PGC 015259, PGC 1127938, PGC 133344, PGC 170392, UGC 01791, UGC 03317 and TDE1. As such we have excluded these sources from our general analysis below.

2.1.1. ROSAT

Nearly all TDE candidates listed in Table 1 had either *ROSAT* PSPC/B or *ROSAT* RASS observation overlapping the source of interest. For these sources, we used the screened data from the *HEASARC* or RASS archive that had been quality checked and processed using the *ROSAT* Standard Analysis Software System. To analyse the pointed and RASS observations we used *Xselect* version 2.4c to produce merged event files for observations that occurred around the same Modified Julian Date (MJD) and to extract spectra for observations in which the TDE candidate was bright enough. We considered events in the full 0.1-2.4 keV energy range of *ROSAT*.

Spectra and count rates were extracted from a circular region with a radius of 100", as approximately 85-90% of all source photons at 0.9 keV are enclosed within this extraction region for an on-axis PSPC pointed observation (Boese 2000). For an off-axis PSPC pointed observation roughly 70% of all source photons at 0.9 keV are enclosed using a region of this size, while for a PSPC Survey such as the RASS, only about 50% of all photons are enclosed (Boese 2000). We used a circular, source-free background region that has a radius of at least four times that of our source region (i.e., a radius of 400"). We chose this radius so that the background region was sufficiently large such that the uncertainty on the background region is sufficiently small that it can be neglected. This region was placed either immediately surrounding the source of interest (with the source of interest excluded), or nearby the source of interest if there were point sources that contributed to the background. As the RASS was operated

¹⁰ <http://heasarc.gsfc.nasa.gov/cgi-bin/W3Browse/w3browse.pl>

¹¹ <http://www.xray.mpe.mpg.de/cgi-bin/rosat/rosat-survey>

¹² <http://xmm.esac.esa.int/xsa/>

¹³ The resolution of the on-axis PSF of *ROSAT* PSPC, *XMM* EPIC, *Chandra* ACIS and *Swift* XRT detectors are 20", 14–15", 0.5" and 18" respectively, while for *ASCA* GIS and *Suzaku* XIS detectors, it is 174" and ~ 90" respectively (Arnaud et al. 2011).

Table 1

List name, host, positions and redshifts of TDE candidates and their hosts, irrespective of favoured interpretation. If the right ascension (R.A.) and declination (Decl.) of the TDE is left blank, the host R.A. and Decl. corresponds to the position of the event.

TDE Name	Host Name	Host R.A. (J2000)	Host Decl. (J2000)	TDE R.A. (J2000)	TDE Decl. (J2000)	Redshift
2MASX J0203	2MASX J02030314-0741514	02 : 03 : 03.14	-07 : 41 : 51.41			0.0615
2MASX J0249	2MASX J02491731-0412521	02 : 49 : 17.32	-04 : 12 : 52.20			0.0186
3XMM J152130.7+074916	3XMM J152130.7+074916	15 : 21 : 30.73	+07 : 49 : 16.52	15 : 21 : 30.75	+07 : 49 : 16.70	0.17901
ASASSN-14ae	SDSS J110840.11+340552.2	11 : 08 : 40.12	+34 : 05 : 52.23	11 : 08 : 39.96	+34 : 05 : 52.70	0.0436
ASASSN-14li	SDSS J124815.23+174626.4	12 : 48 : 15.23	+17 : 46 : 26.44	12 : 48 : 15.23	+17 : 46 : 26.22	0.0206
ASASSN-15oi	2MASX J20390918-3045201	20 : 39 : 09.18	-30 : 45 : 20.10	20 : 39 : 09.10	-30 : 45 : 20.71	0.0484
ASASSN-15lh	APMUKS (BJ) B215839.70-615403.9	22 : 02 : 15.39	-61 : 39 : 34.60	22 : 02 : 15.45	-61 : 39 : 34.64	0.2326
CSS100217	CSS100217 : 102913+404220	10 : 29 : 12.56	+40 : 42 : 20.00			0.148
D1-9	GALEX J022517.0-043258	02 : 25 : 17.00	-04 : 32 : 59.00			0.326
D23H-1	SDSS J233159.53+001714.5	23 : 31 : 59.54	+00 : 17 : 14.58			0.1855
D3-13	GALEX J141929.8+525206	14 : 19 : 29.81	+52 : 52 : 06.37			0.3698
DES14C1kia	Uncatalogued, 03:34:47.49 -26:19:35.0	03 : 34 : 47.49	-26 : 19 : 35.00			0.162
Dougie	SDSS J120847.77+430120.1	12 : 08 : 47.78	+43 : 01 : 20.27	12 : 08 : 47.87	+43 : 01 : 20.01	0.191
GRB060218, SN2006aj	SDSS J032139.69+165201.7	03 : 21 : 39.69	+16 : 52 : 01.74			0.0335
HLX-1	ESO 243-49	01 : 10 : 27.75	-46 : 04 : 27.41			0.0223
IC 3599	IC 3599	12 : 37 : 41.18	+26 : 42 : 27.24			0.021245
IGR J12580	NGC 4845	12 : 58 : 01.24	+01 : 34 : 32.09	12 : 58 : 05.09	+01 : 34 : 25.70	0.00411
IGR J17361-4441	NGC 6388	17 : 36 : 17.46	-44 : 44 : 08.34	17 : 36 : 17.42	-44 : 44 : 05.98	0.04
iPTF16fml	Mrk950	00 : 29 : 57.01	32 : 53 : 37.24	00 : 29 : 57.04	32 : 53 : 37.50	0.0163
LEDA 095953	LEDA 095953	13 : 47 : 30.10	-32 : 54 : 52.00	13 : 47 : 30.33	-32 : 54 : 50.63	0.0366
NGC 1097	NGC 1097	02 : 46 : 19.06	-30 : 16 : 29.68			0.0042
NGC 2110	NGC 2110	05 : 52 : 11.41	-07 : 27 : 22.23			0.007579
NGC 247	NGC 247	00 : 47 : 08.55	-20 : 45 : 37.44			0.000531
NGC 3599	NGC 3599	11 : 15 : 26.95	+18 : 06 : 37.33			0.002699
NGC 5905	NGC 5905	15 : 15 : 23.32	+55 : 31 : 01.59			0.01124
NGC 6021	NGC 6021	15 : 57 : 30.68	+15 : 57 : 22.37	15 : 57 : 30.72	+15 : 57 : 21.60	0.015607
OGLE16aaa	GALEXASC J010720.81-641621.4	01 : 07 : 20.88	-64 : 16 : 20.70			0.1655
PGC 015259	2MFGC 3645	04 : 29 : 21.82	-04 : 45 : 35.60	04 : 29 : 21.84	-04 : 45 : 36.00	0.014665
PGC 1127938	2SLAQ J011844.35-010906.8	01 : 18 : 44.36	-01 : 09 : 06.87	01 : 18 : 56.64	-01 : 03 : 10.80	0.02
PGC 1185375	2MASX J15035028+0107366	15 : 03 : 50.29	+01 : 07 : 36.70	15 : 03 : 50.40	+01 : 07 : 37.20	0.00523
PGC 1190358	N5846-162	15 : 05 : 28.75	+01 : 17 : 33.17	15 : 05 : 28.56	+01 : 17 : 31.20	0.00766
PGC 133344	6dFGS gJ214256.0-300758	21 : 42 : 55.98	-30 : 07 : 57.91	21 : 42 : 55.92	-30 : 07 : 58.80	0.02365
PGC 170392	6dFGS gJ222646.4-150123	22 : 26 : 46.35	-15 : 01 : 23.04	22 : 26 : 46.32	-15 : 01 : 22.80	0.016246
Pictor A	Pictor A	05 : 19 : 49.72	-45 : 46 : 43.85			0.034
PS1-10jh	SDSS J160928.27+534023.9	16 : 09 : 28.28	+53 : 40 : 23.99	16 : 09 : 28.29	+53 : 40 : 23.52	0.1696
PS1-1laf	SDSS J095726.82+031400.9	09 : 57 : 26.82	+03 : 14 : 00.94	09 : 57 : 26.82	+03 : 14 : 01.00	0.4046
PS1-12yp	SDSS J133155.90+235405.8	13 : 31 : 55.90	+23 : 54 : 05.8	13 : 31 : 55.91	+23 : 54 : 05.70	0.581
PTF-09axc	SDSS J145313.07+221432.2	14 : 53 : 13.08	+22 : 14 : 32.27	14 : 53 : 13.06	+22 : 14 : 32.20	0.1146
PTF-09djl	SDSS J163355.97+301416.6	16 : 33 : 55.97	+30 : 14 : 16.65	16 : 33 : 55.94	+30 : 14 : 16.30	0.184
PTF-09ge	SDSS J145703.17+493640.9	14 : 57 : 03.18	+49 : 36 : 40.97	14 : 57 : 03.10	+49 : 36 : 40.80	0.064
PTF-10iam	SDSS J154530.83+540231.9	15 : 45 : 30.83	+54 : 02 : 31.91	15 : 45 : 30.85	+54 : 02 : 33.00	0.109
PTF-10iya	SDSS J143840.98+373933.4	14 : 38 : 40.98	+37 : 39 : 33.45	14 : 38 : 41.00	+37 : 39 : 33.60	0.22405
PTF-10nuj	SDSS J162624.66+544221.4	16 : 26 : 24.66	+54 : 42 : 21.44	16 : 26 : 24.70	+54 : 42 : 21.60	0.132
PTF-11glr	SDSS J165406.16+412015.4	16 : 54 : 06.17	+41 : 20 : 15.45	16 : 54 : 06.13	+41 : 20 : 14.80	0.207
RBS 1032	SDSS J114726.69+494257.8	11 : 47 : 26.80	+49 : 42 : 59.00			0.026
RX J1242-11A	RX J1242.6-1119A	12 : 42 : 36.90	-11 : 19 : 35.00	12 : 42 : 38.55	-11 : 19 : 20.80	0.05
RX J1420+53	RX J1420.4+5334	14 : 20 : 24.37	+53 : 34 : 11.72	14 : 20 : 24.20	+53 : 34 : 11.00	0.147
RX J1624+75	RX J1624.9+7554	16 : 24 : 56.66	+75 : 54 : 56.09	16 : 24 : 56.70	+75 : 54 : 57.50	0.0636
SDSS J0159	SDSS J015957.64+003310.4	01 : 59 : 57.64	+00 : 33 : 10.49			0.31167
SDSS J0748	SDSS J074820.67+471214.3	07 : 48 : 20.67	+47 : 12 : 14.23			0.0615
SDSS J0938	SDSS J093801.64+135317.0	09 : 38 : 01.64	+13 : 53 : 17.08			0.1006
SDSS J0939	SDSS J093922.90+370944.0	09 : 39 : 22.89	+37 : 09 : 43.90			0.18589
SDSS J0952	SDSS J095209.56+214313.3	09 : 52 : 09.56	+21 : 43 : 13.24			0.0789
SDSS J1011	SDSS J101152.98+544206.4	10 : 11 : 52.99	+54 : 42 : 06.50			0.24608
SDSS J1055	SDSS J105526.41+563713.1	10 : 55 : 26.42	+56 : 37 : 13.09			0.0743
SDSS J1201	SDSS J120136.02+300305.5	12 : 01 : 36.03	+30 : 03 : 05.52			0.146
SDSS J1241	SDSS J124134.25+442639.2	12 : 41 : 34.26	+44 : 26 : 39.23			0.0419
SDSS J1311	SDSS J131122.15-012345.6	13 : 11 : 22.15	-01 : 23 : 45.61	13 : 11 : 22.18	-01 : 23 : 45.20	0.18
SDSS J1323	SDSS J132341.97+482701.3	13 : 23 : 41.97	+48 : 27 : 01.26			0.08754
SDSS J1342	SDSS J134244.41+053056.1	13 : 42 : 44.42	+05 : 30 : 56.14			0.0366
SDSS J1350	SDSS J135001.49+291609.7	13 : 50 : 01.51	+29 : 16 : 09.71			0.0777
Swift J1112-82	Swift J1112.2-8238	11 : 11 : 47.80	-82 : 38 : 44.71	11 : 11 : 47.32	-82 : 38 : 44.20	0.89
Swift J1644+57	Swift J164449.3+573451	16 : 44 : 49.30	+57 : 34 : 51.00			0.3543
Swift J2058+05	Swift J205819.7+051329	20 : 58 : 19.85	+05 : 13 : 33.00			1.1853
UGC 01791	UGC 01791	02 : 19 : 53.66	+28 : 14 : 52.60	02 : 19 : 53.52	+28 : 14 : 52.80	0.015881
UGC 03317	UGC 03317	05 : 33 : 37.54	+73 : 43 : 26.30	05 : 33 : 37.68	+73 : 43 : 26.40	0.004136
TDE1,VV-1	SDSS J234201.40+010629.2	23 : 42 : 01.41	+01 : 06 : 29.30			0.136
TDE2, VV-2	SDSS J232348.61-010810.3	23 : 23 : 48.62	-01 : 08 : 10.34			0.2515
Wings (A1795)	WINGS J134849.88+263557.5	13 : 48 : 49.88	+26 : 35 : 57.50	13 : 48 : 49.86	+26 : 35 : 57.49	0.062
XMMSL1 J0740-85	2MASX J2007400785-8539307	07 : 40 : 08.09	-85 : 39 : 31.30	07 : 40 : 08.43	-85 : 39 : 31.4	0.0173

in PSPC scanning mode, data are comprised of a number of individual PSPC fields which results in the exposure time to vary across the field of view. Similarly for pointed PSPC observations the exposure time also varies across the field. For a pointed observation, the exposure time for an on-axis source corresponds to the sum of all the accepted times for each field, while off-axis the exposure time will be less. As a consequence for both RASS and pointed observations, we took this fact into account by positioning the background region such that the exposure time of this region was on average similar to that of the source of interest using the corresponding merged exposure maps of each observation as a guide.

2.1.2. *Chandra*

All *Chandra* data was analysed using version 4.7.0 of the *Chandra* analysis software, *CIAO*. We reprocessed level one data using *chandra_repro* to produce new level two event files. All observations were reprocessed using the calibration database CALDB 4.6.9. For observations that occurred around the same MJD, we produced a merged event file using the *CIAO* tool *reproject_obs* by reprojecting the observations to a common tangent plane based on the World Coordinate System (WCS) information of the earliest *Chandra* observation in our dataset that we wanted to combine. For observations in which we could extract a spectrum we used the *CIAO* task *specextract*. To extract spectra for observations which occurred at the same MJD, we extracted individual spectra from each observation that resulted in the merged event file and we combined these extracted spectra using the *combine* option in *specextract*. Spectra and count rates were extracted from both the ACIS-S and ACIS-I detectors using a circular region of 2". A region of this size is able to enclose 95% of all source photons (at 1.496 keV), assuming that the source is on axis¹⁴. We selected a source-free background region with a radius of 20" which, was positioned either nearby or immediately surrounding the source of interest (which was excluded from the background region if the latter option was chosen). Unlike that seen in the *ROSAT* observations, the exposure across the detector does not vary significantly across the detector, allowing us more flexibility for positioning our background region. The only exception to this is when sources are positioned closed to a chip gap or the edge of the detector, however only a handful of observations fall into this category. Exposure times were derived from the header of the event file from each observation.

2.1.3. *XMM-Newton*

For the *XMM* pointed observations, we started from the observational data files of each observation and used the *XMM-Newton* Science System (SAS) version 14.0.0¹⁵, and the most up to date calibration files¹⁶ to produce the data products for our study. As *XMM* suffers from periods of high background and/or proton flares, we checked for these time intervals by generating a count rate histogram using events with an energy between 10 - 12 keV for each observation. Before extracting count rates or spectra, we removed the time intervals which are contaminated by a high background or flares producing

cleaned event files. As suggested in the current SAS analysis threads¹⁷ and *XMM-Newton* Users Handbook¹⁸, we reduced the data following the standard screening of events, with single to quadruple pattern events ($PATTERN \leq 12$) chosen for the MOS detectors, while for the PN detectors only single and double patterned events ($PATTERN \leq 4$) were selected. We also used the standard canned screening set of FLAGS¹⁹ for both the MOS (#XMMEA_EM) and PN (#XMMEA_EP) detector respectively.

For the observations in which the TDE was bright enough to extract spectra, we used the SAS task *evselect* and the cleaned event files from all three EPIC cameras. For each spectrum we extracted, we produced spectral response and effective area files using the tasks *arfgen* and *rmfgen*. For our analysis we consider events between 0.2 – 10.0 keV for the MOS detector and 0.2 – 12.0 keV for the PN detector. Spectra and count rates were extracted from a circular region with a radius of 30". This corresponds to ~85% of all source photons at 1.9 keV are enclosed by the extraction region for both the MOS and PN detectors (assuming that the source of interest is found on-axis)²⁰. We used a circular background region with a radius of 120", which similar to what was completed with *Chandra*, was placed immediately surrounding the source of interest (with the source of interest excluded) or placed in source a free region nearby the TDE candidate. To extract the count rates we used only the PN detector, due to its high sensitivity, large effective area and consistent overlap with all source regions (i.e., some sources fell on CCD3 of MOS1 which suffered significant damage after a micro-meteoroid impact²¹). For each observation, exposure times were taken from the header of the corresponding event files.

2.1.4. *XMM-Newton* slew observations

In addition to analysing the pointed *XMM* observations of each candidate, we also searched for *XMM*-slew observations that overlap the position of the source. As *XMM* manoeuvres between pointed observations, all three detectors (MOS1, MOS2, PN) are still recording data using the observing mode of the previous pointed observation (Saxton et al. 2008). In addition the CCD is set with a medium optical blocking filter to prevent contamination from IR, visible or UV photons from point sources with a V-magnitude of $m_V = 8-10$ or less²². Due to the fast readout time of the PN detector any source detected during the slew observation will not be affected by the motion of the telescope, while the slower readout time of both MOS cameras leads to a highly elongated PSF causing any source detected to appear as long streaks (Turner et al. 2001; Saxton et al. 2008). As a consequence only data from the PN detector is used to produce a slew observation.

Starting from the slew data files that are publicly available in the *XMM-Newton* science archive we follow the current

¹⁴ See section 4.2.3 of <http://cxc.harvard.edu/proposer/POG/html/chap4.html>

¹⁵ <http://xmm.esac.esa.int/sas/current/documentation/>

¹⁶ http://xmm2.esac.esa.int/external/xmm_sw_cal/calib/index.shtml

¹⁷ <http://xmm.esac.esa.int/sas/current/documentation/threads/>

¹⁸ http://xmm.esac.esa.int/external/xmm_user_support/documentation/uhb/index.html

¹⁹ A FLAG value provides information about the event condition, such as whether it was detected near a hot pixel or resulted from outside the field.

²⁰ See http://xmm.esac.esa.int/external/xmm_user_support/documentation/uhb_2.5/node17.html for more information

²¹ <https://heasarc.gsfc.nasa.gov/docs/xmm/uhb/epic.html>

²² http://xmm.esac.esa.int/external/xmm_user_support/documentation/uhb_2.1/node32.html

SAS analysis thread on how to process EPIC slew data²³ and run the command *eslewchain* to produce filtered event files that we use in our analysis. Similar to the analysis for the pointed *XMM* observations we also use SAS version 14.0.0 and the most up to date calibration files, while we use events over the 0.2–12.0 keV range. The number of counts were extracted from a circular source region with a radius of 50'' and a circular background region (with source region excluded if necessary) with a radius of 200''. Using a source region with a radius of 50'', $\sim 90\%$ of all photons at 1.9 keV are enclosed by our extraction region. Due to the low exposure times of each observation ($\lesssim 10$ –20 seconds), which was determined using the corresponding exposure files of each observation, we were unable to extract spectra for these objects, even for the brightest of our sources.

2.1.5. *Swift*

Due to *Swift*'s ability to quickly target transient sources, a large number of TDE candidates have *Swift* observations. For each TDE candidate, we analysed all available and overlapping data that was taken in photon-counting model (PC) by *Swift*'s X-Ray Telescope (XRT). Following the *Swift* XRT Data Reduction Guide²⁴, we reprocessed level one data using the *xrtpipeline* script, producing cleaned event files and exposure maps for each observation. To combine observations which occur around the same MJD, we use *Xselect* version 2.4c. For the brightest sources, we also used *Xselect* to extract spectra from these observations, while exposure times were derived from the header of the event file from each observation.

For each spectrum we produced an ancillary response file (ARF) using the task *xrtmkarf*. This task uses the exposure maps produced during the *xrtpipeline* so that the ARF is corrected for hot columns, bad pixels or loss of counts caused by using an annular extraction region if the source is piled up. To be able to extract spectra from the combined event files, we combined the exposure maps of each observation that went into producing the combined event file before we produced the corresponding ARF file. To combine the exposure maps we used *XIMAGE* version 4.5.0. The response matrix files (RMFs) for each observation were obtained from the CALDB as ready-made files, and was selected such that it matched the suggested RMF file needed in the output of the *xrtmkarf*. To extract spectra and counts, we used a circular source region with a radius of 50'' and a source free, circular background region with a radius of 200'' placed in a similar way as the background sources were position when analysing the *Chandra* and *XMM* observations.

Sources which had a background extracted count rate > 0.5 counts/s are most likely piled-up, which can lead to issues in the data analysis. For these sources, we followed the *Swift* analysis threads²⁵ and estimated where pile-up affects the data by fitting the XRT PSF for that particular observation using *XIMAGE*. We then excluded an additional circular region with a radius defined by when the data and model diverge in our source extraction region when extract spectra for these sources.

²³ http://xmm.esac.esa.int/sas/current/documentation/threads/EPIC_slew_processing_thread.shtml

²⁴ http://swift.gsfc.nasa.gov/analysis/xrt_swguide_v1_2.pdf

²⁵ <http://www.swift.ac.uk/analysis/xrt/pileup.php>

2.2. Count rates and is it a background fluctuation or detection?

To determine the number of counts coming from the position of the TDE candidate we used the *funcnts* task that is a part of the FITS library and utility package for astronomical data analysis *FunTools*²⁶. This calculates the background-subtracted source counts, and the number of background counts from an event file and a region file that lists the source and background regions (and any other source that one wants to exclude or include) of interest. For each source we derived the number of source and background counts in the full energy range of all four X-ray satellites for our analysis. In addition, we also derived the number of counts in a soft (0.3–1.0 keV), medium (1.0–2.0 keV), and hard (2.0–10.0 keV or 2.0–2.4 keV for *ROSAT*) energy bands for each observation by filtering the cleaned event file and running *funcnts*. All extracted count rates used for our analysis were corrected for the fact that our regions only enclose a fraction (encircled energy fraction) of the total number of counts arising from the source.

To determine whether the number of X-ray counts we detect arises from a chance background fluctuation or from emission from an X-ray point source, we calculate the probability (\mathcal{P}) of having N source (background subtracted) counts given M background counts, using $\mathcal{P}(M, N) = 1 - \text{CDF}(M, N - 1)$, where CDF is the Cumulative distribution function assuming Poisson statistics. The corresponding detection confidence is calculated by $\mathcal{D}(M, N) = \text{CDF}(M, N - 1)$. For candidates that have a detection confidence of 0.95 ($\sim 2\sigma$) and above, we classified these as a detection of X-ray emission from the source. For the sources that had a detection confidence less than 0.95 ($\sim 2\sigma$) we classified this emission as a chance background fluctuation and instead derive the 3σ upperlimit. Upperlimits are derived assuming that we would detect a signal if it is 3σ above background.

In Tables 4–8 we have listed the observation IDs (ObsIDs) of the X-ray data we analysed for each TDE candidate, a label for this ObsID so that we can refer to it in later tables, the time in which the observation was taken in Modified Julian Date (MJD) (or the average MJD of the observations which have been merged) and the total exposure time of the cleaned (and merged) event files. In addition, we have listed the extracted source and background counts that we obtained over the full energy range of each instrument, the probability of the counts that we detected arise from a chance fluctuation and its detection confidence as calculated in Section 2.2. Based on these probabilities, we classified the measured count rate as an upperlimit or a data point, and then derived the corresponding source count rate (i.e., the source counts divided by the total exposure time) in the full instrument energy range of the observation. In these tables, the source and background counts extracted from the source have not been corrected for encircled energy fraction. However, the count rate which we use for our analysis, and is listed in the last column of these tables, has been corrected for encircled energy fraction. For simplicity, we have separated the results we obtained into five tables, with each table corresponding to the count properties derived from the different X-ray instruments we used for this analysis.

In Tables 9–13 we have listed the count rates from each source derived in a soft (0.3–1.0 keV), medium (1.0–2.0 keV)

²⁶ <http://hea-www.harvard.edu/RD/funtools/help.html>

and hard (2.0–10.0 keV) energy band for each TDE. For the source counts listed in these tables, we followed the same method as outlined in Section 2.2 to determine whether the emission we detect in each band is a detection or not. For those which we classified as a detection we derive an one sigma uncertainty, but for those which we classify as a chance fluctuation we derive a three sigma upperlimit. All counts in these tables have been corrected for encircled energy fraction. The ObsID label references the observation that these count rates were taken from, which can be found in Tables 4–8. We have also separated our soft, medium and hard count results into five tables corresponding to the different instruments we obtained data from.

2.3. Spectral analysis, and deriving the soft X-ray flux and luminosity of each event.

For observations in which spectra could be extracted, the spectral fitting was performed using the X-ray analysis software XSPEC version 12.9.0c, over an energy range of 0.3–5.0 keV. Each spectrum was grouped with a minimum of 20 counts per energy bin using the FTOOLS command *grppha*, and fitted using χ^2 statistics. We fit all spectra using an absorbed powerlaw (*tbabs*powerlaw*) model. This model consists of three parameters: the normalisation, power-law index (Γ) and the Galactic H I column density (N_H) assuming Wilms et al. (2000) solar abundances. Initially, we let all three parameters be free during our fitting procedure but for a large number of spectra, we find that the fit is unable to constrain the N_H . As a consequence we freeze the N_H to the value derived from the Leiden/Argentine/Bonn (LAB) Survey of Galactic H I (Kalberla et al. 2005) in the direction of the source of interest for these fits. For sources in which we were able to extract an X-ray spectrum, we calculate the absorbed flux, with errors, of the best fit absorbed powerlaw model using the XSPEC command *flux* over the energy range of 0.3–2.0 keV.

The sources in which we were unable to extract a spectrum due to the low number of source counts, we estimated the X-ray flux using the count rate simulator *WebPimms*²⁷. Here one specifies the instrument, the count rate as listed in the last column of Tables 4–8, the energy range that this count rate was derived, the N_H to the source of interest, the redshift and the model parameters assuming a specific model of the source. As a significant fraction of the sources we analysed did not have enough counts for us to extract a spectrum to characterise the emission from these candidates we had to make an assumption about the emission arising from the source itself. For these candidates we assumed a powerlaw index of 4.5 since such a steep spectrum typically mimics thermal emission over the limited X-ray energy band pass of current X-ray satellites (e.g., Donato et al. 2014). For sources which had multiple observations from the same instrument, but only a fraction of these had enough counts such that a spectrum could be extracted and modelled, we assumed the average power law index and N_H derived from fitting the spectra from these other observation of the source.

To derive the corresponding X-ray luminosities of each source from our derived fluxes, we assumed a Λ CDM cosmology with $\Omega_M = 0.27$, $\Omega_\Lambda = 0.73$ and $H_0 = 71 \text{ km s}^{-1} \text{ Mpc}^{-1}$.

In Tables 14–18 we have listed the N_H and powerlaw index Γ we derived (or assumed) from the best fit absorbed power-

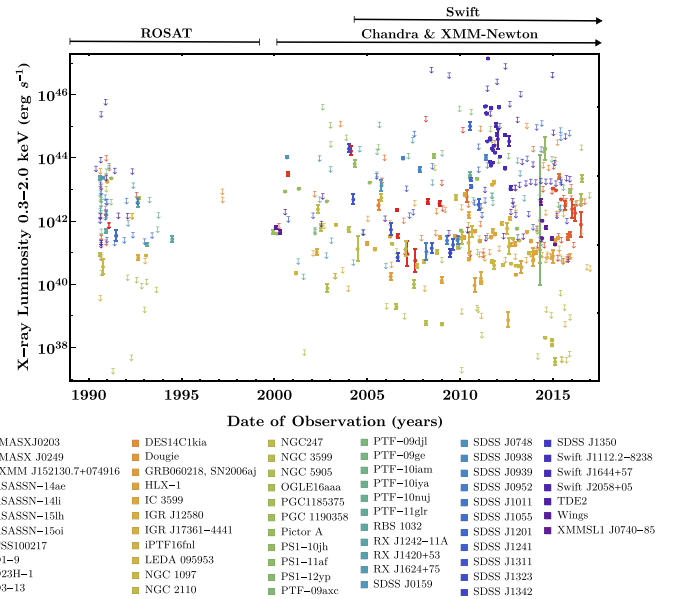


Figure 1. The X-ray light curves of all TDE candidates listed in Table 1. Below the figure is the colour key indicating the different TDE candidates.

law model for each set of data. We have also listed the derived absorbed X-ray flux and corresponding X-ray luminosity in the 0.3–2.0 keV energy band. Again, we have separated the results into five tables, with each table corresponding to a different instrument. Uncertainties on all parameters listed in these tables are one sigma uncertainties, and the ObsID labels refer to the ObsIDs listed in the second column of Tables 4–8.

3. THE X-RAY PROPERTIES OF THE TDE CANDIDATES AND THEIR CLASSIFICATION

A dormant BH at the centre of a quiescent galaxy reveals itself by the detection of emerging flare-like X-ray (or optical/UV) emission that can result from a star being tidally disrupted. However, AGN and numerous other astrophysical processes also result in flare-like emission which can make classifying this emission as a TDE difficult. Long term X-ray light curves can help aid in differentiating recurring flare-like emission from that of TDEs as periodic emission can become apparent over long baselines. Not until recently has X-ray astronomy come into its own, with the advent of a number of high resolution, and high sensitivity X-ray satellites for which we can use to quickly follow up potential candidates. Since the launch of *ROSAT* in the 1990s until now, we are lucky enough that we have nearly 30 years of available X-ray data that we can use to characterise the X-ray emission from these sources.

Taking advantage of this fact, we used the results derived in Tables 14–18, to produce long term 0.3–2.0 keV lightcurves for each of our TDE candidates listed in Table 1. In Figure 1 we have overlaid the light curves derived for each event. From Figure 1, one can see that these candidates cover X-ray luminosities over nearly 10 orders of magnitude.

In the 1990s, *ROSAT* was the only X-ray instrument that was available to search for X-ray emission from TDEs, with the RASS providing the largest number of constraints during this period. Even though the *ROSAT* mission lasted for over eight years before ending in 1999, the lack of observations seen during 1995 and 1999 arises from the shut down of the PSPC in 1994 to minimise the lost of combustibles. The

²⁷ <https://heasarc.gsfc.nasa.gov/cgi-bin/Tools/w3pimms/w3pimms.pl>

PSPC was turned back on briefly during 1997 to take a series of pointings to complete the all-sky survey which resulted in the complete use of the remaining detector gas²⁸. In the early 2000s when *Chandra*, *XMM-Newton* and *Swift* became operational, our ability to localise, detect and constrain emission from these sources dramatically increased. In particular, the ability of *Swift* to quickly follow up potential TDE candidates has improved our capability to well characterise over shorter timescales the X-ray emission arising from these objects.

In Figure 19–22 which can be found in the Appendix, we have also plotted the individual X-ray lightcurves of all TDE candidates listed in Table 1. In these figures, we have colour coded each data point/upperlimit based on the instrument in which we derived this measurement. In addition, we have also overlaid on these plots the optical/UV emission that we took from the literature, for sources which were also detected in these wavelengths. From these plots we can: (1). easily rule out different candidates as TDEs due to the presence of recurring X-ray emission, (2). highlight sources which do not have enough data to classify it as a TDE, and (3). produce the most comprehensive soft X-ray curves for each of these events. In Appendix Section A we have also summarised the properties of each individual TDE candidate listed in Table 1, as well as given an overview of their suggestion/classification as a TDE as presented in the literature.

3.1. Classifying the TDE candidates

The large amount of available archival X-ray data, in addition to future data from triggered or serendipitous X-ray observations, opens the door to potentially detecting a large number of X-ray TDEs. However, due to the difficulty in disentangling the X-ray emission arising from a flare from other transient phenomenon such as AGN activity, it is important to determine a set of well-defined properties that allow individuals to classify a potential candidate as an X-ray TDE.

Apart from taking steps towards removing the degeneracy associated with the nature of these X-ray flares, these well defined characteristics allow us to select a sample of current TDE candidates that encompass the general properties of X-ray TDEs. This is important as this class of events would allow us to (re)define the classification of what constitutes an X-ray TDE observationally. This provides us with the opportunity to perform a global study of the properties of X-ray TDEs and compare these with other transient phenomenon such as AGN (see Auchettl et al. 2017 in preparation).

Based on our analysis, and extending on attempts in the literature to collate the properties of X-ray TDEs (see e.g., Komossa 2015), we rank the TDE candidates listed in Table 1 based upon the quality and quantity of the available X-ray data into six categories: *TDE X-ray*, *likely X-ray TDE*, *possible X-ray TDE*, *veiled X-ray TDE* and *unknown*. We focus predominantly on their X-ray properties, however we also use other wavelengths (such as optical) to characterise observationally an X-ray TDE from another astrophysical object or process.

3.1.1. X-ray TDEs

Our criteria for classifying an X-ray candidate as an *X-ray TDE* are:

1. The X-ray light curve is well defined, where well defined means that there is sufficient data coverage of the

²⁸ <https://heasarc.gsfc.nasa.gov/docs/rosat/pspc.html>

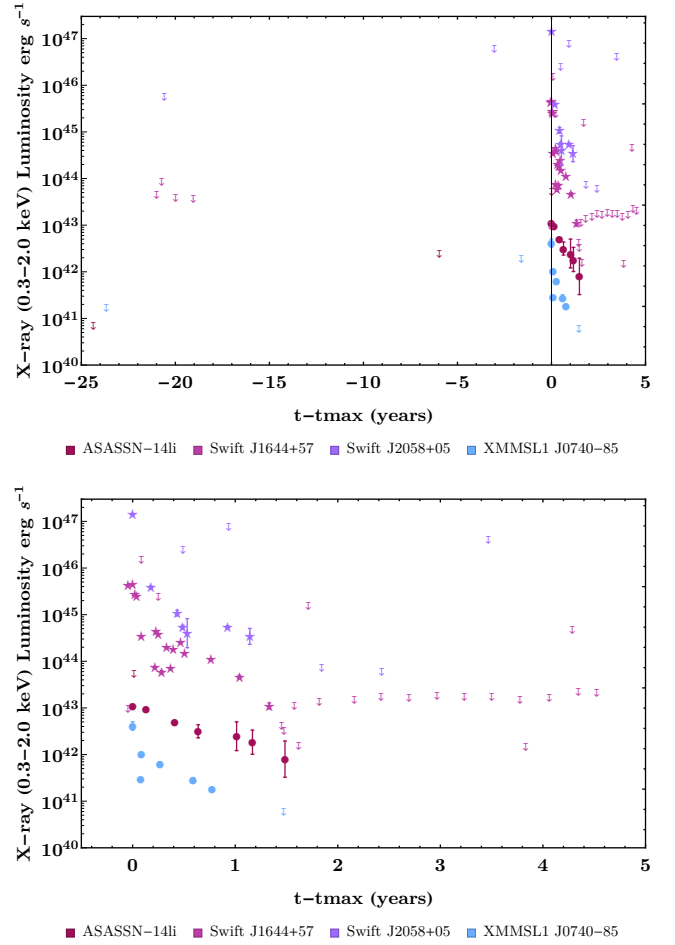


Figure 2. Light curves of the X-ray TDEs sample scaled such that the zero point occurs at the maximum detected X-ray luminosity (t_{\max}). In the *top panel* is the X-ray light curves of the TDE candidates plotted over the full (~ 30 year) range of data currently available for each source. In the *bottom panel* is the X-ray light curve of each X-ray TDE candidates focusing on the detected X-ray emission during and after the original X-ray flare was detected. Sources that are plotted with a star (★) are TDE candidates that have been classified as non-thermal (jetted) TDEs in the literature (e.g., Swift J1644+57), while those plotted with a filled circle (●) are either classified as a thermal (non-jetted) TDE in the literature (e.g., ASASSN-14li) or have no classification. Note that this classification using (★) and (●) will be used throughout the paper. In addition, open arrows are upperlimits, while the colour key for each TDE candidate is shown.

suspected flaring event such that a well defined shape and trend is observable. In addition, there is at least one (but preferably more than one) observation prior to and after the detected flare which can help quantify the pre-flare and post-flare emission of the source.

2. The X-ray light curve shows a rapid increase in X-ray luminosity, which then declines on time-scales of months to years.
3. The general shape of the X-ray light curve decay is monotonically declining, however variability in the X-ray emission on smaller timescales can also be seen but is not necessarily required.
4. The maximum luminosity detected from the event is at least two orders of magnitude larger than the X-ray upperlimit immediately preceding the discovery of the flare.
5. Over the full time range of X-ray data available for the

source of interest, the candidate TDE shows evidence of X-ray emission from only the flare, while no other recurrent X-ray activity is detected.

6. The X-ray flare is coincident with the nucleus of the host galaxy.
7. Based on its optical spectrum or other means, one finds no evidence of AGN activity arising from its host galaxy.
8. The host galaxy shows no evidence of large scale jets in any wavelength.
9. Supernova and Gamma-ray Burst (GRB) origin has been ruled out.

Out of the candidates listed in Table 1 there are four candidates which satisfy all the requirements of the *X-ray TDE* category based on their properties summarised in the Appendix Section A and presented in Tables 4–18. These are the thermal X-ray TDE *ASASSN-14li* and the non-thermal events *Swift J1644+57*, *Swift J2058+05* and *XMMSL1 J0740-85*. Due to the rapid follow up of these events after the initial trigger, each of these three sources has a rich data set that allows us to produce a well defined X-ray light curve of its emission. A clear increase in the X-ray luminosity arising from the centre of their host galaxies, followed by a monotonic decay is observed. In addition, variability is also observed on smaller times scales. The maximum luminosity of the flare is also a few orders of magnitude larger than the X-ray upperlimit immediately prior to the flare. Detailed analysis of its host Galaxy and the events have ruled out the presence of AGN, large scale jets or the possibility that it could arise from a supernova or GRB.

In Figure 2 we have overlaid the X-ray light curves of each of the X-ray TDEs. Here we have plotted the X-ray luminosity as a function of $t - t_{\max}$, where t_{\max} is the time at which the measured X-ray luminosity was at maximum²⁹. We have plotted these such that one can see how the emission from these TDEs compare over the full ~ 30 years of available X-ray observations (Figure 2 top), as well as focusing directly on the X-ray flare emission (Figure 2 bottom). One can see in the bottom panel of Figure 2 that these X-ray events are bright for approximately 1-2 years after the measured luminosity was at its maximum. The variability of the *Swift J1644+57*, *Swift J2058+05* and *XMMSL1 J0740-85* (and to a smaller extent for *ASASSN-14li*) is also obvious in these plots, while no X-ray emission before the observed flare is detected. These events also span nearly six orders of magnitude in X-ray luminosity, with the non-thermal X-ray TDEs *Swift J1644+57* and *Swift J2058+05* peaking at higher X-ray luminosities compared to the thermal X-ray TDE *ASASSN-14li* and *XMMSL1 J0740-85* which peak at much lower luminosities.

3.1.2. Likely X-ray TDEs

A candidate falls into the *likely X-ray TDE* category if it has properties nearly identical to those of the *X-ray TDE* category, but with the following differences:

1. The X-ray light curve is not very well defined due to the limited number of observations available of the source.

²⁹ This does not necessarily indicate that this is when the X-ray emission from the source peaked. The source could have peaked a few days to weeks before the first observation in which we detect the maximum measured X-ray luminosity. The difference between the actual and measured X-ray luminosity arises from the limitation of available X-ray satellite resources. As such, we are usually only able to capture emission from these events after the initial peak in X-rays.

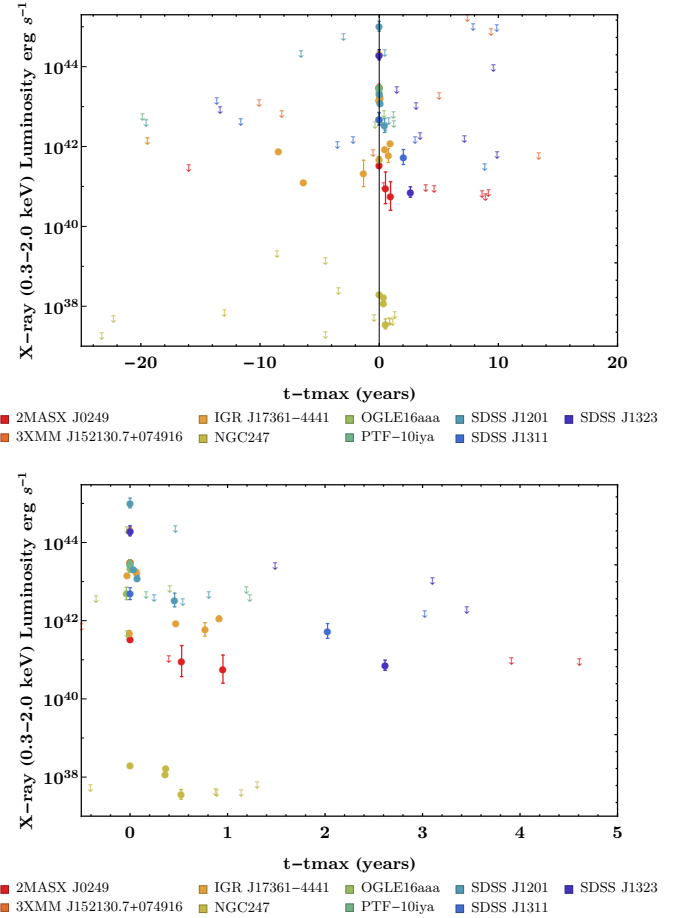


Figure 3. Same as Figure 2, however here we have plotted the *likely* X-ray TDEs.

Regardless, a general shape and trend is observable even if details of the X-ray emission such as variability, or exactly how the emission evolves is not well defined. There should also still be at least one (but preferably more than one) observation prior to and after the detected flare which can help quantify the pre- and post-flare emission of the source.

2. The presence of an AGN is ruled out or highly unlikely.
3. Requirements 2-6, 8-9 of the X-ray TDE category.

There are nine TDE candidates listed in Table 1 which we classify as likely X-ray TDEs. These are: *2MASX J0249*, *3XMM J152130.7+074916*, *IGR J17361-4441*, *NGC 247*, *OGLE16aaa*, *SDSS J1201*, *SDSS J1311*, *SDSS J1323*, *PTF-10iya*. All these events have X-ray light curves which show a $\gtrsim 1.5$ –2 order of magnitude increase in luminosity compared to previous X-ray upperlimits, which then decays. However, due to the limited amount of available X-ray data from these sources we are able to derive only a general trend for their emission. Observations immediately before and after the flare indicate the presence of no recurrent X-ray emission arising from the source and as of writing, the presence of an AGN is either ruled out or highly unlikely. Other astrophysical sources have also been ruled out as responsible for their emission.

In Figure 3 we have overlaid the X-ray light curves of each of the *likely* X-ray TDEs. Similar to Figure 2, we have plotted

the X-ray luminosity as a function of $t - t_{max}$ over the the full 30 years of available X-ray observations, as well as focusing directly on the X-ray flare emission. One can see that these events cover an even wider range of X-ray luminosities than their X-ray TDE counterparts. These events also tend to decay on much shorter timescales ($\lesssim 1$ year).

3.1.3. Possible X-ray TDEs

To fall into the *possible X-ray TDE* category, the source would have the following properties:

1. Based on the available X-ray data (whether this is limited or not), the emission from the source appears to either peak randomly or unpredictably, or it shows evidence of a periodic or extend emission signature.
2. The maximum luminosity detected from the event is one order of magnitude larger than the X-ray upper limit immediately preceding the discovery of the flare.
3. The event is found to be coincident with the nucleus of the host galaxy.
4. The host galaxy shows no evidence of large-scale jet like structures in any wavelength.
5. It appears to be unlikely to arise from an AGN, GRB or a supernova
6. Although not required, it has been classified in the literature as an optical TDE from a detailed analysis by their authors.

ASASSN-15oi, D3-13, LEDA 095953, NGC 3599, NGC 5905, RBS 1032, RX J1242-11A, RX J1420+53, RX J1624+75, SDSS J0159, Swift J1112-82 and Wings are the candidates which we place into this category. For ASASSN-15oi which was classified as an optical/UV TDE by [Holoien et al. \(2016a\)](#), the limited amount of data available make it is difficult to be able to quantify the evolution of the X-ray emission detected and based on the current results it does not decay significantly. For D3-13, which was classified by [Gezari et al. \(2008\)](#) as an optical TDE, the X-ray emission we detect is no more than one order of magnitude larger than the X-ray upper-limit before and after the original flare. LEDA 095953 shows evidence of an X-ray flare in the early 90s that is coincident with the centre of the host Galaxy, however the emission appear to be random due to the limited amount of X-ray data around the time of the flare. No follow up X-ray emission has been detected from this source. Even though NGC 3599 has a significant amount of data that shows a clear increase in the observed X-ray emission by a few orders of magnitude compared to previous X-ray upperlimits which then decays (see Figure 20), we place NGC 3599 into the possible X-ray TDE category rather than the likely X-ray TDE category. This is due to the fact that the AGN origin of the detected flare has not been completely ruled out, while unlike other X-ray TDE events which exhibit a fast rise to peak, and then decays within 1-2 years (see Figure 4), the emission from this event exhibits a slow rise and then a long decay over nearly 10 years. Even though slow-rise TDEs are theoretically expected to also be detected, the origin of this flare is not as clear as other events hence leading us to place it in the *possible X-ray TDE* category. The flare arising from NGC 5905 was detected using ROSAT. As a consequence there is no X-ray upperlimit prior to the detected flare making it difficult to quantify the emission immediately before the flare. In addition the detection of late time emission arising from this event is reminiscent of AGN IC3599, while [Gezari et al. \(2003, 2004\)](#) found using the Hubble Space Telescope (HST) narrow emission lines in

Table 2

TDE candidate classified as either a *X-ray TDE*, *likely X-ray TDE*, *possible X-ray TDE*, *veiled TDE*, *not a TDE* or *unknown* based on the requirements listed in Section 3.1. These events have been listed in no particular order.

X-ray TDE	Likely X-ray TDE	Possible X-ray TDE	Veiled TDE	Not a TDE	Unknown
ASASSN-14li	2MASX J0249	ASASSN-15oi	ASASSN-14ae	2MASXJ0203	Dougie
Swift J1644+57	3XMM	D3-13	ASASSN-15lh	CS5100217	PGC1185375
Swift J2058+05	IGR J137361	LED A 095953	D1-9	GRB060218/SN2006aj	PGC1190358
XMMSL1 J0740-85	NGC247	NGC3599	D23H-1	HLX1	PTF-10nuj
	OGLE16aaa	NGC5905	DES14C1kia	IC3599	PTF-11glr
	PTF-10bya	RBS1032	iPTF16fnl	IGR J12580	PTF-11nuj
	SDSSJ1201	RX J1242-11A	PS1-10jh	NGC1097	
	SDSSJ1311	RX J1420+53	PS1-11af	NGC2110	
	SDSSJ1323	RX J1624+75	PS1-12yp	Pictor A	
		SDSSJ0159	PTF-09axc	PTF-10am	
		Swift J1112-82	PTF-09djl	SDSSJ0938	
		Wings	PTF-09ge	SDSSJ0939	
			SDSSJ0748	SDSSJ1011	
			SDSSJ0952	SDSSJ1055	
			SDSSJ1342	SDSSJ1241	
			SDSSJ1350		
			TDE2		

the inner nucleus of the host, indicating that there is a low level, non-stellar photoionisation powered by accretion that could be contributing to the observed emission. As the AGN origin of this source is not completely ruled out, and based on current observations a TDE origin is more likely we place this source in the possible X-ray TDE category. ROSAT detected an X-ray flare from the centre of inactive Galaxy RX J1242-11A, RX J1420+53 and RX J1624+75 in the early 90s, however there is limited data which can help us to characterise the evolution of the emission immediately before and after these flares. Follow up observations have ruled out further X-ray emission from these sources at later times, but the data is very sparse making it difficult to determine how this flare-like emission evolved. Even though the emission from SDSS J0159 shows evidence of a flare which then decays, [LaMassa et al. \(2015\)](#) showed that the host Galaxy is transitioning from a Type 1 broad-line AGN to a Type 1.9 AGN and the properties of this source could result from the dimming of AGN continuum. However, due to the rarity of this type of dimming, it is possible that this event could arise from a TDE which would be the brightest non-jetted TDE detected. Due to the uncertainty in the actual origin of this event we have placed this event into the possible X-ray TDE category for now. Due to the limited amount of X-ray data and the fact that the soft X-ray emission from each source is of the same order of magnitude as its upperlimit prior to and after the detected X-ray flare, we place Swift J1112-82 and Wings in the possible X-ray TDE category.

3.1.4. Veiled X-ray TDE

For a candidate to be classified as a *veiled X-ray TDE* these sources must show well defined optical/UV light curves that again show a increase in the optical/UV emission that then decays following a powerlaw or show evidence of coronal lines whose strength decays with time. They must be coincident with the centre of their host Galaxy, their host shows no evidence of AGN activity and they have temperature in the range of $\sim 10^4$ K as derived from their optical emission. In addition, they either show no X-ray emission at all, or they show evidence of late time X-ray emission well after the original optical flare has disappeared or decayed. To determine whether a source is an optical/UV TDE we rely heavily on the currently accepted view in the literature of the nature of these events as optical/UV TDEs, while using our results to determine their X-ray emission.

The candidates which fall into this category are ASASSN-14ae, ASASSN-15lh, D1-9, D23H-1, DES14C1kia, iPTF16fnl, PS1-10jh, PS1-11af, PS1-12yp, PTF-09axc, PTF-09djl, PTF-09ge, SDSS J0748, SDSS J0952, SDSS

J1342, *SDSS J1350*, and *TDE2*. These events have been classified as an optical/UV TDE in the literature, however our analysis either detects no X-ray emission arising from the position of these source or well after the original flare weak X-ray emission is detected. Even though *PTF-10iya* was first classified as an optical TDE, we did not place this event into this category as its X-ray emission was detected simultaneously with the optical emission from the source, much like that of *ASASSN-14li*, leading it to be placed in the *likely X-ray TDE* category.

3.1.5. Not a TDE

The candidates from Table 1 which fall into the *not a X-ray TDE* category are either:

1. Known AGNs, show evidence of a large scale jet, is a known GRB which shows a clear supernova counterpart or some other astrophysical object such as a low mass X-ray binary. Its classification as one of these astrophysical objects comes from other observations e.g., such as evidence of nuclear emission in the form of optical emission lines or X-ray fluorescence lines indicating an AGN.
2. The position of the source is not coincident (within uncertainties) with the centre of the host Galaxy.
3. In addition, although not necessarily required, the X-ray luminosity of the source does not change significantly across observations.
4. Shows evidence of X-ray variability or X-ray emission of the same order of magnitude over long time scales.

There are 15 TDE candidates from Table 1 which we categorise as *not a TDE*. This includes *2MASXJ0203*, *CSS100217*, *GRB060218/SN2006aj*, *HLX1*, *IC3599*, *IGR J12580*, *NGC1097*, *NGC2110*, *Pictor A*, *PTF-10iam*, *SDSS J0938*, *SDSS J0939*, *SDSS J1011*, *SDSS J1055*, and *SDSS J1241*. Here we summarise why each of these events were placed into this category, while in Appendix Section A we go into more detail.

2MASXJ0203 was suggested by Strotjohann et al. (2016) to be a highly variable AGN and shows evidence of variable X-ray emission which is approximately constant at peak and does not show a powerlaw decay expected for X-ray TDEs. As discussed in Appendix Section A, we do not detect any X-ray emission arising from TDE candidate *3XMM*, while the properties derived by Lin et al. (2015) do not match those seen in other TDEs. Using multi-wavelength observations, Drake et al. (2011) found that *CSS100217* exhibited spectroscopic features representative of Type II_{in} supernovae. The favoured explanation of *GRB060218/SN2006aj* is an under luminous long GRB with a low ejecta supernova. *HLX-1* shows evidence of variable X-ray emission over 10 years, and radio observations reveal a large scale jet. Using radio observations, Bower et al. (2013) suggested that the properties of *IC3599* is consistent with AGN emission, while Grupe et al. (2015) showed that the periodic X-ray emission observed most likely arises from accretion around the BH not a TDE. *IGR J12580* was classified as a LINER/Seyfert 2 Galaxy based on its optical spectra indicating that this source could be a changing look quasar, while a number of other observations in different wavelengths support the AGN origin of this source. *NGC1097*, and *NGC2110* are thought to be AGN (see e.g., Storchi-Bergmann et al. 1995; Marinucci et al. 2015; Gezari et al. 2003, 2004). *Pictor A* has a large scale jet (Perley et al. 1997), which we believe arises from an underlying AGN. Arcavi et al. (2016) suggested that *PTF-10iam* is most likely

a peculiar Type II or a hybrid Type Ia-Type II SN. Wang et al. (2012) originally suggested that *SDSS J0938* was a TDE based on coronal lines detected from the host, however it is more likely that these lines arise from the presence of an obscured AGN (Yang et al. 2013). The host of *SDSS J0939* was classified as a Narrow line Seyfert 1 galaxy by Esquej et al. (2007). Runnoe et al. (2016) characterised *SDSS J1011* as a changing look quasar. *SDSS J1055* has narrow line ratios indicating that it is an AGN, while the coronal lines that first lead to *SDSS J1241* being classified as a TDE did not change in strength with time making it more likely to be an AGN (Wang et al. 2012).

3.1.6. Unknown classification

Candidates that fall into the *unknown* category show evidence of an X-ray or optical/UV flare in the literature, however due to, e.g., being offset from the center of the host Galaxy or lack of data etc., its classification as a TDE is not certain. There is also no additional information from the literature or archival/additional observations that can either confirm its classification as a optical/UV or X-ray TDE, or rule out the presence of an e.g., AGN etc. The remain five TDE candidates from Table 1 that we classify as *unknown* are *Dougie*, *PGC1185375*, *PGC1190358*, *PTF-10nuij*, *PTF-11glr*.

Dougie was suggested to be an optical TDE based on the evolution of its optical light curve, however this source is systematically offset from the center of its host. We also do not detect any X-ray emission from this source and there is no other information in the literature which rules out or confirms its nature. Even though the *Swift* BAT detected a flare from *PGC1185375* and *PGC1190358*, there is very little soft X-ray data available overlapping the positions of these objects. This makes it difficult to be quantify the nature of these sources. The optical light curve of *PTF-10nuij* and *PTF-11glr* suggests that these source are optical TDEs, however both are found systematically offset from its host Galaxy. We also do not detect any X-ray emission from the source, and there is very limited amount of data about the host placing these sources into the *unknown* category.

4. ANALYSING THE X-RAY PROPERTIES OF X-RAY TDES

Using the *X-ray TDE* and *likely X-ray TDE* sample summarised in Table 2, we use these events to characterise the properties of X-ray TDEs in a systematic and comprehensive way.

4.1. How luminous are X-ray TDEs?

The accretion of stellar material from a star that has been tidally disrupted by its host BH will produce a short-lived, luminous accretion-powered flare. From our systematic analysis we can quantify how luminous these events become relative to their derived pre-flare upperlimits. In Figure 4 we have plotted against $t_i - t_{\text{firstupper}}$, the difference between the X-ray luminosity detected at and after peak relative to the luminosity of the upperlimit immediately preceding the first X-ray detection of the flare ($(L_i - L_{\text{firstupper}})/L_{\text{firstupper}}$). Due to the low exposure times of the *XMM-Newton* slew observations, a large number of the X-ray upperlimits derived from these observations are not very constraining. As such, these upperlimits are either significantly above or equivalent to the peak X-ray emission detected from these TDE candidates and thus provide limited information about the pre- or post-flare emission

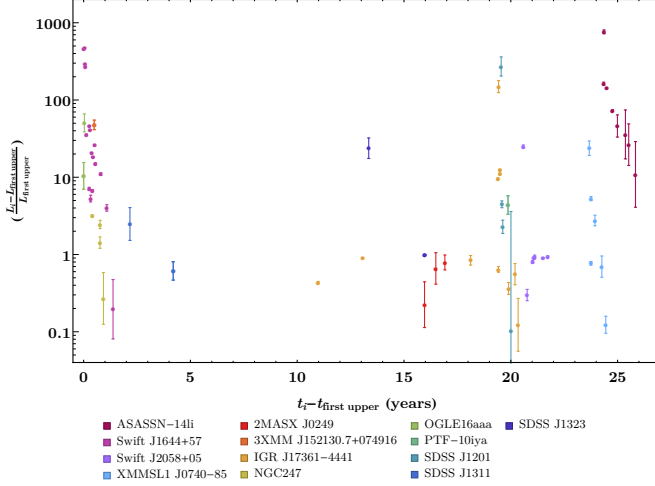


Figure 4. The difference between the X-ray luminosity detected at or after peak compared to the X-ray luminosity derived from the first X-ray upperlimit ($(L_i - L_{\text{firstupper}})/L_{\text{firstupper}}$). Due to the fact that for a large fraction of our events the X-ray upperlimits derived using *XMM-Newton slew* observations are not constraining and are thus larger than the detected X-ray emission from other instruments, we do not use these upperlimits for this plot. This is plotted against the observation date minus the date in which the first upper limit ($t - t_{\text{firstupperlimit}}$) was measured and has been normalised to the X-ray luminosity of the first X-ray upperlimit. One can see that the X-ray luminosity of all sources (with the exception of 2MASX J0249) increases by at least one to two orders of magnitude compared to their first X-ray upperlimit.

from these events. As a consequence, we do not use the upperlimits derived using *XMM-Newton slew* to derive Figure 4, and instead rely on the deeper X-ray upperlimits derived using *ROSAT*, *XMM-Newton pointed* observations, *Chandra* or *Swift*. Here $t_{\text{firstupper}}$ and $L_{\text{firstupper}}$ is the date and measured luminosity of the first upperlimit before the detected X-ray flare, while t_i and L_i is the date and luminosity of the i -th data point measured during the flare.

Figure 4 highlights the importance of having pre-flare constraints for a TDE candidate that are, at the very least, equivalent to an X-ray upperlimit derived using *ROSAT*. These X-ray upperlimits allow us to characterise how luminous an X-ray TDE becomes during the initial flare, and as it evolves. With the exception of 2MASX J0249 whose first upperlimit before the flare is derived from the shallow *ROSAT* RASS observation, all of the TDE candidates we consider show an increase in their X-ray luminosity between one to three orders of magnitudes at peak. The events that show the most dramatic change in their emission are ASASSN-14li, IGR J17361-4441, SDSS J1201 and Swift J1644+57, which display an increase in their X-ray luminosity of nearly three orders of magnitude. Swift J2058+05, 3XMM, OGLE16aaa, SDSS J1323 and XMMSL1 J0740-85 also show a significant increase of nearly two orders of magnitude compared to their pre-flare upperlimit, while all other events differ from their X-ray upperlimits by approximately one order of magnitude. Interestingly, both thermal and non-thermal X-ray TDEs both show this significant increase in their X-ray emission, indicating that X-ray TDEs are intrinsically very luminous events regardless of their nature. For the events that had pre-flare limits nearly immediately before the detected flaring event such as Swift J1644+57, we also find that these events dramatically increase by many orders of magnitude over relatively short timescales. Most of these events are also undetected in X-rays or fall to limits similar to that of their pre-flare limits within a

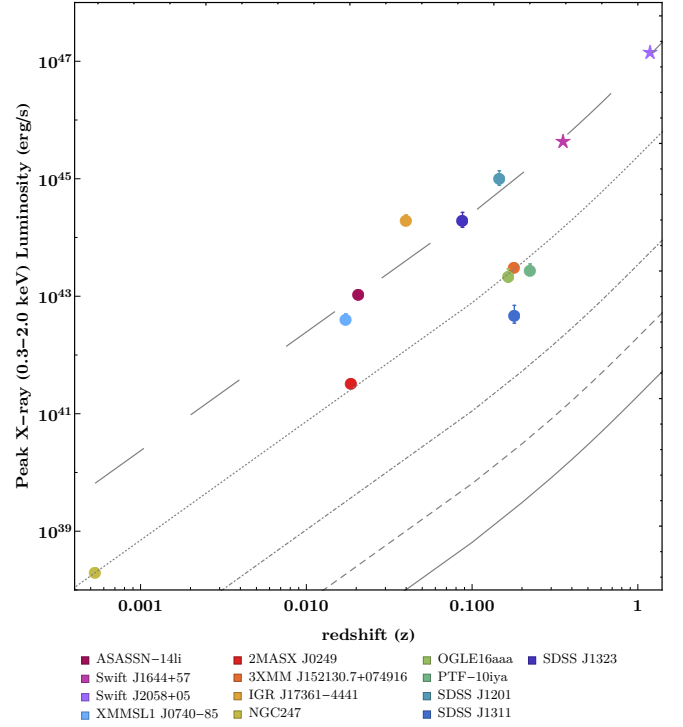


Figure 5. Peak X-ray luminosity as a function of redshift for out X-ray TDE candidates. Overlaid is the sensitivity bands for *ROSAT* all sky survey, *Chandra*, *XMM* and *Swift*. These bands were taken from the most stringent 0.5-2.0 keV flux limits derived from different extragalactic surveys taken by the different instruments (adapted from Figure 1 of Dai et al. 2015). Here the limits derived from the *ROSAT* all sky survey (Voges et al. 1999), *Chandra* 2Ms Deep field North survey (Alexander et al. 2003), *XMM-Newton* Lockman 0.8 Ms survey (Hasinger et al. 2001), *Swift* active galactic nucleus and cluster survey (Dai et al. 2015) and the *Swift* BAT 70 month 14-195 keV all sky survey (Baumgartner et al. 2013) are shown as the grey dotted, solid, dashed, dot-dashed and large dashed lines respectively.

year of the initial flaring event.

In Figure 5 we have plotted the peak X-ray luminosity of each TDE as a function of redshift. Shown as the solid, dashed, dot-dashed, dotted and large dashed grey lines are the most stringent 0.5-2.0 keV flux limits derived from the *ROSAT* all sky survey (Voges et al. 1999), *Chandra* 2Ms deep field north (Alexander et al. 2003), *XMM-Newton* 0.8Ms Lockman hole survey (Hasinger et al. 2001), the *Swift* active galactic nucleus and cluster survey (Dai et al. 2015) and the *Swift* BAT 70 month all sky survey (Baumgartner et al. 2013). One can see that ASASSN-14li, Swift J1644+57, and Swift J2058+05, IGR J17361-4441, SDSS J1201, and SDSS J1323 have a peak luminosity that is either above or comparable with the detection limit associated with the *Swift* BAT, indicating that only the most extreme events are going to be detected through trigger of the BAT. The *ROSAT* all sky survey would have detected nearly all of the X-ray TDE candidates we consider, with the exception of PTF-10iya, and SDSS J1311, which fall below this flux limit.

Due to the limitations of current X-ray satellites, it is not 100% surprising that we are currently susceptible in TDE studies to detecting only the most luminous X-ray TDEs found at close redshifts. Most of our current sample of TDEs are detected at redshifts < 0.2 , with very few detected at a redshift greater than $z \sim 0.7$. In fact, the events detected at the highest redshift are some of the brightest TDE candidates

and are jetted in nature, making these unique events in their own right. X-ray surveys are well designed to search for TDE in the low-redshift universe, while the increase sensitivity of *Chandra*, *XMM-Newton* and *Swift* compared to that of *ROSAT* also allow us to search for fainter TDE candidates at both higher and lower redshifts.

Due to the observational bias towards detecting the brightest TDEs, this leads to the question of why have we not detected a larger number of lower luminosity TDEs, especially at lower redshifts? The discrepancy between the expected theoretical rate of TDEs and our current rate at which we observe these events is well known (see Kochanek 2016, and references therewithin). However, this observational bias might arise from the intrinsic nature of X-ray TDEs themselves. In Section 5.2 and 18, we suggest that X-ray TDEs are viscously delayed (i.e., the timescale for which material from the disrupted star accretes onto the BH very long). Guillochon & Ramirez-Ruiz (2015) showed that this process has a dramatic affect on the properties of these events. In particular, if a TDE is drastically viscously delayed most of these events would be sub-Eddington in nature and will peak over timescales of many years. As our current sample of TDEs are found to peak over a few weeks to months (classified as prompt) and exhibit many orders of magnitude increases in their X-ray luminosity, this implies that there is most likely a large population of low luminosity (possibly slow-rise) TDEs that are being missed by current surveys/observations or mistaken for other phenomenon³⁰. As a consequence, the viscously slowed nature of X-ray TDEs might explain the current discrepancy between the theoretically expected and observationally detected rate of TDEs (Stone & Metzger 2016).

This highlights the need to have a wide range of instruments with quite different capabilities to be able to detect potential X-ray TDEs. Large X-ray surveys provide us with the ability to detect fainter, slow rising and prompt X-ray TDEs over a wide range of redshifts, while monitoring instruments like the *Swift* BAT allow us to detect the most extreme events of these classes at higher redshifts. With upcoming X-ray satellites such as *eROSITA* which have similar capabilities as *ROSAT* but with a larger effective area³¹, will provide us with the ability to detect a wide range of TDEs across the low to high redshift universe. Combined with the continual monitoring of our current X-ray satellites, this will open new doors into studying the formation and evolution of TDEs, as well as the properties and environments of their BHs.

4.2. How do X-ray TDE decay?

The luminosity of a TDE is assumed to decay following a simple $t^{-5/3}$ powerlaw (e.g., Evans & Kochanek 1989; Phinney 1989). However, Lodato et al. (2009) showed analytically, while Guillochon & Ramirez-Ruiz (2013) determined using hydrodynamical simulations, that the powerlaw index for decay depends heavily on the stellar structure (i.e.,

³⁰ For NGC3599 which Esquej et al. (2008) and Saxton et al. (2015) suggest could result from a slow-rise TDE, we find that the emission from this source would exhibit an increase in luminosity similar to those of our brightest, prompt events if we plotted this source on Figure 4. However, rather than increasing and then decreasing in magnitude over a very short time frame, the emission from this candidate would decay over timescales much longer than the other candidates in our sample. If this source is a slow-rise TDE rather than emission arising from thermal instability in the accretion disc of an AGN as suggested by Saxton et al. (2015), then this would be a unique event in its own right as it would be the first and the brightest slow-rise TDE detected.

³¹ See <http://www.mpe.mpg.de/455799/instrument> for more information about *eROSITA*

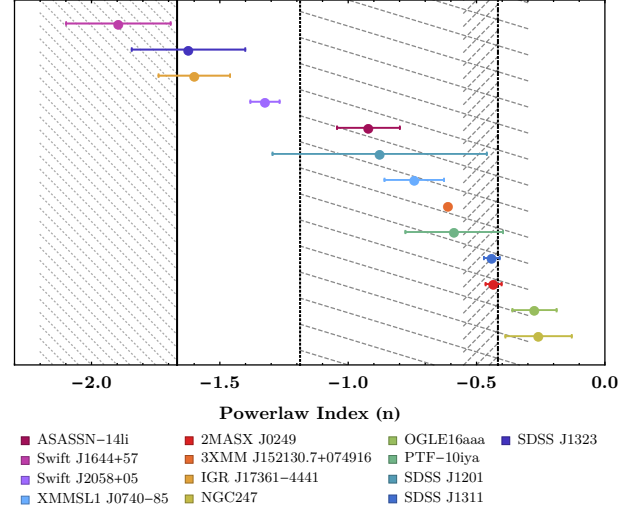


Figure 6. The best fit powerlaw index and its 1σ uncertainty obtained from fitting the X-ray light curves of our TDE sample as shown in Appendix Section B. We have also overlaid the ranges of various powerlaw indexes expected for TDEs. Here the solid black line is the standard $t^{-5/3}$ from fallback (e.g., Evans & Kochanek 1989; Phinney 1989), while the black dotted line is the powerlaw index $t^{-19/16}$ expected from a viscous disk accretion (Cannizzo et al. 1990). The black dot-dashed line represents the much shallower powerlaw index of $t^{-5/12}$ representative of disk emission (Lodato & Rossi 2011). The shaded regions represent the range of powerlaw indexes expected for TDE as determined by Guillochon & Ramirez-Ruiz (2013), assuming either $-5/3$, $-19/16$ or $-5/12$ respectively.

whether their mass is centrally-concentrated or not) and as such dramatically steeper powerlaw indexes than the assumed $-5/3$ can be obtained. Specifically, Guillochon & Ramirez-Ruiz (2013) showed that the expected rate of mass return to the black hole for low and high mass stars asymptotes to ~ -2.2 (from $-5/3$) for nearly half of all stellar disruptions. In addition, Lodato & Rossi (2011) showed that at late times the light curves of optical/UV TDEs tend to follow a powerlaw with an index of $-5/12$, assuming that the observed emission arises from disk emission.

To determine how the X-ray emission from our sample of TDEs decays, we model the full X-ray light curves seen in Figure 2 and 3 using a simple powerlaw, where we allow the normalisation and the powerlaw index Γ to be free parameters. In Figure 6 we have plotted the best fit power law index and its 1σ uncertainty for each TDE candidate we consider. For reference, we have also plotted the individual best fit models and their uncertainties of each of these TDE candidates in Appendix Section B. Overlaid on Figure 6 is the different powerlaw indexes that one expects to see from TDEs as they decay. Plotted as the solid black line is the standard $t^{-5/3}$, while the black dot-dashed and dotted line represents the much shallower powerlaw index of $t^{-5/12}$ and $t^{-19/16}$ derived by Lodato & Rossi (2011) and (Cannizzo et al. 1990) respectively. The grey shaded region to the right of the black solid line is the powerlaw indexes derived by Guillochon & Ramirez-Ruiz (2013). Plotted as the grey shaded region to the right of the black dot-dashed line is the corresponding band of powerlaw indexes one would expect for disk emission, assuming a similar relationship as that derived by Guillochon & Ramirez-Ruiz (2013).

Based on our powerlaw model fits, we find that the X-ray emission of our TDE sample cluster around either the

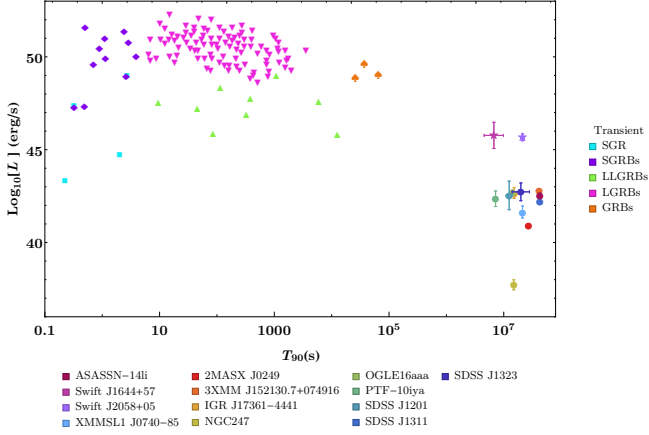


Figure 7. The T_{90} and the corresponding luminosity (L_{90}) over this same time period plotted for our TDE candidates. The T_{90} and L_{90} values of the GRB/GRB-like transient events have been adapted from Figure 2 of [Levan et al. \(2014\)](#).

standard powerlaw index expected from accretion ($t^{-5/3}$), or around the index derived assuming disk emission ($t^{-5/12}$). The events which favour the more shallower powerlaw index are thermal in nature. In comparison, *Swift J1644+57*, *SDSS J1323* and *IGR J17361-4441* exhibit a decay that is consistent within uncertainties with the commonly used index of $-5/3$. Uniquely, non-thermal TDE *Swift J2058+05* has a light-curve decays at a rate in between these two characteristic emission properties.

We find that our powerlaw fits, differ somewhat from those listed in the literature for each TDE. For example, [Cenko et al. \(2012b\)](#) derive a powerlaw decline of ~ -2.2 for the early time 0.3-10.0 keV X-ray emission of *Swift J2058+05*. However we find that taking into account the full X-ray light curve, we derive a shallower index in the 0.3-2.0 keV energy band. The difference in the results derived in our analysis compared to those in the literature most likely arises from two things. Many papers derive the best fit powerlaw decay index associated with the early time X-ray light curve via the 0.3-10.0 keV energy band. This is in contrast to our analysis which focuses on the 0.3-2.0 keV emission of each source and takes advantage of the fact we can now derive and fit the (nearly) complete X-ray light curve of each of these events that include both detected data points and upperlimits. By deriving the X-ray emission in a smaller energy band, we are probing the decay rate of a different component of the TDEs emission which may decay at or contribute at a different rate than that of the harder 2.0-10.0 keV energy band which authors in the literature are also probing. In addition, by combining observations that were taken around the same MJD as discussed in Section 2, we are not as prone to the affect that short term variability and changes in the decay rate has on the derived decay powerlaw index.

The fact that we find that the powerlaw fits derived from the full X-ray light curve are different from those derived at early times, hints towards the possibility that the decay rate of X-ray TDEs changes with time. Following this idea, in Section 5.2 we investigate the differences between the early and late time decay rates of these events and the question of whether the X-ray emission from these events evolve or not.

4.3. How quickly do X-ray TDEs release their energy?

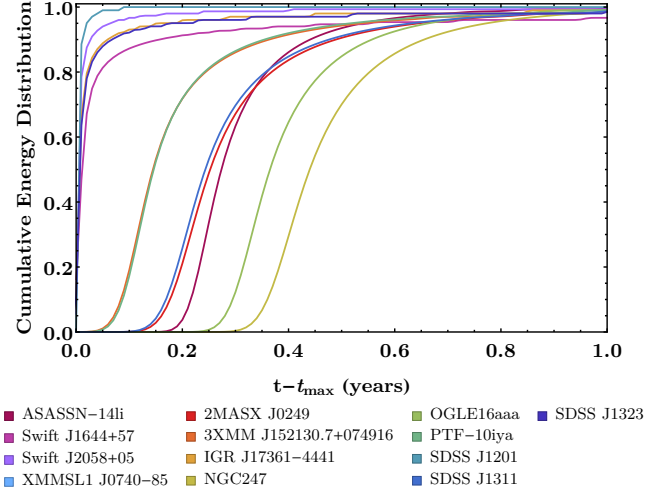


Figure 8. The cumulative energy distribution as a function of time since peak ($t - t_{\max}$) for our TDE candidates.

In studies of GRBs, a commonly derived parameter used to help characterise the properties and type of outburst detected is T_{90} . T_{90} represents the time interval in which between 5% and 95% of the total fluence from a source is observed (see review by e.g., [Levan 2015](#)). Filling in these gaps is not such a problem for short events such as short gamma-ray bursts (SGRBs), since estimating T_{90} is relatively straightforward and a good approximation of the actual T_{90} . However for very long events like TDEs, it is difficult for instruments such as *Swift* to capture the full emission structure of an event, leading to gaps in the observed X-ray light curve. However, as the derivation of T_{90} is dominated by the long lived, lower luminosity emission of the source, this means that the T_{90} derived in these cases is more an approximation of the actual T_{90} . As a consequence, the longer that a source can be followed, the more energy will be integrated over in the T_{90} calculation leading to larger T_{90} values. Indicating that at early times, for long transient events deriving T_{90} values provides more of a lower limit to the actual T_{90} of an event. Regardless of this fact, this still gives us insight into the characteristics of these transient events.

For our TDE candidates, we derived T_{90} and the corresponding isotropic luminosity (L_{90}) over this same time period. In Figure 7 we compare our TDE T_{90} and L_{90} to other well known transient objects including Galactic soft-gamma repeaters (SGRs), long- and short-duration GRBs (LGRBs and SGRBs), low luminosity GRBs (LLGRBs) and ultra-long GRBs. The values of T_{90} and L_{90} for these other transient sources were adapted from Figure 2 of [Levan et al. \(2014\)](#). Similar to that presented by [Levan et al. \(2014\)](#), Figure 7 illustrates that TDEs are extremely long lived events compared to other GRB and GRB-like events, significantly differentiated themselves from these other transient events in the T_{90} and L_{90} parameter space. The values of T_{90} are larger than those presented by [Levan et al. \(2014\)](#) as we have the advantage of having the (nearly) full X-ray light curve available to us for each event, while [Levan et al. \(2014\)](#) focus on T_{90} derived from the early time emission of these sources.

Compared to the GRB/GRB-like sample, our sample of TDEs cover a wide range of lower-luminosity values, with the brightest and most extreme TDEs so far detected in our

sample (jetted TDEs: *Swift J1644+57* and *Swift J2058+05*) fall towards the lower end of the luminosity distribution of GRB/GRB-like events. The fact that these events differ significantly from other extreme events such as GRBs, confirms that these flare-like events arise from significantly different progenitors and provides us with a relatively simple diagnostic to separate these events from GRB/GRB-like event based on their T_{90} and L_{90} .

Based on our derived L_{90} , we find that our sample of events naturally separate into two distinct groups. The non-thermal jetted TDEs have a $L_{90} \sim 10^{44}$ erg s $^{-1}$, while the thermal non-jetted events have a $L_{90} \lesssim 10^{42}$ erg s $^{-1}$. This natural separation implies that there is a bimodal distribution in the bolometric luminosities of X-ray TDEs. This raises the question of why are there no X-ray TDEs with a L_{90} intermediate of these two values? One possibility is that there is a population of X-ray TDEs that may bridge the gap in luminosity, however we are missing these TDEs in the X-ray band as their X-rays are being reprocessed into optical or UV wavelengths. This is not unreasonable, as higher luminosities events have significantly more mass surrounding the source. Due to the highly collimated nature of jetted events, these X-ray TDEs are largely unaffected by the large amount of mass surrounding these events (e.g., *Swift J1644+57* was highly extinct, suggesting a significant amount of stellar debris). For the lower luminosity non-jetted X-ray TDEs there is most likely not a large amount of material surrounding these sources and thus these events can ionise the surrounding material quickly making it transparent to X-rays over a short time period. The population of TDEs that could naturally occupy this “reprocessing valley” are optical UV/TDEs. A large number of these events exhibit significant reprocessing (i.e., *PS1-10jh*: Gezari et al. 2012, 2015; Guillochon et al. 2014, *PS1-11af*: Chornock et al. (2014)) and also exhibit bolometric luminosities that fall within this “reprocessing valley”. These optical/UV TDEs most likely exhibit X-rays, however due to the large amount of material obscuring these events the emission is reprocessed into a lower wavelength.

In Figure 8 we have plotted the cumulative energy distribution as a function of time for the TDE candidates we consider. One notices quickly that the non-thermal and thermal TDE candidates release their energy over quite different time scales. Jetted events *Swift J1644+57*, and *Swift J2058+05* release >80% of their energy within their first month. However, the non-jetted events release their energy much more gradually, taking approximately five months to reach the amount released by the jetted events in their first month. Interestingly, *IGR J17361-4441* which was first discovered as a hard X-ray source, and TDE candidates SDSS J1201 and SDSS J1323 also show similar behaviour to the two jetted events in our sample, which could indicate that these sources also exhibit significant non-thermal emission during their flaring event. This highlights that thermal and non-thermal events emit their energy by two quite different mechanisms and that within ~ 1 month of detecting a non-thermal X-ray TDE, the derived T_{90} value is more or less representative of the actual T_{90} value, while one would need to monitor thermal TDEs over a much long time period to derive T_{90} .

4.4. How absorbed are X-ray TDEs?

2, 5, 6, 8, 9

From the column densities (N_H) derived from fitting the X-ray spectra of each TDE (see Tables 14–18), we can make

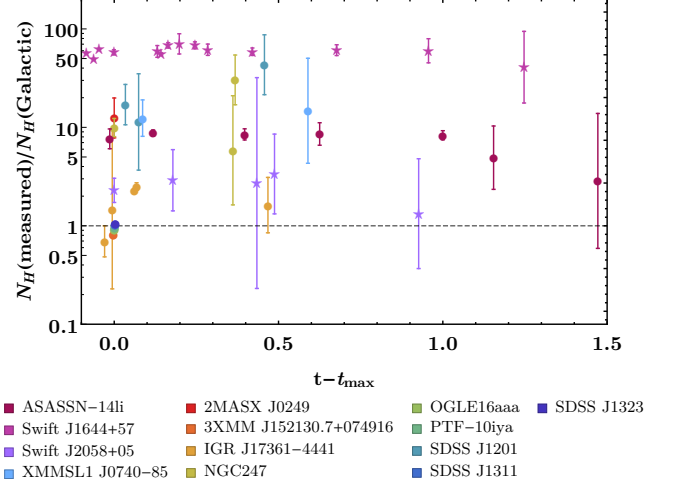


Figure 9. The ratio of the measured column density (N_H) and the Galactic column density along the line of sight as derived from Kalberla et al. (2005), as a function of time $t - t_{\max}$. The dashed black line corresponds to when the measured N_H is equal to the Galactic column density.

a statement about the environment in which these events are found. In Figure 9 we have plotted as a function of time, the ratio of the measured N_H against the Galactic column density along the line of sight as measured by the Leiden/Argentine/Bonn (LAB) Survey of Galactic HI (Kalberla et al. 2005). From this plot one can see that a large fraction of X-ray TDEs have N_H values that are at least two times greater than the Galactic column density measured along the line of sight to these events. For 3XMM, OGLE16aaa, PTF-10iya, SDSS J1311 and SDSS J1323, which we were unable to constrain N_H from the available X-ray observations, and thus assume the N_H derived from the LAB Survey. *Swift J1644+57* is the most highly absorbed event out of all our TDE candidates. We find that both jetted and non-jetted events show evidence of this enhanced absorption, with most of the TDE candidates we consider have a N_H that is between $\sim 2 - 10$ times that of their Galactic N_H .

Based on this analysis, there is no obvious trend in the value of N_H that separates thermal (non-jetted) or non-thermal (thermal) TDEs. Both types of events show evidence of strong enhancement in N_H . We also find that most of the TDE candidates we consider show no significant variation in N_H as a function of time. The exception to this is *Swift J1644+57*, which as Burrows et al. (2011) also highlighted, shows some evidence of variation ($\sim 1\sigma$) with N_H at early times; however this variation is not significant at later times.

Since we find that nearly all these events are quite absorbed in nature, this indicates that there must be a larger amount of extinction surrounding these sources in their host galaxies. In fact, the values we derive for N_H are most likely a lower limit to the actual N_H in these hosts. Recently Arcavi et al. (2014) determined that a significant fraction of optical TDEs are found in post-starburst galaxies. From modelling the optical spectra of these hosts their results imply that optical TDEs occur in galaxies with sub-solar abundances. However, to derive N_H we assume solar abundances, which based on the work by Arcavi et al. (2014) indicates that we are underestimating the actual N_H towards the source. As the N_H of each event as a function of time can be well-approximated using a constant, this could also suggest that the material surrounding

these events is quite dense and the ionising radiation is unable to change its absorption properties. Even though these events are quite absorbed the amount of material required to produce these column densities implied by our fits is quite small compared to what one would expect from the overall mass/energy budget of the event (i.e., $1 - 10\% M_{\odot}$). The exception to this is *IGR J12580*. However, the low mass estimate implied by these fits most likely arises from the fact we are underestimating the actual N_H rather than the amount of material being quite small.

Based on their X-ray light-curves *Swift J1644+57*, *ASASSN-14li*, *XMMSL1 J0740-85* and to a lesser extent *Swift J2058+05* show evidence of variability in their X-ray light curves. This variability is quite pronounced when looking at individual observations of these sources but is also noticeable in our derived light curves (see e.g., Figure 2). One possibility is that this variability is driven by absorption. In this case, one would expect to observe dramatic changes in the N_H as a function of time which correlated with the observed variability. However, we do not see this in Figure 9 indicating that the variability seen in the X-ray emission from these events is intrinsic to the source, rather than a result of the environment.

4.5. How soft are X-ray TDEs and how does this softness evolve?

Using the soft, medium and hard counts listed in Tables 9–13, we constructed hardness ratios for each of the TDE candidates we consider. The hardness ratio (HR) is defined as $(H-S)/(H+S)$, where H is the counts in the equivalent 2.0–10.0 keV energy band and S is the counts in the equivalent 0.3–2.0 keV energy band. In Figure 10 top panel we plotted HR as a function of the soft 0.3–2.0 keV count rate for each TDE candidate, while in Figure 10 bottom panel we have plotted the HR ratio as a function of soft count rate when the luminosity was at peak. By plotting the HR against count rate, we are able to determine how the emission from each source evolves.

From Figure 10 top panel one can see that the emission from all TDEs is quite soft in nature. These events have a HR ratio that ranges between -1 and +0.3 with most events falls between -1 and 0, while nearly all the emission from *Swift J1644+57* and some of the emission from *IGR J17361-4441* has a HR between 0 and +0.3. Interesting, *ASASSN-14li* and *Swift J1644+57* characterise the most extreme HRs seen from these TDEs. Here *ASASSN-14li* is one of the softest events detected with a HR ratio of ~ -1 , while *Swift J1644+57* is one of the hardest TDEs with a HR ratio of ~ 0.3 . At peak, all events have a HR between -1 and 0 (see Figure 10 bottom panel).

Non-thermal jetted TDEs *Swift J1644+57*, and *Swift J2058+05*, along with hard X-ray source *IGR J17361-4441* produce the hardest X-ray emission of our sample, best characterised with a peak HR value $\sim +0.1$, while *ASASSN-14li*, *2MASX J0249*, *SDSS J1201*, and *SDSS J1323* are the softest at peak with a HR of $\sim +1.0$. All other sources fall between these two values.

ASASSN-14li exhibited relatively little hardness evolution as its emission faded, staying extremely soft during its full decay, with *XMMSL1 J0740-85* and *NGC247* also exhibiting similar behaviour even though those sources are not as soft as *ASASSN-14li*. As *Swift J1644+57*, *Swift J2058+05* and *IGR J17361-4441* faded, these sources showed quite a bit of variability in their HRs, especially when the sources were brightest. Even though the early time emission from *Swift J1644+57* varied, a significant fraction of the low count

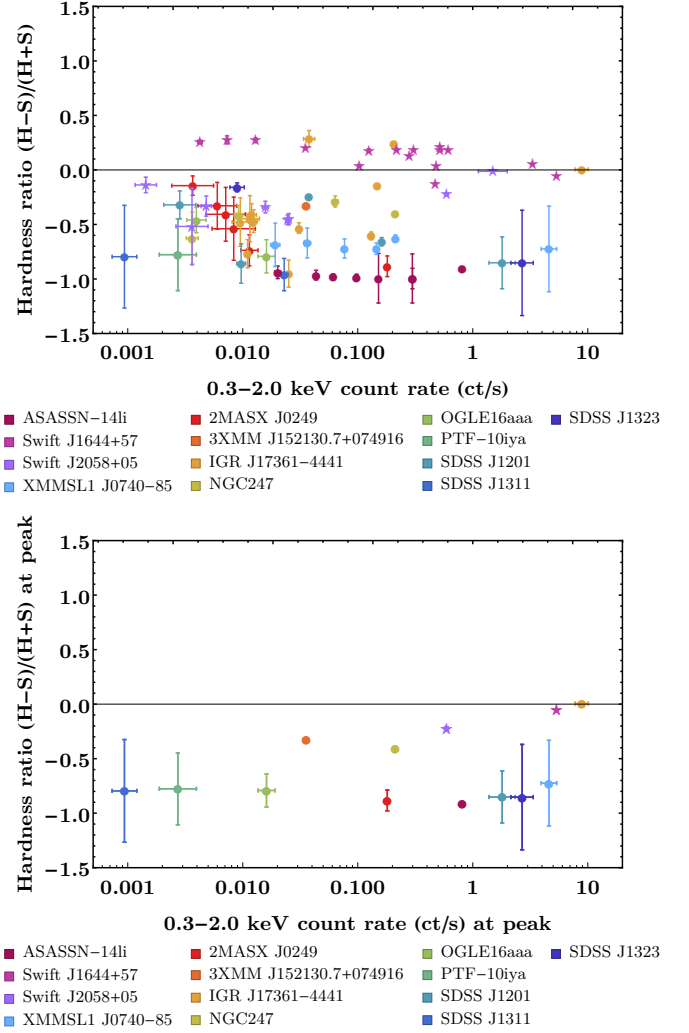


Figure 10. The hardness ratio defined as $(H-S)/(H+S)$, where H is the counts in the equivalent 2.0–10.0 keV energy band and S is the counts in the equivalent 0.3–2.0 keV energy band, plotted against the 0.3–2.0 keV X-ray count rate. The top panel highlights the hardness ratio for the full X-ray emission detected for each source, while bottom panel shows the hardness ratio when the X-ray emission was measured at its peak.

rate emission from this event showed relatively little hardness evolution, consistently staying around a HR ~ 0.3 . This is not the case for *Swift J2058+05* and *IGR J17361-4441*, whose HR varied quite dramatically as it faded. For *2MASX J0249*, *SDSS J1201* and *SDSS J1323*, these events were soft at peak and became harder as they faded. However *IGR J17361-4441* which was proposed to be the tidal disruption of a planet, follow the opposite trend, where they are harder at peak and then becoming softer as they decay.

We saw in Section 4.4, that nearly all X-ray TDEs are quite highly absorbed. As a consequence, the relatively soft HRs that we find for X-ray TDEs could result from the enhanced column densities towards these events. To test this, we plotted HR as function of N_H (see Figure 11). If N_H was responsible for the soft nature of X-ray TDEs, we would expect to see that the sources which have the largest measured N_H value should be the softest sources in our sample (i.e., be predominantly thermal in nature). However, we find that this is not the case with both the hardest and softest sources in our sample

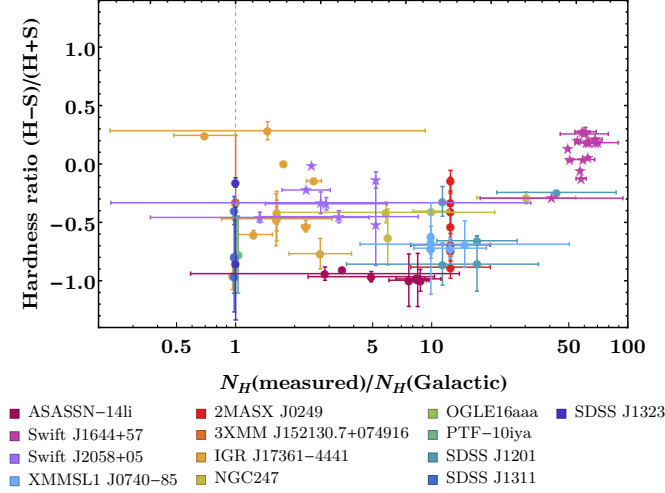


Figure 11. Hardness ratio as a function of the ratio of measured column density, $N_H(\text{measured})$ divided by the Galactic column density, $N_H(\text{Galactic})$ plotted for all TDE candidates.

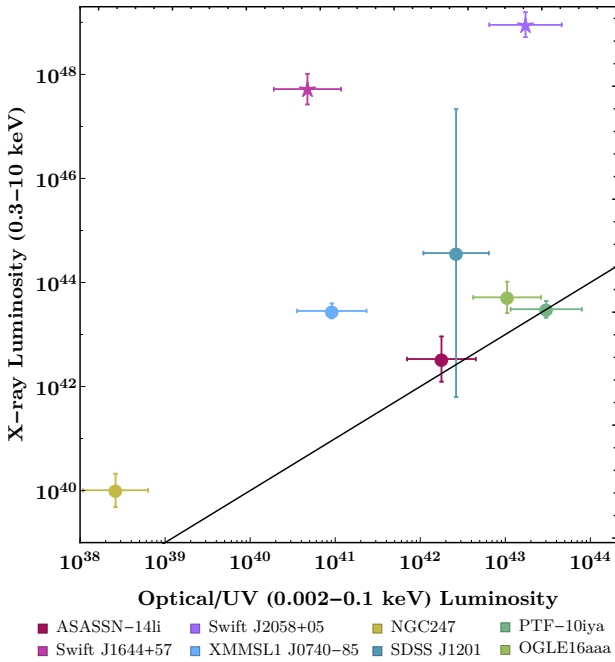


Figure 12. The integrated optical/UV (0.002-0.1 keV) luminosity of each TDE plotted against the integrated X-ray (0.3-10.0 keV) luminosity. Plotted as the black solid line is when the optical/UV and X-ray luminosity are equivalent (i.e., the ratio of these two parameters is unity). Not all of the TDEs listed in Table 2 have optical/UV data available around the time the X-ray emission peaked.

exhibiting enhanced N_H relative to their Galactic N_H . As consequence, the relatively soft HRs derived from our analysis is most likely a inherent property of these events, rather than a consequence of the environment as pointed out in Section 4.4.

4.6. What is the spectral energy distribution of X-ray TDEs?

Using the soft, medium and hard count rates as measured at peak for each TDE candidate, we derive the νF_ν spectral

energy distribution (SED) for each event. Analysing the SED allows one to determine the amount of energy emitted by each event as a function of wavelength (or energy), as well highlighting in what wavelength (or energy band) each event released most of its energy. As we are interested in the broadband SED of each source, we took from the literature (when it was available), radio, optical, and IR/UV data for each source that was taken simultaneously or close to when the original X-ray flare was detected. In Appendix C we have briefly described how we derived the SED and where we obtained the radio, optical/UV data from, while in Figure 24 which is also found in the Appendix C, we have plotted the individual SEDs for each of our TDE sample.

Using Figure 12, we can determine whether these events emit most of their energy in the optical/UV or X-ray energy band. To do this we derive the integrated luminosity in both the optical/UV (0.002-0.1 keV) and X-ray (0.3-10.0 keV) energy bands. As not all events have optical/UV emission around the time the event was discovered, we focus only on the events that have detected optical/UV emission. To derive the integrated luminosity in each energy band, we modelled the emission in the corresponding band using a powerlaw with an exponential cut off which was either left as a free parameter or set to the maximum of our specified energy band (i.e., 0.1 keV in the optical/UV or 10.0 keV in X-rays). We then integrated over the corresponding energy range to obtain the luminosity, while uncertainties are also derived from these model fits. These integrated luminosities are plotted as a function of each other in Figure 12. In this figure, the black solid line indicates when the amount of energy released in both the optical/UV and X-ray energy bands is equivalent. Above (Below) this line indicates that the event releases most of this energy in the X-ray (optical/UV) energy band.

The non-thermal jetted X-ray TDEs *Swift J1644+57* and *Swift J2058+05* emit most of their energy in the X-ray energy band. For thermal events like *ASASSN-14li*, *OGLE16aaa* and *PTF-10iya* they emit approximately the same amount of energy in both the optical/UV and X-ray energy bands, while *NGC247*, *SDSS J1201* and *XMMSL1 J0740-85* emit slightly more energy in the X-ray energy band than they do in optical/UV. If veiled X-ray TDEs were to appear on Figure 12, it is likely that their X-ray emission would fall below the detection thresholds plotted in Figure 5.

4.7. Do non-thermal jetted and thermal non-jetted TDEs naturally separate?

Characterising whether an X-ray TDE is thermal or non-thermal in nature provides information about whether the emission one observes arises from the accretion disk/fallback or from the formation of a relativistic jet. In the literature, detailed studies of their properties in multiple wavelengths, has led to the classification of a some of these events as either non-thermal or thermal. However, due to the lack of multi-wavelength data for a number of these events, the classification of some of these events as either thermal or non-thermal is either non-existent or not very clear. Using our analysis, we can specify the common properties non-thermal and thermal X-ray TDEs seem to have, using events such as *Swift J1644+57* and *ASASSN-14li* whose nature is very well accepted in the literature as baselines. Using these common characteristics, we can attempt to classify the TDEs in our sample as either non-thermal or thermal events.

Based on Tables 14–18, we find that non-thermal events tend to have X-ray emission that is best described by a hard

powerlaw index when modelling their X-ray spectra. Summarising the results presented in Figures 7, 8, 10, and 12, non-thermal TDEs tend to have higher L_{90} values and release a significant amount of their energy over a shorter time period than their thermal counterparts. The emission at peak from a non-thermal TDEs usually has a HR between $\sim -0.5 - 0.0$, and a large X-ray to optical luminosity ratio. They also exhibit more variability in their X-ray emission than thermal TDEs. Discussed in more detail in Section 5.1, one can also see that from Figure 13 that non-thermal events are best characterised as having a soft to medium count ratio that is $\lesssim 1$.

For thermal X-ray TDEs, we find that their X-ray emission is best described by a very soft powerlaw index when modelling their X-ray spectra. As the very soft powerlaw index mimics thermal emission over the X-ray energy band pass of current X-ray satellites, the very soft index from these events is not unexpected. Most thermal events have an $L_{90} \lesssim 10^{42}$ erg s $^{-1}$ and take much longer to release most of their energy compared to the non-thermal events. These sources are also quite soft, with a HR $\lesssim -0.3$ and have a X-ray to optical luminosity ratio around 1. They also seem to show less amount of variability compared to non-thermal events and they also have a soft to medium count ratio that is $\gtrsim 1$.

Using these properties, *Swift* J1644+57, and *Swift* J2058+05, can be classified as non-thermal in nature, while *ASASSN-14li* has properties that seem to characterise the X-ray emission of a thermal TDE. This is consistent with the classification of these events in the literature. However for the likely X-ray TDEs, it is not necessarily as clear cut as their properties do not always fall exactly into only one of the categories specified above. However, it seems that *NGC 247*, and *IGR J17361-4441* have more properties similar to those of the non-thermal TDEs, while *2MASX J0249*, *3XMM*, *SDSS J1201*, *SDSS J1311*, *SDSS J1323*, *OGLE16aaa*, *PTF-10iya*, and *XMM SL1 J0740-85* have more properties common to those of thermal TDEs.

5. DISCUSSION

5.1. The emission from an X-ray TDE peaks in the soft X-ray band.

In Section 4.5, we find that X-ray TDEs are quite soft in nature with HRs $\lesssim +0.3$, while in Section 4.4, we suggested that variability in column densities measured towards these events was not responsible for their soft HRs. To further test this, we used the soft (0.3-1.0 keV), medium (1.0-2.0 keV) and hard (2.0-10.0 keV) count rates that we derived for each event (for Tables 9-13) and plotted these as a function of each other. To remove the effect that N_H can have on the count rate in the different energy bands, we divided each set of counts by the N_H value measured or assumed for that observation (from Tables 14-18). As N_H has the greatest effect in the lower energy bands, while at higher X-ray energies the effect of absorption is minimal, we also took this into account and scaled N_H by $1 - e^{-E_{\text{band}}}$ (e.g., Wilms et al. 2000). In Figure 13, we have plotted the N_H corrected count rate diagrams in which we compare the count rates from energy band, while also plotting the ratio of the soft/medium counts vs. medium/hard counts. We compared these N_H corrected count rate diagrams to those we obtain without correcting for N_H and we find that apart from different values for the count rates (which is expected), we observe exactly the same trends seen in Figure 13. This again highlights that the softness of X-ray TDEs is most likely an inherent property of these events.

In the soft vs. medium and soft vs. hard plots of Figure 13, we find that jetted and non-jetted events seem to occupy different parts of these diagrams, where *Swift* J1644+57 and *ASASSN-14li* naturally provide a boundary in which nearly all X-ray TDEs fall within. One can see that as these events become brighter, the characteristics of the emission from the jetted and non-jetted events diverges from each other. For the same count rate measured in the soft energy band, jetted events increase significantly in the number of medium and hard counts, while non-jetted events tend to have a more flatter evolution in these higher energy bands.

To determine the correlation between these observables we ran a linear regression and plotted these as the blue dashed and black dotted lines in Figure 13. To quantify how correlated the count rates are we derive the coefficient of determination (R^2 value) of each fit, where a high (lower) R^2 implies that these parameters are (not) well correlated. These values are listed in the caption of Figure 13. One can see that this divergence of the non-thermal and thermal events seen in both the soft vs. medium and soft vs. hard count rate plots leads to a low R^2 , indicating that there is little correlation between these energy bands. However, when we look at the medium vs. hard count rate plot we find a completely different story. Regardless of the nature of the TDE, there is very little scatter between our X-ray TDE candidates in these higher energy bands, with both thermal and non-thermal TDEs showing a similar evolution of their emission in these bands. From our linear regression, we find a strong correlation between these count rates, indicating that there is very minimal change in the emission of these events in the 1.0-2.0 keV and 2.0-10.0 keV energies. This is also seen when one considers the ratio of these count rates in the different energy bands (Figure 13 bottom right). The variation in the medium/hard count ratio is significantly less compared to that seen in the soft/medium energy band, which varies over nearly four orders of magnitude compared to only one. As such, this leads us to conclude that the X-ray emission of TDEs peak predominantly in the soft (0.3-1.0 keV) energy band, producing the large scatter seen in the soft vs. medium and soft vs. hard count rate plots. This is not so surprising since Ulmer (1999) determined that accretion powered flares from BH with mass $\lesssim 10^7 M_\odot$ should radiate in the soft X-ray band.

As we have corrected the count rates of our TDE sample for absorption, the large variation seen in the soft count rate band for predominantly non-jetted TDEs likely suggests that there is significant differences in the reprocessing rates experienced by these events. Due to the lack of variation in these higher energy bands, the enhanced column densities and low X-ray to optical ratios of these events supports the fact that a large fraction of their emission is being reprocessed into either soft X-rays or into optical/UV wavelengths. As a consequence, the enhanced column densities surrounding these sources could lead to significant reprocessing and thus be responsible for the intrinsically soft nature of these X-ray TDEs. This observation also ties in nicely with the fact that there are a number of optical TDEs without X-ray emission (i.e., Veiled TDEs in Section 3.1.4), since a large fraction of these events show evidence of significant reprocessing due to a dense surrounding environment (e.g., *PS1-10jh*: Gezari et al. 2012).

In the bottom right panel of Figure 13, we have plotted the ratio of the N_H corrected medium and hard counts (M/H) as a function of the N_H corrected soft and medium counts (S/M). All X-ray TDEs have a $M/H \gtrsim 0.5$. However, thermal and

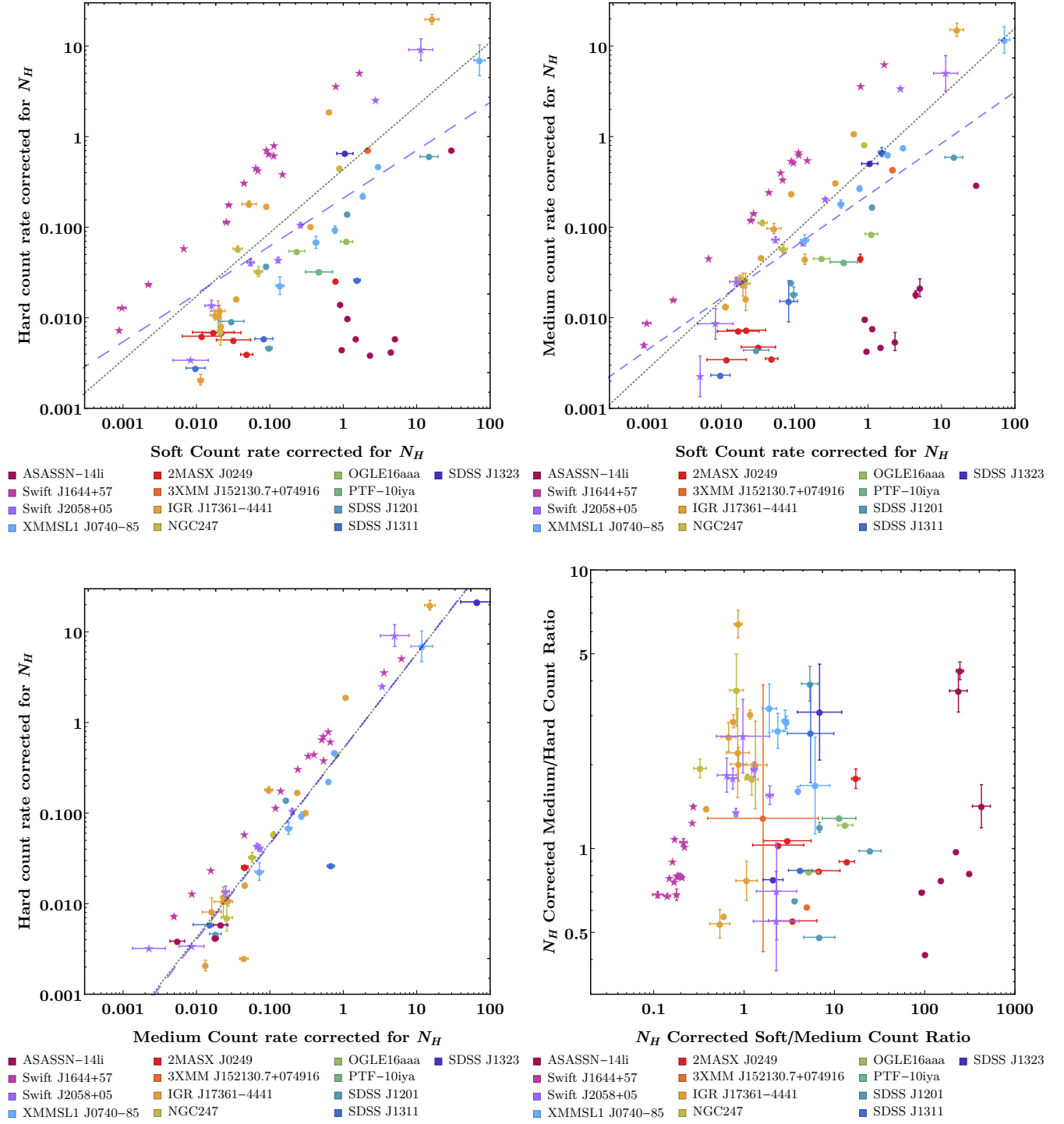


Figure 13. For the TDE candidates we consider, we have plotted the soft (0.3–1.0 keV), medium (1.0–2.0 keV) and hard (2.0–10.0 keV) count rates as a function of one another (top three panels). In the bottom panel we have plotted the ratio of the medium vs. hard counts as a function of soft vs. medium counts. For all plots, we corrected the number of counts for the effect that column density (N_H) has on the emission in each energy band by scaling the count rate by $(1-e^{-E_{\text{band}}})(N_H/(10^{22}\text{cm}^{-2}))$. Here $(1-e^{-E_{\text{band}}})$ factor takes into account the fact that the column density affects soft X-ray emission more significantly than other energy bands. By applying this correction, we remove the biasing affect that N_H might have on our data. Overlaid on the top three panels is the least squares fit of each plot. Shown as the blue dashed line is the best fit using all data from the TDE candidates we consider, while the dotted black line corresponds to the best fit that is obtained when excluding the data points of ASASSN-14li. The coefficient of determination for each of the blue dashed (black dotted) lines is 0.33, 0.41, 0.89 (0.57, 0.69, 0.89) respectively.

non-thermal events naturally separate from each other when looking at their S/M . The emission from non-thermal events have a $S/M \lesssim 2$, while for thermal X-ray TDEs their emission has a $S/M \gtrsim 2$. Things become more complicated around $S/M \sim 2$ with emission from both the non-thermal and thermal events begin to overlap as they become fainter. However when most of these sources are relatively bright, their emission is sufficiently different that one could easily classify the type of event based on this diagram. This provides a unique way of observationally categorising X-ray TDEs as either thermal or non-thermal events, especially ones which have limited observational information about the source.

5.2. The emission from an X-ray TDE evolves with time

In Section 4.2, we fit the full X-ray light curve of each of the TDE candidates we consider using a simple powerlaw model. We find that the powerlaw index we derive differs from those listed in the literature, which are commonly derived from the early time emission of these sources. As a consequence, this brings into question whether it is reasonable to assume that the emission of each event decays following $t^{-5/3}$ as is done frequently in the literature. To investigate this, we separated the emission from each source into early time and late time intervals and then fit these sets of data using a simple powerlaw with the normalisation and powerlaw index set free, much like that done in Section 4.2.

In Figure 14 we have plotted, similar to Figure 6, the best fit power law index and its uncertainty for the early and late time emission of each TDE candidate. We have also overlaid the ranges of various powerlaw indexes expected for TDEs. One can see that at early times the emission from *Swift* J2058+05, and *IGR* J17361-4441 is consistent with fallback. For *2MASX* J0249, *SDSS* J1201, *SDSS* J1311, *XMMSL1* J0740-85 and *PTF-10iya*, these events have indexes consistent with disk emission, while *Swift* J1644+57 and *SDSS* J1323 have indexes that fall between $-5/3$ and $-5/12$. In addition, *ASASSN-14li*, *3XMM*, *NGC247* and *OGLE16aaa* have a powerlaw index slightly lower than that expected from disk emission, however within uncertainties they are consistent with $-5/12$. At late times the emission from each TDE changes quite dramatically. *Swift* J2058+05, *2MASX* J0249, *3XMM*, *OGLE16aaa*, *PTF-10iya*, *SDSS* J1323 have indexes consistent with being flat, while the emission from *SDSS* J1311 is still consistent with disk emission. Within uncertainties, *Swift* J1644+57, *ASASSN-14li*, *XMMSL1* J0740-85, *SDSS* J1201, and *IGR* J17361-4441 is also consistent with disk emission even though their best fit powerlaw model falls slightly above or below this value. Interestingly, *NGC247* is the only event that has late time emission that is consistent with fallback, however, the large uncertainties associated with this fit also suggests that this event is consistent with viscous disk accretion. The large uncertainties seen for some of these events arises from the light curve being more sparsely sampled, especially at late times.

In Figure 15 we have plotted a histogram of the powerlaw indexes for the TDE candidates we consider at both early and late times. At early times, the emission from the *X-ray TDE* candidates arises mostly from fallback or viscous disk accretion, with both the *Swift* events dominating the histogram distribution. Here *ASASSN-14li* and *XMMSL1* J0740-85 is the exception, in which at early times it is consistent with disk emission. For the *likely* X-ray TDE sample, the majority of events exhibit emission consistent with disk emission at early times, with the exception of *IGR* J17361-4441 which favours

fallback like the other *Swift* events. At late times, we see that the emission from our sample of X-ray TDEs evolves such that nearly all events have emission that converges to a powerlaw index consistent with disk emission or viscous disk accretion.

One should also notice that, with the exception of *Swift* J2058+05 and *IGR* J17361-4441 at early times, and potentially *NGC 247* at later times, that the emission from these events decays with a powerlaw index much lower than the canonical $t^{-5/3}$ relationship. Guillochon & Ramirez-Ruiz (2015) showed that if a TDE has a long viscous time scale³² that these events will decay at a rate much shallower than the standard $t^{-5/3}$. This implies that TDEs detected in X-rays are most likely viscously slowed and as such the viscous timescale is important in determining the emission of these events, especially at late times.

To see whether the transition between early and late times is smooth, we determined the best fit powerlaw index for the *X-ray TDE* candidates as the time of peak goes to infinity. Due to the sparseness of the available X-ray data for the *likely* *X-ray TDE* candidates, we were unable to determine how the emission from these events evolve in a similar way. In Figure 16 we have plotted the powerlaw index as a function of $t - t_{\text{peak}}$, where t_{peak} is the time in which we detect the its peak luminosity. Straight away, one can see that the non-thermal *Swift* events shows significant variability in the properties of their emission as a function of time, while the emission from *ASASSN-14li* and *XMMSL1* J0740-85 evolves significantly more smoothly. Even though we find that the powerlaw index for *ASASSN-14* steepens to -1 while it decays, the average emission from *ASASSN-14li* is consistent with disk accretion. Similarly, the emission from *XMMSL1* J0740-85 shows some variation, however it is consistent within uncertainties with viscous disk accretion throughout its full emission. This is not the case for *Swift* J1644+57 and *Swift* J2058+05. *Swift* J1644+57 initially converges towards an index more consistent with disk emission, but suddenly shows a spike indicating that the emission was more consistent with fallback. After this spike, it again converges towards $-5/12$, but then steepens dramatically before falling to $-5/12$. *Swift* J2058+05 was initially consistent with fallback, but approximately half way through its decay, its emission dramatically transitioned such that it was consistent with disk emission. Whether the emission seen for *Swift* J2058+05 at both early and late times was smooth or resulted from more extreme variations in the emission of the source as seen in *Swift* J1644+57 it is difficult to say due to the sparseness of the data during these periods.

As we observe significant evolution in the powerlaw index of each event on both small time scales (Figure 16) and larger time scales (Figure 14) this indicates that we cannot assume that the X-ray emission from all X-ray TDEs decays follow $t^{-5/3}$. In fact, a large fraction of the emission from X-ray TDEs is consistent with disk accretion at both early and late times, while a majority of the non-thermal jetted events at early times has emission that is more consistent with fallback. Based on Figure 16, it seems that particularly jetted X-ray TDEs, will transition multiple times between the two emission processes, while thermal TDEs will tend to fluctuate around a powerlaw index that is consistent with one particular

³² The viscous time scale is defined as the time it takes for material to accrete and is defined by $t_{\text{visc}} = \alpha^{-1}(h/r)^{-2}P$, where α is the viscous parameter, h is the scale height on the disk, P is the orbital period and r is the distance from the BH. See (Guillochon & Ramirez-Ruiz 2015) for more details.

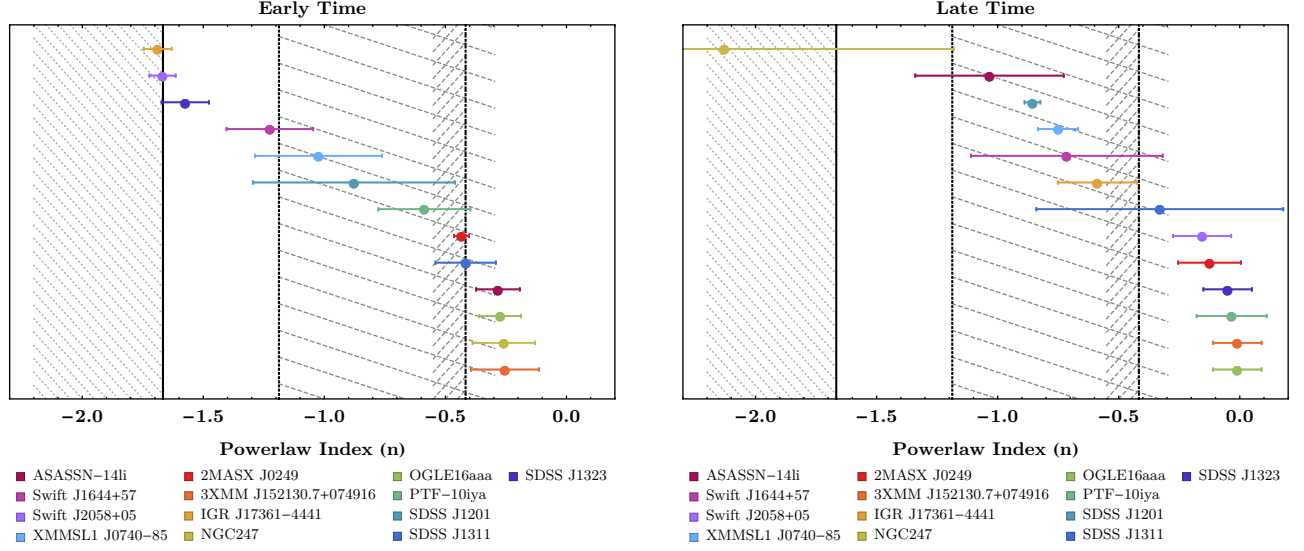


Figure 14. The best fit powerlaw indexes and their 1σ uncertainties obtained from fitting the early time emission (left panel) and the late time emission (right panel) of the TDE candidates we consider. Also overlaid are the different powerlaw indexes expected for TDEs (see the caption of Figure 6 for more details).

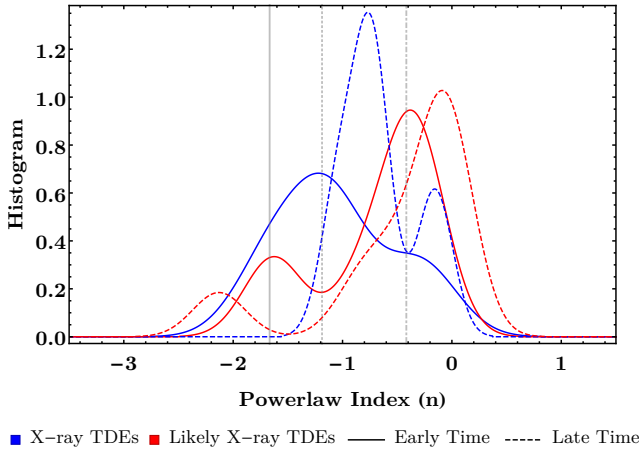


Figure 15. Histogram of the early and late time powerlaw indexes for the TDE candidates we consider seen in red and blue respectively. Here the solid histograms represent the powerlaw index at early times, while the dashed histograms represent the powerlaw index at late times. Plotted as the solid, dotted dash-dotted grey vertical lines are the powerlaw indexes for fallback (-5/3), viscous disk accretion (-19/16) and disk emission (-5/12) respectively.

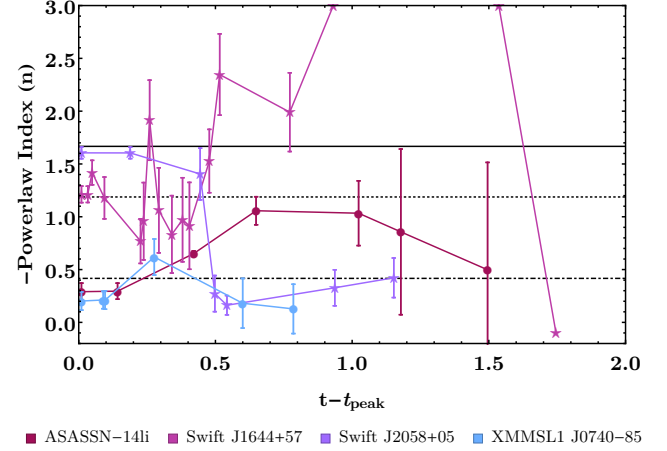


Figure 16. The best fit powerlaw index and its uncertainty for the X-ray TDE sample that was obtained as $t_0 \rightarrow \infty$. Here we have plotted these indexes relative to $t - t_{peak}$, where t_{peak} is taken as the time when the source was brightest. The lines joining the points are to guide the eye and are not fits. Here the solid, dotted and dot-dashed black horizontal lines correspond to a powerlaw index of -5/3, -19/16, and -5/12 respectively. Due to the sparsity of the X-ray data for the likely TDE candidates we are unable to constrain the powerlaw index as $t_0 \rightarrow \infty$.

emission type.

5.3. The emission mechanism(s) of X-ray TDEs.

The SED is a powerful tool as it can put strong constraints on the type of mechanism responsible for the emission detected from an astrophysical object. In an attempt to determine the main emission mechanism responsible for the X-ray TDEs we consider, in Figure 17 we have plotted the SED of each individual TDE. Overlaid on this plot are various radiative astrophysical processes, such as synchrotron emission, Rayleigh-Jeans, thermal black-body, free-free emission and inverse Compton scattering, which are possible processes that can be responsible for the emission observed in each energy band. Details of each radiative process have been described in the caption of Figure 17.

In the X-ray energy band, eight out of the thirteen events

do not show significant X-ray emission above 2 keV. These include well known thermal event *ASASSN-14li*, optical TDE *PTF-10iya*, as well as *2MASX J0249*, *3XMM*, *OGLE16aaa*, *SDSS J1201*, *SDSS J1311* and *SDSS J1232*. The other five events which do show emission above 2 keV include the non-thermal *Swift* events, as well as TDEs *IGR J17361-4441*, *NGC 247* and *XMM SL1 J0740-85*. The emission from the first group of events can be well reproduced using either IC scattering or synchrotron emission with a cut-off energy around ~ 0.1 keV. However, for the TDEs that fall into the second group, their emission can be more complicated. *Swift J1644+57* can be well reproduced by IC scattering with a cut-off ~ 1 GeV, while *Swift J2058+05*, *NGC 247*, *XMM SL1 J0740-85* and *IGR J17361-4441* whose emission seems to be better reproduced using synchrotron emission with a cut-off > 10 GeV.

In the IR to UV energy band the emission from these sources is much more complicated, with each event showing significantly different types of emission. The emission from *Swift J1644+57*, *XMM SL1 J0740-85* and *SDSS J1201* can be well approximated by a thermal blackbody, while *ASASSN-14li*, and *PTF-10iya* are better described by blackbody spectrum from an accretion disc. *Swift J2058+05* has quite different emission in the IR to UV band compared to the other events, as it is better described by optically thin synchrotron emission. These results are consistent with those listed in the literature.

In the radio/sub-mm energy band, only a few of our X-ray TDE sample have data in this energy band. For a majority of these events, their emission (either constrained directly or through upperlimits) is flatter than what is expected from optically thick synchrotron or Rayleigh-Jeans. The flattening of the radio emission may result from differences in the environment that these events are born into, or in the physics associated with the formation of a jet from these events. [Cenko et al. \(2012b\)](#) also suggested that a flattening of the radio emission in its SED may also imply a more extended radio source arising from each events. However, even though most of these events seem to diverge from these standard radiative processes, the emission from *Swift J1644+57* can be reasonably well approximated using synchrotron emission which is consistent with the result of [Metzger et al. \(2012\)](#); [Zauderer et al. \(2013\)](#).

5.4. What is the BH mass of each X-ray TDE?

Using the T_{90} and L_{90} values derived from Section 4.3, we can attempt to estimate the BH masses of each event. In Figure 18 we have plotted our derived L_{90} as a function T_{90} for each of the TDE candidates we consider. Assuming the quintessential type of disruption currently used in the literature of a main sequence star being fully disrupted by a black hole with mass M , we can derive the expected T_{90} and L_{90} for this type of scenario assuming different BH masses. To estimate these values we use the fallback rate curves produced by [Guillochon & Ramirez-Ruiz \(2013\)](#). Here we derive \dot{M}_{90} from these light curves and assume that 10% of this is accreted on the BH to derive L_{90} . To derive T_{90} , we follow the same method as listed in 4.3. As these curves were derived assuming a BH mass of $10^6 M_\odot$ we scale this to derive the equivalent values for a BH mass of $10^5 M_\odot$ and $10^7 M_\odot$. These expected T_{90} and L_{90} are shown as the solid black data points in Figure 18. We also derive the Eddington luminosity for a BH mass of $10^5 M_\odot$, $10^6 M_\odot$ and $10^7 M_\odot$, which are shown as the horizontal lines.

From this plot, one can see that the majority of events have a T_{90} that is consistent with a BH mass between $10^5 M_\odot$ and $10^7 M_\odot$. With the exception of *Swift J1644+57* and *Swift J2058+05*, all events have luminosities less than the Eddington luminosity of their estimated BH mass. For *Swift J1644+57* and *Swift J2058+05* which are known to be non-thermal jetted TDEs, their L_{90} s are super-Eddington, which is consistent with [De Colle et al. \(2012\)](#) who showed that super-Eddington accretion rates are required to power the formation of the jet. Since the Eddington luminosity scales linearly with black hole mass, one would think that TDEs arising from low mass BHs would be super-Eddington, while those from higher mass BHs would be sub-Eddington. Under this assumption, one would expect that our T_{90} estimates would suggest that a significant fraction of the TDEs would have a BH

$> 10^7 M_\odot$, which as seen in Figure 18 is not the case. However, if the viscous timescales for these events are long, [Guillochon & Ramirez-Ruiz \(2015\)](#) showed that this assumption does not necessarily hold, with a larger fraction of TDEs arising from lower mass BHs would actually be sub-Eddington. In fact, [Guillochon & Ramirez-Ruiz \(2015\)](#) determined that a majority of events arising from a BH with a mass below $10^7 M_\odot$ are actually viscously slowed. As all events have a BH mass $< 10^7 M_\odot$, and all events, with exception of the jetted *Swift* events have sub-Eddington luminosities, this implies that nearly all X-ray TDEs are viscously slowed.

6. CONCLUSION

In this paper we performed a systematic analysis of all (as of writing) publicly available X-ray data from *ROSAT*, *Chandra*, *XMM-Newton* and *Swift* for ~ 70 TDE candidates currently presented in the literature. Regardless of their literature classification, we characterised the emission from each candidate by extracting the source counts in different energy bands, and when we were able to, their X-ray spectra. Using either the X-ray spectra or the source counts, we derive the 0.3-2.0 keV flux and luminosity of each source, producing multi-decade X-ray light curves for each event. Using the derived X-ray products, a well-defined criteria of the general properties of a TDE, and some guidance from studies of each source found in the literature, we select a set of candidates that allow us to best characterise the properties of the X-ray emission from TDEs.

We find that the canonical powerlaw index of $t^{-5/3}$ which is commonly assumed as the decay rate of the light curve of a TDE is not necessarily a universal standard in the 0.2-3.0 keV X-ray energy band. Rather, we find that these events have a wide variety of powerlaw indexes, consistent with both fallback and disk emission both over their full X-ray light curve, and during their early and late time emission. We find that the powerlaw index of these TDEs evolves with time, however this evolution is not necessarily smooth and can vary quite dramatically as the TDE decays, particularly for the jetted events. For non-jetted events, we find that at both early times and late times, their emission is consistent with disk emission. However, for jetted events we find that at early times the emission from these events is consistent with fallback, while at later times their emission converges to that seen for non-jetted events. Additionally, we find that for a majority of the events the powerlaw index that we derive is much shallower than $t^{-5/3}$. The shallow nature of their decay is consistent with the emission arising from a TDE that has been viscously slowed, indicating that viscous effects are important for these events.

Both jetted and non-jetted X-ray TDEs exhibit an increase in their X-ray luminosity at peak of two to three orders of magnitude compared to pre-flare constraints indicating that these events are intrinsically very luminous. In addition these pre-flare limits are crucial for distinguishing these events from AGN activity. We find that both jetted and non-jetted X-ray TDEs are highly absorbed with respect to the Galactic column density along the line of sight of the event. In addition, we find that the absorption for each TDE, within uncertainties, is constant with time. This indicates that the variability in the X-ray emission we observe on smaller timescales, like that seen in e.g., *Swift J1644+57*, is intrinsic to the source, rather than a consequence of variability in absorption.

In addition to quantifying the emission from each candidate in the 0.2-3.0 keV energy range, we derive the count

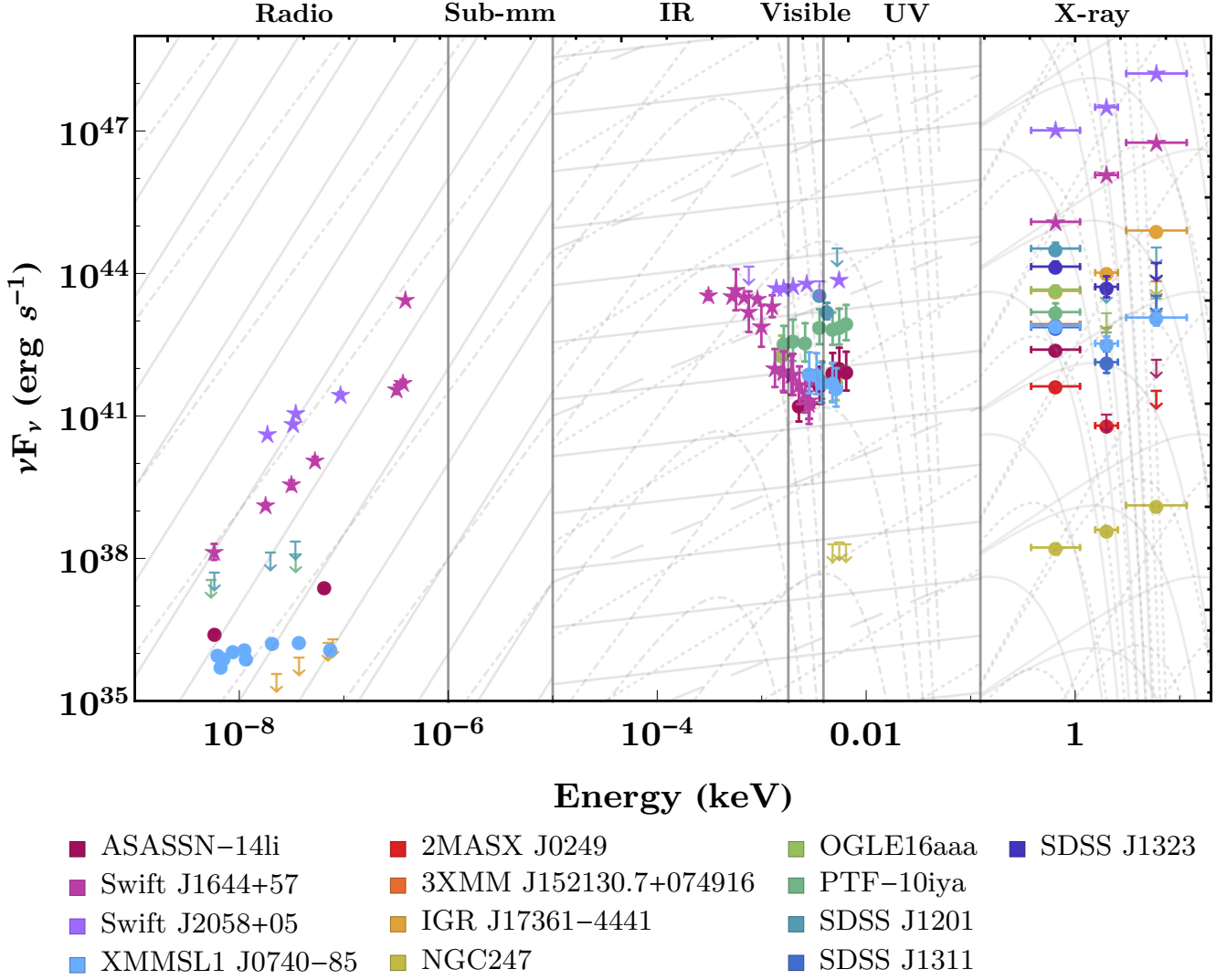


Figure 17. The spectral energy distribution of each TDE candidate plotted together. In addition, we have also overlaid various radiative astrophysical processes which can reproduce the emission in each energy band. In the radio/sub-mm energy band we have plotted optically thick synchrotron emission ($F_\nu \propto \nu^{5/2}$) as the solid line (—) and Rayleigh-Jeans Law ($F_\nu \propto \nu^2$) shown as the dot-dashed line (— · — · —). In the IR/visible/UV energy band we have plotted optically thin synchrotron emission ($F_\nu \propto \nu^{-3/4}$) shown as the solid line (—), thermal black-body emission represented by Planck’s Law ($F_\nu \propto \nu^3 / \exp^{-\nu/(E_{\text{cut}}-1)}$) is shown with $E_{\text{cut}} = 0.0001, 0.01$ keV as the dot-dashed curve (— · — · —), optically thin free-free emission ($F_\nu \propto \nu^{-1/10}$) is shown as the dashed line (— — —) and the spectrum of a blackbody accretion disc ($F_\nu \propto \nu^{-1/3}$) is shown as the dotted line (· · ·). In the X-ray band we have plotted saturated inverse Compton scattering which can be approximated by Wein’s law ($F_\nu \propto \nu^3 \exp^{-\nu/E_{\text{cut}}}$) and is shown with $E_{\text{cut}} = 0.1, 1, 10$ keV as the dotted (· · ·) line. In addition we have also plotted X-ray synchrotron emission which can be approximated using ($F_\nu \propto \nu^{1/2} \exp^{-\nu/E_{\text{cut}}}$). This is plotted $E_{\text{cut}} = 0.1, 1, 10$ keV and is shown as the solid line (—) in this band. The normalisations of these plots have not been derived by fitting the observed emission, but have been chosen artificially.

rates of each event in a soft, medium and hard X-ray energy band. By correlating the counts seen in these different energy bands, we find that X-ray TDEs show significant variation in their soft 0.3-1.0 keV X-ray emission. This is in contrast with that seen in the medium and hard energy bands where we find that emission in these bands is highly correlated. Using these count rates we also derive the hardness ratios (HRs) for each event and we find that their emission is quite soft in nature. Throughout their life, these events have a HR between +0.3 and −1, while at peak their HR is less than 0. The jetted and non-jetted events also naturally separate, with the emission from the non-jetted events being quite soft with a HR between −1 and approximately −0.5, while the emission from jetted events is well-described using a HR between −0.5 and +0.3.

Due to the significant variation in the soft count rates of each TDE, lack of variation in their medium and hard emission and their enhanced column densities, we suggest that the soft nature of these events implied by these HRs and a number of other properties arises from reprocessing.

For each TDE candidate we consider, we derived the broad-band spectral energy distribution (SED) for each event. We find that the X-ray emission from these events is consistent with inverse Compton scattering or synchrotron emission. We find that the non-jetted events tend to have a steeper cutoff in the X-ray band of their SED compared to the jetted events. For the events which had optical/UV data, we also derived the integrated optical/UV and X-ray energy. We found that the jetted events have a X-ray to optical ratio significantly

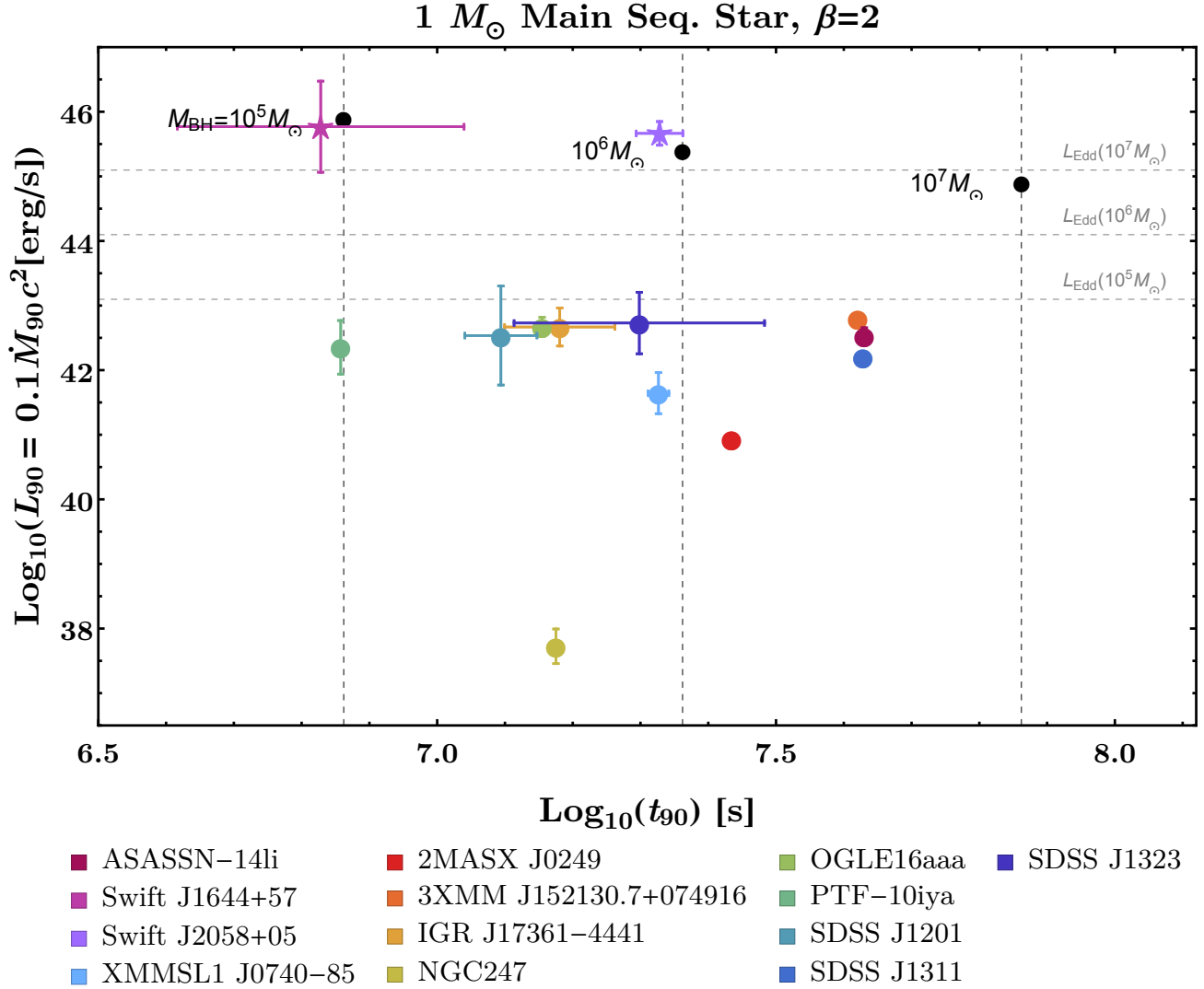


Figure 18. L_{90} (erg/s) as a function of t_{90} (s) as derived in Section 4.3. The solid black symbols represent the equivalent t_{90} and L_{90} values expected for a TDE arising from a low mass (polytropic index $\gamma = 5/3$), main sequence star being disrupted by a $M_{BH} = 10^5 M_{\odot}, 10^6 M_{\odot}, 10^7 M_{\odot}$ respectively. We have also assumed that the pericenter distance is two times the tidal disruption radius (i.e., $\beta=2$) implying full disruption. These results were derived from [Guillochon & Ramirez-Ruiz \(2013\)](#), who calculated the fallback accretion rate expected from the disruption of a $1 M_{\odot}$ star by a $10^6 M_{\odot}$ BH. The horizontal dashed lines correspond to the Eddington Luminosity for a $M_{BH} = 10^5 M_{\odot}, 10^6 M_{\odot}, 10^7 M_{\odot}$.

greater than one, while for non-jetted events this ratio is approximately one. As the non-jetted events had some of the highest measured column densities, and are some of the softest sources in our sample, these low X-ray to optical ratios imply that significant reprocessing must be taking place in these events producing significant optical emission in addition to their detected X-ray emission, as argued by [Guillochon et al. \(2014\)](#) for PS1-10jh.

The disruption of a star will contribute no more than half of the star’s mass to the bound debris surrounding the black hole, with much less being possible in the case of a partial disruption (e.g., [Guillochon & Ramirez-Ruiz 2013](#); [Guillochon et al. 2014](#)). [Roth et al. \(2016\)](#) showed that for $0.5 M_{\odot}$ of bound stellar debris, this material will be optically thick (optical depth $\gg 1$) assuming that this envelope of material is dominated by Thomson scattering. Using our derived T_{90} and L_{90} values to estimate the mass of accreted material and Equation [3] from [Roth et al. \(2016\)](#), we can estimate the optical depth

of these events and thus determine the possible nature of the star tidally disrupted. We find that the properties of the sub-Eddington TDEs suggest that the material surrounding these events is optically thin (the optical depth $\ll 1$) since the mass of accreted material $\ll 0.5 M_{\odot}$, implying that sub-Eddington population of TDEs seen in Figure 18 could potentially arise from either a partial disruption or the disruption of a low mass star.

Compared to other transient events such as GRBs, we find that X-ray TDEs emit the bulk of their emission over significantly longer timescales. GRBs and GRB-like transients release 5–95% of their total fluence on timescales of less than $T_{90} \sim 10^5$ seconds, while in contrast, X-ray TDEs take $T_{90} \sim 10^7$ seconds to release the same amount of energy. Since these T_{90} s indicate that energy is likely to be injected over much longer timescale, this could be crucial for modelling the dynamics of relativistic jets formed in TDEs ([De Colle et al. 2012](#)). We also find that there is a “reprocessing valley”

which separate non-thermal jetted and thermal TDEs based on their derived L_{90} . As we argued above, the presence of a solar mass of material about a black hole can easily opaque its inner regions, which naturally produces a gap between the highly-energetic jetted events and events in which the accreted mass is so low that the X-ray emission remains unattenuated. The "veiled" population in between likely represents events for which no jet was produced, but for which the large amount of matter about the black hole absorbs the bulk of the X-ray emission.

We compare our derive T_{90s} to the equivalent timescale expected for a main sequence star being disrupted by a BH with a mass between $10^5 - 10^7 M_\odot$ and find that most of these events are consistent with being disrupted by a BH with these masses. We also derive the corresponding Eddington luminosity for the same BH masses and find that the jetted TDEs are super-Eddington, while the non-jetted events are sub-Eddington in nature.

Guillochon & Ramirez-Ruiz (2015) recently showed that if the viscous timescales of TDEs are long, a larger fraction of tidal disruptions arising from BHs with a mass $< 10^7 M_\odot$ would be sub-Eddington, indicating that these events are most likely viscously slowed. As a large number of our TDE sample are sub-Eddington in nature and arise from a BH with a mass $< 10^7 M_\odot$, this is consistent with our conclusion that these events are viscously slowed based on the shallower power-law indexes we derived from their X-ray light curves. The super-Eddington luminosities implied for the two non-jetted events *Swift* J1644+57 and *Swift* J2058+05 are consistent with the picture that super-Eddington accretion rates are required to form a jet.

In addition, the viscously slowed nature of X-ray TDEs might be able to explain the current discrepancy between the TDE rate derived from theory and observations. Apart from producing sub-Eddington flares, viscous effects will cause the emission from a TDE to peak over long timescales rather than promptly as seen with currently detected events. As we find that our current sample of X-ray TDEs produce very luminous flares, but the properties of their emission implies that they are viscously slowed, there must be a significant population of low luminosity events that have both prompt or long-rise times that current surveys are missing, potentially because they are too dim to be reliably detected (see Figure 5). As a consequence, new methods to detect these lower luminosity events might be able to shed light on this problem.

In summary, using over three decades of X-ray data we performed a comprehensive and systematic analysis of the X-ray emission from transient events classified as a TDE in the literature. Using the X-ray products derived from this analysis we were able to produce multi-decade X-ray lightcurves for each event, which allowed us to quantify the decay rates of X-ray TDEs. In particular, we find that the canonical decay rate of $t^{-5/3}$ is not necessarily standard in the soft X-ray energy band, and that there is a reprocessing "valley" that separates jetted and non-jetted events that could be naturally populated by optical/UV TDEs. In addition, we were able to quantify the soft nature of X-ray TDEs from extracting counts in a soft, medium and hard energy band, while determining that viscous effects are important in determining the emission from these events. This provides the community with the first catalogue of X-ray TDE candidates, and all results derived from this analysis are publicly available at the *open TDE catalog* which can be found at <https://tde.space>.

K. A. is indebted to K. Poppenhaeger for her helpful discussions related to X-ray point-source analysis. The authors would like to thank L. Zoltan Kelley for help with and use of the *AstroCats* python package, and I. Arcavi, P. Maksym, S. van Velzen, D. Lin, O. Graur, and R. Saxton for their helpful comments related some of the text, and data analysis which helped improve the manuscript. This work was supported by Einstein grant PF3-140108 (J. G.), the Packard grant (E. R.), and NASA ATP grant NNX14AH37G (E. R.). We acknowledge the use of NASA-ADS, HEASARC, the *ROSAT* X-ray All-Sky Survey catalogue, and the *XMM-Newton* Science Archive. The online tde.space catalog was produced using *AstroCats*.

APPENDIX

A. INDIVIDUAL TDE PROPERTIES AND THEIR X-RAY LIGHT CURVES

In this section we briefly summarise the properties of each TDE candidate derived from our analysis and as found in the literature. In Figure 19–22 we have also plotted each individual X-ray light curve as derived from our analysis (Tables 14–18). Here we have colour coded each data point/upperlimit based on the instrument in which we derived this measurement, with results derived using *ROSAT pointed* and *RASS* observations shown in red, *Chandra* observations shown in orange, *XMM-Newton slew* observations shown in magenta, *XMM-Newton pointed* observations shown in blue, and *Swift XRT* observations shown in purple. In green we have also plotted the optical/UV emission as taken from the literature for the events which had published data. Here we begin our summary of each event.

A.1. 2MASXJ0203

This candidate was first suggested to be an X-ray TDE by Esquej et al. (2007). These authors compared the count rate derived from the center of its host galaxy 2MASX J02030314–0741514 using the *XMM-Newton* Slew Survey Source Catalogue with the count rate derived *ROSAT* PSPC All-Sky Survey. They found that the emission from this host galaxy increased by a factor of 63. Within the error circle of the *XMM-Newton* Slew observation, this detected emission was found to be consistent with the centre of the host galaxy. However recently, Strotjohann et al. (2016) suggested that this source could also be a highly variable AGN. We find that the X-ray emission increases by two orders of magnitude compared to the first X-ray detection given by the *XMM-Newton* slew observation. This emission stays approximately constant over a few years, however after 2010 there were no follow-up observations of the source which could help further characterise its emission or to determine whether the emission decays following that expected by a TDE. Our results are similar to that derived by Strotjohann et al. (2016).

A.2. 2MASXJ0249

This candidate was also suggested to be a X-ray TDE by Esquej et al. (2007). By comparing the count rate obtained using their *XMM-Newton* slew observation with the X-ray count rate from the center of galaxy 2MASX J02491731–0412521 as derived using *ROSAT*, they found that the X-ray emission increased by a factor of 21. Strotjohann et al. (2016) had also suggested that this source could be a highly variable AGN

based on the detection of weak [OIII] λ 5007, however the authors highlight that the emission from this source is significantly softer compared to the other candidates in their sample and lacks the standard powerlaw component detected in AGN above $> 2\text{keV}$ making it less likely to an AGN. We find that the X-ray emission from the source peaks and then decreases following a power-law like decay, and shows no recurring periodic emission. However, whether there were flaring emission prior to the detected flare is difficult to say as there is a gap of 15 years in which this host Galaxy was not observed using an X-ray satellite. Similar to [Strotjohann et al. \(2016\)](#), we find that the emission from the source is very soft, as implied by the large powerlaw index derived in our analysis.

A.3. 3XMM

This source was suggested by [Lin et al. \(2015\)](#) to be an X-ray TDE due to its highly transient nature (the authors reported only one data point based on a deep *XMM* observation, however all other observations of the source resulted in upperlimits) and its thermal blackbody ($kT \sim 0.17\text{ keV}$) X-ray spectrum. However, the black hole mass that is implied from their fits $M_{BH} = 10^5 - 10^6 M_{\odot}$ is much lower than that expected for a TDE candidate and their derived temperature is significantly higher than that derived for other TDE candidates such as ASASSN-14li or -14ae ([Holoien et al. 2014](#); [Miller et al. 2015](#); [Holoien et al. 2016b](#); [Brown et al. 2016](#)). In addition, due to the relatively large uncertainty in the error circle of the observation, it is difficult to determine whether the flare is consistent with the centre of its host Galaxy. Much like [Lin et al. \(2015\)](#), we detect X-ray emission in the 0.3-2.0 keV energy range arising from the position of this source using *XMM*. For all other observations we derive X-ray upperlimits.

A.4. ASASSN-14ae

This source was classified as a TDE candidate by [Holoien et al. \(2014\)](#) based on its optical/UV emission using ground-based and follow-up *Swift* observations of the source. This event is the lowest-redshift TDE candidate discovered at optical/UV wavelengths to date (which has been published) and its emission peaks at 10^{43} erg/s and decays following an exponential power law. [Holoien et al. \(2014\)](#) find no X-ray emission arising from the source. We also find no X-ray emission arising from the position of the source and derive upperlimits for all observations.

A.5. ASASSN-14li

This source was first discovered by ASAS-SN in optical wavelengths and due to its detection is a large number of wavelengths (optical and near UV ([Holoien et al. 2016b](#); [Cenko et al. 2016](#); [Brown et al. 2016](#)), X-rays ([Miller et al. 2015](#); [Holoien et al. 2016b](#); [Brown et al. 2016](#)), and radio ([Alexander et al. 2016a](#); [van Velzen et al. 2016](#))) this source is one of the most detailed studied TDEs known. Its classification as an X-ray (and UV/optical) TDE is ubiquitously accepted in the literature. The X-ray emission from the source has been well characterised, and we find that even though we merged X-ray observations rather than consider each individual observation as completed in the literature, we reproduce similar results to those published in the literature. We should also note that radio emission arising from the host Galaxy was detected prior to the detection of ASASSN-14li leading to the possibility of AGN activity, while the detection of narrow [OIII] emission also suggests the presence of a low-luminosity

AGN ([van Velzen et al. 2016](#)). However, regardless of this fact, the observed properties of ASASSN-14li are inconsistent with that expected of an AGN (see [van Velzen et al. 2016](#) for more details).

A.6. ASASSN-15oi

Much like ASASSN-14li and 14ae, this source was first discovered by ASAS-SN and follow up observations using ground based instruments and *Swift* indicate that this source is optical/UV TDE ([Holoien et al. 2016a](#)). However, ASASSN-15oi faded significantly more rapidly than other optically discovered TDEs. This source shows evidence of weak X-ray emission, however due to it rapidly fading the X-ray emission from the source decayed much quicker than its UV/optical emission. We find that we also detect weak (compared to the UV/optical emission) X-ray emission from the source, however as we have no late time or early time constraints on its emission, making it difficult to determine how the X-ray emission from this source evolves beyond the two detections we report.

A.7. ASASSN-15lh

First discovered using ASAS-SN by [Dong et al. \(2016\)](#), this transient event has so far been quite a puzzle. This source had a peak luminosity two times that of any known supernova, and during its early time emission showed features similar to those seen in superluminous supernovae ([Dong et al. 2016](#)). Follow up observations by [Godoy-Rivera et al. \(2016\)](#), showed that its properties differed significantly from those of known TDEs such as ASASSN-14li and -14ae, putting more weight behind its supernova origin. However, using 10 months of multiwavelength data, [Leloudas et al. \(2016\)](#) showed that the properties of this source is more consistent with a TDE rather than a superluminous supernova based on its temperature evolution, the presence of CNO gas along the line of sight and its location being coincident with the centre of a passive Galaxy. However, the mass implied by their analysis is $> 10^8 M_{\odot}$ making it one of the largest BHs in which a TDE has been detected. Recently [Margutti et al. \(2016\)](#) presented deep *Chandra* and *Swift* observations of this source and detected persistent soft X-ray emission consistent with the position of the optical transient. In conjunction with their multi-wavelength campaign in which they also study the optical and UV emission arising from the host, they conclude that if this X-ray source is coincident with the optical transient originally detected by ASAS-SN, then this event is consistent with a TDE of a main sequence star by a massive spinning black hole. Using the *Chandra* data that was available at the time of writing, we do not detect significant X-ray emission arising from the source over the full instrument energy band. Using publicly available *Swift* observations of ASASSN-15lh, we find no significant X-ray emission arising from the position of the source compared to background fluctuation. However, when considering the emission in the soft, medium and hard energy bands we use for our analysis, we do detect faint X-ray emission in the 0.3-1.0 keV energy band arising from the source using one of the later *Swift* observations, consistent with [Margutti et al. \(2016\)](#). The differences in our analysis most likely arises from using different energy ranges, background regions and our different requirements of what constitutes a detection.

A.8. CSS100217

This source was originally discovered by the Catalina Real-time Transient Survey as an extremely luminous optical tran-

sient arising from the centre of a narrow line Seyfert 1 galaxy (Drake et al. 2010, 2011). Drake et al. (2011) performed extensive multi-wavelength follow up observations of this source and found that it is coincident with the centre of its host Galaxy, and spectroscopically exhibited strong narrow Balmer features representative of other Type IIⁿ supernovae such as SN2008iy, SN2007rt and SN1997ab. The detected X-ray luminosity of the event, and its derived temperature is similar to that of luminous Type IIⁿ supernovae such as SN2006gy, while the lack of gamma-ray emission detected from the source rule out the nature of this source as a Type Ib/c or GRB. Due to its coincidence with the centre of its host Galaxy, Drake et al. (2011) also suggested that this event could be consistent with a TDE, however its optical lightcurve, peak optical brightness, and temperature varies greatly from that theoretically expected for TDEs. Similar to Drake et al. (2011), we detect X-ray emission arising from the source coincident with the optical flare detected from this event. Using a follow up *Swift* observation that was taken approximately five years later, we again detect X-ray emission arising from the source. This emission is of the same order of magnitude as the first X-ray emission detection detected, while shallow *XMM* *slew* observations of this source did not detect any X-ray emission from this event. This makes it unlikely that this X-ray emission arises from a TDE.

A.9. D1-9

This source was suggested to be a optical/UV TDE based on the detection of a UV/optical flare using *GALEX* from the center of a quiescent early-type galaxy, which then decayed following a power law (Gezari et al. 2008). The authors triggered a *Chandra* TOO and detected 4 X-ray photons between 0.2-0.4 keV with a detection confidence of 0.93. Due to our more stringent classification of requiring a detection and measuring the emission over a larger energy range we derive only upperlimits to the X-ray emission of the source and find that the 4 photons that these authors detected using *Chandra*, are more likely arose from Poisson fluctuations.

A.10. D23H-1

Gezari et al. (2009) discovered a large magnitude optical/UV flare coincident with the centre of a star forming galaxy using *GALEX*. The spectral energy distribution (SED) from this flare can be well described by a powerlaw decline and is best described by a soft blackbody. Even though a low-luminosity AGN can't be ruled out, the broadband properties of the flare deviate from the average properties observed for AGN and are consistent with that of an optical/UV TDE. They detect no X-ray emission arising from the source and derive 3σ upperlimits. We also find that even at later times, no X-ray emission from the position of this source is detected and derive only 3σ upperlimits.

A.11. D3-13

Similar to D1-9 and D23H-1, this flare like emission representative of an optical/UV TDE was first discovered by Gezari et al. (2008) using *GALEX*. The emission rose sharply and decayed monotonically as expected from an optical TDE, however the light curve is incomplete making it difficult to get a full picture of the emission from the source. In addition the error circle associated with the position of the flare seems to be slightly off-center from the host galaxy. Similar to our analysis, the authors detect X-ray emission from a *Chandra*

observation taken about a year after the optical/UV flare was detected. Later observations presented by Gezari et al. (2008) and analysed in this work only produce upperlimits to the X-ray emission from the source, similar to our analysis.

A.12. DES14C1kia

A possible optical/UV TDE candidate detected in the Dark Energy Survey (Foley et al. 2015). The emission from this source rose for seven weeks prior to peak brightness and then decayed, while not undergoing rapid colour evolution. Based on optical spectroscopy of the host Galaxy, it is thought that the flare arose from a passive Galaxy. Follow up observations in X-rays (Yu et al. 2015) and Radio (Ravi & Shannon 2015) detect no emission in these energy bands. We find no X-ray emission from this source.

A.13. Dougie

An optical transient that was first discovered using *ROTSE* and followed up in the optical using *ROTSE-IIIb* and in the UV using *Swift* (Vinkó et al. 2015). Its optical light curve has a quick rise, followed by a reasonably quick decline of approximately a month. However, the source is systematically offset from the centre of its host Galaxy. We analyse all available X-ray data that overlap this source and we find no X-ray emission arising from the position of the transient. Unlike nearly all other TDE candidates in our sample, this source was not covered by *ROSAT*. As a consequence we only have a few year constraint on the X-ray emission associated with the source.

A.14. GRB060218, SN2006aj

This TDE candidate was first discovered by *Swift* and was first classified as an under-luminous very long GRB, which is thought to be accompanied by a fast, low ejecta mass supernova SN2006aj (Campana et al. 2006; Soderberg et al. 2006; Mazzali et al. 2006). X-ray emission from this source was also detected which Campana et al. (2006) interpreted as arising from shock break-out. However even though the GRB/SN is scenario is the most favoured case to explain the properties of this transient source, Shcherbakov et al. (2013) was also able to show that the unique properties of this source could be equally well described by a TDE from an intermediate black hole at the centre of a dwarf galaxy. From our analysis we detect the increase in the X-ray emission as seen by Campana et al. (2006). Using a follow up *Chandra* observation that was taken immediately after the *Swift* detection, we detect X-ray emission that is two orders of magnitude less than that seen using *Swift*. All later observations of the source produced upper limits and no recurrent emission has been detected.

A.15. HLX-1

This source is an ultra-luminous intermediate-mass black-hole (IMBH) system which exhibits variability with a possible recurrence time of a few hundred days (Lasota et al. 2011). The high luminosity, light curve and X-ray spectrum evolution of HLX-1 can be explained by the recurring mass-transfer that results from the tidal stripping of a star in an eccentric orbit around the IMBH (i.e., a recurring TDE). However, this source shows hard-to-soft X-ray transitions (Servillat et al. 2011), while also showing evidence of a radio jet emission (Webb et al. 2012), which are typically observed for galactic black hole binaries. This makes it difficult to explain the observed variability using a recurring TDE (Godet et al. 2013).

From our analysis, we also detect significant periodic variability over a large number of years.

A.16. IC3599

This source was first characterised as an X-ray TDE by Brandt et al. (1995); Grupe et al. (1995) using *ROSAT*, in which they discovered a rapid decrease in the X-ray flux by two orders of magnitude over a year. Campana et al. (2015) later discovered using follow up *Swift* observations, a recurring flare like event of similar magnitude as that seen using *ROSAT*, which these authors suggest is a periodic, partial TDE. However, Grupe et al. (2015) showed that this periodic emission is most likely consistent with an accretion disk instability around a BH. In addition, its mid-IR (Sani et al. 2010) and radio (Bower et al. 2013) emission is consistent with that of an AGN. From our analysis we also detect the periodic X-ray emission from this source consistent with that in the literature.

A.17. IGR J12580

First detected as a strong, hard X-ray flare using *INTEGRAL*, Nikolajuk & Walter (2013) classified this event as a X-ray TDE of a super Jupiter by a central supermassive BH. Irwin et al. (2015) discovered transient radio emission arising from the position of the TDE candidate, while also highlighting that this source has been classified as a LINER/Seyfert 2 Galaxy based on its optical spectra indicating that this source could be a changing look quasar. The original radio emission detected by Irwin et al. (2015), was detected before the hard X-ray flare and shows evidence of variability, indicative of an AGN jet. In addition, the WISE colours for this event is consistent with those of a luminous AGN (Stern et al. 2012), while based on pre-flare data this source was classified as an AGN in the VCV catalogue (Véron-Cetty & Véron 2010). Irrespectively of the source being more likely to be an AGN, Lei et al. (2016) reinforced the planet TDE interpretation by showing that the observed emission most likely arises from an off-beam relativistic radio jet that formed during the original TDE. Using 37 months of data from the Monitor of All-sky X-ray Image (*MAXI*), Kawamuro et al. (2016) detected significant X-ray flare emission in the 410 keV energy band arising from the position of this source. Similar to Nikolajuk & Walter (2013) we detect an rapid rise in the X-ray emission by several orders of magnitude and then a gradual decay consistent with an X-ray flare. However, we believe the detected X-ray emission most likely arises from AGN activity rather than a TDE.

A.18. IGR J17361-4441

This source was first discovered as a hard X-ray source using *INTEGRAL* near the centre of a globular cluster. Follow up observations showed that the X-ray light curve decays following a powerlaw consistent with that of a X-ray TDE, while its thermal component does not evolve significantly with time. Del Santo et al. (2014) classified this transient event as the tidal disruption of a free-floating terrestrial icy planet by a white dwarf due to the fact that it was located slightly off-center from the host Galaxy. From our analysis we find that the X-ray emission from the position of the source rapidly rises over a short time period, then decays over less than a year. We also find that there is some periodic X-ray emission from the position of the source, which is consistent within uncertainties with the low state X-ray emission of the flare-like

event. We detect no other periodic emission, while no AGN or other transient phenomenon has been suggested as the origin of this event so far.

A.19. iPTF16fnl

Discovered as a nuclear transient by PTF from the nearby Galaxy Mrk 950. Follow up spectra detected a blue continuum, and strong broad He[II] 4686 emission consistent with that of a TDE (Gezari et al. 2016). We detect no X-ray emission arising from the position of iPTF16fnl using *Swift* observations taken after the initial Astronomers Telegram.

A.20. LEDA 095953

Cappelluti et al. (2009) serendipitously discovered flare-like X-ray emission arising from a Galaxy found within a Galaxy cluster. This flare is found significantly off center from the center of the galaxy cluster, however within uncertainties it is consistent with the center of its host Galaxy. Using follow-up *Chandra* and *XMM* observations of the source, they derive a data point and an upperlimit respectively. They also use *ROSAT* HRI observations of the source which we do not analyse and detect emission from the source. Based on these observations, they interpret that the X-ray emission that they detect is the result of an X-ray TDE. From our analysis we only detect X-ray emission from the *ROSAT* observation of the source, while for the late time *Chandra* and *XMM* observation, we derive only a 3σ upperlimit. The difference between our results and the results of Cappelluti et al. (2009) most likely arises from defining the different background regions in our analysis and our more stringent requirements for what constitutes a detection.

A.21. NGC1097

Monitoring observations by Storchi-Bergmann et al. (1995) of this Galaxy showed strong variation in the optical flux and broad double peaked H α emission lines of this host Galaxy. To explain both the variation in the flux and shape of the optical emission, Storchi-Bergmann et al. (1995) suggested that it arose from an elliptical ring of material that arose from the tidal disruption of a star by the central BH. However, it is widely accepted that NGC1097 is an AGN (see e.g., Storchi-Bergmann et al. 1995), which is made quite evident in our analysis of the X-ray emission from this source. One can see that there is strong variability in the observed X-ray emission at late times, with the emission in the high and low state being consistent with each other over a number of years.

A.22. NGC2110

Moran et al. (2007) discovered using polarisation measurements of its optical spectrum, a transient broad, double peaked H α feature arising from NGC2110, which is commonly seen from optical TDE. The discovery of Fe K α lines that vary over timescales of years (e.g., Marinucci et al. 2015) and several of its other properties imply that this source is most likely a prototypical double peaked emission-line AGN. From our analysis, we find that the X-ray emission from this source varies over years similar to other AGNs, with the high and low states having similar orders of magnitude.

A.23. NGC247

Using *XMM-Newton*, Feng et al. (2015) serendipitously discovered a strong X-ray flare from the centre of the inactive Galaxy NGC247. UV spectroscopy shows no evidence for

an AGN. Follow up observations of the source with *Swift* detected an increase in the X-ray luminosity of the source which then peaked and decayed exponentially. Feng et al. (2015) concluded that the properties of this source could result from either an outburst from a low mass X-ray binary with a stellar-mass black hole emitting near its Eddington luminosity, or from a X-ray TDE being accreted onto a $10^5 M_\odot$ nuclear BH. We reproduce the X-ray emission from NGC247 as presented by Feng et al. (2015), while also placing strong constraints on prior X-ray emission from this source, for which we find no prior X-ray emission before the detected flare.

A.24. NGC3599

This candidate was also suggested to be an X-ray TDE based on its detection in the *XMM-Newton* slew survey by Esquej et al. (2007). Within the error circle of the *XMM* observation this source was consistent with the centre of its host Galaxy and increased by a factor of 88 compared to its *ROSAT* detection. Esquej et al. (2008) obtained follow up *XMM-Newton* and *Swift* observations of the source and detected emission that was consistent with the canonical $t^{-5/3}$. Saxton et al. (2015) showed using archival X-ray data that this source flared 18 months before the detection by Esquej et al. (2007), but was still consistent with a slow rising TDE or possibly from a thermal instability in the accretion disc of an AGN. Optical observations of the host indicated that the source is a low-luminosity Seyfert/low-ionization nuclear emission-line region (LINER) Esquej et al. (2008). We similarly find that the source was X-ray bright before the original flaring event was discovered by Esquej et al. (2007) and Saxton et al. (2015). Unlike Esquej et al. (2008) we only derive an upperlimit for the *Swift* observations. This difference most likely arises from using different regions to define the source and background, while we required a source to be detected with a significance of 2σ or more before it was classified as a detection.

A.25. NGC5905

First discovered by *ROSAT* as a very soft X-ray transient source which increased dramatically in flux over a few days and then declined by a factor of 80 two years later, Bade et al. (1996) classified this source as an X-ray TDE. Halpern et al. (2004) followed up this source using *Chandra* and found the emission has decreased such that it is consistent with the basal star burst emission of the host Galaxy. Li et al. (2002) modelled the emission from this event and speculated that it arose from either the partial stripping of a low mass main sequence star or the disruption of a brown dwarf or a giant planet. However, even though the TDE scenario is currently favoured in the literature (see e.g., Halpern et al. 2004), Gezari et al. (2003, 2004) found using the Hubble Space Telescope (*HST*) narrow emission lines in the inner nucleus of the host, indicating that there is a low level of prior non-stellar photoionisation powered by accretion. This raises questions on the TDE origin of the flare, making it more possible that the emission arises from AGN activity. Similar to Bade et al. (1996) and Halpern et al. (2004) we detect X-ray emission arising from the position of the source using *ROSAT* and *Chandra* which then decays. Using a follow up *Chandra* observation of this source taken in 2007, we also detect X-ray emission from the source consistent with the late time emission derived by Halpern et al. (2004). However, unlike Halpern et al. (2004) we derive an X-ray luminosity for the peak of the X-ray flare

that is an order of magnitude less than that derived by Halpern et al. (2004). This difference most likely arises from using different energy ranges, and regions to derive the source counts from this event.

A.26. OGLE16aaa

Discovered by the OGLE-IV survey at the centre of a Galaxy which shows evidence of some weak ongoing star formation and AGN emission, this transient exhibited a long rise, slow decline and broad He and H spectral features similar to those of other optical/UV TDEs (Wyrzykowski et al. 2017). *Swift* observations taken around the same time of optical flare detected no X-ray emission, as noted in (Wyrzykowski et al. 2017). However further follow up observations using *Swift* allowed us to detect significant X-ray emission from this event, which then decayed and faded over a few months.

A.27. PGC1185375

Using the *Swift* BAT, Hryniewicz & Walter (2016) surveyed over 50000 Galaxies to search for X-ray flare emission from inactive Galaxies that could potentially arise from a TDE. From their analysis they found nine X-ray TDE candidates arising from hosts which show no evidence of AGN emission with PGC1185375 being one of these candidates. This X-ray flare had a duration of 41 days and was found offset from the host Galaxy. However, due to its location on the detector the increased PSF dramatically decreases their ability to properly localise the source making it possible for this source to be coincident with the centre of the host. Hryniewicz & Walter (2016) also rule out a contribution from an AGN. There is very limited data available for this source, and as such we are only able to put upperlimit constraints on the X-ray emission. We find no recurring X-ray flare emission from the observations we analyse of the source.

A.28. PGC1190358

Another X-ray TDE candidate suggested by Hryniewicz & Walter (2016). The flare lasted for 108 days and peaked 40 days before the flare was undetectable by the *Swift* BAT. The flare was coincident with the centre of its host, however the uncertainty on this position is large. From peak to non detection the flux decreased by factor of 34. Similar to PGC1185375, there is very little archival X-ray data available for this source and as such we are only able to derive upperlimits to the X-ray emission.

A.29. Pictor A

Sulentic et al. (1995) detected broad, transient double peaked Balmer line emission arising this radio Galaxy, which is also seen in optical TDEs. However, Perley et al. (1997) discovered a faint radio jet connecting two radio lobes to the central nucleus of the host, while Wilson et al. (2001) discovered using *Chandra* an X-ray jet coincident with the radio jet. From our X-ray analysis, we detect significant and variable X-ray emission arising from the central source that varies over many years more indicative of AGN activity

A.30. PS1-10jh

First discovered in the *Pan-STARRS1* survey, this UV-optical flare occurred at the centre of an inactive Galaxy and was quickly classified as an optical/UV TDE Gezari et al. (2012). The UV/optical spectra of this source was characterised by the presence of broad [He II] λ 4686 emission, and

the absence of a number of hydrogen lines, indicating that the disrupted star was a He-rich red giant that had its outer envelope stripped. [Strubbe & Murray \(2015\)](#) determined that to disrupt such a dense object, the BH must of had a mass of $< 10^5 M_\odot$. However, [Guillochon et al. \(2014\)](#) also showed using hydrodynamical simulations that it is possible to explain the properties of this event using a main sequence star that was disrupted by a SMBH. This result was supported by photoionisation modelling by [Gaskell & Rojas Lobos \(2014\)](#). After the original detection in *Pan-STARRS1*, follow up observations by *Chandra* detected no X-ray emission from the source, while ruling out an AGN origin ([Gezari et al. 2012](#)). We also find no X-ray emission immediately after the original UV/Optical flare. However, we detect using a *XMM-Newton* slew observation, week X-ray emission (~ 4 source photons) arising from the position of the source a few years after the flare.

A.31. *PS1-11af*

Another optical/UV TDE candidate that was discovered using *Pan-STARRS*. [Chornock et al. \(2014\)](#) discovered a long-lived optical transient that is coincident with the centre of its host Galaxy. UV spectroscopy revealed broad, transient absorption features arising from the source, while its luminosity and colour changed slowly through its detection. The spectra obtained also showed no other features other than the broad UV absorption component. Based on its properties [Chornock et al. \(2014\)](#) classified it as an optical/UV TDE which arose from the partial disruption of a main sequence star by a $10^6 M_\odot$ BH. The host also shows no evidence of AGN emission. This source is very similar to PS1-10jh. There are very limited X-ray observations of this event, and as such we are only able to constrain upperlimits to the X-ray emission of the source.

A.32. *PS1-12yp*

This event was first discovered in the PanSTARRS1 survey for large amplitude transients that occur at the centre of galaxies that show no evidence of AGN ([Lawrence et al. 2016](#)). This event was the bluest transient in their sample, and showed significant increase in its optical luminosity. The optical emission from the event then decayed similar to that of PS1-10jh, leading the authors to possibly classify it as a TDE or a SNe. There is very little X-ray coverage of this source, with only shallow *XMM-slew* observations of this event. We detect no X-ray emission from the position of this source and derive only X-ray upperlimits.

A.33. *PTF-09axc*

[Arcavi et al. \(2014\)](#) analysed archival Palomar Transient Factory (*PTF*) in search for transients that have a peak magnitude between -21 and -19. These authors found six events which have similar rise times to that of optical/UV TDE PS1-10jh. PTF-09axc shows evidence of broad hydrogen features and is coincident with the centre of its host Galaxy, however its optical light curve is poorly sampled. [Arcavi et al. \(2014\)](#) detect very weak [OIII] $\lambda 5007$ emission from its host Galaxy possibly indicating the presence of a very weak AGN. Using a *Swift* TOO observation of PTF-09axc, [Arcavi et al. \(2014\)](#) detect X-ray emission with a luminosity of $\sim 10^{42}$ erg s $^{-1}$ arising from the position of the source, which they state is consistent with that expected from AGN. However, the AGN origin of this emission was not confirmed. Similar to [Arcavi et al. \(2014\)](#) we also detect X-ray emission arising from PTF-09axc

with a luminosity of $\sim 10^{42}$ erg s $^{-1}$, however the uncertainty on this value is very large. There are not many available X-ray observations of this source, however we do not detect any recurring X-ray emission.

A.34. *PTF-09djl*

Another potential optical/UV TDE candidate discovered in archival *PTF* data by [Arcavi et al. \(2014\)](#). Similar to PTF-09axc this flare like emission is coincident with its host Galaxy and its spectrum shows evidence of broad hydrogen features. [Arcavi et al. \(2014\)](#) find no evidence of AGN emission lines from its host spectra and follow up *Swift* observations of the source detect no X-ray emission. There are only two archival observations which overlap the position of the source, and from these we are only able to derive 3σ upperlimits, consistent with the analysis by [Arcavi et al. \(2014\)](#).

A.35. *PTF-09ge*

One of the six optical/UV TDE candidates discovered in the *PTF* analysis by [Arcavi et al. \(2014\)](#). Spectroscopically, PTF-09ge shows evidence of He-rich features, while hydrogen is absent from this spectrum. Its light curve is very well sampled and is similar to that of PS1-10jh, while its flare like UV/optical emission is coincident with the centre of its host Galaxy. There was no evidence of AGN emission in its host spectrum, and follow up *Swift* TOO observations of the source produce only 3σ upperlimits. We also are only able to extract 3σ upperlimits from our analysis of the three archival observations which overlap the position of the source.

A.36. *PTF-10iam*

Another of the *PTF* optical/UV TDE candidates presented by [Arcavi et al. \(2014\)](#), however this flare is found off set from the centre of its host Galaxy. The spectrum of its host Galaxy shows evidence of Balmer absorption features only. The light curve of PTF-10iam rises significantly faster to peak emission compared to the other TDE candidates suggested by [Arcavi et al. \(2014\)](#). More recently, [Arcavi et al. \(2016\)](#) suggested that this event is more likely to be a peculiar Type II supernova, or a hybrid Type Ia - Type II supernova event. We detect no X-ray emission arising from this source .

A.37. *PTF-10iya*

First discovered by [Cenko et al. \(2012a\)](#) using *PTF* as a short lived, luminous, UV/optical transient event coincident with the centre of its host Galaxy. Based on its host spectrum, they find no evidence of AGN activity. *Swift* TOO observations of this source immediately after the *PTF* detection, detect significant X-ray emission arising from the source. However further observations derive only upperlimits. This is consistent with the X-ray emission we derive for PTF-10iya.

A.38. *PTF-10nuj*

A *PTF* optical/UV TDE candidate that is found systematically offset from its host Galaxy ([Arcavi et al. 2014](#)). Its optical emission rises quickly over ~ 10 days, but then suddenly drops off ~ 30 days after peak. We find no X-ray emission arising from the position of the source and derive 3σ upperlimits.

A.39. *PTF-11glr*

Another *PTF* optical/UV TDE candidate presented by [Arcavi et al. \(2014\)](#) that is systematically offset from its host

Galaxy. Its host shows evidence of Balmer absorption features and emission lines, while its optical light curve rises and falls in a similar way to PTF-10nuj. No other information about the source is available. From our analysis, we detect no X-ray emission from the source over three observational epochs and as such derive 3σ upperlimits.

A.40. RBS 1032

A bright, luminous X-ray flare arising from dwarf Galaxy RBS 1032 was first discovered by Ghosh et al. (2006) using *ROSAT*. Follow up *XMM-Newton* observations by Maksym et al. (2014a) indicated the presence of a very faint X-ray source within the $30''$ error circle of the *ROSAT* position of the source. This emission is 200 times less than that detected in the *ROSAT* observation and is very soft in nature. The optical monitor of *XMM* also detected a source coincident with the faint X-ray source. Ghosh et al. (2006) find no evidence of AGN activity from the host. Maksym et al. (2014a) classifies RBS 1032 as an X-ray TDE, however the suggestion by Ghosh et al. (2006) that the observed emission arises from an intermediate mass BH binary cannot be ruled out. Unlike Maksym et al. (2014a), we find no evidence for a faint X-ray source arising from the position of RBS 1032 using *XMM-Newton* and as such derive 3σ upperlimits from the source. This most likely arises using different background, where our background incorporates the basal emission from the host Galaxy, in addition to our more stringent requirement for emission to be classified as a detection.

A.41. RX J1242-11A

This event was first discovered by Komossa & Greiner (1999) using *ROSAT* as a large increase in the detected X-ray flux from the inactive Galaxy pair RX J1242-1119. The inactive nature of the host was confirmed by Gezari et al. (2003, 2004) using *HST*. Due to its soft spectrum and lack of evidence for AGN activity, Komossa & Greiner (1999) classified this source as an X-ray TDE. Follow up observations using *Chandra* and *XMM-Newton* showed that the emission from this source dropped by a factor 200 compared to its *ROSAT* detection, and was still consistent with that of a TDE (Komossa et al. 2004; Halpern et al. 2004). We similarly find that the X-ray emission of this source has decreased by a factor of ~ 200 compared to its *ROSAT* detection. Follow up observations of this source taken nearly 15 years later show no evidence of recurring X-ray emission.

A.42. RX J1420+53

By comparing the emission from a pointed *ROSAT* observation of this host with the emission detected in the RASS, Greiner et al. (2000) discovered an X-ray transient source which displayed a variation in its flux by a factor of 150. Based on optical observations of the source Greiner et al. (2000) classified the host as inactive, and tentatively classified this emission as an X-ray TDE. Since the original discovery, there has been follow-up *Chandra* observations of the source. From our analysis, we detect no X-ray emission arising from the position of the source, ~ 15 years after the original detection.

A.43. RX J1624+75

Another X-ray transient event discovered using *ROSAT*. Originally detected as bright X-ray emission in the RASS,

Grupe et al. (1999) found that within 1.5 years after the original discovery, that the emission from this source had faded. They took optical spectra of the host and determined that the host is most likely inactive, however they also detected a weak signature of $[\text{Ni II}]\lambda 6584$ emission which could imply weak AGN activity. However Grupe et al. (1999) classify the observed X-ray flare as an X-ray TDE rather than AGN activity based on the timescale in which the X-rays were detected and then disappeared. Follow up *Chandra* observations of the source by Halpern et al. (2004) confirmed that the X-ray emission from this source had decreased by a factor > 1000 and was consistent with that of X-ray TDE. Follow up observations of the host by Gezari et al. (2003, 2004) using *HST* confirmed that this source is an inactive Galaxy. Our analysis of the X-ray emission from the host is consistent with that derived by Grupe et al. (1999); Halpern et al. (2004).

A.44. SDSS J0159

First analysed by LaMassa et al. (2015), these authors performed detailed follow-up optical observations of the SDSS Galaxy SDSS J015957.64+003310.4. This host seems to be transitioning from a Type 1 broad-line AGN to a Type 1.9 AGN, showing weak broad $\text{H}\alpha$ emission lines over a 10 year period. They found that over this period, the optical flux from the source decreased by a factor of 6, while its $\text{H}\alpha$ weakened and became broader. Serendipitous *Chandra* and *XMM-Newton* observations of the source also found that the 2.0-10.0 keV emission in a high state which then decreased by an order of magnitude. LaMassa et al. (2015) attributed this change in both the optical and X-ray emission as the dimming of the AGN continuum, however they caveat that this type of change in the properties of this source is quite rare. Merloni et al. (2015) re-analysed archival data of the source and argued that the properties of its light curve and emission is consistent with that of an optical TDE whose accretion energy is reprocessed by dense, large scale height material (Guillochon et al. 2014). Merloni et al. (2015) also suggested that under certain assumptions, this TDE would be one of the most luminous non-beamed TDE discovered so far. From our analysis, we also detected X-ray emission from the host using both *XMM* and *Chandra*, which then decreases by an order of magnitude between these two observations. However, we find that this detected emission is less than order of magnitude greater than its *ROSAT* upperlimits, which is not commonly seen in TDEs.

A.45. SDSS J0748

Wang et al. (2011, 2012) analysed the SDSS spectrum of Galaxy SDSS J074820.67+471214.3 and found evidence of strong high-ionization coronal lines such as $[\text{Fe X}]\lambda 6376$ and $[\text{Ar XIV}]\lambda 4414$, as well as very broad line emission, which can be interpreted as the blue-shifted He II and Balmer lines. They also found that the source brightened in the g-band by 0.2 magnitudes between the photometric and spectroscopic observations of the source. Follow up optical observations of the source four years later had shown that these lines had weakened significantly, while line ratios ruled out the presence of AGN activity. Based on the detection of these coronal lines and broad line emission, Komossa et al. (2008) that suggested these lines represent a “light echo” of a flare, while Wang et al. (2011, 2012) suggested that this source is an optical TDE. Dou et al. (2016) recently presented a study of the mid-infrared emission from this source and discovered significant emission arising from this source many years after the

original detection. They classified this late time mid-infrared as an general signature of a TDE occurring in a gas-rich environment. There is very limited X-ray data available of this object, with only a *ROSAT* and *XMM-Newton* slew observation of the source. Both observations detect no X-ray emission from the position of the TDE and thus three sigma upperlimits are derived.

A.46. *SDSS J0938*

[Wang et al. \(2012\)](#) performed a survey of SDSS Galaxies to search for strong coronal lines from $[\text{Fe X}]\lambda 6376$ up to $[\text{Fe XIV}]\lambda 5304$ which could represent a “light echo” of a flare arising from a TDE. SDSS J093801.64+135317.0 is one of the seven host Galaxies that they selected which show evidence of these strong coronal lines and they suggested that these lines arise from a TDE. However, follow up spectroscopic observations using the Multi-Mirror Telescope (MMT) of SDSS J0938 by [Yang et al. \(2013\)](#) shows that these coronal lines are super imposed over narrower, low ionisation lines that arise from star forming regions. As such [Yang et al. \(2013\)](#) suggest that the strong coronal lines that were detected by [Wang et al. \(2012\)](#) most likely arise from an obscured AGN, however the TDE scenario cannot be ruled out. We detect no X-ray emission arising from this host and derive only X-ray upperlimits.

A.47. *SDSS J0939*

This candidate was suggested by [Esquej et al. \(2007\)](#) to be an X-ray TDE based on its detection in the *XMM-Newton* slew survey. However, even though the host Galaxy, SDSS J093922.90+370944.0, is found within the error circle of *XMM*, the position of this source is offset from the main optical emission of the host. Based on the width of the $\text{H}\alpha$ line, the strength of the $[\text{Fe II}]$ multiplets and the ratio of $[\text{O III}]\lambda 5007$ to $\text{H}\beta$, [Esquej et al. \(2007\)](#) classify the host as a narrow-line Seyfert 1 galaxy. We detect variable X-ray emission from the host which shows evidence of a high and a low state emission more indicative of AGN emission.

A.48. *SDSS J0952*

[Komossa et al. \(2008\)](#) discovered strong, coronal Fe lines, along with broad Balmer and double peaked, narrow $\text{He } \beta$ emission lines arising from galaxy SDSS J095209.56+214313.3. These lines which were strong in an SDSS spectrum taken during 2005, faded significantly over a two year period. Follow up photometric observations of the source in the NUV, optical and NIR bands showed evidence of variability in these wavelengths, which [Komossa et al. \(2008\)](#) suggest arises from an large X-ray flare. Follow up observations using the Lincoln Near Earth Asteroid Research (LINEAR) survey by [Palaversa et al. \(2016\)](#) detected a strong UV flare 1.8 years after when the flare was expected to have started, that arose from the center of the host Galaxy. *Chandra* X-ray observations taken three years after the flare revealed faint X-ray emission coincident with the host Galaxy. [Dou et al. \(2016\)](#) also detected years after the original event mid-infrared emission that declines following a simple powerlaw model which they attribute to being a signature of the original TDE. We also find X-ray emission arising from the position of the source, but the emission does not decay following a powerlaw, but increases and then plateaus for two years. This type of emission is not consistent with that seen in other X-rays TDEs which usually dramatically peak and then decay following approximately a powerlaw.

A.49. *SDSS J1011*

[Runnoe et al. \(2016\)](#) classified this source as a “changing look” quasar whose broad emission lines and continuum emission, is representative of a quasar. This source was first detected by SDSS in 2003, and then dramatically weakened in follow-up time domain spectroscopy of the source. Even though [Runnoe et al. \(2016\)](#) attribute the changes in the spectrum to changes in the accretion rate onto the BH, they also suggest that a TDE scenario could be responsible for the changes in the observed optical spectrum. However, even though a TDE is consistent with the decay rate of the light curve, this scenario cannot explain the fact that the emission of the source stayed in a high state for many years prior to decay, or explain the strength of the observed emission lines. Unfortunately, there is very little archival X-ray data overlapping the period in which these spectral changes were observed, however from the observations we analysed we detect no X-ray emission from the position of the source and derive only X-ray upperlimits.

A.50. *SDSS J1055*

Another Galaxy which shows evidence of strong coronal lines, and broad Balmer lines which could indicate that a flare from a TDE occurred [Wang et al. \(2012\)](#). However, [Yang et al. \(2013\)](#) detect broad Balmer lines, Fe II and the non-stellar continuum which suggests that it is a Type I Seyfert Galaxy, while its narrow line ratios indicate that it is an AGN. We detect weak X-ray emission from the host using *ROSAT*, however all follow up observations detect only X-ray upperlimits.

A.51. *SDSS J1201*

Using the slew capability of *XMM-Newton*, [Saxton et al. \(2012\)](#) first discovered a soft X-ray flare coincident with the nucleus of the inactive Galaxy SDSS J120136.02+300305.5. Follow-up observations of the source revealed significant variability in the emission of the source, however the emission declined following the canonical $t^{-5/3}$ of a X-ray TDE fading significantly over nearly a year. Deep radio observations of the source revealed that no X-ray jet was launched during the event. [Liu et al. \(2014\)](#) showed that the observed variability in the X-ray light curve of SDSS J1201 can be well explained by a super-massive BH binary system undergoing variability accretion when the star was disrupted. Similar to [Saxton et al. \(2012\)](#) we find flare like X-ray emission using both *XMM* and *Swift*, which shows evidence of variability. Prior to this X-ray flare event, we do not detect any X-ray emission from the source. Even though our X-ray light curve is consistent with that of [Saxton et al. \(2012\)](#), we derive slightly lower luminosities than these authors. This most likely arises from using a different model to reproduce the X-ray spectrum, and from using different background regions to define the spectra and source counts.

A.52. *SDSS J1241*

SDSS J124134.25+442639.2 is another strong coronal line emitting Galaxy that was discovered by [Gelbord et al. \(2009\)](#) and [Wang et al. \(2012\)](#) using SDSS while searching for the imprint of an X-ray flare that could arise from a TDE. [Yang et al. \(2013\)](#) performed follow-up MMT observations of this Galaxy and found that that these emission lines did not show significant variation in their strength with time, indicating that the lines most likely arise from the presence of an AGN, rather

than a transient event like a TDE. We detect using archival *Swift* and *Chandra* observations of the source soft X-ray emission that stays at maximum for over two years, then is suddenly undetectable over a year later making it less likely to be a TDE.

A.53. *SDSS J1311*

Using archival *Chandra* and *XMM* data, Maksym et al. (2010) discovered a transient X-ray event that they suggest most likely arises from a TDE. This event was coincident with the centre of its host Galaxy SDSS J131122.15–012345.6, which shows no evidence of strong optical emission lines that would suggest the presence of an AGN. This event was very soft, showed signs of variability and decayed following a $t^{-5/3}$ over a two year period. The temperature of this TDE (kT \sim 0.12 keV) is one of the highest temperature TDEs discovered so far. Late time radio observations of the source found no evidence of radio emission indicating the formation of a jet (Bower et al. 2013). In our analysis, we are able to reproduce the results of Maksym et al. (2010), however we are able to extend on their work and characterise the emission properties of the source over a longer base line. We find that apart from the original flare detected by Maksym et al. (2010), no detectable X-ray emission arises from the source.

A.54. *SDSS J1323*

This source was originally discovered by Esquej et al. (2007) in the *XMM-Newton* slew survey searching for potential TDE candidates. They found that this source varied by > 80 compared to its *ROSAT* upperlimit. Optical observations of the host taken before the burst showed no evidence of emission lines which could indicate the presence of an AGN (Esquej et al. 2008). Esquej et al. (2008) obtained follow-up *XMM-Newton* and *Swift* observation of the source two years after the original *XMM-Newton* slew observation. They found that X-ray emission detected by *XMM-Newton* and *Swift* had decreased by a factor of ~ 40 compared to the *XMM-Newton* slew observation and decayed following $t^{-5/3}$. Unlike Esquej et al. (2008) we detect X-ray emission from this source using only *XMM-Newton*, while we derive only upper limits for the *XMM-Newton* slew and *Swift* observation. In addition, our derive luminosity is also an order of magnitude lower than (Esquej et al. 2008). The difference in the number of detected data points most likely arises from our more stringent requirement for classifying a detection, while our luminosity estimation is most likely lower due to using regions to extract the source and background spectra, as well as fitting the spectra using a different model.

A.55. *SDSS J1342*

Identified by Yang et al. (2013) as a potential TDE by the detection of coronal emission lines. These lines disappeared years after the original SDSS observation that lead to this object being a source of interest. More recently Dou et al. (2016) detected mid-infrared emission from this source many years after the original flare which they state is most likely a signature of the original TDE. The X-ray data available for this source is quite limited, however a *Swift* observation that overlapped the position of the source detected soft X-ray emission. This emission was comparable to the *ROSAT* upperlimit we derived. However due to the limited data, we are unable to draw any conclusions about the X-ray emission from the source.

A.56. *SDSS J1350*

Another potential TDE classified using its coronal emission lines, while also showing evidence of mid-infrared emission which faded many years after the original flaring event Yang et al. (2013); Dou et al. (2016). No X-ray emission was detected from the position of the source.

A.57. *Swift J1112-82*

First detected as an long duration γ -ray outburst using the *Swift* BAT, Brown et al. (2015) obtained follow up *Swift* observations of the source and found that this burst also exhibited a bright X-ray flare coincident with the centre of its host Galaxy. The X-ray emission decayed following approximately a powerlaw model, while showing significant short-term variability. The X-ray emission was also quite hard in nature, with Kawamuro et al. (2016) also detecting hard X-ray emission from this source using 37 months of *MAXI* observations. Using the Fermi-LAT γ -ray satellite, Peng et al. (2016) searched for γ emission arising from the position of the source, however they were only able to derive upperlimits to the source. Simultaneous *Swift* UVOT observations of the source detected no UV/optical emission arising from the position of the flare, and follow up observations using *Gemini* detected a weak point-like source that decayed quickly. Optical spectra taken of the source reveal a single, weak emission line arising from [OII] λ 3727 but no other additional emission lines or continuum emission was detected. Brown et al. (2015) rule out an AGN origin for this flare and suggest that Swift J1112-82 is a non-thermal (relativistic) X-ray TDE similar to that of Swift J1644+57. This flare fades quickly and disappears ~ 100 days after the original discovery. From *ROSAT* and *XMM-Newton* slew observations of the source, we detect no other X-ray emission arising from the source. The luminosity derived by Brown et al. (2015) is a few orders of magnitude larger than what we derive. The reason behind this is because we derive the luminosity in the 0.3-2.0 keV, while the luminosity presented by Brown et al. (2015) represents the 0.2-10.0 keV. As this source is quite hard in nature, a majority of the emission from this source falls into the hard X-ray band rather than the soft X-ray band presented in this work.

A.58. *Swift J1644+57*

Similar to Swift J1112-82, Swift J1644+57 was first discovered by the *Swift* BAT as a long duration γ -ray outburst (Bloom et al. 2011b; Burrows et al. 2011). Observations by the *Swift* XRT indicated that this source was highly variable, long lived, had an isotropic peak 0.3-10.0 keV luminosity that exceeded 10^{48} erg/s, and decayed following approximately a $t^{-5/3}$ powerlaw law, ruling out the possibility that this source was a GRB. Using follow-up optical observations of the position of the source, Levan et al. (2011) detected an optical counterpart which they associated to be the host Galaxy of this source. Levan et al. (2011) triggered *Chandra* TOO observations of the source and was able to confirmed its highly variable nature and that this source was coincident with the nucleus of its host Galaxy. Levan et al. (2011) was also able to rule out the presence of permanent AGN activity. Following the first month of evolution of this source, Zauderer et al. (2011) detected a radio transient coincident with the centre of the host Galaxy, which was suggested to be a collimated relativistic outflow. The unique properties of this source quickly lead to the conclusion that Swift J1644+57 is

a highly beamed, non-thermal (relativistic) jetted X-ray TDE. The event is thought to arise from a $\sim 10^6 - 10^7 M_\odot$ BH, while the observed X-rays arise from internal dissipation from the inner part of the jet, while the radio emission arises from an expanding shock front (e.g., see [Bloom et al. 2011b](#); [Burrows et al. 2011](#); [Levan et al. 2011](#); [Zauderer et al. 2011](#); [Barres de Almeida & De Angelis 2011](#)).

Swift J1644+57 is one of the most data rich X-ray TDEs detected. This is best shown by [Mangano et al. \(2016\)](#) who present a complete analysis of the all available *Swift* and *Chandra* data of the object, 507 days after the first trigger, while [Levan et al. \(2016\)](#) and [Cheng et al. \(2016\)](#) analyse the late-time *XMM*, *Swift* and *Chandra* emission from the source. Even though we have merged observations of Swift J1644+57 that have a similar MJD, we find the general trend obtained by [Bloom et al. \(e.g., 2011b\)](#); [Burrows et al. \(e.g., 2011\)](#); [Mangano et al. \(e.g., 2016\)](#). However, as we derive the luminosity of the source over 0.3–2.0 keV energy range, our maximum luminosity is lower than that derived in the literature. The literature on Swift J1644+57 focuses predominantly on the rich *Swift* data of this source, however we also take advantage of the number of *XMM-Newton* observations available to derive the X-ray emission from the source. We find that the *XMM* data shows the strong variability seen in the *Swift* data, while also providing a constraint on the X-ray emission immediately before the flare. *ROSAT* observations of the source show that there is no variable X-ray emission arising from the source, however between the *ROSAT* data and the original trigger there is nearly 20 years in which there is no X-ray coverage of the source.

A.59. *Swift* J2058+05

Soon after the discovery by Swift J1644+57, the *Swift* BAT discovered another X-ray transient source, Swift J2058+05, which showed many similarities with Swift J1644+57 ([Krimm et al. 2011](#); [Cenko et al. 2012b](#)). [Cenko et al. \(2012b\)](#) performed a detailed multi-wavelength follow-up campaign of the source and discovered a long-lived, very luminous X-ray transient coincident with the centre of an inactive Galaxy. The X-ray emission from this source decays following a simple powerlaw, and then drops off rapidly much like Swift J1644+57 ([Pasham et al. 2015](#)). However the source does not show such dramatic variability as that seen in the Swift J1644+57 light curve. In addition, [Cenko et al. \(2012b\)](#) also revealed a radio counterpart to this flare which they associate with a jet like outflow. The properties of this source led [Cenko et al. \(2012b\)](#) to conclude that Swift J2058+05 was another non-thermal (relativistic) jetted X-ray TDE. Due to the relatively faint optical emission arising from the host Galaxy, [Cenko et al. \(2012b\)](#) was not able to rule out the presence of an AGN even though the observations suggested that the host did not harbour an AGN. As an alternative to the TDE scenario, [Cenko et al. \(2012b\)](#) also suggested that if this source arose from an AGN, then the discovery of this object would represent a new mode of variability in AGN.

The light curve we derive from our analysis is very similar to that derived by [Cenko et al. \(2012b\)](#) and [Pasham et al. \(2015\)](#). However, our luminosities are lower due to us focusing on the soft X-rays rather than the full energy band that is analysed in the literature. We also take advantage of available *ROSAT* and *XMM-Newton* slew observations of the source and determine that prior to the flare, there was no X-ray emission arising from the source. However, similar to Swift J1644+57 there is no X-ray data available for Swift J2058+05

between $\sim 1990 - 2008$.

A.60. *TDE2*, VV-2

Using archival *SDSS* data, [van Velzen et al. \(2011\)](#) discovered optical TDE, TDE2, coincident with the nucleus of its host Galaxy. Using follow up UV and optical observations [van Velzen et al. \(2011\)](#) were able to rule out the presence of an AGN, or its origin as a supernova explosion or another transient phenomenon. This event had an optical blackbody temperature of 1.82×10^4 K and a peak magnitude of $M_g = -20.4$. The UV and optical light curve of TDE2 decayed following the standard $t^{-5/3}$, while [van Velzen & Farrar \(2014\)](#) found that the light curve has a very similar decay rate as that of PS1-10jh, however it is much more luminous. There is very limited X-ray data about this object, with no X-ray observations taken around the same time the original flare was detected. We find that there is no X-ray emission from this source.

A.61. *Wings* (A1795)

Using the large number of archival X-ray observations of Galaxy cluster Abell 1795, [Maksym et al. \(2013\)](#) and [Donato et al. \(2014\)](#) discovered a very luminous, soft X-ray flare located significantly off centre from the core of cluster. However, the transient flare was found to be coincident with the centre of its inactive host, a dwarf Galaxy called WINGS J134849.88+263557.5 (Wings J1348). The flare lasted for more than five years and decayed following the canonical TDE powerlaw decay rate, making it a strong candidate for being a TDE. Archival observations using the Extreme Ultraviolet Explorer (EUVE) seemed to suggest a strong correlation between the detected X-ray flare in this work and a EUVE transient observed by [Bowyer et al. \(1999\)](#). Based on this observation, [Maksym et al. \(2013\)](#) and [Donato et al. \(2014\)](#) derived a BH mass of $< 10^6 M_\odot$. Follow up optical observations of the host using *Gemini* by [Maksym et al. \(2014b\)](#) revealed that the host Galaxy is an extremely low mass Galaxy making it one of the smallest galaxies to host a BH. Based on their optical spectrum that they obtained of the host, [Maksym et al. \(2014b\)](#) infer the presence of weak or temporary nuclear activity based on broad [O III] emission.

The X-ray emission arising from Wings J1348 is located in a very complicated region. The Galaxy cluster is very bright in X-rays and diffuse X-rays from this host dominate the background emission of Wings J1348. We attempted to remove the contribution of the Galaxy cluster from our analysis by defining a background region that immediately surrounds the position of the possible X-ray TDE. In addition, we used source and background regions similar to the PSF size of each instrument rather than using the region sizes specified in Section 2. By specifying smaller source and background regions, we minimise the contamination from Galaxy cluster emission. However, due to the complicated nature of the X-ray emission from this source, our results differ in some respects to that of [Maksym et al. \(2013\)](#) and [Donato et al. \(2014\)](#).

In our analysis, we are able to reproduce the X-ray lightcurve that [Maksym et al. \(2013\)](#) derived from the *Chandra* data of Wings. Compared to [Donato et al. \(2014\)](#) our luminosity values are much higher due to using a smaller energy range to define our luminosity. Compared to [Maksym et al. \(2013\)](#) we derived an upperlimit to the X-ray flux using *XMM-Newton* rather than an X-ray detection. This discrepancy most likely arises from the use of different source and background regions. In addition to the *Chandra* and *XMM-*

Table 3

The best fit powerlaw models as derived from fitting the full X-ray light curve of the *X-ray TDE* and *likely X-ray TDE* candidates.

Name	Power law index
ASASSN-14li	0.92 ± 0.12
Swift J1644+57	1.89 ± 0.20
Swift J2058+05	1.32 ± 0.06
XMM SL1 J0740-85	0.74 ± 0.10
2MASX J049	0.42 ± 0.03
3XMM J152130.7+074916	0.61 ± 0.01
IGR J17361-4441	1.60 ± 0.14
NGC247	0.26 ± 0.10
OGLE16aa	0.27 ± 0.10
PTF-10iya	0.61 ± 0.20
SDSS J1201	0.88 ± 0.40
SDSS J1311	0.44 ± 0.03
SDSS J1323	0.62 ± 0.22

Newton observations, we find that there are multiple pointed *ROSAT* observations and a RASS observation that overlap the position of the transient which cover the early 1990s, in addition to a *Swift* observation that was taken in ~ 2006 . Neither Maksym et al. (2013) or Donato et al. (2014) analysed the X-ray emission from these *ROSAT* or *Swift* observations. Using these observations, we are able to derive X-ray upperlimits to the emission from the source.

A.62. XMM SL1 J0740-85

During the *XMM-Newton* slew survey, Saxton et al. (2016) detected a bright X-ray flare from the centre of quiescent galaxy, 2MASX 07400785 – 8539307. The event was detected in both the full X-ray energy band and the UV band using *XMM-Newton* and *Swift*, showed signs of X-ray variability, and decayed by a factor of >70 and >12 in X-rays and UV respectively. Alexander et al. (2016b) followed up this source in radio using ATCA and detected weak radio emission consistent with a non-relativistic outflow, similar to that seen in ASASSN-14li (Alexander et al. 2016a). Using CITO and LCO optical observations of the host Galaxy, Saxton et al. (2016) determined that the host shows no evidence of AGN or current star formation activity indicating that the host of this event is a post-starburst Galaxy. As the galaxy showed no signs of previous AGN activity, this lead Saxton et al. (2016) to classify XMM SL1 J0740-85 as a TDE. From our analysis, we are able to produce similar results to that of Saxton et al. (2016).

B. POWERLAW MODEL FITS

In Section 4.2 we model the full X-ray light-curves of our TDE sample listed in Table 2. To do this we assume a simple powerlaw model defined by $a(t - t_{peak})^n$, where a is the normalisation, and n is the powerlaw index. Here we let the normalisation and powerlaw index be free parameters. In Table 3 we have listed our best fit powerlaw models and their one sigma uncertainties. Using these values, we generated the Gaussians seen in Figure 6, where the best fit value defines the peak of the Gaussian and the uncertainty defines the width. In Figure 23 we have plotted the best fit power models and their uncertainties for each of the TDE candidates we consider.

C. INDIVIDUAL SPECTRAL ENERGY DISTRIBUTIONS OF EACH X-RAY TDE.

To derive the νF_ν spectral energy distributions for each of the TDE candidates we consider we took the soft, medium and

hard X-ray counts rates for each as detected at peak. We then covered these counts in to fluxes F_ν , taking into account the effective area of each instrument. To get νF_ν , we then multiplied these fluxes by the energy band of interest. In the optical/UV and radio energy bands, we took the fluxes or magnitudes from the literature and converted these into νF_ν . We selected only measurements in these bands that were taken around approximately the same time as the original TDE flare was detected. In Figure 24 we have plotted the individual SEDs for each of our TDE sample, which are also overlaid with each other in Figure 17.

For ASASSN-14li, we took radio data from van Velzen et al. (2016), while the optical/UV data of this event was taken from Holoien et al. (2016b). The radio and optical/UV data for Swift J1644+57 was taken from Bloom et al. (2011b). For Swift J2058+05, we used the optical/UV data for this event from Cenko et al. (2012b), while its radio data was taken from Pasham et al. (2015). Optical/UV data for NGC 247, SDSS J1201, and PTF-10iya was taken from Feng et al. (2015), Saxton et al. (2012), Cenko et al. (2012a) and Brown et al. (2015) respectively, while radio data for IGR J17361-4441 was taken from Ferrigno et al. (2011) respectively. For XMM SL1 J0740-85, we used the optical/UV data derived using *Swift* in Saxton et al. (2016), and the radio data from Alexander et al. (2016b).

D. TABLE OF RESULTS OBTAINED FROM THIS ANALYSIS

In Tables 4–18, we have listed all the results of our X-ray analysis from each TDE candidate listed in Table 1. For each instrument, we have created three tables. Tables 4–8 contains the details of the observations we used, source and background counts in the full instrument energy band, whether we classified these as a detection or not and the derive count rate we used for our analysis. In Tables 9–13 we listed the counts we extracted in the soft, medium and hard energy bands for each event. In Tables 14–18, we have list the parameters of the absorbed powerlaw model that best describe the emission from the event, and the corresponding 0.3-2.0 keV flux and luminosity we derived from these models. These tables will be made available to download from <https://tde.space>.

In Table 19, we have listed the derived T_{90} and L_{90} values used in this work to produce Figures 7 and 18. Here uncertainties are listed are one sigma uncertainties.

In Table 20 we have listed the ratio of the measured N_H derived from modelling the X-ray spectrum of the observations for which we could extract an X-ray spectrum, and the corresponding Galactic N_H as derived from the Leiden/Argentine/Bonn (LAB) Survey of Galactic H I (Kalberla et al. 2005). Here we have ignored observations in which we were unable to extract an X-ray spectrum and instead assumed the Galactic N_H towards the source of interest. To derive N_H we assume Wilms et al. (2000) solar abundances. This ratio was used to produce Figure 11.

In Table 21 we have listed the hardness ratios (HRs) derived from the Tables 9–13. Here we have listed only the HRs for observations of the *X-ray TDE* and *likely X-ray TDE* candidates for which we used to produce Figure 9, 10 and 11. We do not list observations for which we derive an upperlimit.

In Table 22, we have listed the integrated optical/UV (0.002-0.1 keV) and X-ray (0.3-10 keV) luminosities derived for the events which have both optical/UV and X-ray data (see the individual SEDs listed in Figure 24). These values were used to produce Figure 12.

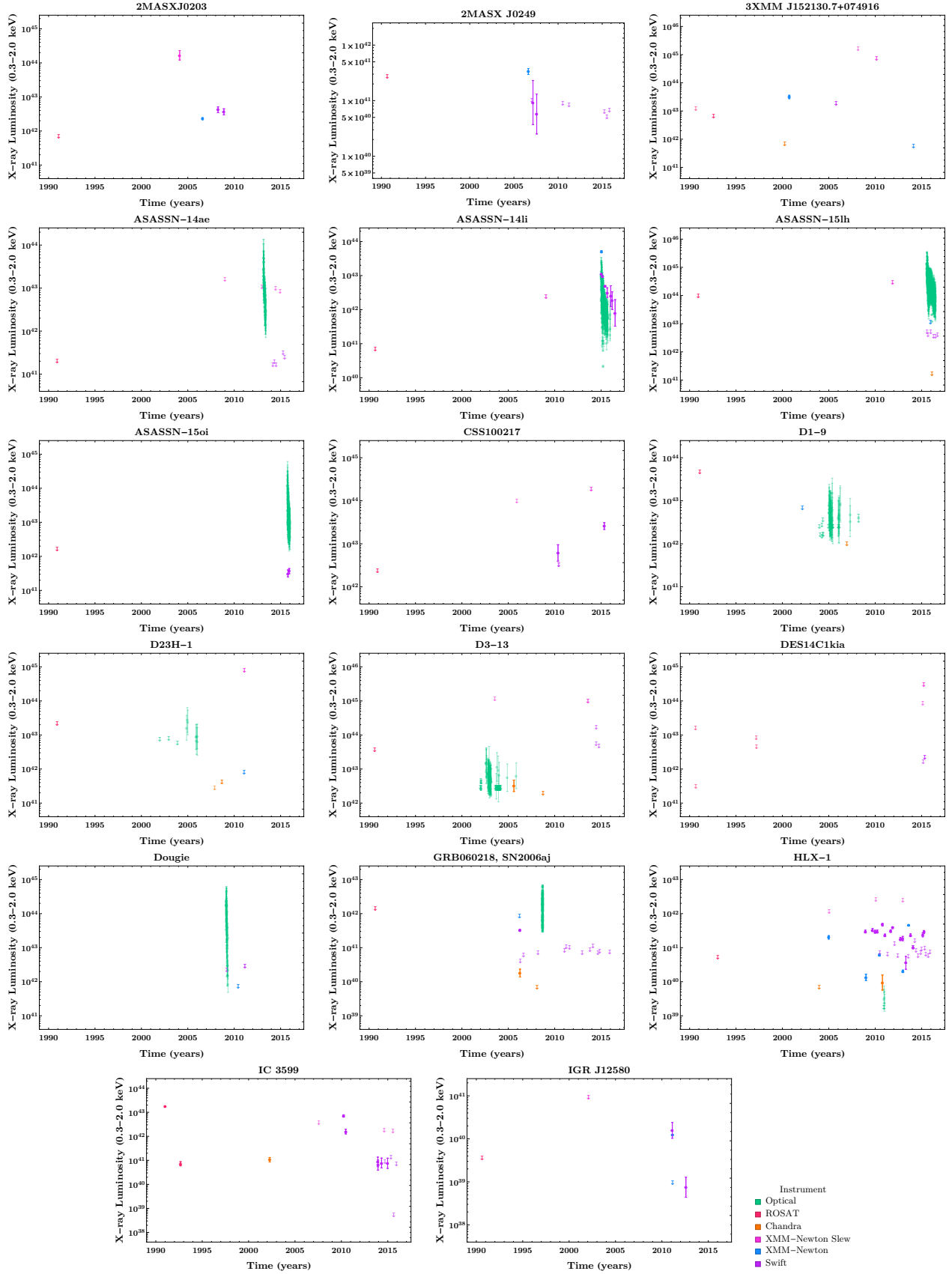


Figure 19. The X-ray/optical light curves of all TDE candidates listed in Table 1. The X-ray data which makes up these plots is derived from this work, while the optical data was taken from the literature. Here we have also coloured the data points based on the X-ray instrument in which we obtained this constraint. The exception is the optical data which is plotted as one colour, even though data points were taken by different instruments. Listed in the last panel in this figure is the colour key for each instrument.

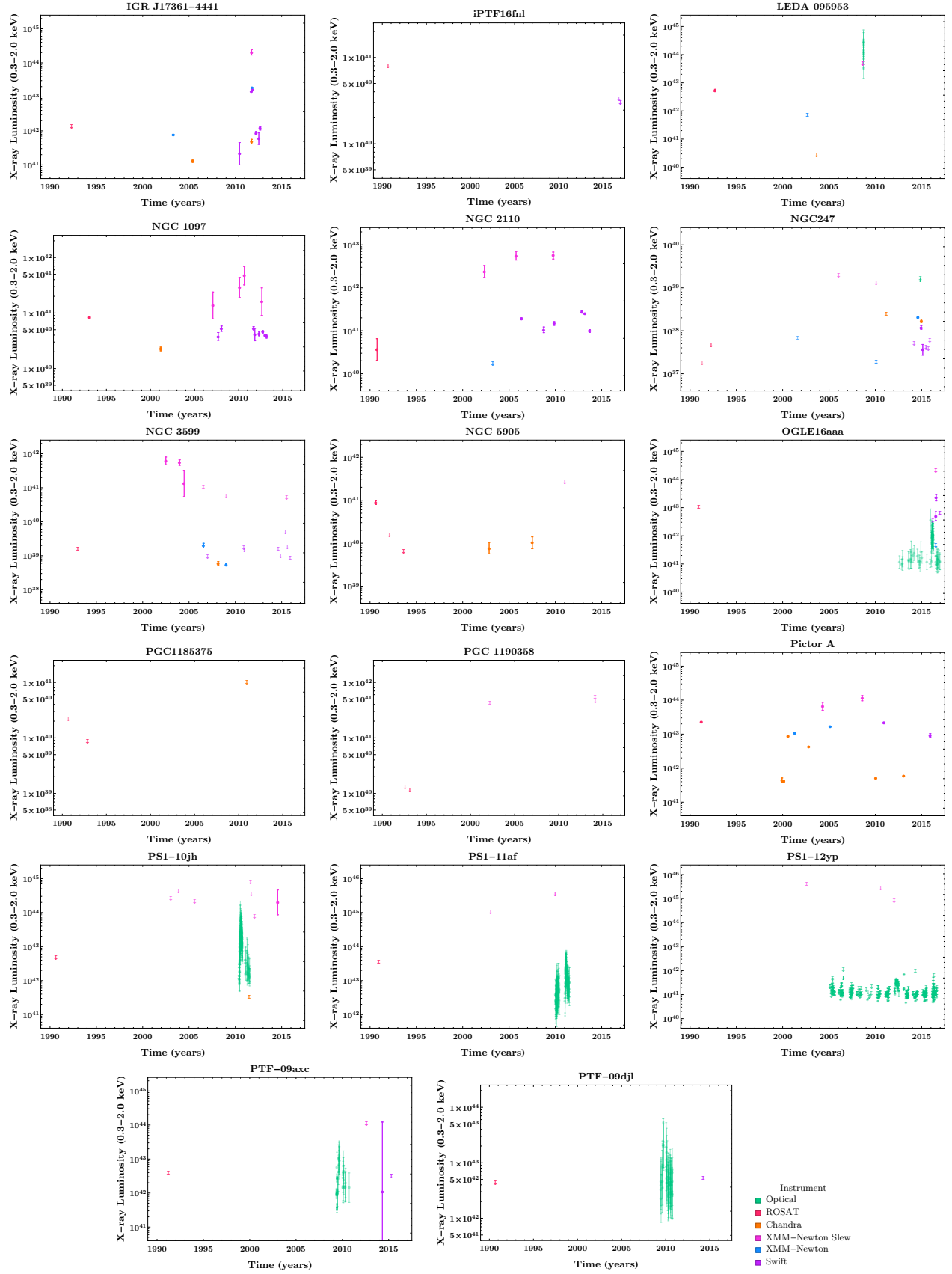


Figure 20. Light Curves for all TDE candidates listed in Table 1 continued. Similar to that of Figure 19.

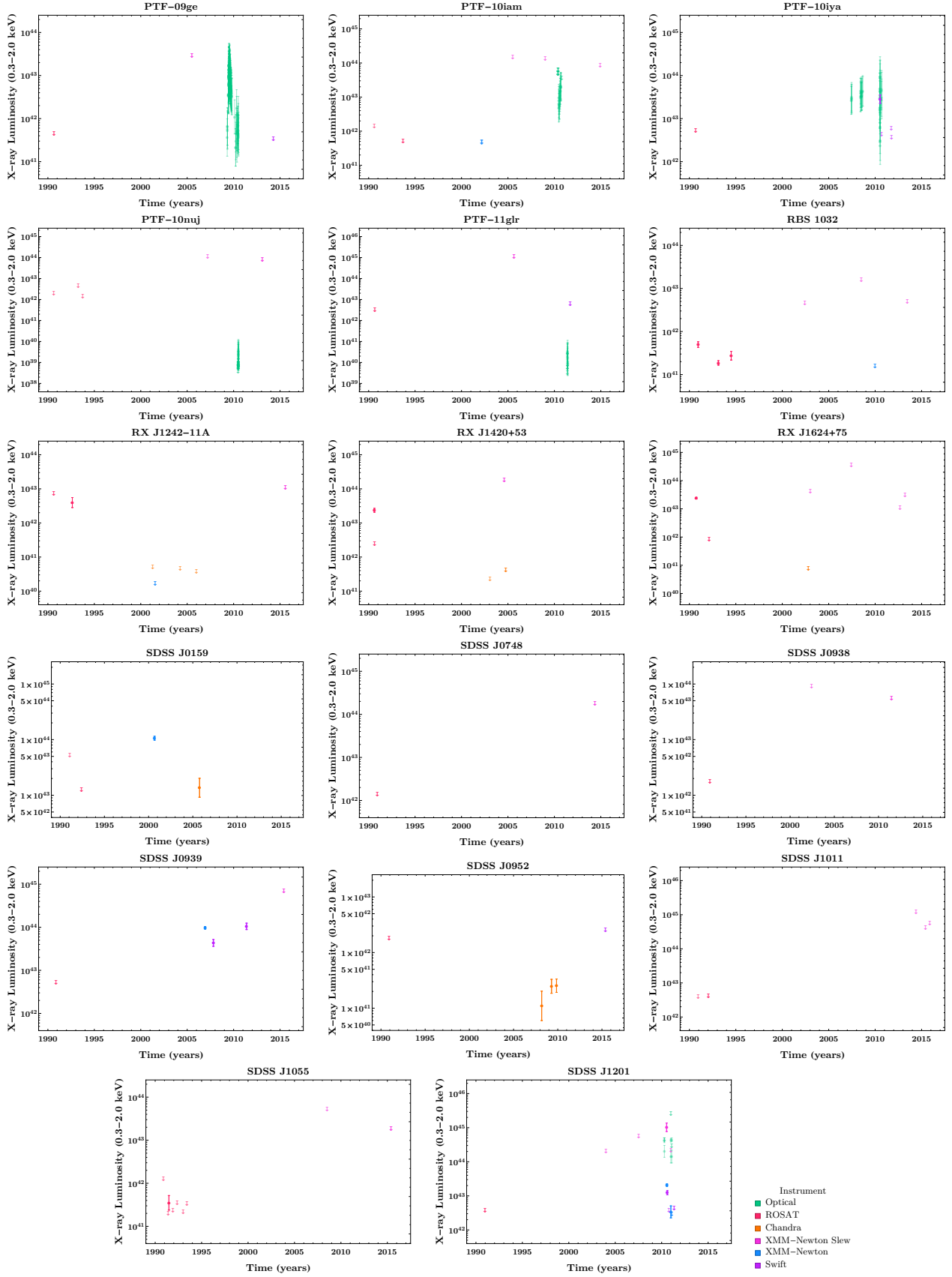


Figure 21. Light Curves for all TDE candidates listed in Table 1 continued. Similar to that of Figure 19.

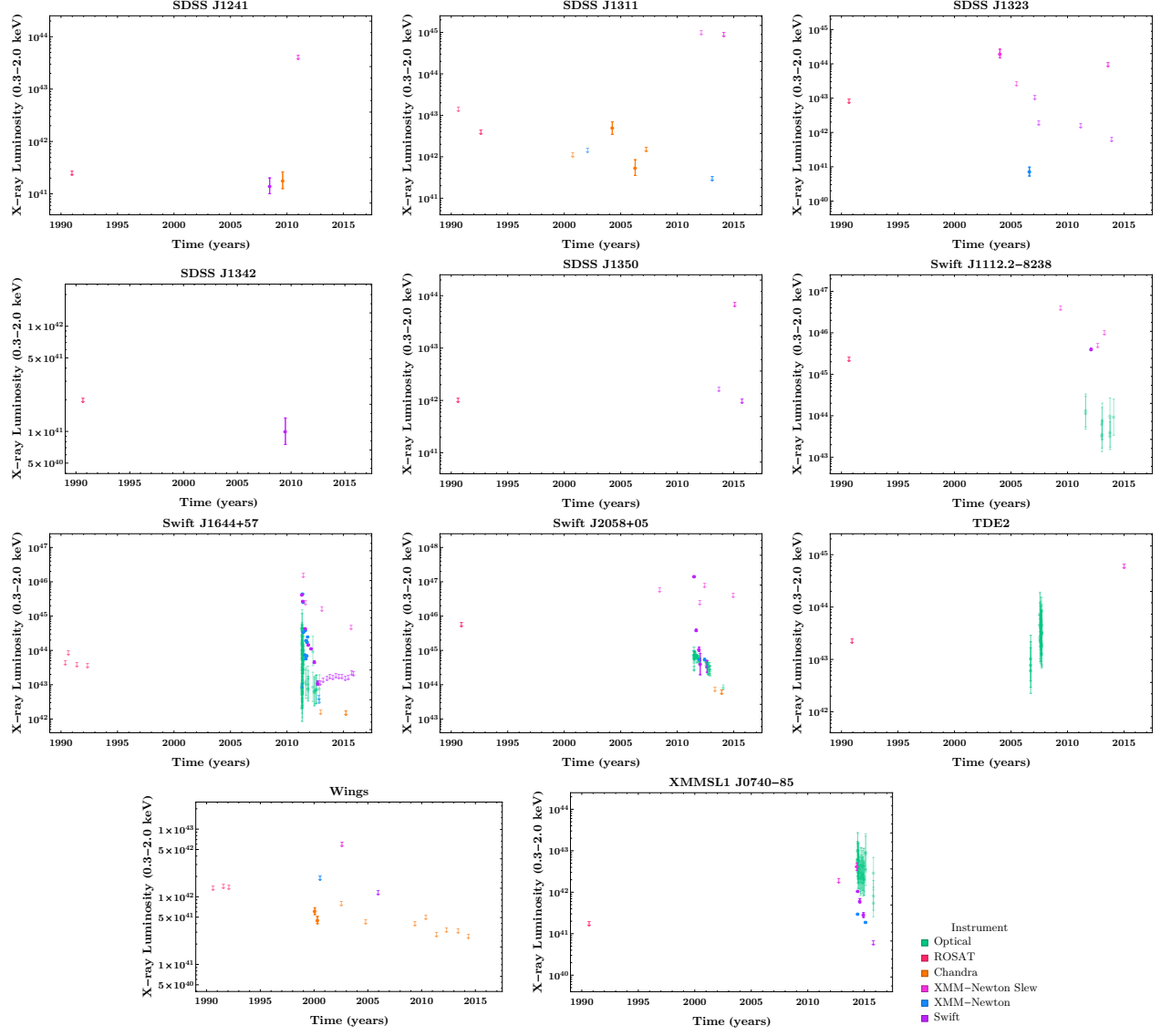


Figure 22. Light Curves for all TDE candidates listed in Table 1 continued. Similar to that in Figure 19.

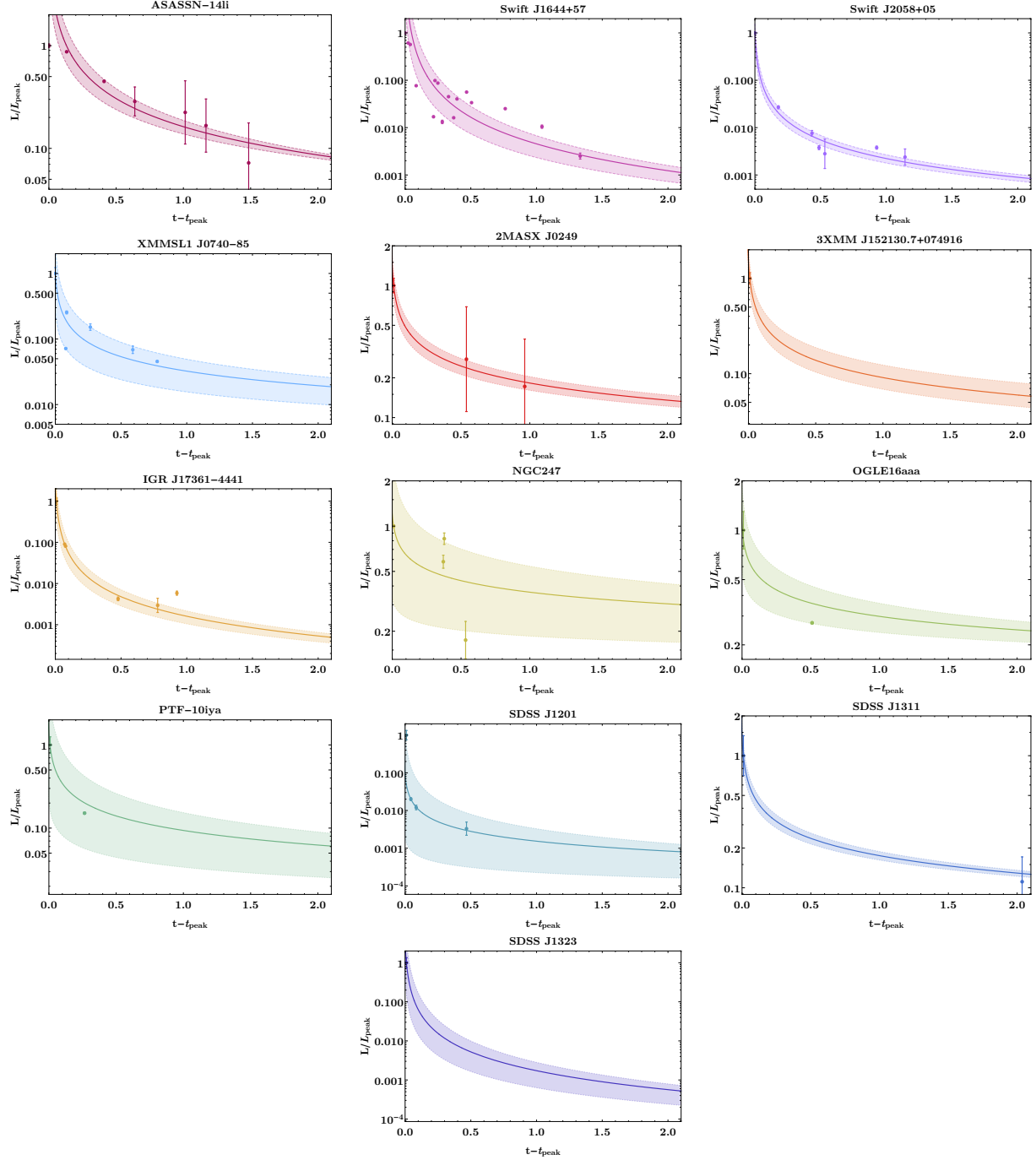


Figure 23. The best fit models (with their uncertainties) of the X-ray light curves of each of our *X-ray TDE* and *likely TDE* sample, that we obtained using a simple powerlaw $a \times (t - t_{\text{peak}})^n$, where a is the normalisation, t_{max} is the time when the maximum X-ray luminosity was measured and n is the powerlaw index. For simplicity, we normalised both the X-ray luminosity and time of observation of each data set by the maximum (peak) X-ray luminosity and the time that this maximum luminosity was detected.

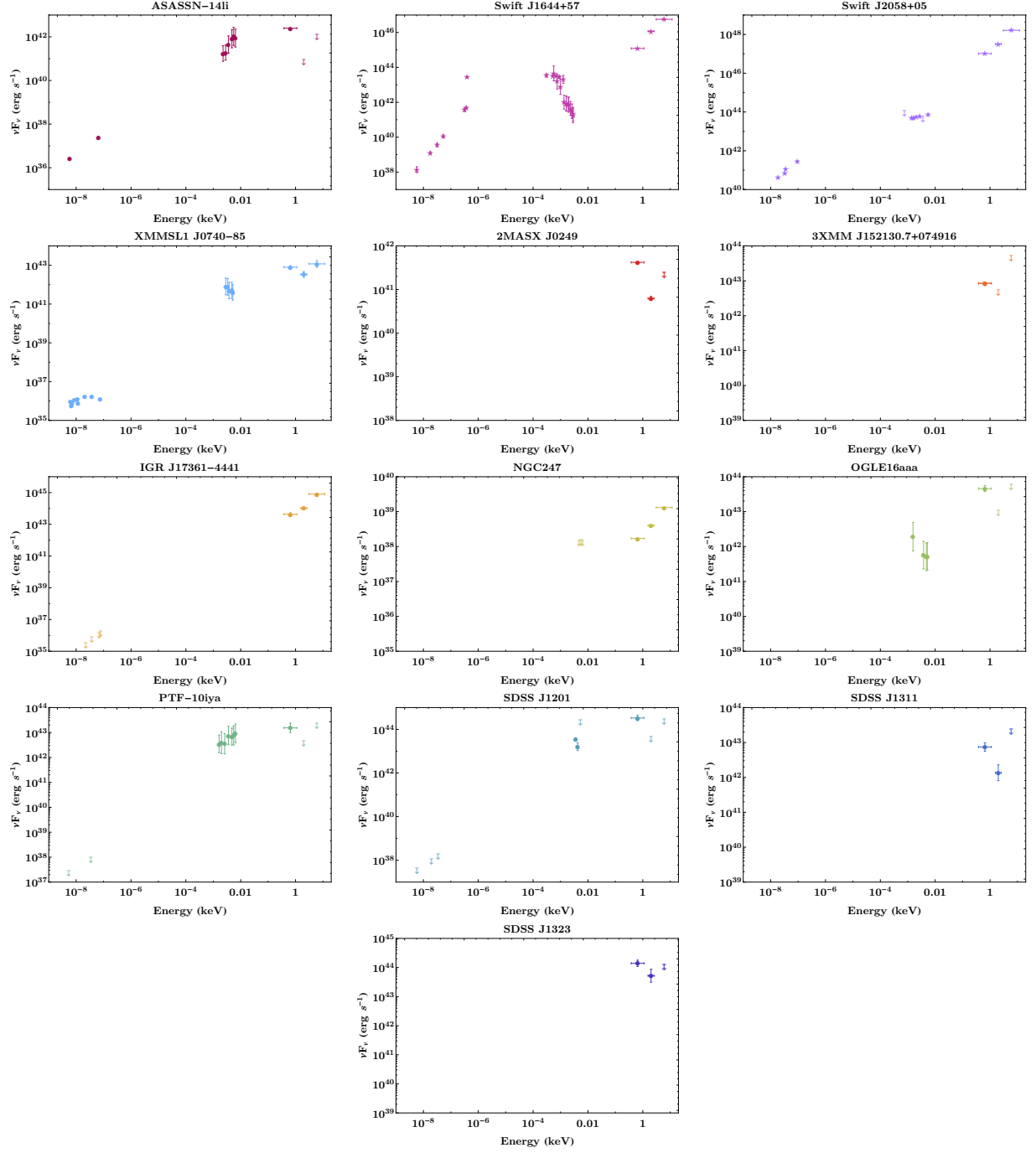


Figure 24. The individual spectral energy distribution of each of our *X-ray TDE* and *likely TDE* candidates in νF_ν (erg s^{-1}) vs. Energy (keV). The νF_ν values in the X-ray energies were derived from the number of counts detected at peak in the soft, medium and hard energy bands, and converted these into their corresponding νF_ν to characterise the X-ray emission of these sources. For sources in which optical, UV and/or radio data was taken simultaneously or close to ($t_{\text{optical}} - t_{\text{peak}} < +/ - 0.5$ year) when the X-ray luminosity was maximum, we have also plotted the corresponding νF_ν in this energy band derived from the literature values.

Table 4
X-ray properties, as derived using *ROSAT*, for TDE candidates which had *ROSAT* pointed
or RASS observations overlapping the position of the source.

Name	ObsID	ObsID label ^a	MJD	Exposure time (s)	Source Counts ^b	Bkg Counts ^c	\mathcal{P}_{fluct}^d	\mathcal{D}^d	U or D ^e	Count Rate ^{f,g} (ct/s)
2MASXJ0203	rs931806n00	r1	48258	400	0.00 ± 1.1	3.40 ± 0.5	1.0	0.0	U	$(2.63) \times 10^{-2}$
2MASX J0249	rs931808n00	r2	48100	237	0.00 ± 1.5	2.22 ± 0.4	1.0	0.0	U	$(3.32) \times 10^{-2}$
3XMM J152130.7+074916	rp800128n00 +rp800376n00	r3	48800	14058	129.32 ± 21.0	290.68 ± 4.4	1.0	0.0	U	$(2.86) \times 10^{-2}$
3XMM J152130.7+074916	rs931641n00	r4	48100	408	7.73 ± 4.2	9.27 ± 0.8	0.8	0.2	U	$(5.31) \times 10^{-2}$
ASASSN-14ae	rs931126n00	r5	48200	323	0.73 ± 2.1	3.27 ± 0.5	1.0	0.0	U	$(3.17) \times 10^{-2}$
ASASSN-14li	rs931434n00	r6	48100	324	2.27 ± 3.1	6.73 ± 0.7	1.0	0.0	U	$(5.27) \times 10^{-2}$
ASASSN-15lh	rs932821n00	r7	48200	396	0.80 ± 2.3	4.20 ± 0.5	1.0	0.0	U	$(3.07) \times 10^{-2}$
ASASSN-15oi	rs932250n00	r8	48200	324	0.00 ± 2.1	5.40 ± 0.6	1.0	0.0	U	$(4.49) \times 10^{-2}$
css100217	rs931023n00	r9	48187	484	0.00 ± 2.9	9.40 ± 0.8	1.0	0.0	U	$(4.52) \times 10^{-2}$
D1-9	rs921807n00	r10	48262	200	0.00 ± 1.1	1.53 ± 0.3	1.0	0.0	U	$(3.09) \times 10^{-2}$
D23H-1	rs931763n00	r11	48200	350	0.00 ± 1.5	3.29 ± 0.5	1.0	0.0	U	$(2.93) \times 10^{-2}$
D3-13	rs930826n00	r12	48084	694	2.27 ± 3.7	10.73 ± 0.8	1.0	0.0	U	$(3.49) \times 10^{-2}$
DES14C1kia	rp150085n00	r13	48090	324	0.00 ± 7.3	59.46 ± 2.0	1.0	0.0	U	$(3.00) \times 10^{-1}$
DES14C1kia	rp190073n00 +rp190115n00	r14	50487	324	0.00 ± 4.6	26.40 ± 1.3	1.0	0.0	U	$(1.52) \times 10^{-1}$
DES14C1kia	rp190472n00	r15	50496	324	3.40 ± 4.1	12.60 ± 0.9	1.0	0.0	U	$(8.44) \times 10^{-2}$
DES14C1kia	rs932209n00	r16	48102	324	0.00 ± 0.1	0.20 ± 0.1	1.0	0.0	U	$(5.60) \times 10^{-3}$
GRB060218, SN2006aj	rs931409n00	r17	48102	456	0.00 ± 1.5	3.47 ± 0.5	1.0	0.0	U	$(2.33) \times 10^{-2}$
HLX-1	rp800276n00 rp600415a01 +rp600415n00 +rp700552a00 +rp700552a01 +rp701097n00 +rp701098n00 +rp701099n00 +rp701100n00 +rp701528n00	r18	48964	18501	0.00 ± 18.7	334.00 ± 6.5	1.0	0.0	U	$(2.47) \times 10^{-2}$
IC 3599	rs931231n00 rs931735n00 rp400077n00 +rp201109n00	r19	48829	27966	865.97 ± 37.0	450.03 ± 7.5	0.0	1.0	D	$(3.64 \pm 0.2) \times 10^{-2}$
IC 3599	rs931231n00	r20	48222	500	1492.72 ± 39.7	81.26 ± 2.3	0.0	1.0	D	$(3.51 \pm 0.1) \times 10^0$
IGR J12580	rs931735n00	r21	48084	291	0.00 ± 1.8	4.80 ± 0.6	1.0	0.0	U	$(4.60) \times 10^{-2}$
IGR J17361-4441	rp400077n00 +rp201109n00	r22	48710	13842	201.27 ± 22.8	296.73 ± 4.4	1.0	0.0	U	$(2.96) \times 10^{-2}$
iPTF16fnl	rs931192n99	r23	48100	399	1.63 ± 2.0	2.38 ± 0.4	1.0	0.0	U	$(2.06) \times 10^{-2}$
LEDA 095953	rp8000287n00	r24	48847	5350	987.73 ± 47.7	1208.27 ± 9.0	1.0	0.0	U	$(2.89) \times 10^{-1}$
NGC 1097	rp600449n00	r25	48983	9249	2075.86 ± 47.1	130.14 ± 3.0	0.0	1.0	D	$(2.64 \pm 0.1) \times 10^{-1}$
NGC 2110	rs931816n00	r26	48137	493	9.33 ± 3.6	3.67 ± 0.5	0.0	1.0	D	$(2.23 \pm 0.9) \times 10^{-2}$
NGC247	rp600159a00 +rp600159a01	r27	48696	18374	67.27 ± 17.8	220.74 ± 5.3	1.0	0.0	U	$(1.70) \times 10^{-2}$
NGC247	rs932102n00	r28	48335	336	5.38 ± 3.4	5.62 ± 0.8	0.7	0.3	U	$(4.46) \times 10^{-2}$
NGC 3599	rp600263n00 +rp300169n00	r29	48955	18896	50.51 ± 18.9	288.49 ± 4.4	1.0	0.0	U	$(2.11) \times 10^{-2}$
NGC 5905	rp600585n00	r30	49187	9647	61.92 ± 14.1	128.08 ± 2.9	0.0	1.0	D	$(1.98) \times 10^{-2}$
NGC 5905	rp600190n00	r31	48627	4700	0.00 ± 11.1	154.80 ± 3.2	1.0	0.0	U	$(4.81) \times 10^{-2}$
NGC 5905	rs930725n00	r32	48084	1000	231.63 ± 15.7	26.73 ± 1.3	0.0	1.0	D	$(2.73 \pm 0.2) \times 10^{-1}$
OGLE16aaa	rs932802n00	r33	48200	161	0.00 ± 0.4	2.33 ± 0.4	1.0	0.0	U	$(5.05) \times 10^{-2}$
PGC1185375	rp600257a01 +rp600257n00	r34	48900	6682	9.20 ± 11.4	112.80 ± 2.7	1.0	0.0	U	$(2.55) \times 10^{-2}$
PGC1185375	rs931741n00	r35	48102	414	0.80 ± 2.7	6.20 ± 0.6	1.0	0.0	U	$(3.88) \times 10^{-2}$
PGC 1190358	rp600257a01	r36	49000	4632	0.00 ± 7.0	51.41 ± 1.9	1.0	0.0	U	$(1.85) \times 10^{-2}$
PGC 1190358	rp600257n00	r37	48800	6717	19.12 ± 10.8	91.88 ± 2.5	1.0	0.0	U	$(2.11) \times 10^{-2}$
Pictor A	rp700075n00 rs930727n00 +rs930829n00 +rs930830n00	r38	48306	4583	3502.73 ± 60.0	88.27 ± 2.4	0.0	1.0	D	$(8.99 \pm 0.2) \times 10^{-1}$
PS1-10jh	rs930727n00 +rs930829n00 +rs930830n00	r39	48084	2873	4.67 ± 7.9	54.33 ± 1.9	1.0	0.0	U	$(3.13) \times 10^{-2}$
PS1-11af	rs931627n00	r40	48200	440	0.00 ± 1.8	4.27 ± 0.5	1.0	0.0	U	$(2.80) \times 10^{-2}$
PTF-09axc	rs931338n00	r41	48300	418	0.00 ± 2.5	7.13 ± 0.7	1.0	0.0	U	$(4.27) \times 10^{-2}$
PTF-09djl	rs931240n00 +rs931241n00	r42	48103	1064	3.93 ± 4.4	14.07 ± 1.0	1.0	0.0	U	$(2.80) \times 10^{-2}$
PTF-09ge	rs930827n00	r43	48100	805	4.60 ± 4.2	12.40 ± 0.9	1.0	0.0	U	$(3.36) \times 10^{-2}$
PTF-10iam	rp701436n00	r44	49214	5060	0.00 ± 7.2	59.99 ± 2.0	1.0	0.0	U	$(1.94) \times 10^{-2}$
PTF-10iam	rs930726n00	r45	48080	1051	0.00 ± 4.1	16.00 ± 1.0	1.0	0.0	U	$(3.13) \times 10^{-2}$
PTF-10iya	rs931032n00	r46	48100	623	0.00 ± 3.3	10.00 ± 0.8	1.0	0.0	U	$(3.68) \times 10^{-2}$
PTF-10nuj	rp201582n00 +rp701372n00	r47	49228	6510	15.89 ± 11.8	115.11 ± 2.8	1.0	0.0	U	$(2.66) \times 10^{-2}$
PTF-10nuj	rp701147n00	r48	49055	996	0.00 ± 6.9	48.67 ± 1.8	1.0	0.0	U	$(8.22) \times 10^{-2}$
PTF-10nuj	rs930727n00	r49	48084	719	0.00 ± 2.8	12.13 ± 0.9	1.0	0.0	U	$(3.70) \times 10^{-2}$
PTF-11glr	rs931037n00	r50	48100	571	1.87 ± 2.0	2.13 ± 0.4	0.9	0.1	U	$(1.34) \times 10^{-2}$

Table 4 — *Continued*

Name	ObsID	ObsID label ^a	MJD	Exposure time (s)	Source Counts ^b	Bkg Counts ^c	\mathcal{P}_{fluct}^d	\mathcal{D}^d	U or D ^e	Count Rate ^{f,g} (ct/s)
RBS 1032	rp201237a01	r51	49500	3333	363.87 ± 20.0	34.13 ± 1.5	0.0	1.0	D	$(1.28 \pm 0.1) \times 10^{-1}$
RBS 1032	rp201237n00	r52	49000	2477	470.80 ± 22.5	33.20 ± 1.5	0.0	1.0	D	$(2.24 \pm 0.1) \times 10^{-1}$
RBS 1032	rs930822n00	r53	48200	366	99.20 ± 10.5	9.80 ± 0.8	0.0	1.0	D	$(3.19 \pm 0.3) \times 10^{-1}$
RX J1242-11A	rp600258n00	r54	48818	5324	675.00 ± 31.3	284.00 ± 4.4	0.0	1.0	D	$(1.49 \pm 0.1) \times 10^{-1}$
RX J1242-11A	rs931934n00	r55	48084	297	0.00 ± 3.6	13.27 ± 0.9	1.0	0.0	U	$(9.58) \times 10^{-2}$
RX J1420+53	rp150046n00	r56	48092	5905	15.76 ± 12.0	119.74 ± 2.8	1.0	0.0	U	$(3.97) \times 10^{-2}$
RX J1420+53	rs930724n00	r57	48084	690	136.60 ± 12.6	20.41 ± 1.2	0.0	1.0	D	$(2.33 \pm 0.2) \times 10^{-1}$
RX J1624+75	rp141820n00 +rp141829n00	r58	48634	3342	0.00 ± 6.5	41.87 ± 1.7	1.0	0.0	U	$(2.16) \times 10^{-2}$
RX J1624+75	rs930311n00	r59	48129	1045	338.27 ± 19.3	32.73 ± 1.5	0.0	1.0	D	$(3.81 \pm 0.5) \times 10^{-1}$
SDSS J0159	rp700225n00 +rp700972n00	r60	48733	7057	68.08 ± 11.7	64.92 ± 2.1	0.4	0.6	U	$(1.49) \times 10^{-2}$
SDSS J0159	rs931706n00	r61	48260	400	3.73 ± 3.1	5.27 ± 0.6	0.9	0.1	U	$(3.57 \pm 100.0) \times 10^{-2}$
SDSS J0748	rs930916n00	r62	48200	447	2.87 ± 2.5	3.13 ± 0.5	0.8	0.2	U	$(2.22) \times 10^{-2}$
SDSS J0938	rs931426n00 +rs931526n00	r63	48200	879	11.67 ± 4.4	7.33 ± 0.7	0.1	0.9	U	$(2.07) \times 10^{-2}$
SDSS J0939	rs931021n00	r64	48179	475	0.00 ± 2.3	5.00 ± 0.6	1.0	0.0	U	$(2.90) \times 10^{-2}$
SDSS J0952	rs931326n00	r65	48195	408	0.00 ± 1.1	3.67 ± 0.5	1.0	0.0	U	$(2.71) \times 10^{-2}$
SDSS J1011	rp900213n00	r66	48600	14094	53.57 ± 19.3	298.43 ± 4.5	1.0	0.0	U	$(2.92) \times 10^{-2}$
SDSS J1011	rs930717n00	r67	48200	504	2.00 ± 2.7	5.00 ± 0.6	1.0	0.0	U	$(2.73) \times 10^{-2}$
SDSS J1055	rp000050n00 +rp900029a04	r68	48365	26430	472.42 ± 31.1	466.58 ± 5.6	0.4	0.6	U	$(2.37) \times 10^{-2}$
SDSS J1055	rp900029a00	r69	48554	34397	528.67 ± 36.5	755.33 ± 7.1	1.0	0.0	U	$(2.87) \times 10^{-2}$
SDSS J1055	rp900029a01	r70	48728	11513	202.54 ± 24.0	351.47 ± 4.8	1.0	0.0	U	$(4.17) \times 10^{-2}$
SDSS J1055	rp900029a02	r71	48955	36621	488.47 ± 35.7	735.53 ± 7.0	1.0	0.0	U	$(2.62) \times 10^{-2}$
SDSS J1055	rp900029a03	r72	49104	934	14.83 ± 5.9	19.18 ± 1.1	0.9	0.1	U	$(4.07) \times 10^{-2}$
SDSS J1055	rp900029m01	r73	48184	28	0.13 ± 1.0	0.87 ± 0.2	1.0	0.0	U	$(1.54) \times 10^{-1}$
SDSS J1055	rs930718n00	r74	48396	569	20.80 ± 5.7	11.20 ± 0.9	0.0	1.0	D	$(4.30 \pm 1.2) \times 10^{-2}$
SDSS J1201	rs931229n00	r75	48216	483	0.00 ± 2.3	6.53 ± 0.7	1.0	0.0	U	$(3.46) \times 10^{-2}$
SDSS J1241	rs930926n00	r76	48213	493	4.40 ± 3.5	4.60 ± 0.6	0.7	0.3	U	$(2.63) \times 10^{-2}$
SDSS J1311	rp800248n00	r77	48821	13187	247.25 ± 22.7	249.75 ± 4.1	0.6	0.4	U	$(2.65) \times 10^{-2}$
SDSS J1311	rs931736n00 rs930824n00	r78	48086	275	10.40 ± 4.1	5.60 ± 0.6	0.1	0.9	U	$(5.43) \times 10^{-2}$
SDSS J1323	+rs930825n00 +rs930927n00	r79	48100	1120	5.33 ± 4.7	15.67 ± 1.0	1.0	0.0	U	$(2.89) \times 10^{-2}$
SDSS J1342	rs931637n00	r80	48100	325	0.00 ± 1.8	4.33 ± 0.5	1.0	0.0	U	$(3.83) \times 10^{-2}$
SDSS J1350	rs931234n00	r81	48080	454	0.00 ± 2.7	7.07 ± 0.7	1.0	0.0	U	$(3.90) \times 10^{-2}$
Swift J1112.2-8238	rs933205n00	r82	48100	301	0.00 ± 1.5	3.20 ± 0.5	1.0	0.0	U	$(3.35) \times 10^{-2}$
Swift J1644+57	rp000014n00	r83	48370	572	3.33 ± 4.0	11.67 ± 0.9	1.0	0.0	U	$(4.51) \times 10^{-2}$
Swift J1644+57	rp150069n00	r84	48094	30	0.00 ± 0.2	0.47 ± 0.2	1.0	0.0	U	$(9.94) \times 10^{-2}$
Swift J1644+57	rp900209n00	r85	48716	3268	0.00 ± 9.1	91.07 ± 2.5	1.0	0.0	U	$(4.31) \times 10^{-2}$
Swift J1644+57	rs930728n00	r86	48000	942	0.00 ± 3.7	13.60 ± 1.0	1.0	0.0	U	$(3.08) \times 10^{-2}$
Swift J2058+05	rs931656n00 +rs931657n00	r87	48189	445	0.00 ± 1.1	4.40 ± 0.5	1.0	0.0	U	$(2.83) \times 10^{-2}$
TDE2	rs931763n00 rp800055n00	r88	48200	378	0.00 ± 0.4	2.73 ± 0.4	1.0	0.0	U	$(2.40) \times 10^{-2}$
Wings	+rp700145a00 +rp700284n00. rp800105n00	r89	48438	43357	3751.94 ± 92.3	4462.06 ± 17.3	1.0	0.0	U	$(1.54) \times 10^{-1}$
Wings	+rp700145a01	r90	48626	36424	2510.89 ± 80.0	3640.11 ± 15.6	1.0	0.0	U	$(1.50) \times 10^{-1}$
Wings	rs931234n00	r91	48084	467	23.91 ± 7.7	31.09 ± 1.4	1.0	0.0	U	$(1.46) \times 10^{-1}$
XMMSL1 J0740-85	rs933203n00 +rs933204n00	r92	48100	733	7.81 ± 3.7	5.19 ± 0.6	0.3	0.7	U	$(1.93) \times 10^{-2}$

Note. — All uncertainties correspond to the 90% confidence level and observations that have similar MJD are combined.

^a Due to the large number of observations used in this analysis, we have listed a label for which we can reference in other Tables which observation ID (ObsID) we are referring to.

^b Obtained from a 100 arcsecond circular region surrounding the position of the TDE candidate. These values listed have **not** been corrected for encircled energy fraction. The exception to this is for TDE candidate *Wings* as discussed in Appendix A.61

^c Obtained from a 400 arcsecond circular region surrounding the position of the TDE which has been scaled such that the equivalent 100 arcsecond background count rate is presented. These values listed have **not** been corrected for encircled energy fraction. The exception to this is for TDE candidate *Wings* as discussed in Appendix A.61

^d Calculated assuming Poisson statistics

^e Here U indicates an upperlimit, while D corresponds to a data point as classified using Poisson statistics (see previous two columns).

^f The count rate **has** been corrected for encircled energy fraction.

^g Values which do not have any uncertainties are upperlimits. These upperlimits are

Table 5
X-ray properties, as derived using *Chandra*, for TDE candidates which had *Chandra* observations overlapping the position of the source.

Name	ObsID	ObsID label ^a	MJD	Exposure time (s)	Source Counts ^b	Bkg Counts ^c	\mathcal{P}_{fluct}^d	\mathcal{D}^d	U or D ^e	Count Rate ^{f,g} (ct/s)
3XMM J152130.7+074916	900	c1	51600	58100	0.49 ± 1.7	2.51 ± 0.2	1.0	0.0	U	$(1.39) \times 10^{-4}$
ASASSN-15lh	17879+17880	c2	57400	19800	0.00 ± 1.7	0.21 ± 0.1	0.2	0.8	U	$(8.97) \times 10^{-5}$
D1-9	6864	c3	54051	29741	2.98 ± 2.5	3.02 ± 0.2	0.8	0.2	U	$(3.08) \times 10^{-4}$
D23H-1	8601	c4	54683	9060	1.34 ± 1.4	0.66 ± 0.1	0.5	0.5	U	$(3.79) \times 10^{-4}$
D23H-1	7867+7868+9719	c5	54400	59850	4.48 ± 3.3	6.52 ± 0.3	0.9	0.1	U	$(2.63) \times 10^{-4}$
D3-13	5848+5847+5850+6216	c6	53556	184025	17.63 ± 4.8	5.37 ± 0.2	0.0	1.0	D	$(1.06 \pm 0.3) \times 10^{-4}$
D3-13	9727+9729+9730+9881+9454+9455+9456+9457+9460+9733+9878+9879+9880	c7	54700	592580	5.70 ± 5.1	20.30 ± 0.5	1.0	0.0	U	$(6.34) \times 10^{-5}$
GRB060218, SN2006aj	7604	c8	54471	19096	1.75 ± 2.2	3.26 ± 0.2	1.0	0.0	U	$(5.04) \times 10^{-4}$
GRB060218, SN2006aj	6307+6308	c9	53797	49273	73.96 ± 9.3	12.04 ± 0.3	0.0	1.0	D	$(1.67 \pm 0.2) \times 10^{-3}$
HLX-1	4971	c10	52960	24791	1.47 ± 1.4	0.53 ± 0.1	0.4	0.6	U	$(1.22) \times 10^{-4}$
HLX-1	13122	c11	55446	9537	9.73 ± 3.5	2.27 ± 0.2	0.0	1.0	D	$(1.13 \pm 0.4) \times 10^{-3}$
IC 3599	2999	c12	52341	10173	389.38 ± 19.8	2.62 ± 0.2	0.0	1.0	D	$(4.25 \pm 0.2) \times 10^{-2}$
IGR J17361-4441	5505	c13	53481	44574	504.05 ± 23.4	40.95 ± 0.6	0.0	1.0	D	$(1.26 \pm 0.1) \times 10^{-2}$
IGR J17361-4441	12453	c14	55803	2481	267.49 ± 16.7	11.51 ± 0.3	0.0	1.0	D	$(1.20 \pm 0.1) \times 10^{-1}$
LEDA 095953	4203	c15	52851	33987	7.09 ± 4.6	13.92 ± 0.4	1.0	0.0	U	$(8.21) \times 10^{-4}$
NGC 1097	1611+2339	c16	51938	11083	2972.41 ± 53.8	23.59 ± 0.5	0.0	1.0	D	$(2.98 \pm 0.1) \times 10^{-1}$
NGC247	12437	c17	55594	4990	0.95 ± 1.0	596.53 ± 24.4	1.0	0.0	U	$(1.49) \times 10^{-1}$
NGC247	17547	c18	56973	5000	464.97 ± 21.6	381.64 ± 19.5	0.0	1.0	D	$(1.03) \times 10^{-1}$
NGC 3599	9556	c19	54491	19905	228.51 ± 15.3	5.49 ± 0.2	0.0	1.0	D	$(1.28 \pm 0.1) \times 10^{-2}$
NGC 5905	3006	c20	52551	9625	30.09 ± 6.6	12.91 ± 0.4	0.0	1.0	D	$(3.47 \pm 0.8) \times 10^{-3}$
NGC 5905	7728+8558	c21	54254	70987	193.81 ± 14.7	22.18 ± 0.5	0.0	1.0	D	$(3.03 \pm 0.2) \times 10^{-3}$
PGC1185375	11314	c22	55500	10200	1.90 ± 1.4	1230.46 ± 35.1	1.0	0.0	U	$(1.46) \times 10^{-1}$
Pictor A	345	c23	51484	1345	178.53 ± 13.4	1.47 ± 0.1	0.0	1.0	D	$(1.48 \pm 0.1) \times 10^{-1}$
Pictor A	346	c24	51561	25834	3107.08 ± 56.0	26.92 ± 0.5	0.0	1.0	D	$(1.34) \times 10^{-1}$
Pictor A	443	c25	51723	5059	1631.81 ± 40.8	35.19 ± 0.6	0.0	1.0	D	$(3.58 \pm 0.1) \times 10^{-1}$
Pictor A	11586+12040	c26	55176	14300	2978.69 ± 55.0	48.31 ± 0.7	0.0	1.0	D	$(2.31) \times 10^{-1}$
Pictor A	14221+14357+15580+15593	c27	56275	146626	16561.22 ± 129.5	196.78 ± 1.4	0.0	1.0	D	$(1.25) \times 10^{-1}$
Pictor A	3090+4369	c28	52537	95486	38319.86 ± 196.1	127.14 ± 1.1	0.0	1.0	D	$(4.46) \times 10^{-1}$
PS1-10jh	13418	c29	55704	9909	1.24 ± 1.7	1.76 ± 0.1	0.8	0.2	U	$(6.43) \times 10^{-4}$
RX J1242-11A	1559	c30	51977	4477	0.00 ± 0.1	0.84 ± 0.1	1.0	0.0	U	$(8.90) \times 10^{-4}$
RX J1242-11A	4758	c31	53064	6871	0.00 ± 1.0	1.45 ± 0.1	1.0	0.0	U	$(8.19) \times 10^{-4}$
RX J1242-11A	6775	c32	53701	17178	1.02 ± 2.2	3.98 ± 0.2	1.0	0.0	U	$(6.44) \times 10^{-4}$
RX J1420+53	3240	c33	52627	9900	0.00 ± 1.0	1.81 ± 0.1	1.0	0.0	U	$(6.56) \times 10^{-4}$
RX J1420+53	4757+6127	c34	53246	9601	2.85 ± 2.7	4.16 ± 0.2	0.9	0.1	U	$(1.19) \times 10^{-3}$
RX J1624+75	3007	c35	52532	10086	3.54 ± 2.5	2.46 ± 0.2	0.4	0.6	U	$(7.90) \times 10^{-4}$
SDSS J0159	5777	c36	53615	19881	14.02 ± 3.9	0.98 ± 0.1	0.0	1.0	D	$(7.83 \pm 2.2) \times 10^{-4}$
SDSS J0952	9814	c37	54502	9782	7.40 ± 3.2	2.61 ± 0.2	0.0	1.0	D	$(8.40 \pm 3.6) \times 10^{-4}$
SDSS J0952	10727	c38	54906	16735	28.30 ± 5.7	4.70 ± 0.2	0.0	1.0	D	$(1.88 \pm 0.4) \times 10^{-3}$
SDSS J0952	10728	c39	55110	16937	29.50 ± 5.7	3.51 ± 0.2	0.0	1.0	D	$(1.93 \pm 0.4) \times 10^{-3}$
SDSS J1241	10729	c40	55022	9520	109.00 ± 10.6	2.04 ± 0.2	0.0	1.0	D	$(1.27 \pm 0.1) \times 10^{-2}$
SDSS J1311	5004	c41	53063	19856	17.23 ± 4.2	0.77 ± 0.1	0.0	1.0	D	$(9.64 \pm 2.4) \times 10^{-4}$
SDSS J1311	7701	c42	54167	4992	0.00	0.14	1.0	0.0	U	$(2.79) \times 10^{-4}$
SDSS J1311	1663+540	c43	51783	21052	0.00 ± 0.1	0.99 ± 0.1	1.0	0.0	U	$(2.10) \times 10^{-4}$
SDSS J1311	6930+7289	c44	53802	151274	14.62 ± 4.5	5.38 ± 0.2	0.0	1.0	D	$(1.07 \pm 0.3) \times 10^{-4}$
Swift J1644+57	15584	c45	56257	24650	0.00 ± 1.7	3.70 ± 0.2	1.0	0.0	U	$(4.27) \times 10^{-4}$
Swift J1644+57	16091	c46	57070	27800	2.00 ± 2.5	4.00 ± 0.2	0.9	0.1	U	$(4.00) \times 10^{-4}$
Swift J2058+05	14975	c47	56384	29585	0.00 ± 1.4	4.87 ± 0.2	1.0	0.0	U	$(4.32) \times 10^{-4}$
Swift J2058+05	16498+14976	c48	56596	49249	0.00 ± 2.5	7.48 ± 0.3	1.0	0.0	U	$(3.54) \times 10^{-4}$
Wings	493	c49	51624	19629	459.45 ± 23.4	87.55 ± 1.0	0.0	1.0	D	$(2.60 \pm 0.1) \times 10^{-2}$
Wings	494	c50	51532	19519	625.72 ± 26.8	89.28 ± 1.0	0.0	1.0	D	$(3.56 \pm 0.2) \times 10^{-2}$
Wings	3666	c51	52436	14416	49.35 ± 10.2	54.65 ± 0.7	0.8	0.2	U	$(5.92) \times 10^{-3}$
Wings	10898+10899+10900+10901	c52	54942	61951	1.84 ± 11.6	132.16 ± 1.2	1.0	0.0	U	$(2.99) \times 10^{-3}$
Wings	12026+12027+12028+12029	c53	55310	54655	0.00 ± 11.6	146.56 ± 1.2	1.0	0.0	U	$(3.72) \times 10^{-3}$
Wings	13106+13107+13108+13109+13110+13111+13112+13113+13412+13413+13414+13415+13416+13417	c54	55668	195620	0.00 ± 16.9	312.05 ± 1.8	1.0	0.0	U	$(2.07) \times 10^{-3}$

Table 5 — Continued

Name	ObsID	ObsID label ^a	MJD	Exposure time (s)	Source Counts ^b	Bkg Counts ^c	\mathcal{P}_{fluct}^d	\mathcal{D}^d	U or D ^e	Count Rate ^{f,g} (ct/s)
Wings	14268+14269+14270 +14271+142+72 +14273+14274+14275 15485+15486+15487	c55	56016	107057	0.00 ± 13.4	192.92 ± 1.4	1.0	0.0	U	$(2.43) \times 10^{-3}$
Wings	+15488+15489+15490 +15491+15492 16432+16433+16434 +16435+16436+16437 +16438+16439+16465 +16466+16467+16468	c56	56404	108010	3.00 ± 13.9	187.00 ± 1.4	1.0	0.0	U	$(2.35) \times 10^{-3}$
Wings	+16469+16470+16471 +16472 5287+5288+5289 +5290+6159+6160 +6161+6162+6163	c57	56758	221000	0.00 ± 18.1	330.58 ± 1.8	1.0	0.0	U	$(1.94) \times 10^{-3}$
Wings		c58	53263	130504	39.29 ± 18.9	315.61 ± 1.8	1.0	0.0	U	$(3.14) \times 10^{-3}$

Note. — All uncertainties correspond to the 90% confidence level and observations that have similar MJD are combined.

^a Due to the large number of observations used in this analysis, we have listed a label for which we can reference in other Tables which observation ID (ObsID) we are referring to.

^b Obtained from a 2 arcsecond circular region surrounding the position of the TDE candidate. These values listed have **not** been corrected for encircled energy fraction.

^c Obtained from a 20 arcsecond circular region surrounding the position of the TDE which has been scaled such that the equivalent 2 arcsecond background count rate is presented. These values listed have **not** been corrected for encircled energy fraction.

^d Calculated assuming Poisson statistics

^e Here U indicates an upperlimit, while D corresponds to a data point as classified using Poisson statistics (see previous two columns).

^f The count rate **has** been corrected for encircled energy fraction.

^g Values which do not have any uncertainties are upperlimits. These upperlimits are derived assuming that we would detect a signal if it is 3σ above background.

Table 6
X-ray properties, as derived using *XMM-Newton*, for TDE candidates which had
XMM-Newton pointed observations overlapping the position of the source.

Name	ObsID	ObsID label ^a	MJD	Exposure time (s)	Source Counts ^b	Bkg Counts ^c	\mathcal{P}_{fluct}^d	\mathcal{D}^d	U or D ^e	Count Rate ^{f,g} (ct/s)
2MASXJ0203	0411980201	x1	53919	9528	1678.00 ± 42.6	127.87 ± 2.9	0.0	1.0	D	$(2.20 \pm 0.1) \times 10^{-1}$
2MASX J0249	0411980401	x2	53931	9760	1396.00 ± 39.5	154.00 ± 3.2	0.0	1.0	D	$(1.68) \times 10^{-1}$
3XMM J152130.7+074916	0109930101, 0109930201	x3	51779	50830	1503.27 ± 59.3	1493.73 ± 10.5	0.0	1.0	D	$(3.48 \pm 0.1) \times 10^{-2}$
3XMM J152130.7+074916	0723801501	x4	56677	114200	367.45 ± 37.0	945.55 ± 7.7	1.0	0.0	U	$(1.14) \times 10^{-2}$
ASASSN-14li	0722480201	x5	57000	33834	21781.06 ± 154.3	1896.94 ± 11.2	0.0	1.0	D	$(7.57 \pm 0.1) \times 10^{-1}$
ASASSN-15lh	0770581201	x6	57345	6430	19.73 ± 18.4	313.27 ± 2.7	1.0	0.0	U	$(6.70) \times 10^{-2}$
D1-9	0112681001, 0112681101	x7	52305	34035	0.00 ± 26.6	675.78 ± 8.2	1.0	0.0	U	$(2.77) \times 10^{-2}$
D23H-1	0652401401	x8	55560	35660	15.53 ± 16.7	247.47 ± 4.1	1.0	0.0	U	$(9.72) \times 10^{-3}$
Dougie	0655800101	x9	55324	3780	0.00 ± 4.9	30.55 ± 1.4	0.0	0.0	U	$(1.47) \times 10^{-2}$
GRB060218, SN2006aj	0311590801	x10	53787	1808	93.47 ± 22.5	386.53 ± 5.1	1.0	0.0	U	$(3.08) \times 10^{-1}$
HLX-1	0204540201	x11	53333	20235	971.45 ± 34.0	166.55 ± 4.1	0.0	1.0	D	$(6.00 \pm 0.2) \times 10^{-2}$
HLX-1	0560180901	x12	56477	50373	4140.80 ± 67.8	414.20 ± 6.4	0.0	1.0	D	$(1.03) \times 10^{-1}$
HLX-1	0655510201	x13	54798	100817	518.93 ± 48.3	1649.08 ± 12.7	1.0	0.0	U	$(2.21) \times 10^{-2}$
HLX-1	0693060301	x14	56254	116356	987.42 ± 48.7	1262.58 ± 11.2	1.0	0.0	U	$(1.47) \times 10^{-2}$
HLX-1	0693060401	x15	55530	49660	1093.70 ± 40.1	465.32 ± 6.8	0.0	1.0	D	$(2.75 \pm 0.1) \times 10^{-2}$
IGR J12580	0658400501	x16	55584	6734	0.00 ± 11.0	118.20 ± 2.8	1.0	0.0	U	$(2.80) \times 10^{-2}$
IGR J12580	0658400601	x17	55584	17913	83960.61 ± 292.2	1346.39 ± 9.5	0.0	1.0	D	$(5.86) \times 10^0$
IGR J17361-4441	0146420101	x18	52720	29343	4021.53 ± 71.5	1025.47 ± 8.3	0.0	1.0	D	$(1.71) \times 10^{-1}$
IGR J17361-4441	0679380301	x19	55827	42217	70339.00 ± 268.1	1435.92 ± 9.8	0.0	1.0	D	$(1.96) \times 10^0$
LEDA 095953	0086950201	x20	52485	23797	0.00 ± 73.4	5077.43 ± 18.4	1.0	0.0	U	$(2.78) \times 10^{-1}$
NGC 2110	0145670101	x21	52704	4499	5.73 ± 20.5	387.27 ± 5.1	1.0	0.0	U	$(1.24) \times 10^{-1}$
NGC247	0110990301	x22	52099	3018	0.00 ± 15.4	234.20 ± 4.0	1.0	0.0	U	$(1.16) \times 10^{-1}$
NGC247	0601010101	x23	55193	29657	0.00 ± 27.2	733.66 ± 7.2	1.0	0.0	U	$(3.23) \times 10^{-2}$
NGC247	0728190101	x24	56839	30717	7981.42 ± 94.1	809.58 ± 7.6	0.0	1.0	D	$(3.25) \times 10^{-1}$
NGC 3599	0411980101	x25	53910	4417	214.00 ± 16.5	54.27 ± 1.9	0.0	1.0	D	$(6.06 \pm 0.5) \times 10^{-2}$
NGC 3599	0556090101	x26	54803	41694	552.27 ± 30.0	326.73 ± 4.7	0.0	1.0	D	$(1.66 \pm 0.1) \times 10^{-2}$
OGLE16aaa	0790181801	x27	57549	12041	22.02 ± 9.6	63.99 ± 2.5	1.0	0.0	U	$(8.60) \times 10^{-3}$
Pictor A	0090050701	x28	51986	16155	39854.00 ± 201.0	512.00 ± 5.7	0.0	1.0	D	$(3.08) \times 10^0$
Pictor A	0206390101	x29	53384	48036	179516.39 ± 427.5	3043.61 ± 14.2	0.0	1.0	D	$(4.67) \times 10^0$
PTF-10iam	0060370101	x30	52308	7497	2.20 ± 4.4	15.80 ± 1.0	1.0	0.0	U	$(4.35) \times 10^{-3}$
PTF-10iam	0060370901	x31	52312	26986	19.20 ± 10.3	81.80 ± 2.3	1.0	0.0	U	$(4.75) \times 10^{-3}$
RBS 1032	0604020101	x32	55156	10651	132.30 ± 42.7	1585.70 ± 10.3	1.0	0.0	U	$(1.88) \times 10^{-1}$
RX J1242-11A	0136950201	x33	52082	26657	8.19 ± 8.5	61.81 ± 1.4	1.0	0.0	U	$(3.86) \times 10^{-3}$
SDSS J0159	0101640201	x34	51755	5900	533.52 ± 24.6	66.48 ± 2.1	0.0	1.0	D	$(1.13 \pm 0.1) \times 10^{-1}$
SDSS J0939	0411980301	x35	54041	4836	1446.80 ± 38.8	55.20 ± 1.9	0.0	1.0	D	$(3.74 \pm 0.1) \times 10^{-1}$
SDSS J1201	0555060301	x36	55369	21819	2875.79 ± 63.4	1070.21 ± 8.4	0.0	1.0	D	$(1.65) \times 10^{-1}$
SDSS J1201	0555060401	x37	55523	18514	457.19 ± 33.0	391.81 ± 6.3	1.0	0.0	D	$(3.05) \times 10^{-2}$
SDSS J1201	0555060501	x38	55553	18956	48.00 ± 26.0	586.99 ± 6.3	1.0	0.0	U	$(4.35) \times 10^{-2}$
SDSS J1311	0093030101	x39	52267	33596	0.00 ± 23.5	676.14 ± 6.7	1.0	0.0	U	$(2.81) \times 10^{-2}$
SDSS J1311	0693820201	x40	56300	49466	0.00 ± 0.1	199.27 ± 3.6	1.0	0.0	U	$(5.75) \times 10^{-3}$
SDSS J1323	0411980501	x41	53931	5017	33.40 ± 8.2	26.93 ± 1.3	0.0	1.0	D	$(8.32 \pm 2.1) \times 10^{-3}$
Swift J1644+57	0658400801	x42	55651	2034	8.60 ± 6.7	34.40 ± 1.5	1.0	0.0	U	$(3.19) \times 10^{-2}$
Swift J1644+57	0678380101	x43	55667	21465	194050.43 ± 444.1	2998.57 ± 14.1	0.0	1.0	D	$(1.13) \times 10^1$
Swift J1644+57	0678380201	x44	55681	22363	142045.20 ± 381.4	3300.80 ± 14.8	0.0	1.0	D	$(7.94) \times 10^0$
Swift J1644+57	0678380301	x45	55697	22569	16770.66 ± 135.1	1380.34 ± 9.6	0.0	1.0	D	$(9.29 \pm 0.1) \times 10^{-1}$
Swift J1644+57	0678380501	x46	55745	16557	3202.13 ± 58.1	165.87 ± 3.3	0.0	1.0	D	$(2.42) \times 10^{-1}$
Swift J1644+57	0678380601	x47	55757	22864	31463.70 ± 179.1	572.27 ± 6.2	0.0	1.0	D	$(1.72) \times 10^0$
Swift J1644+57	0678380701	x48	55769	13915	16218.81 ± 128.6	296.19 ± 4.4	0.0	1.0	D	$(1.46) \times 10^0$
Swift J1644+57	0678380801	x49	55787	27151	32859.28 ± 183.0	578.72 ± 6.2	0.0	1.0	D	$(1.51) \times 10^0$
Swift J1644+57	0678380901	x50	55801	26554	7396.87 ± 87.6	267.13 ± 4.2	0.0	1.0	D	$(3.48) \times 10^{-1}$
Swift J1644+57	0678381001	x51	55811	24657	12123.53 ± 111.9	363.47 ± 4.9	0.0	1.0	D	$(6.15 \pm 0.1) \times 10^{-1}$
Swift J1644+57	0678381201	x52	55837	22053	15181.19 ± 126.9	852.81 ± 7.5	0.0	1.0	D	$(8.60 \pm 0.1) \times 10^{-1}$
Swift J1644+57	0700381501	x53	56198	27665	0.00 ± 16.1	258.60 ± 4.2	1.0	0.0	U	$(1.39) \times 10^{-2}$
Swift J1644+57	0700381601	x54	56206	30666	0.00 ± 15.2	220.20 ± 3.8	1.0	0.0	U	$(1.08) \times 10^{-2}$
Swift J2058+05	0679380801, 0679380901	x55	55887	36000	1200.81 ± 39.4	326.20 ± 4.7	0.0	1.0	D	$(4.17 \pm 0.1) \times 10^{-2}$
Swift J2058+05	0694830201	x56	56049	47940	1379.94 ± 43.8	507.06 ± 5.8	0.0	1.0	D	$(3.60 \pm 0.1) \times 10^{-2}$
Wings	0097820101	x57	51721	47708	11476.40 ± 173.0	17711.60 ± 37.2	1.0	0.0	U	$(4.75) \times 10^{-1}$
XMMSL1 J0740-85	0740340601 0740340301,	x58	57034	24327	3493.13 ± 63.8	546.87 ± 5.9	0.0	1.0	D	$(1.69) \times 10^{-1}$
XMMSL1 J0740-85	0740340401, 0740340501	x59	56777	43276	9635.29 ± 182.5	2852.71 ± 16.2	0.0	1.0	D	$(2.62 \pm 0.1) \times 10^{-1}$

Table 6 — Continued

Name	ObsID	ObsID label ^a	MJD	Exposure time (s)	Source Counts ^b	Bkg Counts ^c	\mathcal{P}_{fluct}^d	\mathcal{D}^d	U or D ^e	Count Rate ^{f,g} (ct/s)
------	-------	-----------------------------	-----	----------------------	----------------------------	-------------------------	-------------------------	-----------------	---------------------	-------------------------------------

Note. — All uncertainties correspond to the 90% confidence level and observations that have similar MJD are combined.

^a Due to the large number of observations used in this analysis, we have listed a label for which we can reference in other Tables which observation ID (ObsID) we are referring to.

^b Obtained from a 30 arcsecond circular region surrounding the position of the TDE candidate. These values listed have **not** been corrected for encircled energy fraction. The exception to this is for TDE candidate *Wings* as discussed in Appendix A.61

^c Obtained from a 120 arcsecond circular region surrounding the position of the TDE which has been scaled such that the equivalent 30 arcsecond background count rate is presented. These values listed have **not** been corrected for encircled energy fraction. The exception to this is for TDE candidate *Wings* as discussed in Appendix A.61

^d Calculated assuming Poisson statistics

^e Here U indicates an upperlimit, while D corresponds to a data point as classified using Poisson statistics (see previous two columns).

^f The count rate **has** been corrected for encircled energy fraction.

^g Values which do not have any uncertainties are upperlimits. These upperlimits are derived assuming that we would detect a signal if it is 3σ above background.

Table 7
X-ray properties, as derived using *XMM-Newton* *slew*, for TDE candidates which had
XMM-Newton *slew* observations overlapping the position of the source.

Name	ObsID	ObsID label ^a	MJD	Exposure time (s)	Source Counts ^b	Bkg Counts ^c	\mathcal{P}_{fluct}^d	\mathcal{D}^d	U or D ^e	Count Rate ^{f,g} (ct/s)
2MASXJ0203	9100500004	xs1	53018	5.00	20.33 ± 4.6	0.67 ± 0.2	0.0	1.0	D	$(4.52 \pm 1.0) \times 10^0$
3XMM J152130.7+074916	9148900002	xs2	54491	5.83	0.00 ± 3.4	12.37 ± 0.9	1.0	0.0	U	$(4.36) \times 10^0$
3XMM J152130.7+074916	9185400002	xs3	55220	3.40	0.00 ± 1.1	1.87 ± 0.4	1.0	0.0	U	$(1.95) \times 10^0$
ASASSN-14ae	9164500004	xs4	54803	5.13	0.00 ± 1.0	1.07 ± 0.3	1.0	0.0	U	$(9.02) \times 10^{-1}$
ASASSN-14ae	9237200005	xs5	56253	5.27	0.00 ± 0.2	0.60 ± 0.2	1.0	0.0	U	$(6.17) \times 10^{-1}$
ASASSN-14ae	9264300002	xs6	56792	8.80	0.80 ± 1.4	1.20 ± 0.3	1.0	0.0	U	$(5.66) \times 10^{-1}$
ASASSN-14ae	9273100003	xs7	56969	9.90	0.00 ± 0.3	1.13 ± 0.3	1.0	0.0	U	$(4.86) \times 10^{-1}$
ASASSN-14li	9165300002	xs8	54819	6.42	0.00 ± 0.2	0.94 ± 0.2	1.0	0.0	U	$(6.64) \times 10^{-1}$
ASASSN-15lh	9216800004	xs9	55846	8.13	0.53 ± 1.0	0.47 ± 0.2	1.0	0.0	U	$(3.46) \times 10^{-1}$
css100217	9107900005	xs10	53674	9.73	1.93 ± 1.8	1.07 ± 0.3	0.7	0.3	U	$(4.76) \times 10^{-1}$
css100217	9254600003	xs11	56599	9.83	0.13 ± 1.8	2.87 ± 0.4	1.0	0.0	U	$(8.98) \times 10^{-1}$
D23H-1	9202500002	xs12	55560	3.86	0.00 ± 1.1	1.60 ± 0.3	1.0	0.0	U	$(1.55) \times 10^0$
D3-13	9064500006	xs13	52809	10.10	0.47 ± 1.5	1.53 ± 0.3	1.0	0.0	U	$(5.75) \times 10^{-1}$
D3-13	9248400002	xs14	56475	8.87	0.00 ± 0.3	1.00 ± 0.3	1.0	0.0	U	$(5.01) \times 10^{-1}$
DES14C1kia	9276400004	xs15	57035	10.30	2.27 ± 1.7	0.73 ± 0.2	0.2	0.8	U	$(3.55) \times 10^{-1}$
DES14C1kia	9278700003	xs16	57080	9.97	0.33 ± 2.3	4.67 ± 0.6	1.0	0.0	U	$(1.24) \times 10^0$
HLX-1	9091500002	xs17	53346	9.10	0.53 ± 1.0	0.47 ± 0.2	1.0	0.0	U	$(3.07) \times 10^{-1}$
HLX-1	9184000003	xs18	55191	8.27	1.47 ± 1.8	1.53 ± 0.3	0.8	0.2	U	$(7.05) \times 10^{-1}$
HLX-1	9237300003	xs19	56255	9.30	0.00 ± 0.3	1.67 ± 0.3	1.0	0.0	U	$(6.62) \times 10^{-1}$
IC 3599	9137800003	xs20	54270	4.83	0.00 ± 0.3	1.13 ± 0.3	1.0	0.0	U	$(9.90) \times 10^{-1}$
IC 3599	9267000002	xs21	56847	3.93	0.00	0.25 ± 0.1	1.0	0.0	U	$(4.94) \times 10^{-1}$
IC 3599	9284400002	xs22	57193	10.10	0.00 ± 1.0	1.06 ± 0.3	1.0	0.0	U	$(4.57) \times 10^{-1}$
IGR J12580	9037400004	xs23	52268	5.67	0.00 ± 0.2	0.60 ± 0.2	1.0	0.0	U	$(5.73) \times 10^{-1}$
IGR J17361-4441	9214800002 + 9214800003	xs24	55806	7.68	132.27 ± 16.7	7.73 ± 1.0	0.0	1.0	D	$(1.91 \pm 0.2) \times 10^1$
LEDA 095953	9157600002	xs25	54665	6.57	1.13 ± 3.3	8.87 ± 0.8	1.0	0.0	U	$(3.01) \times 10^0$
NGC 1097	9128900002	xs26	54092	9.43	7.67 ± 3.0	1.33 ± 0.3	0.0	1.0	D	$(9.03 \pm 3.6) \times 10^{-1}$
NGC 1097	9184200003	xs27	55196	7.30	12.53 ± 3.8	1.47 ± 0.3	0.0	1.0	D	$(1.91 \pm 0.6) \times 10^0$
NGC 1097	9194100003	xs28	55393	5.50	15.40 ± 4.1	1.60 ± 0.3	0.0	1.0	D	$(3.11 \pm 0.8) \times 10^0$
NGC 1097	9230600002	xs29	56121	7.80	7.47 ± 3.0	1.53 ± 0.3	0.0	1.0	D	$(1.06 \pm 0.4) \times 10^0$
NGC 2110	9042300006	xs30	52366	8.07	27.40 ± 6.1	9.60 ± 0.8	0.0	1.0	D	$(3.77 \pm 0.8) \times 10^0$
NGC 2110	9104900003	xs31	53614	5.00	39.20 ± 6.4	1.80 ± 0.3	0.0	1.0	D	$(8.71 \pm 1.4) \times 10^0$
NGC 2110	9178400003	xs32	55080	7.63	60.53 ± 7.9	1.47 ± 0.3	0.0	1.0	D	$(8.81 \pm 1.1) \times 10^0$
NGC247	9110000002	xs33	53715	4.80	0.00 ± 0.3	1.27 ± 0.3	1.0	0.0	U	$(1.07) \times 10^0$
NGC247	9184100002	xs34	55193	7.63	0.00 ± 0.3	1.40 ± 0.3	1.0	0.0	U	$(7.20) \times 10^{-1}$
NGC 3599	9045100003	xs35	52421	3.80	30.00 ± 5.6	1.00 ± 0.3	0.0	1.0	D	$(8.77 \pm 1.6) \times 10^0$
NGC 3599	9072400006	xs36	52966	8.47	59.73 ± 7.8	1.27 ± 0.3	0.0	1.0	D	$(7.84 \pm 1.0) \times 10^0$
NGC 3599	9081400004	xs37	53145	1.60	2.73 ± 1.7	0.27 ± 0.1	0.0	1.0	D	$(1.90 \pm 1.2) \times 10^0$
NGC 3599	9119700005	xs38	53910	7.97	0.60 ± 2.3	4.40 ± 0.5	1.0	0.0	U	$(1.49) \times 10^0$
NGC 3599	9164500004	xs39	54803	10.40	3.40 ± 2.5	2.60 ± 0.4	0.5	0.5	U	$(7.97) \times 10^{-1}$
NGC 3599	9284100002	xs40	57187	7.03	0.00 ± 0.3	1.20 ± 0.3	1.0	0.0	U	$(7.09) \times 10^{-1}$
NGC 5905	9201100006 + 9201200005 + 9201500004	xs41	55536	4.18	1.13 ± 2.7	2.88 ± 0.7	0.9	0.1	U	$(2.12) \times 10^0$
OGLE16aaa	9302200003	xs42	57549	8.83	0.00 ± 1.0	1.20 ± 0.3	1.0	0.0	U	$(5.64) \times 10^{-1}$
PGC 1190358	9039700004	xs43	52314	10.20	0.00 ± 0.4	1.87 ± 0.4	1.0	0.0	U	$(6.52) \times 10^{-1}$
PGC 1190358	9258400002	xs44	56676	19.00	9.60 ± 4.1	6.40 ± 0.7	0.2	0.8	U	$(8.17) \times 10^{-1}$
PGC 1190358	9258600002	xs45	56679	18.40	2.00 ± 2.7	5.00 ± 0.6	1.0	0.0	U	$(7.06) \times 10^{-1}$
Pictor A	9078500005	xs46	53088	4.87	29.67 ± 5.6	1.33 ± 0.3	0.0	1.0	D	$(6.77 \pm 1.3) \times 10^0$
Pictor A	9156600004	xs47	54645	6.33	66.47 ± 8.3	1.53 ± 0.3	0.0	1.0	D	$(1.17 \pm 0.1) \times 10^1$
PS1-10jh	9055000002	xs48	52618	6.23	0.00 ± 1.0	1.33 ± 0.3	1.0	0.0	U	$(8.55) \times 10^{-1}$
PS1-10jh	9070200009	xs49	52923	9.07	1.20 ± 2.5	4.80 ± 0.6	1.0	0.0	U	$(1.39) \times 10^0$
PS1-10jh	9102100003	xs50	53558	2.50	0.00 ± 0.1	0.20 ± 0.1	1.0	0.0	U	$(6.85) \times 10^{-1}$
PS1-10jh	9212400002	xs51	55757	1.18	0.00 ± 0.2	0.53 ± 0.2	1.0	0.0	U	$(2.58) \times 10^0$
PS1-10jh	9214000006	xs52	55790	3.37	0.20 ± 1.0	0.80 ± 0.2	1.0	0.0	U	$(1.15) \times 10^0$
PS1-10jh	9220500003	xs53	55919	6.63	0.00 ± 0.1	0.20 ± 0.1	1.0	0.0	U	$(2.58) \times 10^{-1}$
PS1-10jh	9266300002	xs54	56833	5.63	3.40 ± 2.0	0.60 ± 0.2	0.0	1.0	D	$(6.71 \pm 4.0) \times 10^{-1}$
PS1-11af	9054600004	xs55	52611	6.40	0.67 ± 1.0	0.33 ± 0.2	1.0	0.0	U	$(3.58) \times 10^{-1}$
PS1-11af	9182000004	xs56	55152	5.93	0.00 ± 1.1	2.07 ± 0.4	1.0	0.0	U	$(1.19) \times 10^0$
PS1-12yp	9047000006	xs57	52460	6.87	0.00 ± 3.0	10.87 ± 0.9	1.0	0.0	U	$(3.36) \times 10^0$
PS1-12yp	9193400005	xs58	55380	8.67	2.73 ± 3.6	9.27 ± 0.8	1.0	0.0	U	$(2.36) \times 10^0$
PS1-12yp	9220000002	xs59	55909	5.67	0.20 ± 1.0	0.80 ± 0.2	1.0	0.0	U	$(6.83) \times 10^{-1}$
PTF-09axc	9230300002	xs60	56114	7.47	1.73 ± 1.8	1.27 ± 0.3	0.7	0.3	U	$(6.91) \times 10^{-1}$
PTF-09ge	9100500004	xs61	53527	6.83	0.00 ± 0.3	1.27 ± 0.3	1.0	0.0	U	$(7.54) \times 10^{-1}$
PTF-10iam	9100700002	xs62	53530	4.83	1.00 ± 1.8	2.00 ± 0.4	0.9	0.1	U	$(1.44) \times 10^0$

Table 7 — *Continued*

Name	ObsID	ObsID label ^a	MJD	Exposure time (s)	Source Counts ^b	Bkg Counts ^c	\mathcal{P}_{fluct}^d	\mathcal{D}^d	U or D ^e	Count Rate ^{f,g} (ct/s)
PTF-10iam	9164700002	xs63	54806	2.83	0.00 ± 0.2	0.73 ± 0.2	1.0	0.0	U	$(1.29) \times 10^0$
PTF-10iam	9273100003	xs64	56969	6.17	0.00 ± 0.3	1.27 ± 0.3	1.0	0.0	U	$(8.37) \times 10^{-1}$
PTF-10nuj	9131700004	xs65	54149	4.80	0.47 ± 1.0	0.53 ± 0.2	1.0	0.0	U	$(6.30) \times 10^{-1}$
PTF-10nuj	9239400002	xs66	56296	8.17	0.00 ± 0.2	0.73 ± 0.2	1.0	0.0	U	$(4.49) \times 10^{-1}$
PTF-11glr	9102900004	xs67	53575	7.13	0.67 ± 2.5	5.33 ± 0.6	1.0	0.0	U	$(1.91) \times 10^0$
RBS 1032	9044100004	xs68	52401	8.57	0.00 ± 1.1	1.73 ± 0.3	1.0	0.0	U	$(7.37) \times 10^{-1}$
RBS 1032	9155200003	xs69	54617	6.03	7.73 ± 3.8	6.27 ± 0.6	0.4	0.6	U	$(2.54) \times 10^0$
RBS 1032	9245800002	xs70	56423	7.60	0.00 ± 0.3	1.67 ± 0.3	1.0	0.0	U	$(8.10) \times 10^{-1}$
RX J1242-11A	9284400003	xs71	57194	9.43	0.00 ± 0.2	0.73 ± 0.2	1.0	0.0	U	$(3.89) \times 10^{-1}$
RX J1420+53	9083600005	xs72	53189	5.17	1.00 ± 1.4	1.00 ± 0.3	0.6	0.4	U	$(8.60) \times 10^{-1}$
RX J1624+75	9054800002	xs73	52614	3.23	0.53 ± 1.0	0.47 ± 0.2	1.0	0.0	U	$(8.65) \times 10^{-1}$
RX J1624+75	9135800002	xs74	54230	0.57	0.13 ± 1.0	0.87 ± 0.2	1.0	0.0	U	$(7.18) \times 10^0$
RX J1624+75	9231900004	xs75	56147	9.00	0.73 ± 1.0	0.27 ± 0.1	1.0	0.0	U	$(2.24) \times 10^{-1}$
RX J1624+75	9241900002	xs76	56346	5.78	0.27 ± 1.0	0.73 ± 0.2	1.0	0.0	U	$(6.35) \times 10^{-1}$
SDSS J0748	9262400003	xs77	56755	4.23	0.00 ± 2.3	6.33 ± 0.7	1.0	0.0	U	$(3.64) \times 10^0$
SDSS J0938	9044000002	xs78	52399	7.70	0.00 ± 1.0	1.47 ± 0.3	1.0	0.0	U	$(7.36) \times 10^{-1}$
SDSS J0938	9209400002	xs79	55698	6.30	0.53 ± 1.0	0.47 ± 0.2	1.0	0.0	U	$(4.44) \times 10^{-1}$
SDSS J0939	9281700002	xs80	57140	4.97	5.80 ± 2.9	2.20 ± 0.4	0.1	0.9	U	$(1.49) \times 10^0$
SDSS J1011	9263100006	xs81	56770	5.87	0.00 ± 1.8	4.00 ± 0.5	1.0	0.0	U	$(1.89) \times 10^0$
SDSS J1011	9281900002	xs82	57144	6.10	0.00 ± 0.2	0.87 ± 0.2	1.0	0.0	U	$(6.67) \times 10^{-1}$
SDSS J1011	9290400002	xs83	57313	6.00	0.00 ± 1.0	1.40 ± 0.3	1.0	0.0	U	$(9.17) \times 10^{-1}$
SDSS J1055	9155100004	xs84	54616	2.33	0.00 ± 0.2	0.53 ± 0.2	1.0	0.0	U	$(1.30) \times 10^0$
SDSS J1055	9281700002	xs85	57140	9.60	1.00 ± 1.4	1.00 ± 0.3	0.6	0.4	U	$(4.63) \times 10^{-1}$
SDSS J1201	9072500005	xs86	52968	4.93	0.00 ± 0.2	0.60 ± 0.2	1.0	0.0	U	$(6.59) \times 10^{-1}$
SDSS J1201	9137400004	xs87	54262	2.10	1.27 ± 1.4	0.73 ± 0.2	0.5	0.5	U	$(1.75) \times 10^0$
SDSS J1201	9192300005	xs88	55357	8.50	25.27 ± 5.1	0.73 ± 0.2	0.0	1.0	D	$(3.30 \pm 0.7) \times 10^0$
SDSS J1201	9200800002	xs89	55526	7.70	0.00 ± 1.0	1.33 ± 0.3	1.0	0.0	U	$(6.91) \times 10^{-1}$
SDSS J1241	9200800002	xs90	55526	1.57	0.00 ± 0.2	0.87 ± 0.2	1.0	0.0	U	$(2.60) \times 10^0$
SDSS J1311	9221900003	xs91	55947	2.27	0.00 ± 0.3	1.53 ± 0.3	1.0	0.0	U	$(2.57) \times 10^0$
SDSS J1311	9258200003	xs92	56671	2.53	0.47 ± 1.5	1.54 ± 0.3	1.0	0.0	U	$(2.30) \times 10^0$
SDSS J1323	9072900002	xs93	52975	8.50	23.93 ± 5.0	1.07 ± 0.3	0.0	1.0	D	$(3.13 \pm 0.7) \times 10^0$
SDSS J1323	9100300002	xs94	53522	9.93	2.20 ± 1.7	0.80 ± 0.2	0.2	0.8	U	$(3.90) \times 10^{-1}$
SDSS J1323	9248600003	xs95	56480	3.43	0.00 ± 1.0	1.13 ± 0.3	1.0	0.0	U	$(1.40) \times 10^0$
SDSS J1350	9276000002	xs96	57026	8.50	0.20 ± 2.6	3.80 ± 0.5	1.0	0.0	U	$(1.26) \times 10^0$
Swift J1112.2-8238	9171700003	xs97	54946	6.97	2.33 ± 2.3	2.67 ± 0.4	0.7	0.3	U	$(1.21) \times 10^0$
Swift J1112.2-8238	9231600003	xs98	56141	7.13	-0.07 ± 0.2	0.73 ± 0.2	1.0	0.0	U	$(5.14) \times 10^{-1}$
Swift J1112.2-8238	9242400004	xs99	56356	9.82	0.47 ± 1.0	0.53 ± 0.2	1.0	0.0	U	$(3.08) \times 10^{-1}$
Swift J1644+57	9209400002	xs100	55698	1.40	0.00 ± 2.4	11.80 ± 0.9	1.0	0.0	U	$(1.75) \times 10^1$
Swift J1644+57	9212400002	xs101	55757	1.37	0.00 ± 0.2	0.80 ± 0.2	1.0	0.0	U	$(2.83) \times 10^0$
Swift J1644+57	9239400002	xs102	56296	4.60	0.00 ± 1.1	2.60 ± 0.4	1.0	0.0	U	$(1.80) \times 10^0$
Swift J1644+57	9286300002	xs103	57231	8.31	0.00 ± 1.0	1.00 ± 0.3	1.0	0.0	U	$(5.35) \times 10^{-1}$
Swift J2058+05	9154300002	xs104	54599	6.30	0.00 ± 1.1	2.53 ± 0.4	1.0	0.0	U	$(1.29) \times 10^0$
Swift J2058+05	9218900005	xs105	55888	8.80	0.87 ± 1.4	1.13 ± 0.3	1.0	0.0	U	$(5.46) \times 10^{-1}$
Swift J2058+05	9227200002	xs106	56053	2.20	0.00 ± 0.2	0.73 ± 0.2	1.0	0.0	U	$(1.67) \times 10^0$
Swift J2058+05	9273500002	xs107	56976	8.93	0.53 ± 1.8	2.47 ± 0.4	1.0	0.0	U	$(8.93) \times 10^{-1}$
TDE2	9274500003	xs108	56996	7.57	0.07 ± 1.0	0.93 ± 0.3	1.0	0.0	U	$(5.63) \times 10^{-1}$
Wings	9047000006	xs109	52460	3.64	3.87 ± 2.2	1.13 ± 0.1	0.1	0.9	U	$(1.48) \times 10^0$
XMMSL1 J0740-85	9232600004	xs110	56161	4.17	0.63 ± 1.0	0.38 ± 0.2	1.0	0.0	U	$(5.90) \times 10^{-1}$
XMMSL1 J0740-85	9262100003	xs111	56749	10.30	56.19 ± 7.6	0.81 ± 0.2	0.0	1.0	D	$(6.06 \pm 0.8) \times 10^0$

Note. — All uncertainties correspond to the 90% confidence level and observations that have similar MJD are combined.

^a Due to the large number of observations used in this analysis, we have listed a label for which we can reference in other Tables which observation ID (ObsID) we are referring to.

^b Obtained from a 50 arcsecond circular region surrounding the position of the TDE candidate. These values listed have **not** been corrected for encircled energy fraction. The exception to this is for TDE candidate *Wings* as discussed in Appendix A.61

^c Obtained from a 200 arcsecond circular region surrounding the position of the TDE which has been scaled such that the equivalent 50 arcsecond background count rate is presented. These values listed have **not** been corrected for encircled energy fraction. The exception to this is for TDE candidate *Wings* as discussed in Appendix A.61

^d Calculated assuming Poisson statistics

^e Here U indicates an upperlimit, while D corresponds to a data point as classified using Poisson statistics (see previous two columns).

^f The count rate **has** been corrected for encircled energy fraction.

^g Values which do not have any uncertainties are upperlimits. These upperlimits are derived assuming that we would detect a signal if it is 3σ above background.

Table 8
X-ray properties, as derived using *Swift* *XRT*, for TDE candidates which had *Swift* *XRT* observations overlapping the position of the source.

Name	ObsID	ObsID label ^a	MJD	Exposure time (s)	Source Counts ^b	Bkg Counts ^c	\mathcal{P}_{fluct}^d	\mathcal{D}^d	U or D ^e	Count Rate ^{f,g} (ct/s)
2MASXJ0203	00035746001, 00040304001	sw1	54756	5621	175.34 ± 13.5	7.66 ± 0.7	0.0	1.0	D	$(3.47 \pm 0.3) \times 10^{-2}$
2MASXJ0203	00035746002	sw2	54527	3634	118.86 ± 11.2	5.14 ± 0.6	0.0	1.0	D	$(3.63 \pm 0.3) \times 10^{-2}$
2MASX J0249	00035748002, 00035748003	sw3	54076	829	2.80 ± 2.0	1.20 ± 0.3	0.3	0.7	U	$(6.01) \times 10^{-3}$
2MASX J0249	00035748004	sw4	54127	617	3.34 ± 2.0	0.67 ± 0.2	0.0	1.0	D	$(5.60 \pm 3.6) \times 10^{-3}$
2MASX J0249	00035748005	sw5	54279	3042	27.26 ± 5.6	3.74 ± 0.5	0.0	1.0	D	$(3.49 \pm 2.0) \times 10^{-3}$
2MASX J0249	00040306001	sw6	55361	689	2.27 ± 1.7	0.74 ± 0.2	0.2	0.8	U	$(5.33) \times 10^{-3}$
2MASX J0249	00040306002–003	sw7	55618	1456	3.87 ± 2.5	2.13 ± 0.4	0.4	0.6	U	$(4.97) \times 10^{-3}$
2MASX J0249	00040306004–005	sw8	57086	2812	0.00 ± 1.8	3.81 ± 0.5	1.0	0.0	U	$(3.82) \times 10^{-3}$
2MASX J0249	00040306006	sw9	57189	2987	2.93 ± 2.5	3.07 ± 0.5	0.8	0.2	U	$(3.10) \times 10^{-3}$
2MASX J0249	00040306007–008	sw10	57285	2028	2.39 ± 2.3	2.61 ± 0.4	0.7	0.3	U	$(4.08) \times 10^{-3}$
3XMM J152130.7+074916	00035189001	sw11	53624	9338	4.92 ± 7.1	42.08 ± 1.7	1.0	0.0	U	$(7.32) \times 10^{-3}$
ASASSN-14ae	00033130001–003	sw12	56690	6840	0.00 ± 2.1	8.85 ± 0.8	1.0	0.0	U	$(2.89) \times 10^{-3}$
ASASSN-14ae	00033130004–018	sw13	56751	25984	0.00 ± 7.5	56.62 ± 2.0	1.0	0.0	U	$(3.39) \times 10^{-3}$
ASASSN-14ae	00033130019–023	sw14	56816	9038	1.27 ± 3.9	12.73 ± 0.9	1.0	0.0	U	$(2.88) \times 10^{-3}$
ASASSN-14ae	00033130024	sw15	57094	2410	0.00 ± 2.3	5.05 ± 0.6	1.0	0.0	U	$(5.44) \times 10^{-3}$
ASASSN-14ae	00033130025–027	sw16	57151	6181	1.48 ± 3.9	12.52 ± 0.9	1.0	0.0	U	$(4.16) \times 10^{-3}$
ASASSN-14li	00033539001–004	sw17	56995	11660	3779.63 ± 61.8	40.37 ± 1.5	0.0	1.0	D	$(3.60 \pm 0.1) \times 10^{-1}$
ASASSN-14li	00033539005–012, 00033539014–030, 00033539032–034	sw18	57047	70225	22980.31 ± 152.4	237.69 ± 3.7	0.0	1.0	D	$(3.64) \times 10^{-1}$
ASASSN-14li	00033539035–043, 00033539045–060	sw19	57146	46452	9057.91 ± 95.9	135.09 ± 2.8	0.0	1.0	D	$(2.17) \times 10^{-1}$
ASASSN-14li	00033539061–068	sw20	57228	15421	1877.24 ± 43.8	35.76 ± 1.4	0.0	1.0	D	$(1.35) \times 10^{-1}$
ASASSN-14li	00033539069–080	sw21	57365	25757	1832.73 ± 43.2	35.28 ± 1.4	0.0	1.0	D	$(7.91 \pm 0.2) \times 10^{-2}$
ASASSN-14li	00033539082, 00033539084–090	sw22	57426	11400	736.15 ± 27.4	11.85 ± 0.7	0.0	1.0	D	$(7.17 \pm 0.3) \times 10^{-2}$
ASASSN-14li	00033539091–098	sw23	57539	13900	529.97 ± 23.6	26.03 ± 1.0	0.0	1.0	D	$(4.24 \pm 0.2) \times 10^{-2}$
ASASSN-15lh	00033830001–002	sw24	57198	4840	6.70 ± 3.5	5.30 ± 0.6	0.4	0.6	U	$(2.80) \times 10^{-3}$
ASASSN-15lh	00033830003, 00033830005–010, 00033830012, 00033830016, 00033830020–041, 00033874002–010, 00033886001–003	sw25	57246	107871	0.00 ± 13.2	174.33 ± 3.2	1.0	0.0	U	$(2.20) \times 10^{-3}$
ASASSN-15lh	00033830042, 00033830044–057, 00033830059–061, 00033886004–010, 00034112001–009	sw26	57347	72821	0.00 ± 12.0	140.08 ± 2.9	1.0	0.0	U	$(2.68) \times 10^{-3}$
ASASSN-15lh	00033830062–068, 00033886011–013, 00033886015–023	sw27	57461	44290	3.67 ± 7.8	53.33 ± 1.8	1.0	0.0	U	$(1.89) \times 10^{-3}$
ASASSN-15lh	00033886024–043	sw28	57540	52293	7.84 ± 8.6	63.16 ± 1.9	1.0	0.0	U	$(1.85) \times 10^{-3}$
ASASSN-15lh	00033886044–047, 00033886049–056	sw29	57615	23899	0.00 ± 4.9	30.10 ± 1.3	1.0	0.0	U	$(2.16) \times 10^{-3}$
ASASSN-15oi	00033999001–007, 00033999009–012	sw30	57277	24731	3779.63 ± 61.8	40.37 ± 1.5	0.0	1.0	D	$(1.70) \times 10^{-1}$
ASASSN-15oi	00033999013–027	sw31	57325	36428	22980.31 ± 152.4	237.69 ± 3.7	0.0	1.0	D	$(7.01) \times 10^{-1}$
css100217	00031681001	sw32	55293	3484	14.46 ± 4.5	5.54 ± 0.6	0.0	1.0	D	$(4.61 \pm 1.4) \times 10^{-3}$
css100217	00031681002–004	sw33	55326	10279	10.22 ± 4.8	11.78 ± 0.9	0.7	0.3	U	$(2.39) \times 10^{-3}$
css100217	00085568001– 006,00085568008	sw34	57114	4618	87.18 ± 10.2	15.82 ± 1.0	0.0	1.0	D	$(2.10 \pm 0.2) \times 10^{-2}$
D3-13	00080739003, 00080740003	sw35	56904	1266	3.00 ± 2.0	1.00 ± 0.3	0.3	0.7	U	$(3.52) \times 10^{-3}$
D3-13	00080740001–002, 00080741001	sw36	56797	3544	0.00 ± 1.6	6.12 ± 0.6	1.0	0.0	U	$(4.25) \times 10^{-3}$
D3-13	00080742001	sw37	56800	2248	0.00 ± 3.6	14.46 ± 1.0	1.0	0.0	U	$(1.28) \times 10^{-2}$
DES14C1kia	00033565001–011	sw38	57064	26332	0.00 ± 5.9	35.00 ± 1.5	1.0	0.0	U	$(2.23) \times 10^{-3}$
DES14C1kia	00033565012–016	sw39	57120	9030	0.00 ± 3.3	13.85 ± 1.0	1.0	0.0	U	$(3.08) \times 10^{-3}$
Dougie	00031338001–009	sw40	54874	18319	5.16 ± 4.7	15.84 ± 1.0	1.0	0.0	U	$(1.69) \times 10^{-3}$
Dougie	00031338010–011, 00049888001	sw41	55584	7444	0.00 ± 2.5	6.93 ± 0.7	1.0	0.0	U	$(2.21) \times 10^{-3}$
GRB060218, SN2006aj	00054610001–002	sw42	54508	7402	4.50 ± 3.1	4.50 ± 0.6	0.7	0.3	U	$(1.63) \times 10^{-3}$
GRB060218, SN2006aj	00054610004	sw43	55622	4630	3.78 ± 2.9	4.22 ± 0.5	0.8	0.2	U	$(2.49) \times 10^{-3}$
GRB060218, SN2006aj	00054610005	sw44	55744	3758	3.09 ± 2.5	2.91 ± 0.4	0.6	0.4	U	$(2.37) \times 10^{-3}$
GRB060218, SN2006aj	00054610006–007	sw45	56247	7941	2.79 ± 2.9	5.21 ± 0.6	1.0	0.0	U	$(1.69) \times 10^{-3}$

Table 8 — Continued

Name	ObsID	ObsID label ^a	MJD	Exposure time (s)	Source Counts ^b	Bkg Counts ^c	\mathcal{P}_{fluct}^d	\mathcal{D}^d	U or D ^e	Count Rate ^{f,g} (ct/s)
GRB060218, SN2006aj	00054610008	sw46	56551	4088	2.37 ± 2.3	2.63 ± 0.4	0.7	0.3	U	$(2.04) \times 10^{-3}$
GRB060218, SN2006aj	00054610009	sw47	56672	4750	0.00 ± 1.5	4.56 ± 0.6	1.0	0.0	U	$(2.56) \times 10^{-3}$
GRB060218, SN2006aj	00054610010	sw48	56871	3911	0.14 ± 1.5	1.86 ± 0.4	1.0	0.0	U	$(1.69) \times 10^{-3}$
GRB060218, SN2006aj	00054610011–015	sw49	56936	9542	2.68 ± 3.2	7.32 ± 0.7	1.0	0.0	U	$(1.80) \times 10^{-3}$
GRB060218, SN2006aj	00054610016– 017,00054610019	sw50	57331	3926	1.05 ± 1.8	1.95 ± 0.4	0.9	0.1	U	$(1.74) \times 10^{-3}$
GRB060218, SN2006aj	00191157000–021	sw51	53793	239159	1756.24 ± 44.0	169.77 ± 3.4	0.0	1.0	D	$(8.16 \pm 0.2) \times 10^{-3}$
GRB060218, SN2006aj	00191157025–042	sw52	53811	110873	5.31 ± 8.9	68.69 ± 2.2	1.0	0.0	U	$(9.38) \times 10^{-4}$
GRB060218, SN2006aj	00191157050–052	sw53	53942	11675	3.78 ± 3.4	7.23 ± 0.7	1.0	0.0	U	$(1.46) \times 10^{-3}$
GRB060218, SN2006aj	000191157053	sw54	55545	3449	0.06 ± 1.5	1.94 ± 0.4	1.0	0.0	U	$(1.97) \times 10^{-3}$
HLX-1	00031287001–004	sw55	54774	33319	385.80 ± 20.8	44.20 ± 1.8	0.0	1.0	D	$(1.29 \pm 0.1) \times 10^{-2}$
HLX-1	00031287005–010	sw56	55057	38119	578.04 ± 25.1	48.96 ± 1.9	0.0	1.0	D	$(1.68 \pm 0.1) \times 10^{-2}$
HLX-1	00031287011–014, 00031287016–021	sw57	55157	38740	533.42 ± 24.2	49.58 ± 1.9	0.0	1.0	D	$(1.53 \pm 0.1) \times 10^{-2}$
HLX-1	00031287022–034	sw58	55247	27428	154.78 ± 14.4	50.22 ± 1.9	0.0	1.0	D	$(2.90) \times 10^{-3}$
HLX-1	00031287035–043, 00031287045–047	sw59	55347	25552	7.87 ± 7.4	44.13 ± 1.8	1.0	0.0	U	$(2.79) \times 10^{-3}$
HLX-1	00031287048–062 00031287063–067, 00031287069–074, 00031287077–079,	sw60	55449	50615	985.58 ± 32.7	79.42 ± 2.4	0.0	1.0	D	$(2.16 \pm 0.1) \times 10^{-2}$
HLX-1	00031896001 00031287080–089, 00031287090–092 00031287093–109, 00031287111	sw61	55544	112603	534.40 ± 24.8	77.61 ± 2.3	0.0	1.0	D	$(5.27 \pm 0.2) \times 10^{-3}$
HLX-1	00031287112–170 00031287172–174, 00031287176–179, 00031287181–185, 00031287187–191	sw62	55646	25752	19.82 ± 7.9	40.18 ± 1.7	1.0	0.0	U	$(2.55) \times 10^{-3}$
HLX-1	00031287192–202 00031287203–220, 00031287223–243, 00031287245–246, 00031287248–252, 00031287254–255	sw63	55771	26976	322.35 ± 19.7	62.65 ± 2.1	0.0	1.0	D	$(1.33 \pm 0.1) \times 10^{-2}$
HLX-1	00032577001–022, 00080013001	sw64	55847	83165	1114.74 ± 36.9	232.26 ± 4.0	0.0	1.0	D	$(1.49) \times 10^{-2}$
HLX-1	00032577023–029	sw65	55932	21216	30.70 ± 10.3	71.30 ± 2.2	1.0	0.0	U	$(5.06) \times 10^{-3}$
HLX-1	00032577070–075 00032577077–080	sw66	56053	24621	13.62 ± 6.9	32.38 ± 1.5	1.0	0.0	U	$(2.23) \times 10^{-3}$
HLX-1	00032577081–097 00032577098–099	sw67	56153	47379	365.36 ± 21.1	75.64 ± 2.3	0.0	1.0	D	$(8.57 \pm 0.5) \times 10^{-3}$
HLX-1	00049794001–004 00091907001–006 00091907007–013 00091907014–026 00091907027–037 00092116001–010 00092116011–018, 00092116020–021 00092116022–025	sw68	56245	23255	166.96 ± 14.3	36.04 ± 1.6	0.0	1.0	D	$(7.98 \pm 0.7) \times 10^{-3}$
HLX-1	00032577003	sw69	56463	15456	18.11 ± 6.1	17.89 ± 1.1	0.5	0.5	U	$(2.20) \times 10^{-3}$
HLX-1	00032577030–049	sw70	56552	42586	391.88 ± 21.5	65.12 ± 2.1	0.0	1.0	D	$(1.02 \pm 0.1) \times 10^{-2}$
HLX-1	00032577050–068	sw71	56649	48937	200.36 ± 16.8	75.64 ± 2.3	0.0	1.0	D	$(4.55 \pm 0.4) \times 10^{-3}$
HLX-1	00032577070–075	sw72	56722	17359	0.00 ± 7.4	71.60 ± 2.2	1.0	0.0	U	$(6.21) \times 10^{-3}$
HLX-1	00032577077–080	sw73	56991	5644	7.11 ± 4.1	8.89 ± 0.8	0.8	0.2	U	$(3.51) \times 10^{-3}$
HLX-1	00032577081–097	sw74	57083	29273	345.32 ± 20.7	78.68 ± 2.4	0.0	1.0	D	$(1.31 \pm 0.1) \times 10^{-2}$
HLX-1	00032577098–099	sw75	57112	3816	10.33 ± 4.0	5.67 ± 0.6	0.1	0.9	U	$(3.73) \times 10^{-3}$
HLX-1	00049794001–004	sw76	56368	12804	17.01 ± 5.1	7.99 ± 0.7	0.0	1.0	D	$(1.43 \pm 0.4) \times 10^{-3}$
HLX-1	00091907001–006	sw77	56776	10966	0.00 ± 4.3	18.92 ± 1.2	1.0	0.0	U	$(3.24) \times 10^{-3}$
HLX-1	00091907007–013	sw78	56849	19459	12.69 ± 6.2	24.31 ± 1.3	1.0	0.0	U	$(2.23) \times 10^{-3}$
HLX-1	00091907014–026	sw79	56953	26119	27.05 ± 8.7	44.95 ± 1.8	1.0	0.0	U	$(2.77) \times 10^{-3}$
HLX-1	00091907027–037	sw80	57038	19574	173.02 ± 14.2	27.98 ± 1.4	0.0	1.0	D	$(9.82 \pm 0.8) \times 10^{-3}$
HLX-1	00092116001–010	sw81	57159	24638	15.71 ± 7.4	36.29 ± 1.6	1.0	0.0	U	$(2.45) \times 10^{-3}$
HLX-1	00092116011–018, 00092116020–021 00092116022–025	sw82	57248	26758	23.52 ± 8.0	37.48 ± 1.6	1.0	0.0	U	$(2.32) \times 10^{-3}$
HLX-1	00037507001	sw83	57322	10481	0.77 ± 4.3	16.23 ± 1.1	1.0	0.0	U	$(3.00) \times 10^{-3}$
IC 3599	00037507003	sw84	55252	2120	318.39 ± 18.0	4.61 ± 0.5	0.0	1.0	D	$(1.67 \pm 0.1) \times 10^{-1}$
IC 3599	00037507004	sw85	55333	1234	88.44 ± 9.5	1.56 ± 0.3	0.0	1.0	D	$(7.97 \pm 0.9) \times 10^{-2}$
IC 3599	00037507005	sw86	56595	4780	16.08 ± 4.8	6.92 ± 0.7	0.0	1.0	D	$(3.44 \pm 1.1) \times 10^{-3}$
IC 3599	00037507006	sw87	56602	4832	9.36 ± 3.8	4.64 ± 0.5	0.0	1.0	D	$(2.55 \pm 0.9) \times 10^{-3}$
IC 3599	00037569001	sw88	56742	4644	12.25 ± 4.3	5.76 ± 0.6	0.0	1.0	D	$(3.10 \pm 1.0) \times 10^{-3}$
IC 3599	00037569002–003	sw89	56877	1606	2.69 ± 2.0	1.31 ± 0.3	0.4	0.6	U	$(3.29) \times 10^{-3}$
IC 3599	00037569004	sw90	56980	4967	14.87 ± 4.6	6.13 ± 0.6	0.0	1.0	D	$(3.03 \pm 1.0) \times 10^{-3}$
IC 3599	00037569005–010, 00037569012	sw91	57111	2829	2.24 ± 2.9	5.76 ± 0.6	1.0	0.0	U	$(5.09) \times 10^{-3}$
IC 3599	00037569013	sw92	57225	400574	3.43 ± 2.5	2.57 ± 0.4	0.5	0.5	U	$(2.05) \times 10^{-5}$
IC 3599	00031911001–002	sw93	57327	4697	6.82 ± 3.5	5.18 ± 0.6	0.4	0.6	U	$(2.84) \times 10^{-3}$
IGR J12580	00031911003	sw94	55574	5127	2305.50 ± 48.3	29.50 ± 1.4	0.0	1.0	D	$(5.00 \pm 0.1) \times 10^{-1}$
IGR J12580	00032072001–009	sw95	56107	3359	9.27 ± 3.6	3.73 ± 0.5	0.0	1.0	D	$(3.15 \pm 1.2) \times 10^{-3}$
IGR J17361–4441	00032072010–018, 00032072020–033	sw96	55794	23477	12270.69 ± 111.6	176.31 ± 3.4	0.0	1.0	D	$(5.81 \pm 0.1) \times 10^{-1}$
IGR J17361–4441		sw97	55830	59660	14405.91 ± 121.1	232.09 ± 3.9	0.0	1.0	D	$(2.68) \times 10^{-1}$

Table 8 — Continued

Name	ObsID	ObsID label ^a	MJD	Exposure time (s)	Source Counts ^b	Bkg Counts ^c	\mathcal{P}_{fluct}^d	\mathcal{D}^d	U or D ^e	Count Rate ^{f,g} (ct/s)
IGR J17361-4441	00032072034-038	sw98	55979	16509	258.06 ± 17.3	38.94 ± 1.6	0.0	1.0	D	$(1.74 \pm 0.1) \times 10^{-2}$
IGR J17361-4441	00090434001	sw99	55328	1828	22.26 ± 5.1	3.74 ± 0.5	0.0	1.0	D	$(5.80 \pm 3.1) \times 10^{-3}$
IGR J17361-4441	00091446001-003	sw100	56087	2889	27.76 ± 6.4	12.24 ± 0.9	0.0	1.0	D	$(8.74 \pm 2.5) \times 10^{-3}$
IGR J17361-4441	00091446004-010, 00091446012-017	sw101	56139	11852	184.15 ± 14.8	31.85 ± 1.5	0.0	1.0	D	$(1.73 \pm 0.1) \times 10^{-2}$
iPTF16fnl	00034706001-003, 00034706005-024	sw102	57657	37227	0.00 ± 7.9	66.13 ± 1.9	1.0	0.0	U	$(2.70) \times 10^{-3}$
iPTF16fnl	00034706025-028	sw103	57719	9327	3.28 ± 2.8	10.73 ± 0.8	1.0	0.0	U	$(2.45) \times 10^{-3}$
NGC 1097	00036582001	sw104	54314	2745	154.41 ± 12.7	7.59 ± 0.7	0.0	1.0	D	$(6.25 \pm 0.5) \times 10^{-2}$
NGC 1097	00036582002	sw105	54450	3396	302.86 ± 17.6	6.14 ± 0.6	0.0	1.0	D	$(9.91 \pm 0.6) \times 10^{-2}$
NGC 1097	00045597001	sw106	55779	3034	264.95 ± 16.5	7.05 ± 0.7	0.0	1.0	D	$(9.70 \pm 0.6) \times 10^{-2}$
NGC 1097	00045597002-004	sw107	55830	5296	374.48 ± 20.1	28.52 ± 1.4	0.0	1.0	D	$(7.86 \pm 0.4) \times 10^{-2}$
NGC 1097	00045597005-007	sw108	56008	5432	409.40 ± 20.6	12.60 ± 0.9	0.0	1.0	D	$(8.37 \pm 0.4) \times 10^{-2}$
NGC 1097	00045597008-023	sw109	56165	14107	1161.23 ± 34.6	31.77 ± 1.5	0.0	1.0	D	$(9.15 \pm 0.3) \times 10^{-2}$
NGC 1097	00045597025-034, 00045597036-037, 00045597039-049	sw110	56251	22945	1406.89 ± 38.3	56.11 ± 1.9	0.0	1.0	D	$(6.81 \pm 0.2) \times 10^{-2}$
NGC 1097	00045597050-055, 00551030000	sw111	56320	6713	386.52 ± 20.0	13.48 ± 0.9	0.0	1.0	D	$(6.40 \pm 0.3) \times 10^{-2}$
NGC 2110	00035459001-003	sw112	53831	19842	12284.48 ± 111.6	153.52 ± 3.2	0.0	1.0	D	$(6.88 \pm 0.1) \times 10^{-1}$
NGC 2110	00035459004	sw113	54709	2233	1062.65 ± 32.8	11.36 ± 0.9	0.0	1.0	D	$(5.29 \pm 0.2) \times 10^{-1}$
NGC 2110	00035459005	sw114	55116	3574	2638.09 ± 51.7	30.91 ± 1.4	0.0	1.0	D	$(8.20 \pm 0.2) \times 10^{-1}$
NGC 2110	00035459006, 00080364002	sw115	56332	15064	14834.92 ± 122.7	198.08 ± 3.6	0.0	1.0	D	$(1.09) \times 10^0$
NGC 2110	00035459008	sw116	56512	8214	3335.05 ± 58.1	36.95 ± 1.6	0.0	1.0	D	$(4.51 \pm 0.1) \times 10^{-1}$
NGC 2110	00080364001	sw117	56206	7107	7234.64 ± 85.7	106.37 ± 2.7	0.0	1.0	D	$(1.13) \times 10^0$
NGC247	00033469001-009	sw118	56971	19069	222.56 ± 16.5	47.44 ± 1.8	0.0	1.0	D	$(1.30 \pm 0.1) \times 10^{-2}$
NGC247	00033469010-018	sw119	57034	16754	49.57 ± 8.9	28.43 ± 1.4	0.0	1.0	D	$(2.95 \pm 0.6) \times 10^{-3}$
NGC247	00033469019-022	sw120	57164	7076	0.00 ± 3.3	10.40 ± 0.9	1.0	0.0	U	$(3.15) \times 10^{-3}$
NGC247	00033469023-026	sw121	57256	5846	1.03 ± 3.1	7.97 ± 0.8	1.0	0.0	U	$(3.12) \times 10^{-3}$
NGC247	00033469027	sw122	57314	2058	0.00 ± 1.1	3.45 ± 0.5	1.0	0.0	U	$(4.87) \times 10^{-3}$
NGC247	00082125001	sw123	56695	717	1.51 ± 1.4	0.50 ± 0.2	0.4	0.6	U	$(4.04) \times 10^{-3}$
NGC247	00082125002-006	sw124	57159	2660	1.18 ± 2.0	2.82 ± 0.4	0.9	0.1	U	$(3.29) \times 10^{-3}$
NGC 3599	00035745001	sw125	54070	5699	27.53 ± 5.8	5.48 ± 0.6	0.0	1.0	U	$(2.44) \times 10^{-3}$
NGC 3599	00040331001	sw126	55492	946	3.07 ± 2.0	0.93 ± 0.3	0.1	0.9	U	$(4.50) \times 10^{-3}$
NGC 3599	00040331002	sw127	55517	1636	3.20 ± 2.3	1.80 ± 0.3	0.3	0.7	U	$(3.95) \times 10^{-3}$
NGC 3599	00084368001	sw128	56855	1998	4.53 ± 2.7	2.47 ± 0.4	0.2	0.8	U	$(4.00) \times 10^{-3}$
NGC 3599	00084368002	sw129	56952	3940	7.34 ± 3.4	3.66 ± 0.5	0.1	0.9	U	$(2.65) \times 10^{-3}$
NGC 3599	00084368003	sw130	57138	397	0.67 ± 1.4	1.33 ± 0.3	1.0	0.0	U	$(1.34) \times 10^{-2}$
NGC 3599	00084368005	sw131	57216	872	1.13 ± 1.4	0.87 ± 0.2	0.6	0.4	U	$(4.67) \times 10^{-3}$
NGC 3599	00084368006-007	sw132	57324	3256	1.81 ± 2.0	2.20 ± 0.4	0.9	0.1	U	$(2.27) \times 10^{-3}$
OGLE16aaa	00034281020	sw133	57561	1960	31.54 ± 5.8	2.46 ± 0.4	0.0	1.0	D	$(1.79 \pm 0.3) \times 10^{-2}$
OGLE16aaa	00034281021	sw134	57709	1666	1.46 ± 2.0	2.54 ± 0.4	0.9	0.1	U	$(4.88) \times 10^{-3}$
OGLE16aaa	00031681002-004 00085568001-006, 00085568008	sw135	57436	25537	0.00 ± 6.0	42.21 ± 1.7	1.0	0.0	U	$(2.68) \times 10^{-3}$
OGLE16aaa	00041515001-002	sw136	57548	6026	21.48 ± 5.5	8.52 ± 0.8	0.0	1.0	D	$(3.96 \pm 1.0) \times 10^{-3}$
Pictor A	00049664001	sw137	55501	4623	2556.49 ± 50.9	31.51 ± 1.5	0.0	1.0	D	$(6.15 \pm 0.1) \times 10^{-1}$
Pictor A	00033154001-007, 00033154009	sw138	57323	1865	419.95 ± 20.7	8.05 ± 0.7	0.0	1.0	D	$(2.50 \pm 0.1) \times 10^{-1}$
PTF-09axc	00033154001-007, 00033154009	sw139	56739	2977	21.53 ± 5.1	4.47 ± 0.6	0.0	1.0	D	$(8.03 \pm 1.9) \times 10^{-3}$
PTF-09axc	00033154010	sw140	57098	1638	4.01 ± 2.7	3.00 ± 0.5	0.4	0.6	U	$(5.55) \times 10^{-3}$
PTF-09djl	00033155001, 00033155003-007	sw141	56722	3401	0.00 ± 2.3	5.14 ± 0.6	1.0	0.0	U	$(3.90) \times 10^{-3}$
PTF-09ge	00033153001-002	sw142	56725	2595	3.00 ± 2.3	2.00 ± 0.4	0.3	0.7	U	$(2.67) \times 10^{-3}$
PTF-10iya	00031737001	sw143	55359	2919	43.67 ± 6.8	2.33 ± 0.4	0.0	1.0	D	$(1.66 \pm 0.3) \times 10^{-2}$
PTF-10iya	00031737002	sw144	55419	5836	0.00 ± 2.1	5.91 ± 0.6	1.0	0.0	U	$(2.51) \times 10^{-3}$
PTF-10iya	00082074005-008	sw145	55807	7270	0.00 ± 2.1	6.20 ± 0.6	1.0	0.0	U	$(2.09) \times 10^{-3}$
PTF-10iya	00092116001-010	sw146	55795	2260	0.61 ± 1.8	2.39 ± 0.4	1.0	0.0	U	$(3.46) \times 10^{-3}$
PTF-11glr	00032056001	sw147	55785	3940	1.14 ± 2.5	4.87 ± 0.6	1.0	0.0	U	$(3.24) \times 10^{-3}$
SDSS J0939	00035747001	sw148	54365	6520	121.93 ± 11.4	7.07 ± 0.7	0.0	1.0	D	$(2.08 \pm 0.2) \times 10^{-2}$
SDSS J0939	00040325001-002	sw149	55671	1826	73.07 ± 8.7	1.94 ± 0.4	0.0	1.0	D	$(4.45 \pm 0.5) \times 10^{-2}$
SDSS J0952	00092115001-002, 00092115004-008	sw150	57139	9829	11.60 ± 7.2	37.40 ± 1.6	1.0	0.0	U	$(6.30) \times 10^{-3}$
SDSS J1201	00031743001-005	sw151	55384	15616	156.91 ± 13.2	17.10 ± 1.1	0.0	1.0	D	$(1.12 \pm 0.1) \times 10^{-2}$
SDSS J1201	00031743006-007	sw152	55448	3693	7.68 ± 3.4	3.32 ± 0.5	0.1	0.9	U	$(2.65) \times 10^{-3}$
SDSS J1201	00031743008-010	sw153	55653	7869	0.37 ± 3.6	11.63 ± 0.9	1.0	0.0	U	$(3.09) \times 10^{-3}$
SDSS J1241	00037504001-002	sw154	54603	20388	26.21 ± 6.5	14.79 ± 1.0	0.0	1.0	D	$(1.43 \pm 0.4) \times 10^{-3}$

Table 8 — Continued

Name	ObsID	ObsID label ^a	MJD	Exposure time (s)	Source Counts ^b	Bkg Counts ^c	\mathcal{P}_{fluct}^d	\mathcal{D}^d	U or D ^e	Count Rate ^{f,g} (ct/s)
SDSS J1323	00020310001, 00020311001, 00020315001, 00020316001	sw155	56595	3634	0.94 ± 1.8	2.06 ± 0.4	1.0	0.0	U	$(1.95) \times 10^{-3}$
SDSS J1323	00035749001	sw156	54112	75	0.00 ± 0.1	0.20 ± 0.1	1.0	0.0	U	$(2.29) \times 10^{-2}$
SDSS J1323	00035749002	sw157	54238	1900	0.60 ± 1.8	2.40 ± 0.4	1.0	0.0	U	$(4.12) \times 10^{-3}$
SDSS J1323	00040336001	sw158	55596	1798	1.40 ± 1.8	1.60 ± 0.3	0.8	0.2	U	$(3.34) \times 10^{-3}$
SDSS J1342	00090102001–003	sw159	54969	16582	35.30 ± 7.2	15.70 ± 1.0	0.0	1.0	D	$(2.37 \pm 0.5) \times 10^{-3}$
SDSS J1350	00082074001–003	sw160	56512	2647	0.00 ± 1.8	4.47 ± 0.5	1.0	0.0	U	$(4.54) \times 10^{-3}$
SDSS J1350	00082074005–008	sw161	57261	14322	0.81 ± 4.8	21.19 ± 1.2	1.0	0.0	U	$(2.72) \times 10^{-3}$
Swift J1112.2–8238	00032025001–012 00031955002–013, 00031955032–033, 00031955041–052 00031955053, 00031955055–080, 00031955082–088, 00031955090–094, 00031955096–102, 00031955104–141, 00031955143–151, 00031955153 00031955154–157, 00031955159–172, 00031955174–206, 00031955209–253 00031955254–255, 00032200001–034, 00032200036–067, 00032200069–089, 00032200092–096 00032200097–134, 00032200136–161, 00032200163–174, 00032200176–189 00032200190–208, 00032200210–237, 00032526001–003, 00032526005–045 00032526046–070, 00032526072–116, 00032526118–127, 00032526129–130	sw162	55923	36351	2227.22 ± 48.2	93.78 ± 2.5	0.0	1.0	D	$(6.81 \pm 0.1) \times 10^{-2}$
Swift J1644+57	00031955032–033, 00031955041–052 00031955053, 00031955055–080, 00031955082–088, 00031955090–094, 00031955096–102, 00031955104–141, 00031955143–151, 00031955153 00031955154–157, 00031955159–172, 00031955174–206, 00031955209–253 00031955254–255, 00032200001–034, 00032200036–067, 00032200069–089, 00032200092–096 00032200097–134, 00032200136–161, 00032200163–174, 00032200176–189 00032200190–208, 00032200210–237, 00032526001–003, 00032526005–045 00032526046–070, 00032526072–116, 00032526118–127, 00032526129–130	sw163	55676	316984	194478.95 ± 444.0	2505.05 ± 12.9	0.0	1.0	D	$(6.82) \times 10^{-1}$
Swift J1644+57	00031955090–094, 00031955096–102, 00031955104–141, 00031955143–151, 00031955153 00031955154–157, 00031955159–172, 00031955174–206, 00031955209–253 00031955254–255, 00032200001–034, 00032200036–067, 00032200069–089, 00032200092–096 00032200097–134, 00032200136–161, 00032200163–174, 00032200176–189 00032200190–208, 00032200210–237, 00032526001–003, 00032526005–045 00032526046–070, 00032526072–116, 00032526118–127, 00032526129–130	sw164	55749	626119	57250.49 ± 241.8	1151.51 ± 8.8	0.0	1.0	D	$(1.02) \times 10^{-1}$
Swift J1644+57	00031955154–157, 00031955159–172, 00031955174–206, 00031955209–253 00031955254–255, 00032200001–034, 00032200036–067, 00032200069–089, 00032200092–096 00032200097–134, 00032200136–161, 00032200163–174, 00032200176–189 00032200190–208, 00032200210–237, 00032526001–003, 00032526005–045 00032526046–070, 00032526072–116, 00032526118–127, 00032526129–130	sw165	55850	286775	9352.17 ± 99.2	463.83 ± 5.6	0.0	1.0	D	$(3.62) \times 10^{-2}$
Swift J1644+57	00031955154–157, 00031955159–172, 00031955174–206, 00031955209–253 00031955254–255, 00032200001–034, 00032200036–067, 00032200069–089, 00032200092–096 00032200097–134, 00032200136–161, 00032200163–174, 00032200176–189 00032200190–208, 00032200210–237, 00032526001–003, 00032526005–045 00032526046–070, 00032526072–116, 00032526118–127, 00032526129–130	sw166	55948	248320	5046.17 ± 73.0	258.83 ± 4.1	0.0	1.0	D	$(2.26) \times 10^{-2}$
Swift J1644+57	00031955154–157, 00031955159–172, 00031955174–206, 00031955209–253 00031955254–255, 00032200001–034, 00032200036–067, 00032200069–089, 00032200092–096 00032200097–134, 00032200136–161, 00032200163–174, 00032200176–189 00032200190–208, 00032200210–237, 00032526001–003, 00032526005–045 00032526046–070, 00032526072–116, 00032526118–127, 00032526129–130	sw167	56048	126356	1391.51 ± 38.9	113.49 ± 2.8	0.0	1.0	D	$(1.22) \times 10^{-2}$
Swift J1644+57	00031955154–157, 00031955159–172, 00031955174–206, 00031955209–253 00031955254–255, 00032200001–034, 00032200036–067, 00032200069–089, 00032200092–096 00032200097–134, 00032200136–161, 00032200163–174, 00032200176–189 00032200190–208, 00032200210–237, 00032526001–003, 00032526005–045 00032526046–070, 00032526072–116, 00032526118–127, 00032526129–130	sw168	56154	141042	381.79 ± 22.3	110.21 ± 2.7	0.0	1.0	D	$(3.01 \pm 0.2) \times 10^{-3}$
Swift J1644+57	00031955154–157, 00031955159–172, 00031955174–206, 00031955209–253 00031955254–255, 00032200001–034, 00032200036–067, 00032200069–089, 00032200092–096 00032200097–134, 00032200136–161, 00032200163–174, 00032200176–189 00032200190–208, 00032200210–237, 00032526001–003, 00032526005–045 00032526046–070, 00032526072–116, 00032526118–127, 00032526129–130	sw169	56243	78561	6.50 ± 8.7	65.50 ± 2.1	1.0	0.0	U	$(1.27) \times 10^{-3}$
Swift J1644+57	00031955154–157, 00031955159–172, 00031955174–206, 00031955209–253 00031955254–255, 00032200001–034, 00032200036–067, 00032200069–089, 00032200092–096 00032200097–134, 00032200136–161, 00032200163–174, 00032200176–189 00032200190–208, 00032200210–237, 00032526001–003, 00032526005–045 00032526046–070, 00032526072–116, 00032526118–127, 00032526129–130	sw170	56336	26746	4.87 ± 5.4	23.13 ± 1.2	1.0	0.0	U	$(1.56) \times 10^{-3}$
Swift J1644+57	00031955154–157, 00031955159–172, 00031955174–206, 00031955209–253 00031955254–255, 00032200001–034, 00032200036–067, 00032200069–089, 00032200092–096 00032200097–134, 00032200136–161, 00032200163–174, 00032200176–189 00032200190–208, 00032200210–237, 00032526001–003, 00032526005–045 00032526046–070, 00032526072–116, 00032526118–127, 00032526129–130	sw171	56457	18460	-2.58 ± 3.9	16.58 ± 1.1	1.0	0.0	U	$(1.73) \times 10^{-3}$
Swift J1644+57	00031955154–157, 00031955159–172, 00031955174–206, 00031955209–253 00031955254–255, 00032200001–034, 00032200036–067, 00032200069–089, 00032200092–096 00032200097–134, 00032200136–161, 00032200163–174, 00032200176–189 00032200190–208, 00032200210–237, 00032526001–003, 00032526005–045 00032526046–070, 00032526072–116, 00032526118–127, 00032526129–130	sw172	56552	21731	8.49 ± 5.8	23.51 ± 1.3	1.0	0.0	U	$(1.95) \times 10^{-3}$
Swift J1644+57	00031955154–157, 00031955159–172, 00031955174–206, 00031955209–253 00031955254–255, 00032200001–034, 00032200036–067, 00032200069–089, 00032200092–096 00032200097–134, 00032200136–161, 00032200163–174, 00032200176–189 00032200190–208, 00032200210–237, 00032526001–003, 00032526005–045 00032526046–070, 00032526072–116, 00032526118–127, 00032526129–130	sw173	56649	22626	0.00 ± 4.9	23.33 ± 1.2	1.0	0.0	U	$(1.86) \times 10^{-3}$
Swift J1644+57	00031955154–157, 00031955159–172, 00031955174–206, 00031955209–253 00031955254–255, 00032200001–034, 00032200036–067, 00032200069–089, 00032200092–096 00032200097–134, 00032200136–161, 00032200163–174, 00032200176–189 00032200190–208, 00032200210–237, 00032526001–003, 00032526005–045 00032526046–070, 00032526072–116, 00032526118–127, 00032526129–130	sw174	56751	21085	-8.75 ± 4.2	24.75 ± 1.3	1.0	0.0	U	$(2.09) \times 10^{-3}$
Swift J1644+57	00031955154–157, 00031955159–172, 00031955174–206, 00031955209–253 00031955254–255, 00032200001–034, 00032200036–067, 00032200069–089, 00032200092–096 00032200097–134, 00032200136–161, 00032200163–174, 00032200176–189 00032200190–208, 00032200210–237, 00032526001–003, 00032526005–045 00032526046–070, 00032526072–116, 00032526118–127, 00032526129–130	sw175	56848	23175	7.20 ± 5.9	25.80 ± 1.3	1.0	0.0	U	$(1.97) \times 10^{-3}$
Swift J1644+57	00031955154–157, 00031955159–172, 00031955174–206, 00031955209–253 00031955254–255, 00032200001–034, 00032200036–067, 00032200069–089, 00032200092–096 00032200097–134, 00032200136–161, 00032200163–174, 00032200176–189 00032200190–208, 00032200210–237, 00032526001–003, 00032526005–045 00032526046–070, 00032526072–116, 00032526118–127, 00032526129–130	sw176	56945	23240	8.66 ± 6.1	26.34 ± 1.3	1.0	0.0	U	$(2.00) \times 10^{-3}$
Swift J1644+57	00031955154–157, 00031955159–172, 00031955174–206, 00031955209–253 00031955254–255, 00032200001–034, 00032200036–067, 00032200069–089, 00032200092–096 00032200097–134, 00032200136–161, 00032200163–174, 00032200176–189 00032200190–208, 00032200210–237, 00032526001–003, 00032526005–045 00032526046–070, 00032526072–116, 00032526118–127, 00032526129–130	sw177	57049	24767	-3.68 ± 4.6	23.68 ± 1.3	1.0	0.0	U	$(1.72) \times 10^{-3}$
Swift J1644+57	00031955154–157, 00031955159–172, 00031955174–206, 00031955209–253 00031955254–255, 00032200001–034, 00032200036–067, 00032200069–089, 00032200092–096 00032200097–134, 00032200136–161, 00032200163–174, 00032200176–189 00032200190–208, 00032200210–237, 00032526001–003, 00032526005–045 00032526046–070, 00032526072–116, 00032526118–127, 00032526129–130	sw178	57151	24526	-7.58 ± 4.4	25.58 ± 1.3	1.0	0.0	U	$(1.85) \times 10^{-3}$
Swift J1644+57	00031955154–157, 00031955159–172, 00031955174–206, 00031955209–253 00031955254–255, 00032200001–034, 00032200036–067, 00032200069–089, 00032200092–096 00032200097–134, 00032200136–161, 00032200163–174, 00032200176–189 00032200190–208, 00032200210–237, 00032526001–003, 00032526005–045 00032526046–070, 00032526072–116, 00032526118–127, 00032526129–130	sw179	57254	18041	0.00 ± 5.0	25.74 ± 1.3	1.0	0.0	U	$(2.52) \times 10^{-3}$
Swift J1644+57	00031955154–157, 00031955159–172, 00031955174–206, 00031955209–253 00031955254–255, 00032200001–034, 00032200036–067, 00032200069–089, 00032200092–096 00032200097–134, 00032200136–161, 00032200163–174, 00032200176–189 00032200190–208, 00032200210–237, 00032526001–003, 00032526005–045 00032526046–070, 00032526072–116, 00032526118–127, 00032526129–130	sw180	57318	7012	5.01 ± 3.5	6.99 ± 0.7	0.8	0.2	U	$(2.36) \times 10^{-3}$
Swift J1644+57	00031955154–157, 00031955159–172, 00031955174–206, 00031955209–253 00031955254–255, 00032200001–034, 00032200036–067, 00032200069–089, 00032200092–096 00032200097–134, 00032200136–161, 00032200163–174, 00032200176–189 00032200190–208, 00032200210–237, 00032526001–003, 00032526005–045 00032526046–070, 00032526072–116, 00032526118–127, 00032526129–130	sw181	55650	49896	47070.73 ± 218.7	714.27 ± 6.9	0.0	1.0	D	$(1.05) \times 10^0$
Swift J2058+05	00032004001	sw182	55709	2952	2654.75 ± 51.8	30.25 ± 1.4	0.0	1.0	D	$(9.99 \pm 0.2) \times 10^{-1}$
Swift J2058+05	00032004011–012	sw183	56127	8965	15.88 ± 5.1	9.12 ± 0.8	0.0	1.0	D	$(2.25 \pm 0.6) \times 10^{-3}$
Swift J2058+05	00032026003–011	sw184	55774	20306	442.62 ± 21.7	26.38 ± 1.3	0.			

Table 8 — *Continued*

Name	ObsID	ObsID label ^a	MJD	Exposure time (s)	Source Counts ^b	Bkg Counts ^c	\mathcal{P}_{fluct}^d	\mathcal{D}^d	U or D ^e	Count Rate ^{f,g} (ct/s)
XMMSL1 J0740-85	00033229015	sw191	57286	1473	0.94 ± 1.8	2.07 ± 0.4	1.0	0.0	U	$(4.81) \times 10^{-3}$

Note. — All uncertainties correspond to the 90% confidence level and observations that have similar MJD are combined.

^a Due to the large number of observations used in this analysis, we have listed a label for which we can reference in other Tables which observation ID (ObsID) we are referring to.

^b Obtained from a 50 arcsecond circular region surrounding the position of the TDE candidate. These values listed have **not** been corrected for encircled energy fraction. The exception to this is for TDE candidate *Wings* as discussed in Appendix A.61

^c Obtained from a 200 arcsecond circular region surrounding the position of the TDE which has been scaled such that the equivalent 50 arcsecond background count rate is presented. These values listed have **not** been corrected for encircled energy fraction. The exception to this is for TDE candidate *Wings* as discussed in Appendix A.61

^d Calculated assuming Poisson statistics

^e Here U indicates an upperlimit, while D corresponds to a data point as classified using Poisson statistics (see previous two columns).

^f The count rate **has** been corrected for encircled energy fraction.

^g Values which do not have any uncertainties are upperlimits. These upperlimits are derived assuming that we would detect a signal if it is 3σ above background.

Table 9

The soft, medium and hard counts derived for the TDE candidates which have *ROSAT* pointed and RASS observations overlapping the position of the event.

Name	ObsID label	Soft Counts 0.3-1.0 keV	Medium Counts 1.0-2.0 keV	Hard Counts 2.0-10.0keV
2MASXJ0203	r1	4.31	2.96	0.84
2MASX J0249	r2	4.51	0.99	1.00
3XMM J152130.7+074916	r3	178.38	85.86	7.82
3XMM J152130.7+074916	r4	10.93	4.90	1.54
ASASSN-14ae	r5	4.31	2.14	1.00
ASASSN-14li	r6	6.52	3.44	1.00
ASASSN-15lh	r7	5.82	2.05	1.00
ASASSN-15oi	r8	10.65	1.81	1.00
css100217	r9	8.60	2.43	0.99
D1-9	r10	2.43	1.81	1.00
D23H-1	r11	6.00	2.96	1.00
D3-13	r12	8.60	3.20	1.00
DES14C1kia	r13	31.53	12.58	4.17
DES14C1kia	r14	15.70	6.00	1.54
DES14C1kia	r15	8.90	3.67	1.23
DES14C1kia	r16	2.43	0.99	1.00
GRB060218, SN2006aj	r17	4.71	1.44	0.84
HLX-1	r18	171.47	87.16	5.45
IC 3599	r19	305.58 ± 23.2	41.47	5.72
IC 3599	r20	677.06 ± 29.6	52.79 ± 8.3	1.00
IGR J12580	r21	4.71	2.14	1.00
IGR J17361-4441	r22	228.05	119.22 ± 15.5	8.57
iPTF16fml	r23	5.07	0.96	1.00
LEDA 095953	r24	695.26	724.16	46.26
NGC 1097	r25	1182.66 ± 38.0	876.55 ± 32.3	38.00 ± 6.3
NGC 2110	r26	5.28	6.12 ± 2.9	0.84
NGC247	r27	116.15	44.16	5.17
NGC247	r28	9.36	3.94	1.00
NGC 3599	r29	112.08	31.54	5.10
NGC 5905	r30	55.33	19.99 ± 3.2	4.98
NGC 5905	r31	85.39	18.30	2.95
NGC 5905	r32	70.98 ± 9.7	6.41	1.75
OGLE16aaa	r33	3.20	2.14	1.00
PGC1185375	r34	71.41	21.29	2.30
PGC1185375	r35	9.64	3.44	1.00
PGC 1190358	r36	41.82	16.46	1.23
PGC 1190358	r37	57.42	21.76	2.92
Pictor A	r38	1979.45 ± 48.9	1671.76 ± 44.6	70.80 ± 8.5
PS1-10jh	r39	35.72	10.08	1.54
PS1-11af	r40	6.00	2.70	1.00
PTF-09axc	r41	10.22	3.67	0.84
PTF-09djl	r42	12.85	3.20	1.23
PTF-09ge	r43	11.63	4.71	0.84
PTF-10iam	r44	30.44	11.90	2.06
PTF-10iam	r45	13.51	5.64	0.84
PTF-10iya	r46	9.64	4.31	0.84
PTF-10nuj	r47	55.62	16.46	4.00
PTF-10nuj	r48	28.91	6.85	0.84
PTF-10nuj	r49	10.22	3.44	0.84
PTF-11glr	r50	7.98	3.44	1.00
RBS 1032	r51	114.67 ± 12.1	6.52	1.82
RBS 1032	r52	121.96 ± 12.5	8.44	1.00
RBS 1032	r53	26.82 ± 5.9	2.96	1.00
RX J1242-11A	r54	319.69 ± 22.9	51.42	4.49
RX J1242-11A	r55	13.64	5.82	1.23
RX J1420+53	r56	66.86	19.15	4.33
RX J1420+53	r57	38.74 ± 7.3	3.44	1.00
RX J1624+75	r58	32.40	8.45	1.82
RX J1624+75	r59	206.35 ± 16.2	43.06 ± 7.5	0.84
SDSS J0159	r60	48.24 ± 9.2	17.69	2.30
SDSS J0159	r61	6.00	4.10	1.23
SDSS J0748	r62	3.44	1.44	1.00
SDSS J0938	r63	7.98	6.00	1.00
SDSS J0939	r64	6.35	2.70	1.23
SDSS J0952	r65	6.00	1.81	0.84
SDSS J1011	r66	144.82	33.70	8.07
SDSS J1011	r67	6.00	1.44	1.00
SDSS J1055	r68	180.64	55.62	5.39
SDSS J1055	r69	328.08	72.19	7.05
SDSS J1055	r70	182.16	36.58	4.64
SDSS J1055	r71	352.07	72.48	7.31
SDSS J1055	r72	12.71	2.70	0.84
SDSS J1055	r73	2.96	4.71	1.00

Table 9 — *Continued*

Name	ObsID label	Soft Counts 0.3-1.0 keV	Medium Counts 1.0-2.0 keV	Hard Counts 2.0-10.0keV
SDSS J1055	r74	10.93	4.51	1.00
SDSS J1201	r75	8.14	2.70	0.84
SDSS J1241	r76	5.09	2.96	1.00
SDSS J1311	r77	176.47 ± 18.5	125.88 ± 14.2	6.24
SDSS J1311	r78	19.99	16.08	2.30
SDSS J1323	r79	9.35	2.14	0.84
SDSS J1342	r80	7.02	2.43	1.00
SDSS J1350	r81	7.34	2.96	1.00
Swift J1112.2-8238	r82	4.10	2.43	2.30
Swift J1644+57	r83	13.91	4.31	1.00
Swift J1644+57	r84	2.43	4.71	1.00
Swift J1644+57	r85	50.71	12.04	1.54
Swift J1644+57	r86	11.90	4.31	1.54
Swift J2058+05	r87	6.00	2.96	1.23
TDE2	r88	5.09	1.81	1.00
Wings	r89	2794.26	2271.83	125.85
Wings	r90	2281.23	1891.01	111.45
Wings	r91	32.01	27.29	3.60
XMMSL1 J0740-85	r92	7.39	3.68	1.19

Note. — All uncertainties correspond to the 90% confidence level. The soft, medium and hard count rates have been corrected for encircled energy fraction. Values which do not have any uncertainties are upperlimits. These upperlimits are derived assuming that we would detect a signal if it is 3σ above background in that energy band.

Table 10
The soft, medium and hard counts derived for the TDE candidates which have *Chandra* observations overlapping the position of the event.

Name	ObsID label	Soft Counts 0.3-1.0 keV	Medium Counts 1.0-2.0 keV	Hard Counts 2.0-10.0keV
3XMM J152130.7+074916	c1	2.30	2.90	2.95
ASASSN-15lh	c2	1.00	1.18	3.48
D1-9	c3	1.46	1.66	4.82
D23H-1	c4	1.82	0.89	1.68
D23H-1	c5	2.34	2.09	8.35
D3-13	c6	16.23 ± 4.3	2.65	7.23
D3-13	c7	5.26	5.77	19.10
GRB060218, SN2006aj	c8	1.44	1.08	4.12
GRB060218, SN2006aj	c9	34.12 ± 6.2	39.81 ± 6.7	6.87
HLX-1	c10	0.62	1.18	1.81
HLX-1	c11	4.24 ± 2.2	3.17 ± 1.9	2.56
IC 3599	c12	215.35 ± 15.5	34.28 ± 6.2	9.44 ± 3.2
IGR J17361-4441	c13	170.00 ± 14.1	321.03 ± 19.4	64.47 ± 8.6
IGR J17361-4441	c14	23.33 ± 5.2	70.28 ± 9.0	168.09 ± 13.2
LEDA 095953	c15	8.02	15.27	11.80
NGC 1097	c16	1081.58 ± 34.9	1189.59 ± 36.5	765.34 ± 27.7
NGC247	c17	0.61	0.71	1.37
NGC247	c18	53.25 ± 7.7	265.26 ± 17.2	175.58 ± 13.3
NGC 3599	c19	112.09 ± 11.2	50.90 ± 7.5	22.86 ± 4.9
NGC 5905	c20	16.72 ± 4.4	12.11 ± 3.9	13.55
NGC 5905	c21	127.03 ± 12.0	63.35 ± 8.5	13.43 ± 4.1
PGC1185375	c22	1.25	1.37	2.89
Pictor A	c23	37.24 ± 6.5	45.04 ± 7.1	87.68 ± 9.4
Pictor A	c24	662.21 ± 27.4	766.21 ± 29.3	1562.12 ± 39.6
Pictor A	c25	712.22 ± 28.4	683.48 ± 27.8	332.10 ± 18.4
Pictor A	c26	537.49 ± 24.7	1022.63 ± 34.0	1315.71 ± 36.5
Pictor A	c27	2391.09 ± 52.1	5227.22 ± 76.8	8145.50 ± 90.6
Pictor A	c28	10515.30 ± 108.3	17634.70 ± 140.2	12558.80 ± 112.2
PS1-10jh	c29	0.79	0.70	2.34
RX J1242-11A	c30	0.49	1.00	1.28
RX J1242-11A	c31	1.17	0.61	1.71
RX J1242-11A	c32	1.58	0.97	2.99
RX J1420+53	c33	1.15	0.70	3.34
RX J1420+53	c34	1.47	1.42	4.52
RX J1624+75	c35	1.03	1.35	3.04
SDSS J0159	c36	2.19 ± 1.6	8.80 ± 3.1	4.70 ± 2.2
SDSS J0952	c37	4.32 ± 2.2	0.88	4.57 ± 2.2
SDSS J0952	c38	4.29 ± 2.2	8.85 ± 3.1	13.09 ± 3.7
SDSS J0952	c39	4.29 ± 2.2	6.47 ± 2.7	17.11 ± 4.2
SDSS J1241	c40	59.94 ± 8.2	44.37 ± 7.0	3.51 ± 2.0
SDSS J1311	c41	14.32 ± 4.0	4.26 ± 2.2	2.11
SDSS J1311	c42	0.34	0.34	1.15
SDSS J1311	c43	0.96	1.29	2.06
SDSS J1311	c44	12.81 ± 3.9	4.97	7.64
Swift J1644+57	c45	1.71	1.23	3.35
Swift J1644+57	c46	1.29	1.17	3.24
Swift J2058+05	c47	1.51	1.51	4.42
Swift J2058+05	c48	1.92	2.01	6.03
Wings	c49	342.90 ± 20.6	51.20	27.12
Wings	c50	459.18 ± 23.6	52.17	27.15
Wings	c51	34.78	39.87	21.84
Wings	c52	46.64	94.96	57.69
Wings	c53	50.93	100.69	59.91
Wings	c54	69.78	214.02	140.33
Wings	c55	49.35	138.86	87.88
Wings	c56	44.39	135.16	88.80
Wings	c57	62.94	223.54	154.58
Wings	c58	110.86	206.85	116.35

Note. — All uncertainties correspond to the 90% confidence level. The soft, medium and hard count rates have been corrected for encircled energy fraction. Values which do not have any uncertainties are upperlimits. These upperlimits are derived assuming that we would detect a signal if it is 3σ above background in that energy band.

Table 11
The soft, medium and hard counts derived for the TDE candidates which have
XMM-Newton pointed observations overlapping the position of the event.

Name	ObsID label	Soft Counts 0.3-1.0 keV	Medium Counts 1.0-2.0 keV	Hard Counts 2.0-10.0keV
2MASXJ0203	x1	958.67 \pm 35.3	665.08 \pm 29.7	380.07 \pm 21.2
2MASX J0249	x2	1610.75 \pm 45.6	151.58 \pm 15.6	109.24
3XMM J152130.7+074916	x3	1366.57 \pm 46.2	447.25	927.39
3XMM J152130.7+074916	x4	371.45	303.55	562.47
ASASSN-14li	x5	26914.80 \pm 185.1	432.16	1331.46
ASASSN-15lh	x6	65.30	87.20	248.00
D1-9	x7	136.06	217.48	430.19
D23H-1	x8	61.32	84.56	207.33
Dougie	x9	11.91	14.07	36.16
GRB060218, SN2006aj	x10	53.66	95.26	357.75
HLX-1	x11	823.04 \pm 33.3	310.11 \pm 21.2	111.57
HLX-1	x12	3969.67 \pm 72.0	982.93 \pm 37.1	221.46
HLX-1	x13	411.89 \pm 31.5	441.38	794.12
HLX-1	x14	640.30 \pm 37.3	463.93	673.21
HLX-1	x15	817.94 \pm 35.3	410.77 \pm 26.5	270.32
IGR J12580	x16	24.48	57.72	104.89
IGR J12580	x17	545.75 \pm 27.8	4181.59 \pm 73.3	80186.60 \pm 285.4
IGR J17361-4441	x18	1610.08 \pm 49.6	2238.33 \pm 56.0	949.20 \pm 39.3
IGR J17361-4441	x19	416.08 \pm 24.9	885.75 \pm 34.8	396.87 \pm 22.6
LEDA 095953	x20	2167.97	2566.54	1664.57
NGC 2110	x21	41.77	184.53	299.48
NGC247	x22	78.95	98.56	169.26
NGC247	x23	219.09	262.70	525.99
NGC247	x24	2609.58 \pm 59.6	3879.42 \pm 72.1	2754.40 \pm 57.0
NGC 3599	x25	157.92 \pm 14.7	75.58 \pm 10.7	47.79
NGC 3599	x26	397.67 \pm 24.7	216.50 \pm 19.6	239.40
OGLE16aaa	x27	14.10	16.30	44.00
Pictor A	x28	18320.70 \pm 153.1	17629.40 \pm 150.2	10439.30 \pm 105.0
Pictor A	x29	83790.00 \pm 326.5	82081.10 \pm 323.1	46977.80 \pm 218.9
PTF-10iam	x30	10.09	12.21	18.00
PTF-10iam	x31	22.12	41.10	75.32
RBS 1032	x32	371.02	537.74	1012.29
RX J1242-11A	x33	40.87	27.37	47.39
SDSS J0159	x34	301.08 \pm 20.2	221.58 \pm 17.4	108.07 \pm 12.3
SDSS J0939	x35	1204.42 \pm 39.2	431.75 \pm 23.7	138.73 \pm 12.8
SDSS J1201	x36	2845.33 \pm 62.2	675.41 \pm 35.1	727.69
SDSS J1201	x37	479.58 \pm 28.0	213.83	421.67
SDSS J1201	x38	146.43	186.72	439.91
SDSS J1311	x39	345.75	329.98	271.40
SDSS J1311	x40	1.00	1.05	1.00
SDSS J1323	x41	25.25 \pm 6.4	19.58	32.52
Swift J1644+57	x42	9.30	22.75	36.95
Swift J1644+57	x43	16162.80 \pm 143.4	98434.20 \pm 353.5	102494.00 \pm 322.8
Swift J1644+57	x44	8790.42 \pm 106.8	65351.30 \pm 288.5	82807.70 \pm 291.7
Swift J1644+57	x45	1539.33 \pm 47.0	9108.33 \pm 109.2	8265.13 \pm 96.0
Swift J1644+57	x46	198.08 \pm 17.1	1508.83 \pm 44.2	1839.60 \pm 44.1
Swift J1644+57	x47	1403.08 \pm 42.8	12586.30 \pm 126.5	20290.90 \pm 143.8
Swift J1644+57	x48	749.58 \pm 31.4	6472.75 \pm 90.7	10445.70 \pm 103.2
Swift J1644+57	x49	1319.17 \pm 41.6	12752.80 \pm 127.3	21616.30 \pm 148.4
Swift J1644+57	x50	357.17 \pm 22.7	2953.33 \pm 61.6	4757.40 \pm 70.2
Swift J1644+57	x51	551.75 \pm 27.6	4821.67 \pm 78.6	7828.73 \pm 89.9
Swift J1644+57	x52	757.00 \pm 33.2	5992.00 \pm 88.3	9793.53 \pm 102.0
Swift J1644+57	x53	86.39	87.40	199.66
Swift J1644+57	x54	84.36	75.26	166.77
Swift J2058+05	x55	490.42 \pm 26.7	413.31 \pm 28.9	341.74 \pm 23.7
Swift J2058+05	x56	522.00 \pm 28.8	656.25 \pm 31.5	438.20 \pm 27.4
Wings	x57	8610.00	8830.00	5580.00
XMMSL1 J0740-85	x58	2280.00 \pm 53.0	1260.00 \pm 40.7	571.00 \pm 34.2
XMMSL1 J0740-85	x59	6530.00 \pm 89.6	2680.00 \pm 61.3	2130.00 \pm 75.9

Note. — All uncertainties correspond to the 90% confidence level. The soft, medium and hard count rates have been corrected for encircled energy fraction. Values which do not have any uncertainties are upperlimits. These upperlimits are derived assuming that we would detect a signal if it is 3σ above background in that energy band.

Table 12
The soft, medium and hard counts derived for the TDE candidates which have
XMM-Newton slew observations overlapping the position of the event.

Name	ObsID label	Soft Counts 0.3-1.0 keV	Medium Counts 1.0-2.0 keV	Hard Counts 2.0-10.0keV
2MASXJ0203	xs1	10.89 ± 3.5	4.37 ± 2.2	1.23
3XMM J152130.7+074916	xs2	7.18	6.44	14.16
3XMM J152130.7+074916	xs3	±	±	±
ASASSN-14ae	xs4	2.29	1.36	1.54
ASASSN-14ae	xs5	0.94	0.94	1.54
ASASSN-14ae	xs6	2.80	0.94	1.54
ASASSN-14ae	xs7	1.36	0.94	1.82
ASASSN-14li	xs8	1.59	0.87	1.43
ASASSN-15lh	xs9	1.15	1.00	1.69
css100217	xs10	0.96 ± 1.1	0.96 ± 1.1	3.03
css100217	xs11	3.03	3.03	5.16
D23H-1	xs12	2.02	1.36	1.82
D3-13	xs13	2.55	0.94	2.06
D3-13	xs14	1.36	1.71	1.23
DES14C1kia	xs15	2.29	1.00	1.54
DES14C1kia	xs16	3.03	2.29	6.78
HLX-1	xs17	0.94	0.94	1.23
HLX-1	xs18	2.55	1.71	1.54
HLX-1	xs19	2.02	2.02	2.52
IC 3599	xs20	1.94	1.32	1.75
IC 3599	xs21	1.00	1.00	0.81
IC 3599	xs22	2.69	1.00	1.19
IGR J12580	xs23	1.00	0.94	1.82
IGR J17361-4441	xs24	26.96 ± 5.8	41.04 ± 6.9	68.73 ± 8.4
LEDA 095953	xs25	9.79	7.54	5.82
NGC 1097	xs26	6.30 ± 2.7	0.94	2.52
NGC 1097	xs27	10.37 ± 3.5	2.29	1.82
NGC 1097	xs28	8.59 ± 3.1	4.15 ± 2.2	2.80 ± 1.7
NGC 1097	xs29	3.93 ± 2.2	2.29	1.54
NGC 2110	xs30	5.33	5.50	22.27 ± 5.2
NGC 2110	xs31	0.94	5.11 ± 2.5	33.27 ± 5.8
NGC 2110	xs32	2.29	6.44 ± 2.7	51.40 ± 7.2
NGC247	xs33	1.36	1.71	2.06
NGC247	xs34	3.03	1.36	1.54
NGC 3599	xs35	24.00 ± 5.2	1.00	0.84
NGC 3599	xs36	38.15 ± 6.6	1.36	1.23
NGC 3599	xs37	1.00	1.00	0.84
NGC 3599	xs38	8.26	3.25	2.72
NGC 3599	xs39	1.36	3.03	2.92
NGC 3599	xs40	2.55	0.94	1.23
NGC 5905	xs41	3.12	1.31	2.42
OGLE16aaa	xs42	2.02	1.36	2.29
PGC 1190358	xs43	2.02	2.02	3.12
PGC 1190358	xs44	10.72	1.36	2.30
PGC 1190358	xs45	3.03	1.36	3.12
Pictor A	xs46	11.78 ± 3.7	9.93 ± 3.3	9.47 ± 3.2
Pictor A	xs47	35.04 ± 6.3	19.70 ± 4.7	10.67 ± 3.3
PS1-10jh	xs48	2.02	2.80	1.23
PS1-10jh	xs49	4.63	3.87	6.65
PS1-10jh	xs50	1.00	1.00	1.23
PS1-10jh	xs51	1.00	1.00	1.23
PS1-10jh	xs52	1.71	0.94	1.23
PS1-10jh	xs53	1.00	1.00	1.00
PS1-10jh	xs54	2.02	1.00	0.84
PS1-11af	xs55	0.94	1.00	1.82
PS1-11af	xs56	1.00	0.94	2.30
PS1-12yp	xs57	1.71	1.71	1.71
PS1-12yp	xs58	2.80	2.16	12.39
PS1-12yp	xs59	1.71	1.36	1.36
PTF-09axc	xs60	2.29	1.00	2.06
PTF-09ge	xs61	1.36	1.36	1.54
PTF-10iam	xs62	2.80	1.36	2.30
PTF-10iam	xs63	1.36	0.94	0.84
PTF-10iam	xs64	6.47	0.94	2.52
PTF-10nuj	xs65	1.71	0.94	1.54
PTF-10nuj	xs66	4.07	1.36	1.23
PTF-11glr	xs67	3.11 ± 1.9	3.25	7.31
RBS 1032	xs68	2.29	0.94	1.82
RBS 1032	xs69	7.11 ± 3.4	3.46	6.10
RBS 1032	xs70	4.81	0.94	0.84
RX J1242-11A	xs71	1.36	1.00	1.54
RX J1420+53	xs72	0.94	0.94	1.82
RX J1624+75	xs73	1.36	0.94	1.23

Table 12 — *Continued*

Name	ObsID label	Soft Counts 0.3-1.0 keV	Medium Counts 1.0-2.0 keV	Hard Counts 2.0-10.0keV
RX J1624+75	xs74	0.94	1.00	3.12
RX J1624+75	xs75	0.94	1.00	1.00
RX J1624+75	xs76	1.36	1.00	1.23
SDSS J0748	xs77	3.46	3.25	5.97
SDSS J0938	xs78	2.29	1.00	2.06
SDSS J0938	xs79	0.94	1.36	0.84
SDSS J0939	xs80	1.71	3.46	3.12
SDSS J1011	xs81	3.03	2.80	5.39
SDSS J1011	xs82	1.36	0.94	1.23
SDSS J1011	xs83	2.80	0.94	1.23
SDSS J1055	xs84	2.80	1.00	0.84
SDSS J1055	xs85	2.02	0.94	1.23
SDSS J1201	xs86	0.94	1.00	0.84
SDSS J1201	xs87	0.94	0.94	0.84
SDSS J1201	xs88	14.37 ± 4.0	0.94	1.23
SDSS J1201	xs89	2.55	1.71	1.82
SDSS J1241	xs90	1.36	1.00	1.23
SDSS J1311	xs91	3.46	3.03	1.23
SDSS J1311	xs92	2.29	2.29	2.72
SDSS J1323	xs93	18.44 ± 4.6	4.37 ± 2.2	1.82
SDSS J1323	xs94	2.02	1.00	1.54
SDSS J1323	xs95	5.50	1.71	1.82
SDSS J1350	xs96	2.80	2.55	6.10
Swift J1112.2-8238	xs97	6.16	0.94	2.52
Swift J1112.2-8238	xs98	1.71	0.94	1.54
Swift J1112.2-8238	xs99	1.71	1.36	0.84
Swift J1644+57	xs100	1.71	2.55	7.69
Swift J1644+57	xs101	0.94	1.00	0.84
Swift J1644+57	xs102	3.87	0.94	0.84
Swift J1644+57	xs103	1.71	1.00	1.54
Swift J2058+05	xs104	3.25	1.36	3.83
Swift J2058+05	xs105	2.55	1.36	2.30
Swift J2058+05	xs106	2.02	1.00	1.23
Swift J2058+05	xs107	7.78 ± 2.9	5.56 ± 2.5	13.00 ± 3.6
TDE2	xs108	1.36	1.71	1.23
Wings	xs109	3.41	3.79 ± 2.0	2.15
XMMSL1 J0740-85	xs110	1.94	1.00	4.44
XMMSL1 J0740-85	xs111	37.40 ± 6.5	9.93 ± 3.3	7.57 ± 2.9

Note. — All uncertainties correspond to the 90% confidence level. The soft, medium and hard count rates have been corrected for encircled energy fraction. Values which do not have any uncertainties are upperlimits. These upperlimits are derived assuming that we would detect a signal if it is 3σ above background in that energy band.

Table 13
The soft, medium and hard counts derived for the TDE candidates which have *Swift XRT* observations overlapping the position of the event.

Name	ObsID label	Soft Counts 0.3-1.0 keV	Medium Counts 1.0-2.0 keV	Hard Counts 2.0-10.0keV
2MASXJ0203	sw1	78.22 ± 9.5	60.15 ± 8.3	41.47 ± 6.6
2MASXJ0203	sw2	42.89 ± 7.0	49.55 ± 7.5	29.86 ± 5.7
2MASX J0249	sw3	2.96 ± 1.9	2.01	2.51
2MASX J0249	sw4	4.15 ± 2.2	1.00	1.54
2MASX J0249	sw5	31.03 ± 6.0	3.67	5.25
2MASX J0249	sw6	3.18 ± 1.9	1.72	2.07
2MASX J0249	sw7	3.63 ± 2.2	1.71	4.00
2MASX J0249	sw8	5.50	3.03	4.95
2MASX J0249	sw9	5.17	3.47	3.84
2MASX J0249	sw10	3.26	1.37	3.67
3XMM J152130.7+074916	sw11	32.30	25.91	21.51
ASASSN-14ae	sw12	6.93	2.55	5.53
ASASSN-14ae	sw13	24.08	8.56	16.62
ASASSN-14ae	sw14	7.68	4.98	8.19
ASASSN-14ae	sw15	5.15	2.29	3.27 ± 2.0
ASASSN-14ae	sw16	6.62	2.79	5.96
ASASSN-14li	sw17	3453.97 ± 62.3	23.74 ± 5.3	8.28
ASASSN-14li	sw18	20871.90 ± 152.9	137.96 ± 12.9	40.77
ASASSN-14li	sw19	7010.62 ± 88.7	26.81 ± 6.1	24.26
ASASSN-14li	sw20	1497.87 ± 41.0	7.80	12.30
ASASSN-14li	sw21	1564.68 ± 42.0	11.41	15.06
ASASSN-14li	sw22	490.00 ± 22.2	5.27	8.82
ASASSN-14li	sw23	275.00 ± 16.7	4.80	8.81
ASASSN-15lh	sw24	5.29 ± 2.7	4.57	5.76
ASASSN-15lh	sw25	64.40	30.50	58.00
ASASSN-15lh	sw26	56.20	24.80	39.80
ASASSN-15lh	sw27	31.00	14.50	27.80
ASASSN-15lh	sw28	32.00	18.10	28.80
ASASSN-15lh	sw29	16.50	10.70	16.10
ASASSN-15oi	sw30	46.75 ± 8.2	20.82 ± 5.4	22.19
ASASSN-15oi	sw31	76.38 ± 10.4	27.37 ± 6.4	27.91
css100217	sw32	5.73 ± 2.7	5.87 ± 2.7	7.35
css100217	sw33	8.27 ± 3.5	7.33	11.60
css100217	sw34	60.86 ± 8.0	4.90	4.33 ± 2.5
D3-13	sw35	2.30	1.72	1.82
D3-13	sw36	6.15	2.79	4.94
D3-13	sw37	2.01	1.00	2.06
DES14C1kia	sw38	21.87	10.98	16.69
DES14C1kia	sw39	9.24	4.44	7.81
Dougie	sw40	10.45	8.54	13.76
Dougie	sw41	5.33	5.16	7.43
GRB060218, SN2006aj	sw42	3.96	3.96	6.12
GRB060218, SN2006aj	sw43	3.10	2.35	5.82
GRB060218, SN2006aj	sw44	2.35	2.06	5.23
GRB060218, SN2006aj	sw45	6.48	3.10	6.55
GRB060218, SN2006aj	sw46	3.32	2.06	4.27
GRB060218, SN2006aj	sw47	3.54	2.60	5.22
GRB060218, SN2006aj	sw48	4.15	2.34	2.78
GRB060218, SN2006aj	sw49	6.30	5.28	8.27
GRB060218, SN2006aj	sw50	3.33	2.62	3.00
GRB060218, SN2006aj	sw51	645.20 ± 27.8	991.91 ± 34.0	301.33 ± 19.6
GRB060218, SN2006aj	sw52	32.24	23.61	53.53
GRB060218, SN2006aj	sw53	5.47	5.30	8.30
GRB060218, SN2006aj	sw54	3.10	2.07	3.93
HLX-1	sw55	289.32 ± 18.4	89.67 ± 10.7	26.16 ± 6.3
HLX-1	sw56	49.73	31.32	27.60
HLX-1	sw57	32.91	27.85	29.81
HLX-1	sw58	32.80	28.18	31.90
HLX-1	sw59	26.51	17.82	19.62
HLX-1	sw60	840.86 ± 31.0	210.74 ± 16.0	31.59
HLX-1	sw61	406.66 ± 22.0	127.23 ± 12.8	37.42
HLX-1	sw62	25.20	18.66	21.47
HLX-1	sw63	256.78 ± 17.7	97.38 ± 10.9	22.07
HLX-1	sw64	924.90 ± 33.3	244.20 ± 17.4	44.60
HLX-1	sw65	43.87	14.98	17.18
HLX-1	sw66	23.40	18.42	19.00
HLX-1	sw67	240.95 ± 17.3	103.19 ± 11.6	29.97
HLX-1	sw68	116.51 ± 12.1	48.08 ± 8.0	19.04
HLX-1	sw69	16.13	12.71	12.37
HLX-1	sw70	318.08 ± 19.5	96.44 ± 11.2	33.66
HLX-1	sw71	151.21 ± 14.2	52.53 ± 9.0	30.70
HLX-1	sw72	38.01	13.74	14.73
HLX-1	sw73	10.41	5.85	5.57

Table 13 — *Continued*

Name	ObsID label	Soft Counts 0.3-1.0 keV	Medium Counts 1.0-2.0 keV	Hard Counts 2.0-10.0keV
HLX-1	sw74	249.49 ± 17.7	91.99 ± 10.8	31.61 ± 6.7
HLX-1	sw75	8.24	4.62 ± 2.5	5.57
HLX-1	sw76	9.13	6.02	7.15
HLX-1	sw77	15.75	9.57	12.59
HLX-1	sw78	19.04	14.65	14.65
HLX-1	sw79	25.95	18.88	18.88
HLX-1	sw80	150.04 ± 13.5	32.95 ± 6.6	16.72
HLX-1	sw81	26.18	16.61	20.44
HLX-1	sw82	25.25	16.77	21.21
HLX-1	sw83	13.08	10.54	9.61
IC 3599	sw84	290.98 ± 18.0	16.25 ± 4.3	4.14
IC 3599	sw85	68.68 ± 8.8	1.32	3.31 ± 2.0
IC 3599	sw86	10.98 ± 4.0	5.11	6.61
IC 3599	sw87	6.22	3.91	5.46
IC 3599	sw88	6.21	5.69 ± 2.7	6.37
IC 3599	sw89	3.13	2.21	1.99
IC 3599	sw90	8.45	4.62	5.19 ± 2.7
IC 3599	sw91	5.12	2.21	3.52
IC 3599	sw92	19.93	13.03	17.09
IC 3599	sw93	6.64	5.11	5.98
IGR J12580	sw94	3.63 ± 2.2	38.44 ± 6.6	762.13 ± 27.8
IGR J12580	sw95	5.99	2.55	5.54 ± 2.7
IGR J17361-4441	sw96	1293.45 ± 38.6	3533.08 ± 63.1	7953.82 ± 89.7
IGR J17361-4441	sw97	1669.75 ± 44.1	7123.60 ± 89.5	6561.77 ± 81.5
IGR J17361-4441	sw98	60.00 ± 9.6	144.78 ± 13.1	73.97 ± 9.1
IGR J17361-4441	sw99	7.25	13.85 ± 4.0	8.07 ± 3.0
IGR J17361-4441	sw100	12.41	15.10 ± 4.5	9.73 ± 3.5
IGR J17361-4441	sw101	49.31 ± 8.6	92.29 ± 10.5	58.99 ± 8.2
iPTF16fnl	sw102	29.30	17.70	30.80
iPTF16fnl	sw103	8.18	6.47	9.54
NGC 1097	sw104	82.15 ± 9.8	51.34 ± 7.7	32.94 ± 5.9
NGC 1097	sw105	138.44 ± 12.5	103.63 ± 10.8	82.40 ± 9.2
NGC 1097	sw106	109.49 ± 11.2	103.86 ± 10.8	70.14 ± 8.5
NGC 1097	sw107	155.49 ± 13.8	154.13 ± 13.3	97.18 ± 10.1
NGC 1097	sw108	169.18 ± 13.9	176.15 ± 14.2	98.27 ± 10.1
NGC 1097	sw109	462.13 ± 23.0	482.29 ± 23.4	323.06 ± 18.2
NGC 1097	sw110	574.63 ± 25.8	613.45 ± 26.4	345.04 ± 19.0
NGC 1097	sw111	180.66 ± 14.4	152.89 ± 13.2	79.00 ± 9.1
NGC 2110	sw112	130.65 ± 12.3	1367.66 ± 39.2	10947.20 ± 105.3
NGC 2110	sw113	22.44 ± 5.1	99.78 ± 10.6	952.98 ± 31.0
NGC 2110	sw114	27.63 ± 5.7	235.12 ± 16.3	2408.94 ± 49.4
NGC 2110	sw115	122.01 ± 11.9	1465.15 ± 40.6	13429.70 ± 116.7
NGC 2110	sw116	44.23 ± 7.2	334.30 ± 19.4	3002.04 ± 55.1
NGC 2110	sw117	57.63 ± 8.2	698.00 ± 28.1	6566.90 ± 81.7
NGC247	sw118	74.94 ± 9.9	100.11 ± 11.0	72.48 ± 9.0
NGC247	sw119	20.48	40.49 ± 7.2	14.05 ± 4.8
NGC247	sw120	10.48	6.40	10.05
NGC247	sw121	7.36	7.04	8.39
NGC247	sw122	5.70	3.58	2.81
NGC247	sw123	2.64	1.00	0.87
NGC247	sw124	3.59	4.61	3.79
NGC 3599	sw125	12.81 ± 4.0	5.33	6.39
NGC 3599	sw126	2.55	2.02	1.82
NGC 3599	sw127	3.03	1.71	3.66
NGC 3599	sw128	4.81 ± 2.5	2.30	3.12
NGC 3599	sw129	5.26 ± 2.7	4.25	4.16
NGC 3599	sw130	1.36	0.94	1.23
NGC 3599	sw131	1.36	1.36	1.82
NGC 3599	sw132	2.01	1.71	2.29
OGLE16aaa	sw133	28.07 ± 5.4	3.46	3.66
OGLE16aaa	sw134	4.63	2.56	3.47
OGLE16aaa	sw135	22.60	15.80	24.20
OGLE16aaa	sw136	18.14 ± 4.6	5.66	8.82
Pictor A	sw137	861.89 ± 31.2	1097.88 ± 35.1	795.17 ± 28.4
Pictor A	sw138	145.64 ± 12.9	176.90 ± 14.2	129.07 ± 11.5
PTF-09axc	sw139	2.56	1.00	1.00
PTF-09axc	sw140	3.02	1.00	1.00
PTF-09djl	sw141	4.81	1.00	1.00
PTF-09ge	sw142	3.67	1.00	1.00
PTF-10iya	sw143	6.96 ± 3.0	1.00	1.00
PTF-10iya	sw144	7.95	1.00	1.00
PTF-10iya	sw145	4.98	0.94	1.00
PTF-10iya	sw146	3.45	1.00	1.00
PTF-11glr	sw147	3.87	0.94	1.00
SDSS J0939	sw148	68.22 ± 8.9	41.93 ± 6.9	10.60 ± 3.6
SDSS J0939	sw149	55.85 ± 7.9	18.59 ± 4.6	4.33 ± 2.2

Table 13 — *Continued*

Name	ObsID label	Soft Counts 0.3-1.0 keV	Medium Counts 1.0-2.0 keV	Hard Counts 2.0-10.0keV
SDSS J0952	sw150	15.45	6.48	14.75
SDSS J1201	sw151	116.02 ± 11.7	35.19 ± 6.5	11.58
SDSS J1201	sw152	8.45 ± 3.4	2.01	5.39
SDSS J1201	sw153	9.67	6.80	7.06
SDSS J1241	sw154	19.11 ± 5.2	7.93 ± 3.4	15.14
SDSS J1323	sw155	3.46	2.29	2.72
SDSS J1323	sw156	1.36	1.00	1.00
SDSS J1323	sw157	3.46	1.71	3.66
SDSS J1323	sw158	2.30	2.56	2.93
SDSS J1342	sw159	20.95 ± 5.5	7.10	12.83
SDSS J1350	sw160	6.47	3.46	4.49
SDSS J1350	sw161	16.63	11.65	13.05
Swift J1112.2-8238	sw162	408.89 ± 22.2	940.00 ± 32.6	1020.00 ± 32.3
Swift J1644+57	sw163	8032.54 ± 95.5	80666.30 ± 301.2	115414.00 ± 342.0
Swift J1644+57	sw164	1850.53 ± 47.9	20140.50 ± 150.4	33107.70 ± 183.2
Swift J1644+57	sw165	297.03 ± 21.7	3410.20 ± 62.0	6480.30 ± 81.3
Swift J1644+57	sw166	115.88 ± 14.8	1696.82 ± 43.9	3192.31 ± 57.3
Swift J1644+57	sw167	53.20	482.74 ± 23.7	907.06 ± 30.8
Swift J1644+57	sw168	58.89	26.08	46.42
Swift J1644+57	sw169	6.92	2.29	4.79
Swift J1644+57	sw170	5.65	2.29	3.99
Swift J1644+57	sw171	2.80	1.00	2.30
Swift J1644+57	sw172	8.54	6.93	9.28
Swift J1644+57	sw173	19.07	9.90	13.96
Swift J1644+57	sw174	4.62	1.71	2.72
Swift J1644+57	sw175	8.83	3.87	5.82
Swift J1644+57	sw176	18.35	9.12	15.90
Swift J1644+57	sw177	2.02	2.02	2.30
Swift J1644+57	sw178	20.47	7.69	16.10
Swift J1644+57	sw179	5.67	4.26	7.44
Swift J1644+57	sw180	8.54	4.44	6.78
Swift J1644+57	sw181	2272.94 ± 50.7	21663.60 ± 156.3	25721.90 ± 161.7
Swift J2058+05	sw182	582.43 ± 25.6	1162.72 ± 36.1	1109.11 ± 33.5
Swift J2058+05	sw183	7.53	5.34 ± 2.7	9.75
Swift J2058+05	sw184	101.10 ± 11.1	218.29 ± 15.7	157.12 ± 12.9
Swift J2058+05	sw185	34.20 ± 7.2	86.29 ± 10.1	60.38 ± 8.3
Swift J2058+05	sw186	4.52 ± 2.5	7.56 ± 2.9	3.83
Wings	sw187	156.20 ±	190.68	147.87
XMMSL1 J0740-85	sw188	510.47 ± 24.0	291.00 ± 18.0	130.00 ± 12.2
XMMSL1 J0740-85	sw189	149.93 ± 13.1	103.00 ± 10.7	50.00 ± 7.6
XMMSL1 J0740-85	sw190	74.09 ± 9.3	63.20 ± 8.5	25.50 ± 5.7
XMMSL1 J0740-85	sw191	3.35	1.75	2.62

Note. — All uncertainties correspond to the 90% confidence level. The soft, medium and hard count rates have been corrected for encircled energy fraction. Values which do not have any uncertainties are upperlimits. These upperlimits are derived assuming that we would detect a signal if it is 3σ above background in that energy band.

Table 14

The best fit, or assumed parameters for our absorbed powerlaw model that was used to derive the 0.3-2.0 keV X-ray flux and luminosity of each TDE candidate from the *ROSAT* pointed or RASS observations overlapping the position of the source.

Name	ObsID label	N_H^a (10^{22} cm $^{-2}$)	Γ^b	χ^2 (dof)	X-ray flux ^c (erg/s/cm 2)	X-ray Luminosity ^c (erg/s)
2MASXJ0203	r1	0.02	4.50		$(7.55) \times 10^{-14}$	$(6.86) \times 10^{41}$
2MASX J0249	r2	$0.44^{+0.15}_{-0.14}$	7.70		$(3.57) \times 10^{-13}$	$(2.73) \times 10^{41}$
3XMM J152130.7+074916	r3	0.03	4.50		$(6.62) \times 10^{-14}$	$(6.29) \times 10^{42}$
3XMM J152130.7+074916	r4	0.03	4.50		$(1.23) \times 10^{-13}$	$(1.17) \times 10^{43}$
ASASSN-14ae	r5	0.02	4.50		$(4.50) \times 10^{-14}$	$(1.99) \times 10^{41}$
ASASSN-14li	r6	0.02	4.50		$(7.11) \times 10^{-14}$	$(6.70) \times 10^{40}$
ASASSN-15lh	r7	0.03	4.50		$(5.29) \times 10^{-13}$	$(9.27) \times 10^{43}$
ASASSN-15oi	r8	0.06	4.50		$(2.95) \times 10^{-13}$	$(1.62) \times 10^{42}$
css100217	r9	0.01	4.50		$(3.80) \times 10^{-14}$	$(2.34) \times 10^{42}$
D1-9	r10	0.02	4.50		$(1.15) \times 10^{-13}$	$(4.57) \times 10^{43}$
D23H-1	r11	0.04	4.50		$(2.04) \times 10^{-13}$	$(2.10) \times 10^{43}$
D3-13	r12	0.01	4.50		$(6.56) \times 10^{-14}$	$(3.58) \times 10^{43}$
DES14C1kia	r13	0.01	4.50		$(2.10) \times 10^{-13}$	$(1.59) \times 10^{43}$
DES14C1kia	r14	0.01	4.50		$(1.07) \times 10^{-13}$	$(8.09) \times 10^{42}$
DES14C1kia	r15	0.01	4.50		$(5.92) \times 10^{-14}$	$(4.47) \times 10^{42}$
DES14C1kia	r16	0.01	4.50		$(3.93) \times 10^{-15}$	$(2.97) \times 10^{41}$
GRB060218, SN2006aj	r17	0.11	4.50		$(5.32) \times 10^{-13}$	$(1.36) \times 10^{42}$
HLX-1	r18	0.02	4.50		$(4.69) \times 10^{-14}$	$(5.21) \times 10^{40}$
IC 3599	r19	$0.03^{+0.01}_{-0.01}$	$4.63^{+0.8}_{-0.6}$	0.95 (42)	$(7.19^{+8.3}_{-6.3}) \times 10^{-14}$	$(7.19^{+8.3}_{-6.3}) \times 10^{40}$
IC 3599	r20	0.03^d	4.63^d		$(1.78^{+1.8}_{-1.7}) \times 10^{-11}$	$(1.78^{+1.8}_{-1.7}) \times 10^{43}$
IGR J12580	r21	0.02	4.50		$(9.67) \times 10^{-14}$	$(3.51) \times 10^{39}$
IGR J17361-4441	r22	0.25	4.50		$(3.66) \times 10^{-13}$	$(1.35) \times 10^{42}$
iPTF16fnl	r23	0.06	4.50		$(1.36) \times 10^{-13}$	$(7.96) \times 10^{40}$
LEDA 095953	r24	$0.06^{+0.01}_{-0.01}$	$2.50^{+0.4}_{-0.4}$	0.79 (133)	$(1.76^{+1.9}_{-1.7}) \times 10^{-12}$	$(5.40^{+5.8}_{-5.2}) \times 10^{42}$
NGC 1097	r25	$0.04^{+0.01}_{-0.01}$	$1.99^{+0.2}_{-0.2}$	1.12 (131)	$(2.19^{+2.3}_{-2.1}) \times 10^{-12}$	$(8.30^{+8.5}_{-8.1}) \times 10^{40}$
NGC 2110	r26	0.20	4.50		$(2.95^{+4.3}_{-1.9}) \times 10^{-13}$	$(3.66^{+5.1}_{-2.3}) \times 10^{40}$
NGC247	r27	0.02	4.50		$(7.53) \times 10^{-14}$	$(4.53) \times 10^{37}$
NGC247	r28	0.02	4.50		$(2.87) \times 10^{-14}$	$(1.73) \times 10^{37}$
NGC 3599	r29	0.01	4.50		$(9.56) \times 10^{-14}$	$(1.49) \times 10^{39}$
NGC 5905	r30	0.01	4.50		$(2.30) \times 10^{-14}$	$(6.34) \times 10^{39}$
NGC 5905	r31	0.01	4.50		$(5.59) \times 10^{-14}$	$(1.54) \times 10^{40}$
NGC 5905	r32	0.01	4.50		$(3.17^{+3.4}_{-3.0}) \times 10^{-13}$	$(8.74^{+9.3}_{-8.1}) \times 10^{40}$
OGLE16aaa	r33	0.03	4.50		$(1.23) \times 10^{-13}$	$(9.76) \times 10^{42}$
PGC1185375	r34	0.05	4.50		$(1.43) \times 10^{-13}$	$(8.43) \times 10^{39}$
PGC1185375	r35	0.05	4.50		$(3.70) \times 10^{-13}$	$(2.18) \times 10^{40}$
PGC 1190358	r36	0.05	4.50		$(8.93) \times 10^{-14}$	$(1.13) \times 10^{40}$
PGC 1190358	r37	0.05	4.50		$(1.02) \times 10^{-13}$	$(1.30) \times 10^{40}$
Pictor A	r38	$0.05^{+0.01}_{-0.01}$	$1.94^{+0.1}_{-0.1}$	0.92 (165)	$(8.75^{+8.9}_{-8.6}) \times 10^{-12}$	$(2.31^{+2.3}_{-2.3}) \times 10^{43}$
PS1-10jh	r39	0.01	4.50		$(5.67) \times 10^{-14}$	$(4.76) \times 10^{42}$
PS1-11af	r40	0.02	4.50		$(5.09) \times 10^{-14}$	$(3.49) \times 10^{43}$
PTF-09axc	r41	0.03	4.50		$(1.09) \times 10^{-13}$	$(3.79) \times 10^{42}$
PTF-09djl	r42	0.02	4.50		$(4.28) \times 10^{-14}$	$(4.32) \times 10^{42}$
PTF-09ge	r43	0.02	4.50		$(4.44) \times 10^{-14}$	$(4.39) \times 10^{41}$
PTF-10iam	r44	0.01	4.50		$(1.64) \times 10^{-14}$	$(5.11) \times 10^{41}$
PTF-10iam	r45	0.01	4.50		$(4.51) \times 10^{-14}$	$(1.41) \times 10^{42}$
PTF-10iya	r46	0.01	4.50		$(3.30) \times 10^{-14}$	$(5.28) \times 10^{42}$
PTF-10nuj	r47	0.01	4.50		$(3.03) \times 10^{-14}$	$(1.44) \times 10^{42}$
PTF-10nuj	r48	0.01	4.50		$(9.35) \times 10^{-14}$	$(4.45) \times 10^{42}$
PTF-10nuj	r49	0.01	4.50		$(4.21) \times 10^{-14}$	$(2.00) \times 10^{42}$
PTF-11glr	r50	0.02	4.50		$(2.42) \times 10^{-14}$	$(3.22) \times 10^{42}$
RBS 1032	r51	0.02	$4.51^{+0.5}_{-0.3}$	1.41 (11)	$(1.81^{+2.1}_{-1.1}) \times 10^{-13}$	$(2.75^{+3.2}_{-2.3}) \times 10^{41}$
RBS 1032	r52	0.02	$5.94^{+1.3}_{-1.3}$	1.309 (15)	$(1.23^{+1.4}_{-1.3}) \times 10^{-13}$	$(1.87^{+2.1}_{-1.8}) \times 10^{41}$
RBS 1032	r53	0.02	5.22^e		$(3.28^{+3.6}_{-2.9}) \times 10^{-13}$	$(4.98^{+5.5}_{-4.4}) \times 10^{41}$
RX J1242-11A	r54	$0.11^{+0.05}_{-0.04}$	$7.48^{+1.1}_{-1.6}$	0.86 (43)	$(6.75^{+7.8}_{-4.8}) \times 10^{-13}$	$(3.97^{+4.6}_{-2.8}) \times 10^{42}$
RX J1242-11A	r55	0.11^d	7.48^d		$(1.21) \times 10^{-12}$	$(7.11) \times 10^{42}$
RX J1420+53	r56	0.01	4.50		$(3.89) \times 10^{-14}$	$(2.36) \times 10^{42}$
RX J1420+53	r57	0.01	4.50		$(3.88^{+4.2}_{-3.5}) \times 10^{-13}$	$(2.35^{+2.6}_{-2.1}) \times 10^{43}$
RX J1624+75	r58	0.04	4.50		$(8.24) \times 10^{-14}$	$(8.04) \times 10^{41}$
RX J1624+75	r59	0.04	4.50		$(2.47^{+2.6}_{-2.4}) \times 10^{-12}$	$(2.41^{+2.5}_{-2.3}) \times 10^{43}$
SDSS J0159	r60	0.03	4.50		$(3.55) \times 10^{-14}$	$(1.26) \times 10^{43}$
SDSS J0159	r61	0.03	4.50		$(1.45) \times 10^{-13}$	$(5.16) \times 10^{43}$
SDSS J0748	r62	0.06	4.50		$(1.54) \times 10^{-13}$	$(1.40) \times 10^{42}$
SDSS J0938	r63	0.03	4.50		$(6.65) \times 10^{-14}$	$(1.74) \times 10^{42}$

Table 14 — *Continued*

Name	ObsID label	N_H^a (10^{22} cm^{-2})	Γ^b	χ^2 (dof)	X-ray flux ^c (erg/s/cm ²)	X-ray Luminosity ^c (erg/s)
SDSS J0939	r64	0.01	4.50		$(5.06) \times 10^{-14}$	$(5.26) \times 10^{42}$
SDSS J0952	r65	0.03	4.50		$(1.17) \times 10^{-13}$	$(1.81) \times 10^{42}$
SDSS J1011	r66	0.01	4.50		$(2.07) \times 10^{-14}$	$(4.14) \times 10^{42}$
SDSS J1011	r67	0.01	4.50		$(1.94) \times 10^{-14}$	$(3.88) \times 10^{42}$
SDSS J1055	r68	0.01	4.50		$(1.43) \times 10^{-14}$	$(1.94) \times 10^{41}$
SDSS J1055	r69	0.01	4.50		$(1.73) \times 10^{-14}$	$(2.35) \times 10^{41}$
SDSS J1055	r70	0.01	4.50		$(2.51) \times 10^{-14}$	$(3.41) \times 10^{41}$
SDSS J1055	r71	0.01	4.50		$(1.58) \times 10^{-14}$	$(2.15) \times 10^{41}$
SDSS J1055	r72	0.01	4.50		$(2.45) \times 10^{-14}$	$(3.33) \times 10^{41}$
SDSS J1055	r73	0.01	4.50		$(9.26) \times 10^{-14}$	$(1.26) \times 10^{42}$
SDSS J1055	r74	0.01	4.50		$(2.59^{+3.3}_{-1.9}) \times 10^{-14}$	$(3.52^{+4.5}_{-2.6}) \times 10^{41}$
SDSS J1201	r75	0.01	4.50		$(6.31) \times 10^{-14}$	$(3.77) \times 10^{42}$
SDSS J1241	r76	0.02	4.50		$(5.93) \times 10^{-14}$	$(2.41) \times 10^{41}$
SDSS J1311	r77	0.02	4.50		$(4.03) \times 10^{-14}$	$(3.88) \times 10^{42}$
SDSS J1311	r78	0.02	4.50		$(1.40) \times 10^{-13}$	$(1.35) \times 10^{43}$
SDSS J1323	r79	0.01	4.50		$(4.16) \times 10^{-13}$	$(8.04) \times 10^{42}$
SDSS J1342	r80	0.02	4.50		$(6.36) \times 10^{-14}$	$(1.95) \times 10^{41}$
SDSS J1350	r81	0.01	4.50		$(6.60) \times 10^{-14}$	$(9.87) \times 10^{41}$
Swift J1112.2-8238	r82	0.09	4.50		$(3.91) \times 10^{-13}$	$(2.26) \times 10^{45}$
Swift J1644+57	r83	0.02	4.50		$(7.53) \times 10^{-14}$	$(3.69) \times 10^{43}$
Swift J1644+57	r84	0.02	4.50		$(1.66) \times 10^{-13}$	$(8.13) \times 10^{43}$
Swift J1644+57	r85	0.02	4.50		$(7.20) \times 10^{-14}$	$(3.53) \times 10^{43}$
Swift J1644+57	r86	0.02	4.50		$(8.75) \times 10^{-14}$	$(4.28) \times 10^{43}$
Swift J2058+05	r87	0.07	4.50		$(4.22) \times 10^{-13}$	$(5.48) \times 10^{45}$
TDE2	r88	0.04	4.50		$(1.06) \times 10^{-13}$	$(2.24) \times 10^{43}$
Wings	r89	0.01	4.50		$(1.52) \times 10^{-13}$	$(1.41) \times 10^{42}$
Wings	r90	0.01	4.50		$(1.48) \times 10^{-13}$	$(1.37) \times 10^{42}$
Wings	r91	0.01	4.50		$(1.44) \times 10^{-13}$	$(1.33) \times 10^{42}$
XMMSL1 J0740-85	r92	0.11	4.50		$(2.51) \times 10^{-13}$	$(1.66) \times 10^{41}$

Note. — All uncertainties correspond to the 90% confidence level and observations that have similar MJD are combined.

^a N_H is determined either directly from fitting the X-ray emitting spectrum or using the column density derived from the Leiden/Argentine/Bonn (LAB) Survey of Galactic H I (Kalberla et al. 2005)

^b Powerlaw index was derived from either fitting X-ray spectra from either *ROSAT*, *XMM* or *Chandra* with a powerlaw model or was assumed to be equal to 4.5. If the following Γ has an uncertainty, the powerlaw index was derived from fitting the X-ray spectrum extracted from *ROSAT*.

^c Absorbed X-ray flux and X-ray luminosity is calculated for an energy range of 0.3-2.0 keV.

^d Value frozen to that obtained from modelling the *ROSAT* X-ray spectrum.

^e Value set to the average of that obtained from modelling multiple *ROSAT* spectra.

Table 15
The best fit, or assumed parameters for our absorbed powerlaw model that was used to derive the 0.3-2.0 keV X-ray flux and luminosity of each TDE candidate from the *Chandra* observations overlapping the position of the source.

Name	ObsID label	N_H^a (10^{22} cm^{-2})	Γ^b	χ^2 (dof)	X-ray flux ^c (erg/s/cm ²)	X-ray Luminosity ^c (erg/s)
3XMM J152130.7+074916	c1	0.03	4.50		$(6.83) \times 10^{-15}$	$(6.49) \times 10^{41}$
ASASSN-15lh	c2	0.03	4.50		$(9.52) \times 10^{-16}$	$(1.67) \times 10^{41}$
D1-9	c3	0.02	4.50		$(2.46) \times 10^{-15}$	$(9.78) \times 10^{41}$
D23H-1	c4	0.04	4.50		$(3.89) \times 10^{-15}$	$(4.01) \times 10^{41}$
D23H-1	c5	0.04	4.50		$(2.70) \times 10^{-15}$	$(2.78) \times 10^{41}$
D3-13	c6	0.01	4.50		$(5.91^{+7.5}_{-4.3}) \times 10^{-15}$	$(3.22^{+4.1}_{-2.4}) \times 10^{42}$
D3-13	c7	0.01	4.50		$(3.54) \times 10^{-15}$	$(1.93) \times 10^{42}$
GRB060218, SN2006aj	c8	0.11	2.38		$(2.71) \times 10^{-15}$	$(6.93) \times 10^{39}$
GRB060218, SN2006aj	c9	0.11	$2.38^{+1.17}_{-1.14}$	0.21 (3)	$(7.02^{+8.7}_{-1.6}) \times 10^{-15}$	$(1.80^{+2.2}_{-1.6}) \times 10^{40}$
HLX-1	c10	0.02	4.50		$(6.23) \times 10^{-15}$	$(6.92) \times 10^{39}$
HLX-1	c11	0.02	4.50		$(8.51^{+11.6}_{-5.5}) \times 10^{-15}$	$(9.45^{+12.9}_{-6.1}) \times 10^{39}$
IC 3599	c12	0.01	$3.79^{+0.61}_{-0.55}$	0.9 (10)	$(1.06^{+1.3}_{-0.9}) \times 10^{-13}$	$(1.06^{+1.3}_{-0.9}) \times 10^{41}$
IGR J17361-4441	c13	$0.70^{+0.20}_{-0.16}$	$3.78^{+0.62}_{-0.51}$	1.12 (39)	$(3.48^{+3.6}_{-3.3}) \times 10^{-14}$	$(1.28^{+1.3}_{-1.2}) \times 10^{41}$
IGR J17361-4441	c14	$0.38^{+0.63}_{-0.30}$	$0.64^{+0.37}_{-0.42}$	0.59 (16)	$(1.31^{+1.4}_{-1.1}) \times 10^{-13}$	$(4.83^{+5.2}_{-4.2}) \times 10^{41}$
LEDA 095953	c15	0.04	4.50		$(8.58) \times 10^{-15}$	$(2.63) \times 10^{40}$
NGC 1097	c16	$0.06^{+0.08}_{-0.06}$	$1.42^{+0.15}_{-0.14}$	0.88 (113)	$(5.94^{+6.3}_{-5.7}) \times 10^{-13}$	$(2.25^{+2.4}_{-2.1}) \times 10^{40}$
NGC247	c17	0.61^d	1.98^d		$(3.89) \times 10^{-13}$	$(2.34) \times 10^{38}$
NGC247	c18	$0.61^{+0.27}_{-0.23}$	$1.98^{+0.38}_{-0.35}$	0.80 (35)	$(2.83^{+2.9}_{-2.6}) \times 10^{-13}$	$(1.70^{+1.8}_{-1.6}) \times 10^{38}$
NGC 3599	c19	0.01	$2.58^{+0.35}_{-0.32}$	0.95 (13)	$(3.78^{+4.1}_{-3.4}) \times 10^{-14}$	$(5.90^{+6.4}_{-5.4}) \times 10^{38}$
NGC 5905	c20	0.01	3.90		$(2.79^{+3.4}_{-2.2}) \times 10^{-14}$	$(7.69^{+9.4}_{-6.0}) \times 10^{39}$
NGC 5905	c21	0.01	$3.90^{+0.66}_{-0.56}$	0.91 (10)	$(3.71^{+4.5}_{-2.9}) \times 10^{-14}$	$(1.02^{+1.2}_{-0.8}) \times 10^{40}$
PGC1185375	c22	0.05	4.50		$(1.67) \times 10^{-12}$	$(9.85) \times 10^{40}$
Pictor A	c23	0.04	$0.55^{+0.37}_{-0.38}$	0.88 (8)	$(1.69^{+1.9}_{-1.5}) \times 10^{-13}$	$(4.46^{+4.9}_{-4.0}) \times 10^{41}$
Pictor A	c24	0.04	$0.67^{+0.07}_{-0.07}$	1.07 (159)	$(1.56^{+1.6}_{-1.5}) \times 10^{-13}$	$(4.11^{+4.2}_{-4.0}) \times 10^{41}$
Pictor A	c25	$0.04^{+0.03}_{-0.03}$	$1.58^{+0.14}_{-0.13}$	0.75 (112)	$(3.35^{+3.4}_{-3.2}) \times 10^{-12}$	$(8.83^{+9.0}_{-8.5}) \times 10^{42}$
Pictor A	c26	0.04	$1.02^{+0.07}_{-0.07}$	0.92 (149)	$(1.97^{+2.0}_{-1.9}) \times 10^{-13}$	$(5.19^{+5.3}_{-5.0}) \times 10^{41}$
Pictor A	c27	0.04	$0.92^{+0.03}_{-0.03}$	1.08 (209)	$(2.23^{+2.3}_{-2.2}) \times 10^{-13}$	$(5.88^{+6.0}_{-5.8}) \times 10^{41}$
Pictor A	c28	0.04	$1.35^{+0.02}_{-0.02}$	1.31 (292)	$(1.63^{+1.6}_{-1.6}) \times 10^{-12}$	$(4.30^{+4.3}_{-4.2}) \times 10^{42}$
PS1-10jh	c29	0.01	4.50		$(3.82) \times 10^{-15}$	$(3.20) \times 10^{41}$
RX J1242-11A	c30	0.04	4.50		$(8.55) \times 10^{-15}$	$(5.03) \times 10^{40}$
RX J1242-11A	c31	0.04	4.50		$(7.87) \times 10^{-15}$	$(4.63) \times 10^{40}$
RX J1242-11A	c32	0.04	4.50		$(6.19) \times 10^{-15}$	$(3.64) \times 10^{40}$
RX J1420+53	c33	0.01	4.50		$(3.77) \times 10^{-15}$	$(2.28) \times 10^{41}$
RX J1420+53	c34	0.01	4.50		$(6.84) \times 10^{-15}$	$(4.15) \times 10^{41}$
RX J1624+75	c35	0.04	4.50		$(7.90) \times 10^{-15}$	$(7.71) \times 10^{40}$
SDSS J0159	c36	0.03	4.50		$(3.83^{+4.9}_{-1.0}) \times 10^{-14}$	$(1.36^{+1.7}_{-1.0}) \times 10^{43}$
SDSS J0952	c37	0.03	4.50		$(7.13^{+10.2}_{-4.1}) \times 10^{-15}$	$(1.10^{+1.6}_{-0.6}) \times 10^{41}$
SDSS J0952	c38	0.03	4.50		$(1.60^{+1.9}_{-1.3}) \times 10^{-14}$	$(2.47^{+3.0}_{-2.0}) \times 10^{41}$
SDSS J0952	c39	0.03	4.50		$(1.64^{+2.0}_{-1.3}) \times 10^{-14}$	$(2.53^{+3.0}_{-2.0}) \times 10^{41}$
SDSS J1241	c40	$0.09^{+0.31}_{-0.09}$	$3.01^{+1.37}_{-0.85}$	0.76 (5)	$(4.47^{+5.3}_{-3.1}) \times 10^{-14}$	$(1.82^{+2.1}_{-1.2}) \times 10^{41}$
SDSS J1311	c41	0.02	4.50		$(5.12^{+6.4}_{-3.9}) \times 10^{-14}$	$(4.93^{+6.1}_{-3.7}) \times 10^{42}$
SDSS J1311	c42	0.02	4.50		$(1.48) \times 10^{-14}$	$(1.42) \times 10^{42}$
SDSS J1311	c43	0.02	4.50		$(1.12) \times 10^{-14}$	$(1.08) \times 10^{42}$
SDSS J1311	c44	0.02	4.50		$(5.69^{+7.4}_{-4.0}) \times 10^{-15}$	$(5.47^{+7.2}_{-3.8}) \times 10^{41}$
Swift J1644+57	c45	0.02	4.50		$(3.05) \times 10^{-15}$	$(1.49) \times 10^{42}$
Swift J1644+57	c46	0.02	4.50		$(2.86) \times 10^{-15}$	$(1.40) \times 10^{42}$
Swift J2058+05	c47	0.07	4.50		$(5.48) \times 10^{-15}$	$(7.11) \times 10^{43}$
Swift J2058+05	c48	0.07	4.50		$(4.49) \times 10^{-15}$	$(5.83) \times 10^{43}$
Wings	c49	$0.09^{+0.06}_{-0.05}$	$5.37^{+0.92}_{-0.80}$	0.97 (26)	$(4.90^{+5.4}_{-4.5}) \times 10^{-14}$	$(4.53^{+5.0}_{-4.2}) \times 10^{41}$
Wings	c50	$0.03^{+0.05}_{-0.02}$	$4.46^{+0.84}_{-0.60}$	1.49 (30)	$(6.63^{+6.9}_{-5.9}) \times 10^{-14}$	$(6.13^{+6.3}_{-5.5}) \times 10^{41}$
Wings	c51	0.06^e	4.92^e		$(8.38) \times 10^{-14}$	$(7.75) \times 10^{41}$
Wings	c52	0.06^e	4.92^e		$(4.23) \times 10^{-14}$	$(3.91) \times 10^{41}$
Wings	c53	0.06^e	4.92^e		$(5.26) \times 10^{-14}$	$(4.86) \times 10^{41}$
Wings	c54	0.06^e	4.92^e		$(2.94) \times 10^{-14}$	$(2.72) \times 10^{41}$
Wings	c55	0.06^e	4.92^e		$(3.45) \times 10^{-14}$	$(3.19) \times 10^{41}$
Wings	c56	0.06^e	4.92^e		$(3.32) \times 10^{-14}$	$(3.07) \times 10^{41}$
Wings	c57	0.06^e	4.92^e		$(2.74) \times 10^{-14}$	$(2.53) \times 10^{41}$
Wings	c58	0.06^e	4.92^e		$(4.45) \times 10^{-14}$	$(4.12) \times 10^{41}$

Note. — All uncertainties correspond to the 90% confidence level and observations that have similar MJD are combined.

^a N_H is determined either directly from fitting the X-ray emitting spectrum or using the column density derived from the Leiden/Argentine/Bonn (LAB) Survey of Galactic H I (Kalberla et al. 2005)

^b Powerlaw index was derived from either fitting X-ray spectra from either *ROSAT*, *XMM* or *Chandra* with a powerlaw model or was assumed to be equal to 4.5. If the following Γ has an uncertainty, the normal-coupled mag-

Table 16
The best fit, or assumed parameters for our absorbed powerlaw model that was used to derive the 0.3-2.0 keV X-ray flux and luminosity of each TDE candidate from the *XMM-Newton* pointed observations overlapping the position of the source.

Name	ObsID label	N_H^a (10^{22} cm^{-2})	Γ^b	χ^2 (dof)	X-ray flux ^c (erg/s/cm ²)	X-ray Luminosity ^c (erg/s)
2MASXJ0203	x1	0.02	$1.62^{+0.11}_{-0.10}$	0.99 (53)	$(2.52^{+2.6}_{-2.4}) \times 10^{-13}$	$(2.29^{+2.4}_{-2.2}) \times 10^{42}$
2MASX J0249	x2	$0.44^{+0.15}_{-0.14}$	$7.70^{+0.06}_{-0.02}$	0.96 (53)	$(4.37^{+4.7}_{-4.0}) \times 10^{-13}$	$(3.35^{+3.6}_{-3.0}) \times 10^{41}$
3XMM J152130.7+074916	x3	0.03	$5.18^{+0.31}_{-0.30}$	1.36(72)	$(3.32^{+3.7}_{-3.1}) \times 10^{-13}$	$(3.15^{+3.5}_{-2.9}) \times 10^{43}$
3XMM J152130.7+074916	x4	0.03	5.18		$(5.76) \times 10^{-15}$	$(5.47) \times 10^{41}$
ASASSN-14li	x5	0.06	$10.00^{+0.50}_{-0.50}$	1.52 (100)	$(5.43^{+5.7}_{-5.4}) \times 10^{-11}$	$(5.12^{+5.4}_{-5.1}) \times 10^{43}$
ASASSN-15lh	x6	0.03	4.50		$(6.42) \times 10^{-14}$	$(1.12) \times 10^{43}$
D1-9	x7	0.02	4.50		$(1.70) \times 10^{-14}$	$(6.76) \times 10^{42}$
D23H-1	x8	0.04	4.50		$(7.51) \times 10^{-15}$	$(7.74) \times 10^{41}$
Dougie	x9	0.01	4.50		$(6.41) \times 10^{-15}$	$(7.07) \times 10^{41}$
GRB060218, SN2006aj	x10	0.11	4.50		$(3.24) \times 10^{-13}$	$(8.28) \times 10^{41}$
HLX-1	x11	0.02	$3.16^{+0.34}_{-0.31}$	0.56 (15)	$(1.81^{+2.0}_{-1.7}) \times 10^{-13}$	$(2.01^{+2.2}_{-1.8}) \times 10^{41}$
HLX-1	x12	0.02	$3.73^{+0.08}_{-0.08}$	1.44 (140)	$(4.09^{+4.2}_{-4.4}) \times 10^{-13}$	$(4.54^{+4.7}_{-4.4}) \times 10^{41}$
HLX-1	x13	0.02	$2.37^{+0.47}_{-0.41}$	1.16 (98)	$(1.21^{+1.4}_{-1.1}) \times 10^{-14}$	$(1.34^{+1.6}_{-1.2}) \times 10^{40}$
HLX-1	x14	0.02	$2.29^{+0.19}_{-0.18}$	1.28 (83)	$(1.84^{+1.9}_{-1.8}) \times 10^{-14}$	$(2.04^{+2.1}_{-1.9}) \times 10^{40}$
HLX-1	x15	0.02	$2.61^{+0.18}_{-0.14}$	1.08 (66)	$(5.57^{+5.8}_{-5.3}) \times 10^{-14}$	$(6.18^{+6.5}_{-5.8}) \times 10^{40}$
IGR J12580	x16	0.02	2.30		$(2.63) \times 10^{-14}$	$(9.55) \times 10^{38}$
IGR J12580	x17	$10.90^{+0.30}_{-0.29}$	$2.30^{+0.08}_{-0.08}$	1.44 (724)	$(3.39^{+3.5}_{-3.3}) \times 10^{-13}$	$(1.23^{+1.3}_{-1.3}) \times 10^{40}$
IGR J17361-4441	x18	$0.32^{+0.05}_{-0.05}$	$2.33^{+0.07}_{-0.12}$	1.13 (200)	$(2.07^{+2.1}_{-2.0}) \times 10^{-13}$	$(7.64^{+7.7}_{-7.5}) \times 10^{41}$
IGR J17361-4441	x19	$0.59^{+0.02}_{-0.02}$	$1.62^{+0.02}_{-0.02}$	1.26 (1077)	$(4.96^{+5.0}_{-4.9}) \times 10^{-12}$	$(1.83^{+1.8}_{-1.8}) \times 10^{43}$
LEDA 095953	x20	0.04	4.50		$(2.18) \times 10^{-13}$	$(6.69) \times 10^{41}$
NGC 2110	x21	0.20	4.50		$(1.39) \times 10^{-13}$	$(1.72) \times 10^{40}$
NGC247	x22	0.20^d	1.62^d		$(1.10) \times 10^{-13}$	$(6.62) \times 10^{37}$
NGC247	x23	0.20^d	1.62^d		$(3.05) \times 10^{-14}$	$(1.84) \times 10^{37}$
NGC247	x24	$0.20^{+0.03}_{-0.03}$	$1.62^{+0.07}_{-0.07}$	1.09 (306)	$(3.43^{+3.5}_{-3.4}) \times 10^{-13}$	$(2.06^{+2.1}_{-2.0}) \times 10^{38}$
NGC 3599	x25	0.01	$2.71^{+0.37}_{-0.32}$	1.00 (9)	$(1.27^{+1.2}_{-1.2}) \times 10^{-13}$	$(1.98^{+2.2}_{-2.0}) \times 10^{39}$
NGC 3599	x26	0.01	$2.43^{+0.21}_{-0.20}$	1.36 (34)	$(3.49^{+3.7}_{-3.3}) \times 10^{-14}$	$(5.44^{+5.7}_{-5.1}) \times 10^{38}$
OGLE16aaa	x27	0.03	4.50		$(5.50) \times 10^{-15}$	$(4.36) \times 10^{41}$
Pictor A	x28	0.04	$1.73^{+0.01}_{-0.01}$	0.98 (718)	$(4.06^{+4.1}_{-4.0}) \times 10^{-12}$	$(1.07^{+1.1}_{-1.1}) \times 10^{43}$
Pictor A	x29	0.04	$1.74^{+0.01}_{-0.01}$	0.99 (1331)	$(6.39^{+6.4}_{-6.4}) \times 10^{-12}$	$(1.68^{+1.7}_{-1.7}) \times 10^{43}$
PTF-10iam	x30	0.01	4.50		$(1.43) \times 10^{-14}$	$(4.46) \times 10^{41}$
PTF-10iam	x31	0.01	4.50		$(1.56) \times 10^{-14}$	$(4.86) \times 10^{41}$
RBS 1032	x32	0.02	4.50		$(1.03) \times 10^{-13}$	$(1.56) \times 10^{41}$
RX J1242-11A	x33	0.04	4.50		$(2.81) \times 10^{-15}$	$(1.65) \times 10^{40}$
SDSS J0159	x34	0.03	$2.03^{+0.16}_{-0.13}$	0.68 (25)	$(2.98^{+3.2}_{-2.9}) \times 10^{-13}$	$(1.06^{+1.1}_{-1.0}) \times 10^{44}$
SDSS J0939	x35	0.01	$3.03^{+0.12}_{-0.12}$	1.25 (58)	$(9.35^{+9.8}_{-8.6}) \times 10^{-13}$	$(9.72^{+10.0}_{-9.2}) \times 10^{43}$
SDSS J1201	x36	$0.24^{+0.08}_{-0.08}$	$5.06^{+0.50}_{-0.45}$	1.17 (126)	$(3.45^{+3.6}_{-3.2}) \times 10^{-13}$	$(2.06^{+2.1}_{-1.9}) \times 10^{43}$
SDSS J1201	x37	$0.61^{+0.23}_{-0.36}$	$8.24^{+2.40}_{-2.40}$	0.92 (37)	$(5.67^{+5.9}_{-3.4}) \times 10^{-14}$	$(3.38^{+3.5}_{-2.0}) \times 10^{42}$
SDSS J1201	x38	0.43^e	6.65^e		$(4.76) \times 10^{-14}$	$(2.84) \times 10^{42}$
SDSS J1311	x39	0.02	4.50		$(1.47) \times 10^{-14}$	$(1.41) \times 10^{42}$
SDSS J1311	x40	0.02	4.50		$(3.00) \times 10^{-15}$	$(2.89) \times 10^{41}$
SDSS J1323	x41	0.01	4.50		$(3.75^{+4.5}_{-3.0}) \times 10^{-15}$	$(7.25^{+8.8}_{-5.7}) \times 10^{40}$
Swift J1644+57	x42	1.05^e	1.51^e		$(1.89) \times 10^{-14}$	$(9.25) \times 10^{42}$
Swift J1644+57	x43	$0.95^{+0.01}_{-0.01}$	$1.71^{+0.01}_{-0.01}$	1.27 (1642)	$(9.03^{+9.1}_{-9.0}) \times 10^{-12}$	$(4.42^{+4.4}_{-4.4}) \times 10^{45}$
Swift J1644+57	x44	$1.04^{+0.01}_{-0.01}$	$1.54^{+0.01}_{-0.01}$	1.11 (1579)	$(5.14^{+5.2}_{-5.1}) \times 10^{-12}$	$(2.52^{+2.5}_{-2.5}) \times 10^{45}$
Swift J1644+57	x45	$0.96^{+0.04}_{-0.04}$	$1.87^{+0.04}_{-0.04}$	1.03 (583)	$(6.93^{+7.0}_{-6.9}) \times 10^{-13}$	$(3.39^{+3.4}_{-3.4}) \times 10^{44}$
Swift J1644+57	x46	$0.98^{+0.10}_{-0.09}$	$1.56^{+0.09}_{-0.09}$	1.23 (139)	$(1.53^{+1.6}_{-1.5}) \times 10^{-13}$	$(7.49^{+7.7}_{-7.3}) \times 10^{43}$
Swift J1644+57	x47	$1.13^{+0.05}_{-0.05}$	$1.35^{+0.05}_{-0.05}$	0.93 (615)	$(7.87^{+8.0}_{-7.8}) \times 10^{-13}$	$(3.85^{+3.9}_{-3.8}) \times 10^{44}$
Swift J1644+57	x48	$1.17^{+0.21}_{-0.18}$	$1.48^{+0.23}_{-0.22}$	1.10 (123)	$(1.19^{+1.2}_{-1.1}) \times 10^{-13}$	$(5.83^{+6.0}_{-5.4}) \times 10^{43}$
Swift J1644+57	x49	$1.13^{+0.07}_{-0.06}$	$1.31^{+0.08}_{-0.07}$	0.93 (482)	$(4.07^{+4.1}_{-4.0}) \times 10^{-13}$	$(1.99^{+2.0}_{-2.0}) \times 10^{44}$
Swift J1644+57	x50	$1.02^{+0.10}_{-0.09}$	$1.29^{+0.11}_{-0.11}$	1.05 (192)	$(1.46^{+1.5}_{-1.4}) \times 10^{-13}$	$(7.15^{+7.3}_{-7.1}) \times 10^{43}$
Swift J1644+57	x51	1.05^e	1.51^e		$(3.64^{+3.7}_{-3.6}) \times 10^{-13}$	$(1.78^{+1.8}_{-1.8}) \times 10^{44}$
Swift J1644+57	x52	1.05^e	1.51^e		$(5.08^{+5.1}_{-5.0}) \times 10^{-13}$	$(2.49^{+2.5}_{-2.5}) \times 10^{44}$
Swift J1644+57	x53	1.05^e	1.51^e		$(8.22) \times 10^{-15}$	$(4.02) \times 10^{42}$
Swift J1644+57	x54	1.05^e	1.51^e		$(6.38) \times 10^{-15}$	$(3.12) \times 10^{42}$
Swift J2058+05	x55	$0.22^{+0.15}_{-0.14}$	$1.98^{+0.30}_{-0.27}$	0.67 (51)	$(4.15^{+4.3}_{-4.0}) \times 10^{-14}$	$(5.39^{+5.8}_{-5.1}) \times 10^{44}$
Swift J2058+05	x56	$0.09^{+0.08}_{-0.08}$	$1.51^{+0.23}_{-0.21}$	1.10 (70)	$(4.16^{+4.4}_{-4.0}) \times 10^{-14}$	$(5.40^{+5.1}_{-5.1}) \times 10^{44}$
Wings	x57	0.01	4.50		$(1.99) \times 10^{-13}$	$(1.84) \times 10^{42}$
XMMSL1 J0740-85	x58	0.11	$2.78^{+0.08}_{-0.08}$	1.32 (159)	$(2.82^{+2.9}_{-2.8}) \times 10^{-13}$	$(1.86^{+1.9}_{-1.8}) \times 10^{41}$
XMMSL1 J0740-85	x59	0.11	$3.28^{+0.08}_{-0.08}$	2.37(475)	$(4.44^{+4.5}_{-4.4}) \times 10^{-13}$	$(2.93^{+3.0}_{-2.9}) \times 10^{41}$

Note. — All uncertainties correspond to the 90% confidence level and observations that have similar MJD are combined.

^a N_H is determined either directly from fitting the X-ray emitting spectrum or using the column density derived from the Leiden/Argentine/Bonn (LAB) Survey of Galactic H I (Kalberla et al. 2005)

^b Powerlaw index was derived from either fitting X-ray spectra from either

Table 17
The best fit, or assumed parameters for our absorbed powerlaw model that was used to
derive the 0.3-2.0 keV X-ray flux and luminosity of each TDE candidates from the
XMM-Newton slew observations overlapping the position of the source.

Name	ObsID label	N_H^a (10^{22} cm^{-2})	Γ^b	χ^2 (dof)	X-ray flux ^c (erg/s/cm ²)	X-ray Luminosity ^c (erg/s)
2MASXJ0203	xs1	0.02	4.50		$(1.84^{+2.3}_{-1.4}) \times 10^{-11}$	$(1.67^{+2.0}_{-1.3}) \times 10^{44}$
3XMM J152130.7+074916	xs2	0.03	5.18		$(1.70) \times 10^{-11}$	$(1.61) \times 10^{45}$
3XMM J152130.7+074916	xs3	0.03	5.18		$(7.59) \times 10^{-12}$	$(7.21) \times 10^{44}$
ASASSN-14ae	xs4	0.02	4.50		$(3.49) \times 10^{-12}$	$(1.54) \times 10^{43}$
ASASSN-14ae	xs5	0.02	4.50		$(2.39) \times 10^{-12}$	$(1.06) \times 10^{43}$
ASASSN-14ae	xs6	0.02	4.50		$(2.19) \times 10^{-12}$	$(9.67) \times 10^{42}$
ASASSN-14ae	xs7	0.02	4.50		$(1.88) \times 10^{-12}$	$(8.30) \times 10^{42}$
ASASSN-14li	xs8	0.02	4.50		$(2.53) \times 10^{-12}$	$(2.39) \times 10^{42}$
ASASSN-15lh	xs9	0.03	4.50		$(1.62) \times 10^{-12}$	$(2.84) \times 10^{44}$
css100217	xs10	0.01	4.50		$(1.56) \times 10^{-12}$	$(9.60) \times 10^{43}$
css100217	xs11	0.01	4.50		$(2.95) \times 10^{-12}$	$(1.82) \times 10^{44}$
D23H-1	xs12	0.04	4.50		$(7.66) \times 10^{-12}$	$(7.89) \times 10^{44}$
D3-13	xs13	0.01	4.50		$(2.06) \times 10^{-12}$	$(1.12) \times 10^{45}$
D3-13	xs14	0.01	4.50		$(1.80) \times 10^{-12}$	$(9.82) \times 10^{44}$
DES14C1kia	xs15	0.01	4.50		$(1.09) \times 10^{-12}$	$(8.24) \times 10^{43}$
DES14C1kia	xs16	0.01	4.50		$(3.82) \times 10^{-12}$	$(2.89) \times 10^{44}$
HLX-1	xs17	0.02	2.83 ^e		$(1.01) \times 10^{-12}$	$(1.12) \times 10^{42}$
HLX-1	xs18	0.02	2.83 ^e		$(2.31) \times 10^{-12}$	$(2.56) \times 10^{42}$
HLX-1	xs19	0.02	2.83 ^e		$(2.17) \times 10^{-12}$	$(2.41) \times 10^{42}$
IC 3599	xs20	0.01	4.50		$(3.50) \times 10^{-12}$	$(3.50) \times 10^{42}$
IC 3599	xs21	0.01	4.50		$(1.75) \times 10^{-12}$	$(1.75) \times 10^{42}$
IC 3599	xs22	0.01	4.50		$(1.61) \times 10^{-12}$	$(1.61) \times 10^{42}$
IGR J12580	xs23	0.02	2.30 ^e		$(2.50) \times 10^{-12}$	$(9.08) \times 10^{40}$
IGR J17361-4441	xs24	0.46 ^e	1.98 ^e		$(5.50^{+6.2}_{-4.8}) \times 10^{-11}$	$(2.03^{+2.3}_{-1.8}) \times 10^{44}$
LEDA 095953	xs25	0.04	4.50		$(1.50) \times 10^{-11}$	$(4.61) \times 10^{43}$
NGC 1097	xs26	0.02	4.50		$(3.61^{+5.0}_{-2.2}) \times 10^{-12}$	$(1.37^{+1.9}_{-0.8}) \times 10^{41}$
NGC 1097	xs27	0.02	4.50		$(7.64^{+9.9}_{-3.4}) \times 10^{-12}$	$(2.90^{+3.8}_{-2.0}) \times 10^{41}$
NGC 1097	xs28	0.02	4.50		$(1.24^{+1.6}_{-0.9}) \times 10^{-11}$	$(4.70^{+5.0}_{-3.5}) \times 10^{41}$
NGC 1097	xs29	0.02	4.50		$(4.24^{+6.0}_{-2.5}) \times 10^{-12}$	$(1.61^{+2.3}_{-1.0}) \times 10^{41}$
NGC 2110	xs30	0.20	4.50		$(1.94^{+2.4}_{-1.5}) \times 10^{-11}$	$(2.41^{+3.0}_{-1.9}) \times 10^{42}$
NGC 2110	xs31	0.20	4.50		$(4.49^{+5.2}_{-3.8}) \times 10^{-11}$	$(5.57^{+6.5}_{-4.7}) \times 10^{42}$
NGC 2110	xs32	0.20	4.50		$(4.54^{+3.1}_{-4.0}) \times 10^{-11}$	$(5.63^{+6.4}_{-4.9}) \times 10^{42}$
NGC247	xs33	0.20 ^e	1.62 ^e		$(3.19) \times 10^{-12}$	$(1.92) \times 10^{39}$
NGC247	xs34	0.20 ^e	1.62 ^e		$(2.15) \times 10^{-12}$	$(1.29) \times 10^{39}$
NGC 3599	xs35	0.01	2.57 ^e		$(3.94^{+4.7}_{-3.2}) \times 10^{-11}$	$(6.15^{+7.3}_{-5.0}) \times 10^{41}$
NGC 3599	xs36	0.01	2.57 ^e		$(3.52^{+4.0}_{-3.1}) \times 10^{-11}$	$(5.49^{+6.0}_{-4.8}) \times 10^{41}$
NGC 3599	xs37	0.01	2.57 ^e		$(8.54^{+13.9}_{-3.1}) \times 10^{-12}$	$(1.33^{+2.2}_{-0.5}) \times 10^{41}$
NGC 3599	xs38	0.01	2.57 ^e		$(6.70) \times 10^{-12}$	$(1.05) \times 10^{41}$
NGC 3599	xs39	0.01	2.57 ^e		$(3.58) \times 10^{-12}$	$(5.58) \times 10^{40}$
NGC 3599	xs40	0.01	2.57 ^e		$(3.19) \times 10^{-12}$	$(4.98) \times 10^{40}$
NGC 5905	xs41	0.01	4.50		$(9.70) \times 10^{-13}$	$(2.67) \times 10^{41}$
OGLE16aaa	xs42	0.03	4.50		$(2.51) \times 10^{-12}$	$(1.99) \times 10^{44}$
PGC 1190358	xs43	0.05	4.50		$(3.31) \times 10^{-12}$	$(4.20) \times 10^{41}$
PGC 1190358	xs44	0.05	4.50		$(4.14) \times 10^{-12}$	$(5.26) \times 10^{41}$
PGC 1190358	xs45	0.05	4.50		$(3.58) \times 10^{-12}$	$(4.55) \times 10^{41}$
Pictor A	xs46	0.04	1.73 ^e		$(2.50^{+3.0}_{-2.0}) \times 10^{-11}$	$(6.59^{+7.9}_{-5.4}) \times 10^{43}$
Pictor A	xs47	0.04	1.73 ^e		$(4.33^{+4.8}_{-3.8}) \times 10^{-11}$	$(1.14^{+1.3}_{-1.0}) \times 10^{44}$
PS1-10jh	xs48	0.01	4.50		$(3.03) \times 10^{-12}$	$(2.54) \times 10^{44}$
PS1-10jh	xs49	0.01	4.50		$(4.93) \times 10^{-12}$	$(4.14) \times 10^{44}$
PS1-10jh	xs50	0.01	4.50		$(2.43) \times 10^{-12}$	$(2.04) \times 10^{44}$
PS1-10jh	xs51	0.01	4.50		$(9.16) \times 10^{-12}$	$(7.69) \times 10^{44}$
PS1-10jh	xs52	0.01	4.50		$(4.08) \times 10^{-12}$	$(3.42) \times 10^{44}$
PS1-10jh	xs53	0.01	4.50		$(9.16) \times 10^{-13}$	$(7.69) \times 10^{43}$
PS1-10jh	xs54	0.01	4.50		$(2.38^{+3.8}_{-1.0}) \times 10^{-12}$	$(2.00^{+3.2}_{-0.8}) \times 10^{44}$
PS1-11af	xs55	0.02	4.50		$(1.48) \times 10^{-12}$	$(1.02) \times 10^{45}$
PS1-11af	xs56	0.02	4.50		$(4.93) \times 10^{-12}$	$(3.38) \times 10^{45}$
PS1-12yp	xs57	0.01	4.50		$(2.17) \times 10^{-12}$	$(3.83) \times 10^{45}$
PS1-12yp	xs58	0.01	4.50		$(1.52) \times 10^{-12}$	$(2.69) \times 10^{45}$
PS1-12yp	xs59	0.01	4.50		$(4.41) \times 10^{-13}$	$(7.79) \times 10^{44}$
PTF-09axc	xs60	0.03	4.50		$(3.11) \times 10^{-12}$	$(1.08) \times 10^{44}$
PTF-09ge	xs61	0.02	4.50		$(2.86) \times 10^{-12}$	$(2.83) \times 10^{43}$
PTF-10iam	xs62	0.01	4.50		$(4.74) \times 10^{-12}$	$(1.48) \times 10^{44}$
PTF-10iam	xs63	0.01	4.50		$(4.25) \times 10^{-12}$	$(1.32) \times 10^{44}$

Table 17 — *Continued*

Name	ObsID label	N_H^a (10^{22} cm $^{-2}$)	Γ^b	χ^2 (dof)	X-ray flux ^c (erg/s/cm 2)	X-ray Luminosity ^c (erg/s)
PTF-10iam	xs64	0.01	4.50		$(2.75) \times 10^{-12}$	$(8.57) \times 10^{43}$
PTF-10nuj	xs65	0.01	4.50		$(2.28) \times 10^{-12}$	$(1.09) \times 10^{44}$
PTF-10nuj	xs66	0.01	4.50		$(1.63) \times 10^{-12}$	$(7.76) \times 10^{43}$
PTF-11glr	xs67	0.02	4.50		$(7.90) \times 10^{-12}$	$(1.05) \times 10^{45}$
RBS 1032	xs68	0.02	4.50		$(2.98) \times 10^{-12}$	$(4.52) \times 10^{42}$
RBS 1032	xs69	0.02	4.50		$(1.03) \times 10^{-11}$	$(1.56) \times 10^{43}$
RBS 1032	xs70	0.02	4.50		$(3.28) \times 10^{-12}$	$(4.98) \times 10^{42}$
RX J1242-11A	xs71	0.04	4.50		$(1.86) \times 10^{-12}$	$(1.09) \times 10^{43}$
RX J1420+53	xs72	0.01	4.50		$(2.97) \times 10^{-12}$	$(1.80) \times 10^{44}$
RX J1624+75	xs73	0.04	4.50		$(4.22) \times 10^{-12}$	$(4.12) \times 10^{43}$
RX J1624+75	xs74	0.04	4.50		$(3.51) \times 10^{-11}$	$(3.43) \times 10^{44}$
RX J1624+75	xs75	0.04	4.50		$(1.09) \times 10^{-12}$	$(1.06) \times 10^{43}$
RX J1624+75	xs76	0.04	4.50		$(3.10) \times 10^{-12}$	$(3.03) \times 10^{43}$
SDSS J0748	xs77	0.06	4.50		$(1.93) \times 10^{-11}$	$(1.75) \times 10^{44}$
SDSS J0938	xs78	0.03	4.50		$(3.48) \times 10^{-12}$	$(9.08) \times 10^{43}$
SDSS J0938	xs79	0.03	4.50		$(2.10) \times 10^{-12}$	$(5.48) \times 10^{43}$
SDSS J0939	xs80	0.01 ^d	3.03 ^d		$(6.71) \times 10^{-12}$	$(6.98) \times 10^{44}$
SDSS J1011	xs81	0.01	4.50		$(5.84) \times 10^{-12}$	$(1.17) \times 10^{45}$
SDSS J1011	xs82	0.01	4.50		$(2.06) \times 10^{-12}$	$(4.12) \times 10^{44}$
SDSS J1011	xs83	0.01	4.50		$(2.84) \times 10^{-12}$	$(5.68) \times 10^{44}$
SDSS J1055	xs84	0.01	4.50		$(3.77) \times 10^{-12}$	$(5.12) \times 10^{43}$
SDSS J1055	xs85	0.01	4.50		$(1.34) \times 10^{-12}$	$(1.82) \times 10^{43}$
SDSS J1201	xs86	0.24 ^e	5.06 ^e		$(3.44) \times 10^{-12}$	$(2.05) \times 10^{44}$
SDSS J1201	xs87	0.24 ^e	5.06 ^e		$(9.12) \times 10^{-12}$	$(5.44) \times 10^{44}$
SDSS J1201	xs88	0.24 ^e	5.06 ^e		$(1.72^{+2.1}_{-1.4}) \times 10^{-11}$	$(1.03^{+1.2}_{-0.8}) \times 10^{45}$
SDSS J1201	xs89	0.24 ^e	5.06 ^e		$(3.60) \times 10^{-12}$	$(2.15) \times 10^{44}$
SDSS J1241	xs90	0.02	4.50		$(9.86) \times 10^{-12}$	$(4.01) \times 10^{43}$
SDSS J1311	xs91	0.02	4.50		$(1.01) \times 10^{-11}$	$(9.72) \times 10^{44}$
SDSS J1311	xs92	0.02	4.50		$(9.07) \times 10^{-12}$	$(8.73) \times 10^{44}$
SDSS J1323	xs93	0.01	4.50		$(1.03^{+1.2}_{-0.8}) \times 10^{-11}$	$(1.99^{+2.4}_{-1.6}) \times 10^{44}$
SDSS J1323	xs94	0.01	4.50		$(1.28) \times 10^{-12}$	$(2.47) \times 10^{43}$
SDSS J1323	xs95	0.01	4.50		$(4.61) \times 10^{-12}$	$(8.91) \times 10^{43}$
SDSS J1350	xs96	0.01	4.50		$(4.38) \times 10^{-12}$	$(6.55) \times 10^{43}$
Swift J1112.2-8238	xs97	0.09	4.50		$(6.64) \times 10^{-12}$	$(3.83) \times 10^{46}$
Swift J1112.2-8238	xs98	0.09	4.50		$(8.20) \times 10^{-13}$	$(4.73) \times 10^{45}$
Swift J1112.2-8238	xs99	0.09	4.50		$(1.69) \times 10^{-12}$	$(9.75) \times 10^{45}$
Swift J1644+57	xs100	1.05 ^e	1.51 ^e		$(3.01) \times 10^{-11}$	$(1.47) \times 10^{46}$
Swift J1644+57	xs101	1.05 ^e	1.51 ^e		$(4.86) \times 10^{-12}$	$(2.38) \times 10^{45}$
Swift J1644+57	xs102	1.05 ^e	1.51 ^e		$(3.09) \times 10^{-12}$	$(1.51) \times 10^{45}$
Swift J1644+57	xs103	1.05 ^e	1.51 ^e		$(9.19) \times 10^{-13}$	$(4.50) \times 10^{44}$
Swift J2058+05	xs104	0.16 ^e	1.89 ^e		$(4.42) \times 10^{-12}$	$(5.74) \times 10^{46}$
Swift J2058+05	xs105	0.16 ^e	1.89 ^e		$(1.87) \times 10^{-12}$	$(2.43) \times 10^{46}$
Swift J2058+05	xs106	0.16 ^e	1.89 ^e		$(5.72) \times 10^{-12}$	$(7.43) \times 10^{46}$
Swift J2058+05	xs107	0.16 ^e	1.89 ^e		$(3.06) \times 10^{-12}$	$(3.97) \times 10^{46}$
TDE2	xs108	0.04	4.50		$(2.82) \times 10^{-12}$	$(5.95) \times 10^{44}$
Wings	xs109	0.01	4.50		$(6.22) \times 10^{-13}$	$(5.75) \times 10^{42}$
XMMSL1 J0740-85	xs110	0.11 ^e	3.03 ^e		$(2.80) \times 10^{-12}$	$(1.85) \times 10^{42}$
XMMSL1 J0740-85	xs111	0.11 ^e	3.03 ^e		$(6.21^{+7.1}_{-5.3}) \times 10^{-12}$	$(4.10^{+4.7}_{-3.5}) \times 10^{42}$

Note. — All uncertainties correspond to the 90% confidence level and observations that have similar MJD are combined.

^a N_H is determined either directly from fitting the X-ray emitting spectrum or using the column density derived from the Leiden/Argentine/Bonn (LAB) Survey of Galactic H I (Kalberla et al. 2005)

^b Powerlaw index was derived from either fitting X-ray spectra from either *ROSAT*, *XMM* or *Chandra* with a powerlaw model or was assumed to be equal to 4.5. If the following Γ has an uncertainty, the powerlaw index was derived from fitting the X-ray spectrum extracted from *ROSAT*.

^c Absorbed X-ray flux and X-ray luminosity is calculated for an energy range of 0.3-2.0 keV.

^d Value frozen to that obtained from modelling the *XMM-Newton* X-ray spectrum.

^e Value set to the average of that obtained from modelling multiple *XMM-Newton* spectra.

Table 18

The best fit, or assumed parameters for our absorbed powerlaw model that was used to derive the 0.3-2.0 keV X-ray flux and luminosity of each TDE candidate from the *Swift* *XRT* observations overlapping the position of the source.

Name	ObsID label	N_H^a (10^{22} cm $^{-2}$)	Γ^b	χ^2 (dof)	X-ray flux ^c (erg/s/cm 2)	X-ray Luminosity ^c (erg/s)
2MASXJ0203	sw1	0.02	$1.40^{+0.35}_{-0.33}$	1.30 (4)	$(4.01^{+4.6}_{-3.5}) \times 10^{-13}$	$(3.65^{+4.2}_{-3.2}) \times 10^{42}$
2MASXJ0203	sw2	0.02	$1.28^{+0.46}_{-0.46}$	1.30 (2)	$(4.61^{+3.3}_{-3.0}) \times 10^{-13}$	$(4.19^{+3.8}_{-3.6}) \times 10^{42}$
2MASX J0249	sw3	0.44	4.50		$(1.30) \times 10^{-13}$	$(9.95) \times 10^{40}$
2MASX J0249	sw4	0.44	4.50		$(1.21^{+2.0}_{-0.4}) \times 10^{-13}$	$(9.26^{+15.2}_{-3.3}) \times 10^{40}$
2MASX J0249	sw5	0.44	4.50		$(7.52^{+11.9}_{-3.1}) \times 10^{-14}$	$(5.76^{+9.1}_{-2.4}) \times 10^{40}$
2MASX J0249	sw6	0.44	4.50		$(1.15) \times 10^{-13}$	$(8.81) \times 10^{40}$
2MASX J0249	sw7	0.44	4.50		$(1.07) \times 10^{-13}$	$(8.19) \times 10^{40}$
2MASX J0249	sw8	0.44	4.50		$(8.24) \times 10^{-14}$	$(6.31) \times 10^{40}$
2MASX J0249	sw9	0.44	4.50		$(6.68) \times 10^{-14}$	$(5.11) \times 10^{40}$
2MASX J0249	sw10	0.44	4.50		$(8.80) \times 10^{-14}$	$(6.74) \times 10^{40}$
3XMM J152130.7+074916	sw11	0.03	4.50		$(1.89) \times 10^{-13}$	$(1.80) \times 10^{43}$
ASASSN-14ae	sw12	0.02	4.50		$(3.74) \times 10^{-14}$	$(1.65) \times 10^{41}$
ASASSN-14ae	sw13	0.02	4.50		$(4.39) \times 10^{-14}$	$(1.94) \times 10^{41}$
ASASSN-14ae	sw14	0.02	4.50		$(3.73) \times 10^{-14}$	$(1.65) \times 10^{41}$
ASASSN-14ae	sw15	0.02	4.50		$(7.05) \times 10^{-14}$	$(3.11) \times 10^{41}$
ASASSN-14ae	sw16	0.02	4.50		$(5.39) \times 10^{-14}$	$(2.38) \times 10^{41}$
ASASSN-14li	sw17	$0.12^{+0.02}_{-0.02}$	$7.65^{+0.32}_{-0.30}$	1.60 (41)	$(1.17^{+1.2}_{-1.1}) \times 10^{-11}$	$(1.10^{+1.1}_{-1.1}) \times 10^{43}$
ASASSN-14li	sw18	$0.14^{+0.01}_{-0.01}$	$8.04^{+0.13}_{-0.12}$	2.99 (66)	$(1.02^{+1.0}_{-1.0}) \times 10^{-11}$	$(9.62^{+9.7}_{-9.5}) \times 10^{42}$
ASASSN-14li	sw19	$0.14^{+0.01}_{-0.01}$	$8.60^{+0.12}_{-0.24}$	1.68 (45)	$(5.26^{+3.3}_{-3.2}) \times 10^{-12}$	$(4.96^{+3.0}_{-3.9}) \times 10^{42}$
ASASSN-14li	sw20	$0.14^{+0.02}_{-0.03}$	$9.25^{+0.07}_{-0.70}$	0.93 (26)	$(3.35^{+3.9}_{-2.4}) \times 10^{-12}$	$(3.16^{+3.6}_{-2.3}) \times 10^{42}$
ASASSN-14li	sw21	$0.13^{+0.01}_{-0.01}$	10.00^f	1.241 (26)	$(2.62^{+4.2}_{-1.7}) \times 10^{-12}$	$(2.47^{+4.0}_{-1.7}) \times 10^{42}$
ASASSN-14li	sw22	$0.08^{+0.03}_{-0.05}$	$8.83^{+1.17}_{-1.70}$	0.74 (19)	$(1.95^{+2.0}_{-0.8}) \times 10^{-12}$	$(1.84^{+1.8}_{-0.7}) \times 10^{42}$
ASASSN-14li	sw23	$0.05^{+0.06}_{-0.04}$	$7.82^{+2.10}_{-2.60}$	1.09 (12)	$(8.45^{+9.0}_{-0.9}) \times 10^{-13}$	$(7.97^{+8.5}_{-0.9}) \times 10^{41}$
ASASSN-15lh	sw24	0.03	4.50		$(2.92) \times 10^{-14}$	$(5.12) \times 10^{42}$
ASASSN-15lh	sw25	0.03	4.50		$(2.30) \times 10^{-14}$	$(4.03) \times 10^{42}$
ASASSN-15lh	sw26	0.03	4.50		$(2.80) \times 10^{-14}$	$(4.91) \times 10^{42}$
ASASSN-15lh	sw27	0.03	4.50		$(1.97) \times 10^{-14}$	$(3.45) \times 10^{42}$
ASASSN-15lh	sw28	0.03	4.50		$(1.93) \times 10^{-14}$	$(3.38) \times 10^{42}$
ASASSN-15lh	sw29	0.03	4.50		$(2.25) \times 10^{-14}$	$(3.94) \times 10^{42}$
ASASSN-15oi	sw30	0.06	$2.95^{+0.88}_{-0.77}$	2.87 (3)	$(5.74^{+6.8}_{-4.9}) \times 10^{-14}$	$(3.15^{+3.7}_{-2.7}) \times 10^{41}$
ASASSN-15oi	sw31	0.06	$3.91^{+0.88}_{-0.77}$	3427 (5)	$(6.72^{+7.4}_{-5.8}) \times 10^{-14}$	$(3.69^{+4.1}_{-3.1}) \times 10^{41}$
css100217	sw32	0.06^d	3.99^d		$(9.93^{+13.0}_{-6.8}) \times 10^{-14}$	$(6.11^{+8.0}_{-4.2}) \times 10^{42}$
css100217	sw33	0.06^d	3.99^d		$(5.15^{+0.0}_{-0.00}) \times 10^{-14}$	$(3.17) \times 10^{42}$
css100217	sw34	$0.06^{+0.16}_{-0.06}$	$3.99^{+2.15}_{-1.10}$	2.06 (5)	$(4.21^{+4.6}_{-2.6}) \times 10^{-13}$	$(2.59^{+2.9}_{-2.2}) \times 10^{43}$
D3-13	sw35	0.01	4.50		$(8.39) \times 10^{-14}$	$(4.58) \times 10^{43}$
D3-13	sw36	0.01	4.50		$(1.01) \times 10^{-13}$	$(5.51) \times 10^{43}$
D3-13	sw37	0.01	4.50		$(3.05) \times 10^{-13}$	$(1.66) \times 10^{44}$
DES14C1kia	sw38	0.01	4.50		$(2.13) \times 10^{-14}$	$(1.61) \times 10^{42}$
DES14C1kia	sw39	0.01	4.50		$(2.94) \times 10^{-14}$	$(2.22) \times 10^{42}$
Dougie	sw40	0.01	4.50		$(1.95) \times 10^{-14}$	$(2.15) \times 10^{42}$
Dougie	sw41	0.01	4.50		$(2.55) \times 10^{-14}$	$(2.81) \times 10^{42}$
GRB060218, SN2006aj	sw42	0.41^d	3.03^d		$(2.67) \times 10^{-14}$	$(6.83) \times 10^{40}$
GRB060218, SN2006aj	sw43	0.41^d	3.03^d		$(4.08) \times 10^{-14}$	$(1.04) \times 10^{41}$
GRB060218, SN2006aj	sw44	0.41^d	3.03^d		$(3.88) \times 10^{-14}$	$(9.92) \times 10^{40}$
GRB060218, SN2006aj	sw45	0.41^d	3.03^d		$(2.77) \times 10^{-14}$	$(7.08) \times 10^{40}$
GRB060218, SN2006aj	sw46	0.41^d	3.03^d		$(3.34) \times 10^{-14}$	$(8.54) \times 10^{40}$
GRB060218, SN2006aj	sw47	0.41^d	3.03^d		$(4.19) \times 10^{-14}$	$(1.07) \times 10^{41}$
GRB060218, SN2006aj	sw48	0.41^d	3.03^d		$(2.77) \times 10^{-14}$	$(7.08) \times 10^{40}$
GRB060218, SN2006aj	sw49	0.41^d	3.03^d		$(2.95) \times 10^{-14}$	$(7.54) \times 10^{40}$
GRB060218, SN2006aj	sw50	0.41^d	3.03^d		$(2.85) \times 10^{-14}$	$(7.29) \times 10^{40}$
GRB060218, SN2006aj	sw51	$0.41^{+0.07}_{-0.07}$	$3.03^{+0.22}_{-0.20}$	1.05 (68)	$(1.29^{+1.3}_{-1.2}) \times 10^{-13}$	$(3.30^{+3.3}_{-3.2}) \times 10^{41}$
GRB060218, SN2006aj	sw52	0.41^d	3.03^d		$(1.54) \times 10^{-14}$	$(3.94) \times 10^{40}$
GRB060218, SN2006aj	sw53	0.41^d	3.03^d		$(2.39) \times 10^{-14}$	$(6.11) \times 10^{40}$
GRB060218, SN2006aj	sw54	0.41^d	3.03^d		$(3.23) \times 10^{-14}$	$(8.26) \times 10^{40}$
HLX-1	sw55	$0.07^{+0.06}_{-0.05}$	$3.56^{+0.52}_{-0.43}$	1.35 (15)	$(2.68^{+2.9}_{-2.5}) \times 10^{-13}$	$(2.97^{+3.2}_{-2.8}) \times 10^{41}$
HLX-1	sw56	$0.67^{+0.06}_{-0.05}$	$3.56^{+0.52}_{-0.43}$	1.35 (15)	$(2.98^{+3.2}_{-2.8}) \times 10^{-13}$	$(3.31^{+3.3}_{-3.1}) \times 10^{41}$
HLX-1	sw57	$0.07^{+0.06}_{-0.05}$	$3.56^{+0.52}_{-0.43}$	1.35 (15)	$(2.65^{+2.8}_{-2.5}) \times 10^{-13}$	$(2.94^{+3.1}_{-2.7}) \times 10^{41}$
HLX-1	sw58	$0.07^{+0.06}_{-0.05}$	$3.56^{+0.52}_{-0.43}$	1.35 (15)	$(2.68^{+2.9}_{-2.5}) \times 10^{-13}$	$(2.97^{+3.2}_{-2.8}) \times 10^{41}$
HLX-1	sw59	0.18^e	3.85^e		$(6.28) \times 10^{-14}$	$(6.97) \times 10^{40}$
HLX-1	sw60	$0.36^{+0.14}_{-0.12}$	$5.59^{+0.78}_{-0.78}$	0.77 (29)	$(4.26^{+4.5}_{-4.0}) \times 10^{-13}$	$(4.73^{+5.0}_{-4.0}) \times 10^{41}$
HLX-1	sw61	$0.11^{+0.06}_{-0.05}$	$3.74^{+0.58}_{-0.41}$	1.46 (22)	$(2.09^{+2.3}_{-2.0}) \times 10^{-13}$	$(2.32^{+2.3}_{-2.2}) \times 10^{41}$
HLX-1	sw62	0.18^e	3.85^e		$(5.74) \times 10^{-14}$	$(6.37) \times 10^{40}$
HLX-1	sw63	$0.16^{+0.11}_{-0.08}$	$3.79^{+0.75}_{-0.61}$	0.83 (13)	$(2.77^{+3.0}_{-2.6}) \times 10^{-13}$	$(3.07^{+3.3}_{-2.9}) \times 10^{41}$

Table 18 — Continued

Name	ObsID label	N_H^a (10^{22} cm^{-2})	Γ^b	χ^2 (dof)	X-ray flux ^c (erg/s/cm ²)	X-ray Luminosity ^c (erg/s)
HLX-1	sw64	$0.18^{+0.05}_{-0.04}$	$4.34^{+0.37}_{-0.32}$	1.58 (42)	$(3.48^{+3.6}_{-3.4}) \times 10^{-13}$	$(3.86^{+4.0}_{-3.7}) \times 10^{41}$
HLX-1	sw65	0.18^e	3.85^e		$(1.14) \times 10^{-13}$	$(1.27) \times 10^{41}$
HLX-1	sw66	0.18^e	3.85^e		$(5.02) \times 10^{-14}$	$(5.57) \times 10^{40}$
HLX-1	sw67	$0.13^{+0.10}_{-0.07}$	$3.55^{+0.68}_{-0.57}$	1.36 (13)	$(1.62^{+1.7}_{-1.5}) \times 10^{-13}$	$(1.80^{+1.9}_{-1.7}) \times 10^{41}$
HLX-1	sw68	$0.10^{+0.15}_{-0.09}$	$3.17^{+0.05}_{-0.68}$	1.09 (6)	$(1.67^{+1.8}_{-1.5}) \times 10^{-13}$	$(1.85^{+2.0}_{-1.6}) \times 10^{41}$
HLX-1	sw69	0.18^e	3.85^e		$(4.95) \times 10^{-14}$	$(5.49) \times 10^{40}$
HLX-1	sw70	$0.21^{+0.10}_{-0.08}$	$4.35^{+0.71}_{-0.56}$	0.75 (17)	$(2.09^{+2.2}_{-2.0}) \times 10^{-13}$	$(2.32^{+2.5}_{-2.2}) \times 10^{41}$
HLX-1	sw71	$0.10^{+0.15}_{-0.09}$	$3.47^{+0.99}_{-0.67}$	1.08 (8)	$(9.32^{+10.0}_{-8.6}) \times 10^{-14}$	$(1.03^{+1.1}_{-1.0}) \times 10^{41}$
HLX-1	sw72	0.18^e	3.85^e		$(1.40) \times 10^{-13}$	$(1.55) \times 10^{41}$
HLX-1	sw73	0.18^e	3.85^e		$(7.90) \times 10^{-14}$	$(8.77) \times 10^{40}$
HLX-1	sw74	$0.13^{+0.09}_{-0.07}$	$3.48^{+79.00}_{-0.58}$	1.79 (14)	$(2.61^{+2.8}_{-2.4}) \times 10^{-13}$	$(2.90^{+3.1}_{-2.7}) \times 10^{41}$
HLX-1	sw75	0.18^e	3.85^e		$(8.40) \times 10^{-14}$	$(9.32) \times 10^{40}$
HLX-1	sw76	0.18^e	3.85^e		$(3.22^{+4.2}_{-2.2}) \times 10^{-14}$	$(3.57^{+4.7}_{-2.5}) \times 10^{40}$
HLX-1	sw77	0.18^e	3.85^e		$(7.29) \times 10^{-14}$	$(8.09) \times 10^{40}$
HLX-1	sw78	0.18^e	3.85^e		$(5.02) \times 10^{-14}$	$(5.57) \times 10^{40}$
HLX-1	sw79	0.18^e	3.85^e		$(6.24) \times 10^{-14}$	$(6.93) \times 10^{40}$
HLX-1	sw80	$0.12^{+0.16}_{-0.09}$	$4.18^{+1.20}_{-0.79}$	1.75 (6)	$(2.15^{+2.4}_{-2.0}) \times 10^{-13}$	$(2.39^{+2.6}_{-2.2}) \times 10^{41}$
HLX-1	sw81	0.18^e	3.85^e		$(5.52) \times 10^{-14}$	$(6.13) \times 10^{40}$
HLX-1	sw82	0.18^e	3.85^e		$(5.22) \times 10^{-14}$	$(5.79) \times 10^{40}$
HLX-1	sw83	0.18^e	3.85^e		$(6.75) \times 10^{-14}$	$(7.49) \times 10^{40}$
IC 3599	sw84	$0.08^{+0.08}_{-0.06}$	$4.49^{+1.01}_{-0.87}$	0.91 (9)	$(7.11^{+7.7}_{-6.7}) \times 10^{-12}$	$(7.11^{+7.7}_{-6.7}) \times 10^{42}$
IC 3599	sw85	$0.07^{+0.07}_{-0.06}$	$4.14^{+0.91}_{-0.83}$	0.81 (1)	$(1.57^{+1.8}_{-1.3}) \times 10^{-12}$	$(1.57^{+1.8}_{-1.3}) \times 10^{42}$
IC 3599	sw86	0.07^e	4.31^e		$(8.61^{+11.4}_{-5.8}) \times 10^{-14}$	$(8.61^{+11.4}_{-5.8}) \times 10^{40}$
IC 3599	sw87	0.07^e	4.31^e		$(6.38^{+8.6}_{-4.2}) \times 10^{-14}$	$(6.38^{+8.6}_{-4.2}) \times 10^{40}$
IC 3599	sw88	0.07^e	4.31^e		$(7.76^{+10.3}_{-5.2}) \times 10^{-14}$	$(7.76^{+10.3}_{-5.2}) \times 10^{40}$
IC 3599	sw89	0.07^e	4.31^e		$(8.23) \times 10^{-14}$	$(8.23) \times 10^{40}$
IC 3599	sw90	0.07^e	4.31^e		$(7.58^{+10.2}_{-5.0}) \times 10^{-14}$	$(7.58^{+10.2}_{-5.0}) \times 10^{40}$
IC 3599	sw91	0.07^e	4.31^e		$(1.27) \times 10^{-13}$	$(1.27) \times 10^{41}$
IC 3599	sw92	0.07^e	4.31^e		$(5.13) \times 10^{-16}$	$(5.13) \times 10^{38}$
IC 3599	sw93	0.07^e	4.31^e		$(7.11) \times 10^{-14}$	$(7.11) \times 10^{40}$
IGR J12580	sw94	$7.93^{+2.28}_{-2.03}$	$1.73^{+0.43}_{-0.40}$	1.47 (34)	$(4.34^{+5.6}_{-3.0}) \times 10^{-13}$	$(1.58^{+2.0}_{-1.1}) \times 10^{40}$
IGR J12580	sw95	$7.93^{+2.28}_{-2.03}$	1.73		$(2.07^{+2.9}_{-1.3}) \times 10^{-14}$	$(7.52^{+10.4}_{-4.7}) \times 10^{38}$
IGR J17361-4441	sw96	$0.18^{+0.05}_{-0.04}$	$0.63^{+0.04}_{-0.04}$	1.59 (430)	$(3.87^{+3.9}_{-1.3}) \times 10^{-12}$	$(1.43^{+1.5}_{-1.4}) \times 10^{43}$
IGR J17361-4441	sw97	$0.65^{+0.04}_{-0.04}$	$1.79^{+0.05}_{-0.05}$	1.08 (372)	$(4.43^{+4.3}_{-4.4}) \times 10^{-12}$	$(1.63^{+1.6}_{-1.6}) \times 10^{43}$
IGR J17361-4441	sw98	$0.42^{+0.22}_{-0.16}$	$2.26^{+0.45}_{-0.37}$	0.93 (11)	$(2.33^{+2.5}_{-2.2}) \times 10^{-13}$	$(8.60^{+9.2}_{-4.9}) \times 10^{41}$
IGR J17361-4441	sw99	0.42^e	1.56^e		$(5.76^{+8.8}_{-3.7}) \times 10^{-14}$	$(2.13^{+1.9}_{-1.9}) \times 10^{41}$
IGR J17361-4441	sw100	0.42^e	1.56^e		$(1.62^{+2.1}_{-1.2}) \times 10^{-13}$	$(5.98^{+7.7}_{-4.3}) \times 10^{41}$
IGR J17361-4441	sw101	0.42^e	1.56^e		$(3.21^{+3.5}_{-3.0}) \times 10^{-13}$	$(1.18^{+1.3}_{-1.1}) \times 10^{42}$
iPTF16fml	sw102	0.06	4.50		$(5.62) \times 10^{-14}$	$(3.29) \times 10^{40}$
iPTF16fml	sw103	0.06	4.50		$(5.10) \times 10^{-14}$	$(2.98) \times 10^{40}$
NGC 1097	sw104	$0.17^{+0.20}_{-0.14}$	$2.84^{+1.18}_{-0.80}$	2.61 (4)	$(1.00^{+1.1}_{-0.9}) \times 10^{-12}$	$(3.79^{+4.2}_{-3.3}) \times 10^{40}$
NGC 1097	sw105	$0.05^{+0.08}_{-0.04}$	$1.82^{+0.41}_{-0.35}$	1.63 (11)	$(1.38^{+1.5}_{-1.3}) \times 10^{-12}$	$(5.23^{+5.6}_{-4.8}) \times 10^{40}$
NGC 1097	sw106	$0.07^{+0.08}_{-0.07}$	$1.89^{+0.30}_{-0.28}$	0.78 (10)	$(1.37^{+1.3}_{-1.3}) \times 10^{-12}$	$(5.19^{+5.6}_{-4.9}) \times 10^{40}$
NGC 1097	sw107	$0.11^{+0.07}_{-0.06}$	$1.85^{+0.28}_{-0.25}$	1.61 (16)	$(1.08^{+1.4}_{-1.0}) \times 10^{-12}$	$(4.09^{+5.1}_{-3.8}) \times 10^{40}$
NGC 1097	sw108	$0.17^{+0.09}_{-0.07}$	$2.23^{+0.41}_{-0.36}$	2.06 (16)	$(1.11^{+1.2}_{-1.1}) \times 10^{-12}$	$(4.21^{+4.4}_{-4.0}) \times 10^{40}$
NGC 1097	sw109	$0.10^{+0.04}_{-0.03}$	$1.84^{+0.15}_{-0.14}$	1.44 (49)	$(1.21^{+1.2}_{-1.2}) \times 10^{-12}$	$(4.59^{+4.7}_{-4.4}) \times 10^{40}$
NGC 1097	sw110	$0.11^{+0.03}_{-0.03}$	$1.99^{+0.14}_{-0.13}$	0.87 (61)	$(1.05^{+1.1}_{-1.0}) \times 10^{-12}$	$(3.98^{+4.1}_{-3.9}) \times 10^{40}$
NGC 1097	sw111	$0.17^{+0.09}_{-0.07}$	$2.28^{+0.35}_{-0.30}$	1.76 (13)	$(1.01^{+1.1}_{-1.0}) \times 10^{-12}$	$(3.83^{+4.0}_{-3.6}) \times 10^{40}$
NGC 2110	sw112	$3.34^{+0.21}_{-0.20}$	$0.80^{+0.07}_{-0.07}$	0.99 (451)	$(1.55^{+1.6}_{-1.5}) \times 10^{-12}$	$(1.92^{+2.0}_{-1.9}) \times 10^{41}$
NGC 2110	sw113	$3.56^{+0.96}_{-0.76}$	$0.70^{+0.25}_{-0.23}$	1.18 (47)	$(8.48^{+9.4}_{-7.6}) \times 10^{-13}$	$(1.05^{+1.2}_{-0.9}) \times 10^{41}$
NGC 2110	sw114	$4.38^{+0.62}_{-0.55}$	$0.86^{+0.16}_{-0.16}$	1.33 (16)	$(1.19^{+1.3}_{-1.1}) \times 10^{-12}$	$(1.48^{+1.6}_{-1.4}) \times 10^{41}$
NGC 2110	sw115	$4.00^{+0.22}_{-0.21}$	$0.88^{+0.07}_{-0.07}$	1.05 (499)	$(2.01^{+2.1}_{-2.0}) \times 10^{-12}$	$(2.49^{+2.4}_{-2.4}) \times 10^{41}$
NGC 2110	sw116	$4.18^{+0.51}_{-0.46}$	$0.94^{+0.14}_{-0.13}$	0.93 (144)	$(7.96^{+8.3}_{-7.5}) \times 10^{-13}$	$(9.87^{+10.3}_{-9.2}) \times 10^{40}$
NGC 2110	sw117	$4.07^{+0.31}_{-0.30}$	$0.93^{+0.10}_{-0.09}$	1.06 (280)	$(2.23^{+2.3}_{-2.2}) \times 10^{-12}$	$(2.77^{+2.8}_{-2.7}) \times 10^{41}$
NGC247	sw118	$0.12^{+0.12}_{-0.09}$	$1.79^{+0.36}_{-0.31}$	0.70 (9)	$(1.99^{+2.1}_{-1.8}) \times 10^{-13}$	$(1.20^{+1.8}_{-1.1}) \times 10^{38}$
NGC247	sw119	0.12^d	1.79^d		$(5.99^{+7.2}_{-4.8}) \times 10^{-14}$	$(3.61^{+4.3}_{-2.9}) \times 10^{37}$
NGC247	sw120	0.12^d	1.79^d		$(6.40) \times 10^{-14}$	$(3.85) \times 10^{37}$
NGC247	sw121	0.12^d	1.79^d		$(6.34) \times 10^{-14}$	$(3.82) \times 10^{37}$
NGC247	sw122	0.12^d	1.79^d		$(9.89) \times 10^{-14}$	$(5.95) \times 10^{37}$
NGC247	sw123	0.12^d	1.79^d		$(8.21) \times 10^{-14}$	$(4.94) \times 10^{37}$
NGC247	sw124	0.12^d	1.79^d		$(6.68) \times 10^{-14}$	$(4.02) \times 10^{37}$
NGC 3599	sw125	0.01	4.50		$(5.86) \times 10^{-14}$	$(9.14) \times 10^{38}$
NGC 3599	sw126	0.01	4.50		$(1.08) \times 10^{-13}$	$(1.68) \times 10^{39}$
NGC 3599	sw127	0.01	4.50		$(9.49) \times 10^{-14}$	$(1.48) \times 10^{39}$
NGC 3599	sw128	0.01	4.50		$(9.61) \times 10^{-14}$	$(1.50) \times 10^{39}$

Table 18 — *Continued*

Name	ObsID label	N_H^a (10^{22} cm^{-2})	Γ^b	χ^2 (dof)	X-ray flux ^c (erg/s/cm ²)	X-ray Luminosity ^c (erg/s)
NGC 3599	sw129	0.01	4.50		$(6.36) \times 10^{-14}$	$(9.92) \times 10^{38}$
NGC 3599	sw130	0.01	4.50		$(3.22) \times 10^{-13}$	$(5.02) \times 10^{39}$
NGC 3599	sw131	0.01	4.50		$(1.12) \times 10^{-13}$	$(1.75) \times 10^{39}$
NGC 3599	sw132	0.01	4.50		$(5.45) \times 10^{-14}$	$(8.50) \times 10^{38}$
OGLE16aaa	sw133	0.03	4.50		$(2.84^{+3.4}_{-2.3}) \times 10^{-13}$	$(2.25^{+2.7}_{-1.8}) \times 10^{43}$
OGLE16aaa	sw134	0.03	4.50		$(7.73) \times 10^{-14}$	$(6.13) \times 10^{42}$
OGLE16aaa	sw135	0.03	4.50		$(4.25) \times 10^{-14}$	$(3.37) \times 10^{42}$
OGLE16aaa	sw136	0.03	4.50		$(6.28^{+7.9}_{-4.7}) \times 10^{-14}$	$(4.98^{+6.3}_{-3.7}) \times 10^{42}$
Pictor A	sw137	$0.06^{+0.02}_{-0.02}$	$1.63^{+0.09}_{-0.08}$	1.04 (103)	$(8.27^{+8.4}_{-8.1}) \times 10^{-12}$	$(2.18^{+2.2}_{-2.1}) \times 10^{43}$
Pictor A	sw138	$0.00^{+0.05}_{-0.00}$	$1.43^{+0.24}_{-0.13}$	0.79 (17)	$(3.45^{+3.5}_{-2.0}) \times 10^{-12}$	$(9.10^{+9.3}_{-8.0}) \times 10^{42}$
PTF-09axc	sw139	0.03	4.50		$(3.08^{+16.0}_{-9.9}) \times 10^{-14}$	$(1.07^{+8.0}_{-3.4}) \times 10^{42}$
PTF-09axc	sw140	0.03	4.50		$(8.94) \times 10^{-14}$	$(3.11) \times 10^{42}$
PTF-09djl	sw141	0.02	4.50		$(5.20) \times 10^{-14}$	$(5.25) \times 10^{42}$
PTF-09ge	sw142	0.02	4.50		$(3.36) \times 10^{-14}$	$(3.32) \times 10^{41}$
PTF-10iya	sw143	0.01	4.50		$(1.77^{+2.1}_{-1.5}) \times 10^{-13}$	$(2.83^{+3.3}_{-2.4}) \times 10^{43}$
PTF-10iya	sw144	0.01	4.50		$(2.68) \times 10^{-14}$	$(4.29) \times 10^{42}$
PTF-10iya	sw145	0.01	4.50		$(2.23) \times 10^{-14}$	$(3.57) \times 10^{42}$
PTF-10iya	sw146	0.01	4.50		$(3.69) \times 10^{-14}$	$(5.90) \times 10^{42}$
PTF-11glr	sw147	0.02	4.50		$(4.61) \times 10^{-14}$	$(6.13) \times 10^{42}$
SDSS J0939	sw148	$0.12^{+0.22}_{-0.12}$	$3.19^{+1.56}_{-1.13}$	0.55 (2)	$(4.17^{+4.7}_{-3.6}) \times 10^{-13}$	$(4.34^{+4.9}_{-3.7}) \times 10^{43}$
SDSS J0939	sw149	0.12^d	3.19^d		$(1.01^{+1.1}_{-0.9}) \times 10^{-12}$	$(1.05^{+1.2}_{-0.9}) \times 10^{44}$
SDSS J0952	sw150	0.03	4.50		$(1.63) \times 10^{-13}$	$(2.52) \times 10^{42}$
SDSS J1201	sw151	$0.16^{+0.15}_{-0.10}$	$4.29^{+1.11}_{-0.86}$	0.98 (4)	$(2.07^{+2.3}_{-1.9}) \times 10^{-13}$	$(1.24^{+1.3}_{-1.1}) \times 10^{43}$
SDSS J1201	sw152	0.16^d	4.29^d		$(6.10) \times 10^{-14}$	$(3.64) \times 10^{42}$
SDSS J1201	sw153	0.16^d	4.29^d		$(7.12) \times 10^{-14}$	$(4.25) \times 10^{42}$
SDSS J1241	sw154	0.02	4.50		$(3.50^{+4.4}_{-2.6}) \times 10^{-14}$	$(1.42^{+1.8}_{-1.1}) \times 10^{41}$
SDSS J1323	sw155	0.01	4.50		$(3.13) \times 10^{-14}$	$(6.05) \times 10^{41}$
SDSS J1323	sw156	0.01	4.50		$(5.21) \times 10^{-13}$	$(1.01) \times 10^{43}$
SDSS J1323	sw157	0.01	4.50		$(9.37) \times 10^{-14}$	$(1.81) \times 10^{42}$
SDSS J1323	sw158	0.01	4.50		$(7.60) \times 10^{-14}$	$(1.47) \times 10^{42}$
SDSS J1342	sw159	0.02	4.50		$(3.27^{+3.9}_{-2.6}) \times 10^{-14}$	$(1.00^{+1.2}_{-0.8}) \times 10^{41}$
SDSS J1350	sw160	0.01	4.50		$(1.06) \times 10^{-13}$	$(1.59) \times 10^{42}$
SDSS J1350	sw161	0.01	4.50		$(6.37) \times 10^{-14}$	$(9.53) \times 10^{41}$
Swift J1112.2-8238	sw162	$0.22^{+0.05}_{-0.05}$	$1.31^{+0.09}_{-0.09}$	1.19 (97)	$(7.03^{+7.2}_{-6.8}) \times 10^{-13}$	$(4.06^{+4.1}_{-3.9}) \times 10^{45}$
Swift J1644+57	sw163	$0.82^{+0.01}_{-0.01}$	$1.65^{+0.01}_{-0.01}$	1.31 (644)	$(5.53^{+5.5}_{-5.5}) \times 10^{-12}$	$(2.71^{+2.7}_{-2.7}) \times 10^{45}$
Swift J1644+57	sw164	$0.92^{+0.02}_{-0.02}$	$1.59^{+0.03}_{-0.03}$	1.10 (647)	$(8.91^{+9.0}_{-8.9}) \times 10^{-13}$	$(4.36^{+4.4}_{-4.3}) \times 10^{44}$
Swift J1644+57	sw165	$0.97^{+0.06}_{-0.06}$	$1.44^{+0.06}_{-0.06}$	0.99 (347)	$(3.04^{+3.1}_{-3.0}) \times 10^{-13}$	$(1.49^{+1.5}_{-1.5}) \times 10^{44}$
Swift J1644+57	sw166	$1.01^{+0.09}_{-0.09}$	$1.48^{+0.09}_{-0.09}$	1.13 (189)	$(2.27^{+2.3}_{-2.2}) \times 10^{-13}$	$(1.11^{+1.1}_{-1.1}) \times 10^{44}$
Swift J1644+57	sw167	$1.00^{+0.21}_{-0.19}$	$1.50^{+0.19}_{-0.18}$	0.84 (63)	$(9.46^{+9.9}_{-8.9}) \times 10^{-14}$	$(4.63^{+4.9}_{-4.4}) \times 10^{43}$
Swift J1644+57	sw168	$0.68^{+0.46}_{-0.34}$	$1.17^{+0.45}_{-0.39}$	0.86 (14)	$(2.26^{+2.4}_{-2.0}) \times 10^{-14}$	$(1.11^{+1.2}_{-1.0}) \times 10^{43}$
Swift J1644+57	sw169	0.89^e	1.54^e		$(2.21) \times 10^{-14}$	$(1.08) \times 10^{43}$
Swift J1644+57	sw170	0.89^e	1.54^e		$(2.71) \times 10^{-14}$	$(1.33) \times 10^{43}$
Swift J1644+57	sw171	0.89^e	1.54^e		$(3.00) \times 10^{-14}$	$(1.47) \times 10^{43}$
Swift J1644+57	sw172	0.89^e	1.54^e		$(3.39) \times 10^{-14}$	$(1.66) \times 10^{43}$
Swift J1644+57	sw173	0.89^e	1.54^e		$(3.23) \times 10^{-14}$	$(1.58) \times 10^{43}$
Swift J1644+57	sw174	0.89^e	1.54^e		$(3.63) \times 10^{-14}$	$(1.78) \times 10^{43}$
Swift J1644+57	sw175	0.89^e	1.54^e		$(3.42) \times 10^{-14}$	$(1.67) \times 10^{43}$
Swift J1644+57	sw176	0.89^e	1.54^e		$(3.47) \times 10^{-14}$	$(1.70) \times 10^{43}$
Swift J1644+57	sw177	0.89^e	1.54^e		$(2.99) \times 10^{-14}$	$(1.46) \times 10^{43}$
Swift J1644+57	sw178	0.89^e	1.54^e		$(3.21) \times 10^{-14}$	$(1.57) \times 10^{43}$
Swift J1644+57	sw179	0.89^e	1.54^e		$(4.38) \times 10^{-14}$	$(2.14) \times 10^{43}$
Swift J1644+57	sw180	0.89^e	1.54^e		$(4.10) \times 10^{-14}$	$(2.01) \times 10^{43}$
Swift J1644+57	sw181	$0.84^{+0.02}_{-0.02}$	$1.93^{+0.04}_{-0.03}$	1.16 (429)	$(8.74^{+8.8}_{-8.7}) \times 10^{-12}$	$(4.28^{+4.3}_{-4.3}) \times 10^{45}$
Swift J2058+05	sw182	$0.15^{+0.03}_{-0.03}$	$1.37^{+0.08}_{-0.07}$	0.75 (112)	$(1.10^{+1.1}_{-1.1}) \times 10^{-11}$	$(1.43^{+1.3}_{-1.3}) \times 10^{47}$
Swift J2058+05	sw183	0.34^e	1.60^e		$(2.63^{+3.4}_{-1.9}) \times 10^{-14}$	$(3.41^{+4.4}_{-2.5}) \times 10^{44}$
Swift J2058+05	sw184	$0.19^{+0.11}_{-0.08}$	$1.59^{+0.23}_{-0.21}$	1.14 (19)	$(2.96^{+3.1}_{-2.8}) \times 10^{-13}$	$(3.84^{+4.0}_{-3.6}) \times 10^{45}$
Swift J2058+05	sw185	$0.18^{+0.40}_{-0.18}$	$1.50^{+0.65}_{-0.45}$	1.67 (6)	$(8.33^{+9.1}_{-1.5}) \times 10^{-14}$	$(1.08^{+1.2}_{-1.2}) \times 10^{45}$
Swift J2058+05	sw186	0.34^e	1.60^e		$(3.09^{+4.7}_{-1.5}) \times 10^{-14}$	$(4.01^{+6.0}_{-2.0}) \times 10^{44}$
Wings	sw187	0.01	4.50		$(1.23) \times 10^{-13}$	$(1.14) \times 10^{42}$
XMMSL1 J0740-85	sw188	$0.13^{+0.04}_{-0.04}$	$2.90^{+0.30}_{-0.26}$	1.38 (33)	$(1.58^{+1.6}_{-1.5}) \times 10^{-12}$	$(1.04^{+1.1}_{-1.0}) \times 10^{42}$
XMMSL1 J0740-85	sw189	0.11	$2.50^{+0.21}_{-0.20}$	0.84 (11)	$(9.43^{+10.1}_{-8.6}) \times 10^{-13}$	$(6.23^{+6.7}_{-5.7}) \times 10^{41}$
XMMSL1 J0740-85	sw190	$0.16^{+0.16}_{-0.11}$	$2.73^{+0.79}_{-0.62}$	1.09 (4)	$(4.26^{+4.7}_{-3.9}) \times 10^{-13}$	$(2.81^{+3.1}_{-2.6}) \times 10^{41}$
XMMSL1 J0740-85	sw191	0.15^e	2.71^e		$(8.72) \times 10^{-14}$	$(5.76) \times 10^{40}$

Note. — All uncertainties correspond to the 90% confidence level and observations that have similar MJD are combined.

^a N_H is determined either directly from fitting the X-ray emitting spectrum or using the column density derived from the Leiden/Argentine/Bonn (LAB) Survey of Galactic H I (Kalberla et al. 2005)

^b Powerlaw index was derived from either fitting X-ray spectra from either

Table 19

The T_{90} and L_{90} values derived for our *X-ray TDE* and *likely X-ray TDE* candidates.

Name	$T_{90}(10^7 \text{ seconds})$	$L_{90} \text{ (erg/s)}$
ASASSN-14li	3.888 ± 0.022	$(3.45 \pm 1.25) \times 10^{42}$
Swift J1644+57	0.678 ± 0.263	$(5.83 \pm 23.85) \times 10^{45}$
Swift J2058+05	2.129 ± 0.162	$(4.63 \pm 2.43) \times 10^{45}$
XMMSL1 J0740-85	2.121 ± 0.073	$(4.41 \pm 4.75) \times 10^{41}$
2MASX J0249	2.718 ± 0.005	$(8.54 \pm 1.42) \times 10^{40}$
3XMM J152130.7+074916	4.175 ± 0.004	$(6.38 \pm 0.23) \times 10^{42}$
IGR J17361-4441	1.517 ± 0.259	$(4.66 \pm 4.52) \times 10^{42}$
NGC247	1.497 ± 0.003	$(5.31 \pm 4.54) \times 10^{37}$
OGLE16aaa	1.428 ± 0.002	$(4.70 \pm 1.86) \times 10^{42}$
PTF-10iya	0.721 ± 0.011	$(2.26 \pm 3.61) \times 10^{42}$
SDSS J1201	1.242 ± 0.143	$(3.43 \pm 16.61) \times 10^{42}$
SDSS J1311	4.250 ± 0.010	$(1.60 \pm 0.17) \times 10^{42}$
SDSS J1323	1.987 ± 0.689	$(5.37 \pm 10.71) \times 10^{42}$

Table 20

The ratio of the measured N_{H} derived from modelling the X-ray spectra from each event and the corresponding Galactic N_{H} as derived from the Leiden/Argentine/Bonn (LAB) Survey of Galactic H I (Kalberla et al. 2005). These values were used to produce Figure 11.

Name	MJD	Instrument	$N_{\text{H}}(\text{measured})/N_{\text{H}}(\text{Galactic})$
ASASSN-14li	56994.7	swift	7.64 ± 1.77
ASASSN-14li	57046.7	swift	8.75 ± 0.63
ASASSN-14li	57145.8	swift	8.48 ± 1.11
ASASSN-14li	57228.1	swift	8.56 ± 2.25
ASASSN-14li	57364.5	swift	8.31 ± 0.88
ASASSN-14li	57425.5	swift	4.92 ± 3.64
ASASSN-14li	57538.5	swift	2.86 ± 4.51
Swift J1644+57	55649.6	swift	50.60 ± 1.70
Swift J1644+57	55667.4	xmm	57.23 ± 0.85
Swift J1644+57	55675.6	swift	49.40 ± 0.85
Swift J1644+57	55681.3	xmm	62.65 ± 0.85
Swift J1644+57	55697.3	xmm	57.83 ± 3.41
Swift J1644+57	55745.3	xmm	59.04 ± 8.10
Swift J1644+57	55749.3	swift	55.42 ± 1.70
Swift J1644+57	55757.1	xmm	68.07 ± 4.26
Swift J1644+57	55769.1	xmm	70.48 ± 16.66
Swift J1644+57	55787.1	xmm	68.07 ± 5.55
Swift J1644+57	55801	xmm	61.45 ± 8.10
Swift J1644+57	55850.3	swift	58.66 ± 5.11
Swift J1644+57	55947.6	swift	60.84 ± 7.67
Swift J1644+57	56048.1	swift	59.98 ± 16.90
Swift J1644+57	56153.6	swift	40.84 ± 34.22
Swift J2058+05	55708.9	swift	2.29 ± 0.65
Swift J2058+05	55773.5	swift	2.90 ± 2.08
Swift J2058+05	55867.5	swift	2.72 ± 6.70
Swift J2058+05	55886.6	xmm	3.36 ± 3.13
Swift J2058+05	56048.7	xmm	1.33 ± 1.71
XMMSL1 J0740-85	56779.6	swift	12.41 ± 5.29
XMMSL1 J0740-85	56962.8	swift	14.74 ± 18.09
2MASX J0249	48100.2	rosat	12.46 ± 5.81
2MASX J0249	53930.5	xmm	12.46 ± 5.81
IGR J17361-4441	52720	xmm	1.24 ± 0.27
IGR J17361-4441	53481.1	chandra	2.70 ± 0.99
IGR J17361-4441	55794.2	swift	0.69 ± 0.25
IGR J17361-4441	55802.5	chandra	1.46 ± 2.69
IGR J17361-4441	55827.4	xmm	2.28 ± 0.11
IGR J17361-4441	55829.9	swift	2.51 ± 0.22
IGR J17361-4441	55979.2	swift	1.62 ± 1.05
NGC247	56839.2	xmm	9.95 ± 2.11
NGC247	56970.8	swift	5.85 ± 7.46
NGC247	56973.2	chandra	30.35 ± 17.65
SDSS J1201	55369.4	xmm	17.02 ± 8.02
SDSS J1201	55383.7	swift	11.35 ± 12.79
SDSS J1201	55523	xmm	43.26 ± 30.30

REFERENCES

- Alexander, K. D., Berger, E., Guillochon, J., Zauderer, B. A., & Williams, P. K. G. 2016a, *ApJL*, 819, L25
- Alexander, K. D., Wieringa, M. H., Berger, E., Saxton, R. D., & Komossa, S. 2016b, *ArXiv e-prints*, arXiv:1610.03861
- Arcavi, I., Gal-Yam, A., Sullivan, M., et al. 2014, *ApJ*, 793, 38
- Arcavi, I., Wolf, W. M., Howell, D. A., et al. 2016, *ApJ*, 819, 35
- Arnaud, K., Smith, R., & Siemiginowska, A. 2011, *Handbook of X-ray Astronomy*, ed. R. Ellis, J. Huchra, S. Kahn, G. Rieke, & P. B. Stetson
- Ayal, S., Livio, M., & Piran, T. 2000, *ApJ*, 545, 772
- Bade, N., Komossa, S., & Dahlem, M. 1996, *A&A*, 309, L35
- Barres de Almeida, U., & De Angelis, A. 2011, *ArXiv e-prints*, arXiv:1104.2528
- Baumgartner, W. H., Tueller, J., Markwardt, C. B., et al. 2013, *ApJS*, 207, 19
- Bloom, J. S., Butler, N. R., Cenko, S. B., & Perley, D. A. 2011a, *GRB Coordinates Network*, 11847
- Bloom, J. S., Giannios, D., Metzger, B. D., et al. 2011b, *Science*, 333, 203
- Boese, F. G. 2000, *A&AS*, 141, 507
- Bower, G. C., Metzger, B. D., Cenko, S. B., Silverman, J. M., & Bloom, J. S. 2013, *ApJ*, 763, 84
- Bowyer, S., Berghöfer, T. W., & Korpela, E. J. 1999, *ApJ*, 526, 592
- Brandt, W. N., Pounds, K. A., & Fink, H. 1995, *MNRAS*, 273, L47
- Brown, G. C., Levan, A. J., Stanway, E. R., et al. 2015, *MNRAS*, 452, 4297
- Brown, J. S., W.-S. Holoien, T., Auchettl, K., et al. 2016, *ArXiv e-prints*, arXiv:1609.04403
- Burrows, D. N., Kennea, J. A., Ghisellini, G., et al. 2011, *Nature*, 476, 421
- Campana, S., Mainetti, D., Colpi, M., et al. 2015, *A&A*, 581, A17
- Campana, S., Mangano, V., Blustin, A. J., et al. 2006, *Nature*, 442, 1008
- Cannizzo, J. K., Lee, H. M., & Goodman, J. 1990, *ApJ*, 351, 38
- Cappelluti, N., Ajello, M., Rebusco, P., et al. 2009, *A&A*, 495, L9
- Carter, B., & Luninet, J. P. 1982, *Nature*, 296, 211
- Cenko, S. B., Bloom, J. S., Kulkarni, S. R., et al. 2012a, *MNRAS*, 420, 2684
- Cenko, S. B., Krimm, H. A., Horesh, A., et al. 2012b, *ApJ*, 753, 77
- Cenko, S. B., Cucchiara, A., Roth, N., et al. 2016, *ApJL*, 818, L32
- Cheng, K. S., Chernyshov, D. O., & Dogiel, V. A. 2006, *ApJ*, 645, 1138
- Cheng, K. S., Chernyshov, D. O., Dogiel, V. A., Kong, A. K. H., & Ko, C. M. 2016, *ApJL*, 816, L10
- Cheng, R. M., & Bogdanović, T. 2014, *Phys. Rev. D*, 90, 064020
- Chornock, R., Berger, E., Gezari, S., et al. 2014, *ApJ*, 780, 44
- Dai, X., Griffin, R. D., Kochanek, C. S., Nugent, J. M., & Bregman, J. N. 2015, *ApJS*, 218, 8
- De Colle, F., Guillochon, J., Naiman, J., & Ramirez-Ruiz, E. 2012, *ApJ*, 760, 103
- Del Santo, M., Nucita, A. A., Lodato, G., et al. 2014, *MNRAS*, 444, 93
- Donato, D., Cenko, S. B., Covino, S., et al. 2014, *ApJ*, 781, 59
- Dong, S., Shappee, B. J., Prieto, J. L., et al. 2016, *Science*, 351, 257
- Dou, L., Wang, T.-g., Jiang, N., et al. 2016, *ArXiv e-prints*, arXiv:1605.05145
- Drake, A. J., Mahabal, A. A., Djorgovski, S. G., et al. 2010, *The Astronomer's Telegram*, 2544
- Drake, A. J., Djorgovski, S. G., Mahabal, A., et al. 2011, *ApJ*, 735, 106
- Esquej, P., Saxton, R. D., Freyberg, M. J., et al. 2007, *A&A*, 462, L49
- Esquej, P., Saxton, R. D., Komossa, S., et al. 2008, *A&A*, 489, 543
- Evans, C. R., & Kochanek, C. S. 1989, *ApJL*, 346, L13
- Feng, H., Ho, L. C., Kaaret, P., et al. 2015, *ApJ*, 807, 185
- Ferrigno, C., Stevens, J., Bozzo, E., et al. 2011, *The Astronomer's Telegram*, 3617
- Foley, R. J., Blanchard, P. K., Challis, P., et al. 2015, *The Astronomer's Telegram*, 6877
- Frank, J., & Rees, M. J. 1976, *MNRAS*, 176, 633
- Gaskell, C. M., & Rojas Lobos, P. A. 2014, *MNRAS*, 438, L36
- Gelbord, J. M., Mullaney, J. R., & Ward, M. J. 2009, *MNRAS*, 397, 172
- Genzel, R., Schödel, R., Ott, T., et al. 2003, *ApJ*, 594, 812
- Gezari, S., Chornock, R., Lawrence, A., et al. 2015, *ApJL*, 815, L5
- Gezari, S., Halpern, J. P., Komossa, S., Grupe, D., & Leighly, K. M. 2003, *ApJ*, 592, 42
- . 2004, *ApJ*, 601, 1159
- Gezari, S., Basa, S., Martin, D. C., et al. 2008, *ApJ*, 676, 944
- Gezari, S., Heckman, T., Cenko, S. B., et al. 2009, *ApJ*, 698, 1367
- Gezari, S., Chornock, R., Rest, A., et al. 2012, *Nature*, 485, 217
- Gezari, S., Hung, T., Blagorodnova, N., et al. 2016, *The Astronomer's Telegram*, 9433
- Ghez, A. M., Becklin, E., Duchjné, G., et al. 2003, *Astronomische Nachrichten Supplement*, 324, 527
- Ghosh, K. K., Suleymanov, V., Bikmaev, I., Shimansky, S., & Sakhbullin, N. 2006, *MNRAS*, 371, 1587
- Godet, O., Webb, N., Barret, D., et al. 2013, *The Astronomer's Telegram*, 5439
- Alexander, D. M., Bauer, F. E., Brandt, W. N., et al. 2003, *AJ*, 126, 539

- Godoy-Rivera, D., Stanek, K. Z., Kochanek, C. S., et al. 2016, *ArXiv e-prints*, arXiv:1605.00645
- Graham, A. W. 2016, *Galactic Bulges*, 418, 263
- Greiner, J., Schwarz, R., Zharikov, S., & Orio, M. 2000, *A&A*, 362, L25
- Grupe, D., Beuermann, K., Mannheim, K., et al. 1995, *A&A*, 299, L5
- Grupe, D., Komossa, S., & Saxton, R. 2015, *ApJL*, 803, L28
- Grupe, D., Thomas, H.-C., & Leighly, K. M. 1999, *A&A*, 350, L31
- Guillochon, J., Manukian, H., & Ramirez-Ruiz, E. 2014, *ApJ*, 783, 23
- Guillochon, J., & Ramirez-Ruiz, E. 2013, *ApJ*, 767, 25
- . 2015, *ApJ*, 809, 166
- Gültekin, K., Richstone, D. O., Gebhardt, K., et al. 2009, *ApJ*, 698, 198
- Gurzadian, V. G., & Ozernoi, L. M. 1979, *Nature*, 280, 214
- Halpern, J. P., Gezari, S., & Komossa, S. 2004, *ApJ*, 604, 572
- Hasinger, G., Altieri, B., Arnaud, M., et al. 2001, *A&A*, 365, L45
- Hills, J. G. 1975, *Nature*, 254, 295
- Ho, L. C. 2008, *ARA&A*, 46, 475
- Holoien, T. W.-S., Prieto, J. L., Bersier, D., et al. 2014, *MNRAS*, 445, 3263
- Holoien, T. W.-S., Kochanek, C. S., Prieto, J. L., et al. 2016a, *ArXiv e-prints*, arXiv:1602.01088
- . 2016b, *MNRAS*, 455, 2918
- Hoyle, F., & Fowler, W. A. 1963, *MNRAS*, 125, 169
- Hryniewicz, K., & Walter, R. 2016, *A&A*, 586, A9
- Irwin, J. A., Henriksen, R. N., Krause, M., et al. 2015, *ApJ*, 809, 172
- Jiang, Y.-F., Guillochon, J., & Loeb, A. 2016, *ApJ*, 830, 125
- Kaiser, N., Aussel, H., Burke, B. E., et al. 2002, in *Proc. SPIE*, Vol. 4836, *Survey and Other Telescope Technologies and Discoveries*, ed. J. A. Tyson & S. Wolff, 154–164
- Kalberla, P. M. W., Burton, W. B., Hartmann, D., et al. 2005, *A&A*, 440, 775
- Kato, M., & Hōshi, R. 1978, *Progress of Theoretical Physics*, 60, 1692
- Kawamuro, T., Ueda, Y., Shidatsu, M., et al. 2016, *PASJ*, 68, 58
- Kesden, M. 2012, *Phys. Rev. D*, 85, 024037
- Kim, S. S., Park, M.-G., & Lee, H. M. 1999, *ApJ*, 519, 647
- Kochanek, C. S. 1994, *ApJ*, 422, 508
- . 2016, *MNRAS*, 461, 371
- Komossa, S. 2015, *Journal of High Energy Astrophysics*, 7, 148
- Komossa, S., & Bade, N. 1999, *A&A*, 343, 775
- Komossa, S., & Greiner, J. 1999, *A&A*, 349, L45
- Komossa, S., Halpern, J., Scharrel, N., et al. 2004, *ApJL*, 603, L17
- Komossa, S., & Zensus, J. A. 2015, *ArXiv e-prints*, arXiv:1502.05720
- Komossa, S., Zhou, H., Wang, T., et al. 2008, *ApJL*, 678, L13
- Komossa, S., Zhou, H., Rau, A., et al. 2009, *ApJ*, 701, 105
- Kormendy, J., & Gebhardt, K. 2001, in *American Institute of Physics Conference Series*, Vol. 586, *20th Texas Symposium on relativistic astrophysics*, ed. J. C. Wheeler & H. Martel, 363–381
- Kormendy, J., & Ho, L. C. 2013, *ARA&A*, 51, 511
- Kormendy, J., & Richstone, D. 1995, *ARA&A*, 33, 581
- Krimm, H. A., Kennea, J. A., Holland, S. T., et al. 2011, *The Astronomer's Telegram*, 3384
- Lacy, J. H., Townes, C. H., & Hollenbach, D. J. 1982, *ApJ*, 262, 120
- LaMassa, S. M., Cales, S., Moran, E. C., et al. 2015, *ApJ*, 800, 144
- Lasota, J.-P., Alexander, T., Dubus, G., et al. 2011, *ApJ*, 735, 89
- Law, N. M., Kulkarni, S. R., Dekany, R. G., et al. 2009, *PASP*, 121, 1395
- Lawrence, A., Bruce, A. G., MacLeod, C., et al. 2016, *MNRAS*, 463, 296
- Lei, W.-H., Yuan, Q., Zhang, B., & Wang, D. 2016, *ApJ*, 816, 20
- Leloudas, G., Fraser, M., Stone, N. C., et al. 2016, *ArXiv e-prints*, arXiv:1609.02927
- Levan, A. J. 2015, *Journal of High Energy Astrophysics*, 7, 44
- Levan, A. J., Tanvir, N. R., Cenko, S. B., et al. 2011, *Science*, 333, 199
- Levan, A. J., Tanvir, N. R., Starling, R. L. C., et al. 2014, *ApJ*, 781, 13
- Levan, A. J., Tanvir, N. R., Brown, G. C., et al. 2016, *ApJ*, 819, 51
- Li, L.-X., Narayan, R., & Menou, K. 2002, *ApJ*, 576, 753
- Lidskii, V. V., & Ozernoi, L. M. 1979, *Pisma v Astronomicheskii Zhurnal*, 5, 28
- Lin, D., Maksym, P. W., Irwin, J. A., et al. 2015, *ApJ*, 811, 43
- Liu, F. K., Li, S., & Komossa, S. 2014, *ApJ*, 786, 103
- Lodato, G., King, A. R., & Pringle, J. E. 2009, *MNRAS*, 392, 332
- Lodato, G., & Rossi, E. M. 2011, *MNRAS*, 410, 359
- Luminet, J.-P., & Marck, J.-A. 1985, *MNRAS*, 212, 57
- Lynden-Bell, D. 1969, *Nature*, 223, 690
- MacLeod, M., Guillochon, J., & Ramirez-Ruiz, E. 2012, *ApJ*, 757, 134
- Magorrian, J., & Tremaine, S. 1999, *MNRAS*, 309, 447
- Magorrian, J., Tremaine, S., Richstone, D., et al. 1998, *AJ*, 115, 2285
- Maksym, W. P., Lin, D., & Irwin, J. A. 2014a, *ApJL*, 792, L29
- Maksym, W. P., Ulmer, M. P., & Eracleous, M. 2010, *ApJ*, 722, 1035
- Maksym, W. P., Ulmer, M. P., Eracleous, M. C., Guennou, L., & Ho, L. C. 2013, *MNRAS*, 435, 1904
- Maksym, W. P., Ulmer, M. P., Roth, K. C., et al. 2014b, *MNRAS*, 444, 866
- Mangano, V., Burrows, D. N., Sbarufatti, B., & Cannizzo, J. K. 2016, *ApJ*, 817, 103
- Marconi, A., Risaliti, G., Gilli, R., et al. 2004, *MNRAS*, 351, 169
- Margutti, R., Metzger, B. D., Chornock, R., et al. 2016, *ArXiv e-prints*, arXiv:1610.01632
- Marinucci, A., Matt, G., Bianchi, S., et al. 2015, *MNRAS*, 447, 160
- Mazzali, P. A., Deng, J., Nomoto, K., et al. 2006, *Nature*, 442, 1018
- Merloni, A., Dwelly, T., Salvato, M., et al. 2015, *MNRAS*, 452, 69
- Metzger, B. D., Giannios, D., & Mimica, P. 2012, *MNRAS*, 420, 3528
- Miller, J. M., Kaastra, J. S., Miller, M. C., et al. 2015, *Nature*, 526, 542
- Moran, E. C., Barth, A. J., Eracleous, M., & Kay, L. E. 2007, *ApJL*, 668, L31
- Nikołajuk, M., & Walter, R. 2013, *A&A*, 552, A75
- Palaversa, L., Gezari, S., Sesar, B., et al. 2016, *ApJ*, 819, 151
- Pasham, D. R., Cenko, S. B., Levan, A. J., et al. 2015, *ApJ*, 805, 68
- Peng, F.-K., Tang, Q.-W., & Wang, X.-Y. 2016, *ApJ*, 825, 47
- Perley, R. A., Roser, H.-J., & Meisenheimer, K. 1997, *A&A*, 328, 12
- Phinney, E. S. 1989, *Nature*, 340, 595
- Ramirez-Ruiz, E., & Rosswog, S. 2009, *ApJL*, 697, L77
- Ravi, V., & Shannon, R. M. 2015, *The Astronomer's Telegram*, 6904
- Rees, M. J. 1988, *Nature*, 333, 523
- . 1990, *Science*, 247, 817
- Rees, M. J. 1998, in *Black Holes and Relativistic Stars*, ed. R. M. Wald, 79
- Roth, N., Kasen, D., Guillochon, J., & Ramirez-Ruiz, E. 2016, *ApJ*, 827, 3
- Runnoe, J. C., Cales, S., Ruan, J. J., et al. 2016, *MNRAS*, 455, 1691
- Sani, E., Lutz, D., Risaliti, G., et al. 2010, *MNRAS*, 403, 1246
- Saxton, R. D., Motta, S. E., Komossa, S., & Read, A. M. 2015, *MNRAS*, 454, 2798
- Saxton, R. D., Read, A. M., Esquej, P., et al. 2008, *A&A*, 480, 611
- . 2012, *A&A*, 541, A106
- Saxton, R. D., Read, A. M., Komossa, S., et al. 2016, *ArXiv e-prints*, arXiv:1610.01788
- Servillat, M., Farrell, S. A., Lin, D., et al. 2011, *ApJ*, 743, 6
- Shappee, B. J., Prieto, J. L., Grupe, D., et al. 2014, *ApJ*, 788, 48
- Shcherbakov, R. V., Pe'er, A., Reynolds, C. S., et al. 2013, *ApJ*, 769, 85
- Shiokawa, H., Krolik, J. H., Cheng, R. M., Piran, T., & Noble, S. C. 2015, *ApJ*, 804, 85
- Soderberg, A. M., Kulkarni, S. R., Nakar, E., et al. 2006, *Nature*, 442, 1014
- Stern, D., Assef, R. J., Benford, D. J., et al. 2012, *ApJ*, 753, 30
- Stone, N. C., & Metzger, B. D. 2016, *MNRAS*, 455, 859
- Storch-Bergmann, T., Eracleous, M., Livio, M., et al. 1995, *ApJ*, 443, 617
- Strothjohann, N. L., Saxton, R. D., Starling, R. L. C., et al. 2016, *ArXiv e-prints*, arXiv:1605.02749
- Strubbe, L. E., & Murray, N. 2015, *MNRAS*, 454, 2321
- Strubbe, L. E., & Quataert, E. 2009, *MNRAS*, 400, 2070
- Sulentic, J. W., Marziani, P., Zwitter, T., & Calvani, M. 1995, *ApJL*, 438, L1
- Turner, M. J. L., Abbey, A., Arnaud, M., et al. 2001, *A&A*, 365, L27
- Ulmer, A. 1999, *ApJ*, 514, 180
- van Velzen, S., & Farrar, G. R. 2014, *ApJ*, 792, 53
- van Velzen, S., Farrar, G. R., Gezari, S., et al. 2011, *ApJ*, 741, 73
- van Velzen, S., Anderson, G. E., Stone, N. C., et al. 2016, *Science*, 351, 62
- Vaughan, S., Edelson, R., & Warwick, R. S. 2004, *MNRAS*, 349, L1
- Véron-Cetty, M.-P., & Véron, P. 2010, *A&A*, 518, A10
- Vinkó, J., Yuan, F., Quimby, R. M., et al. 2015, *ApJ*, 798, 12
- Voges, W., Aschenbach, B., Boller, T., et al. 1999, *A&A*, 349, 389
- Wang, J., & Merritt, D. 2004, *ApJ*, 600, 149
- Wang, T.-G., Zhou, H.-Y., Komossa, S., et al. 2012, *ApJ*, 749, 115
- Wang, T.-G., Zhou, H.-Y., Wang, L.-F., Lu, H.-L., & Xu, D. 2011, *ApJ*, 740, 85
- Webb, N., Cseh, D., Lenc, E., et al. 2012, *Science*, 337, 554
- Wilms, J., Allen, A., & McCray, R. 2000, *ApJ*, 542, 914
- Wilson, A. S., Young, A. J., & Shopbell, P. L. 2001, *ApJ*, 547, 740
- Wyzykowski, L., Zieliński, M., Kostrzewa-Rutkowska, Z., et al. 2017, *MNRAS*, 465, L114
- Yang, C.-W., Wang, T.-G., Ferland, G., et al. 2013, *ApJ*, 774, 46
- Yu, W., Yan, Z., & Observatory, W. Z. . A. 2015, *The Astronomer's Telegram*, 6887
- Zauderer, B. A., Berger, E., Margutti, R., et al. 2013, *ApJ*, 767, 152
- Zauderer, B. A., Berger, E., Soderberg, A. M., et al. 2011, *Nature*, 476, 425

Table 21

The derived hardness ratio (HR) used to produce Figures 9, 10 and 11. Here HR is defined as $(H-S)/(H+S)$, where H is the counts in the equivalent 2.0-10.0 keV energy band and S is the counts in the equivalent 0.3-2.0 keV energy band. There values were taken from Tables 9–13. Here we have not listed any observations for which we derive upperlimits for the HR ratio. Here uncertainties are one sigma.

Name	MJD	Instrument	Hardness Ratio
ASASSN-14li	56994.7	swift	-0.995 ± 0.225
ASASSN-14li	56999.5	xmm	-0.907 ± 0.006
ASASSN-14li	57046.7	swift	-0.996 ± 0.094
ASASSN-14li	57145.8	swift	-0.993 ± 0.227
ASASSN-14li	57228.1	swift	-0.984 ± 0.027
ASASSN-14li	57364.5	swift	-0.981 ± 0.026
ASASSN-14li	57425.5	swift	-0.965 ± 0.044
ASASSN-14li	57538.5	swift	-0.939 ± 0.057
Swift J1644+57	55649.6	swift	0.036 ± 0.001
Swift J1644+57	55667.4	xmm	-0.056 ± 0.001
Swift J1644+57	55675.6	swift	0.131 ± 0.002
Swift J1644+57	55681.3	xmm	0.055 ± 0.001
Swift J1644+57	55697.3	xmm	-0.126 ± 0.004
Swift J1644+57	55745.3	xmm	0.037 ± 0.004
Swift J1644+57	55749.3	swift	0.202 ± 0.006
Swift J1644+57	55757.1	xmm	0.184 ± 0.006
Swift J1644+57	55769.1	xmm	0.182 ± 0.008
Swift J1644+57	55787.1	xmm	0.211 ± 0.007
Swift J1644+57	55801	xmm	0.179 ± 0.012
Swift J1644+57	55811	xmm	0.186 ± 0.010
Swift J1644+57	55836.9	xmm	0.184 ± 0.009
Swift J1644+57	55850.3	swift	0.272 ± 0.021
Swift J1644+57	55947.6	swift	0.276 ± 0.036
Swift J1644+57	56048.1	swift	0.257 ± 0.015
Swift J2058+05	55708.9	swift	-0.223 ± 0.014
Swift J2058+05	55773.5	swift	-0.341 ± 0.053
Swift J2058+05	55867.5	swift	-0.332 ± 0.092
Swift J2058+05	55886.6	xmm	-0.451 ± 0.051
Swift J2058+05	55902.3	swift	-0.518 ± 0.351
Swift J2058+05	56048.7	xmm	-0.458 ± 0.044
Swift J2058+05	56126.6	swift	-0.138 ± 0.071
Swift J2058+05	56976.1	slew	-0.013 ± 0.008
XMMSL1 J0740-85	56748.9	slew	-0.724 ± 0.392
XMMSL1 J0740-85	56777.2	xmm	-0.624 ± 0.028
XMMSL1 J0740-85	56779.6	swift	-0.721 ± 0.088
XMMSL1 J0740-85	56844.7	swift	-0.670 ± 0.137
XMMSL1 J0740-85	56962.8	swift	-0.687 ± 0.198
XMMSL1 J0740-85	57033.8	xmm	-0.722 ± 0.052
2MASX J0249	53930.5	xmm	-0.883 ± 0.094
2MASX J0249	54075.7	swift	-0.329 ± 0.214
2MASX J0249	54126.8	swift	-0.539 ± 0.289
2MASX J0249	54278.7	swift	-0.737 ± 0.142
2MASX J0249	55360.7	swift	-0.407 ± 0.246
2MASX J0249	55618	swift	-0.144 ± 0.089
3XMM J152130.7+074916	51779.3	xmm	-0.323 ± 0.011
3XMM J152130.7+074916	55219.6	slew	-0.333 ± 0.577
IGR J17361-4441	48710	rosat	-0.952 ± 0.124
IGR J17361-4441	52720	xmm	-0.604 ± 0.035
IGR J17361-4441	53481.1	chandra	-0.768 ± 0.129
IGR J17361-4441	55327.6	swift	-0.447 ± 0.211
IGR J17361-4441	55794.2	swift	0.245 ± 0.009
IGR J17361-4441	55802.5	chandra	0.285 ± 0.077
IGR J17361-4441	55805.7	slew	0.005 ± 0.002
IGR J17361-4441	55827.4	xmm	-0.533 ± 0.049
IGR J17361-4441	55829.9	swift	-0.145 ± 0.005
IGR J17361-4441	55979.2	swift	-0.469 ± 0.104
IGR J17361-4441	56087.3	swift	-0.478 ± 0.222
IGR J17361-4441	56139.4	swift	-0.412 ± 0.103
NGC247	56839.2	xmm	-0.404 ± 0.015
NGC247	56970.8	swift	-0.414 ± 0.088
NGC247	56973.2	chandra	-0.289 ± 0.051
NGC247	57033.5	swift	-0.626 ± 0.239
OGLE16aaa	57547.5	swift	-0.459 ± 0.116
OGLE16aaa	57560.6	swift	-0.792 ± 0.152
PTF-10iya	55358.8	swift	-0.777 ± 0.329
SDSS J1201	55357.3	slew	-0.852 ± 0.237
SDSS J1201	55369.4	xmm	-0.657 ± 0.037
SDSS J1201	55383.7	swift	-0.858 ± 0.180
SDSS J1201	55447.5	swift	-0.320 ± 0.127
SDSS J1201	55523	xmm	-0.244 ± 0.014
SDSS J1311	48821.3	rosat	-0.960 ± 0.148
SDSS J1311	53063.3	chandra	-0.796 ± 0.471
SDSS J1311	53801.6	chandra	-0.399 ± 0.120
SDSS J1323	52975	slew	-0.852 ± 0.483
SDSS J1323	53931.1	xmm	-0.159 ± 0.040

Table 22
The integrated optical/UV and X-ray luminosities used to produce
Figure 12.

Name	X-ray luminosity [erg/s] (0.3-10.0 keV)	Optical/UV luminosity [erg/s] (0.002-0.1 keV)
ASASSN-14li	$(3.37 \pm 0.01) \times 10^{42}$	$(1.78 \pm 0.13) \times 10^{42}$
Swift J1644+57	$(3.51 \pm 1.69) \times 10^{47}$	$(4.72 \pm 0.41) \times 10^{40}$
Swift J2058+05	$(4.97 \pm 4.03) \times 10^{48}$	$(1.73 \pm 0.04) \times 10^{43}$
XMMSL1 J0740-85	$(0.94 \pm 1.90) \times 10^{43}$	$(9.12 \pm 0.56) \times 10^{40}$
NGC247	$(0.75 \pm 0.27) \times 10^{40}$	$(2.61 \pm 0.32) \times 10^{38}$
OGLE16aaa	$(3.61 \pm 1.56) \times 10^{43}$	$(1.05 \pm 0.09) \times 10^{43}$
PTF-10iya	$(1.13 \pm 1.93) \times 10^{43}$	$(3.03 \pm 0.11) \times 10^{43}$
SDSS J1201	$(23.38 \pm 19.71) \times 10^{44}$	$(2.64 \pm 0.31) \times 10^{42}$